

PhD Dissertation



**International Doctorate School in Information and
Communication Technologies**

DISI - University of Trento

**DEVELOPMENT OF BJT RADIATION SENSORS AND
READ-OUT SYSTEMS FOR RADON DETECTION**

Vladyslav Tyzhnevyi

Advisor:

Prof. Gian-Franco Dalla Betta

Università degli Studi di Trento

December 2011

Abstract

In this thesis we present a novel BJT (Bipolar Junction Transistor) detector that was developed and optimized for alpha particle and radon detection and monitoring. Using functional tests, we have shown that BJT detector operated with floating base can efficiently be used for the purpose of α -particle and, consequently, radon gas detection. Basing on these results, we have designed and fabricated a new batch of optimized BJT detectors. The results of electrical and functional characterization of newly fabricated detectors were presented in this work. Fabricated detectors observed high gain, low leakage currents and good detection properties. In parallel to the development of the detector, we successfully designed and implemented FPGA-based readout electronics ALPHADET. Design of the board and results of electrical tests of the board along with extensive data acquired by BJT detectors coupled to the board are presented in the thesis as well. The results of radon tests acquired using BJT detector confirmed that the detector can be successfully used in systems for radon monitoring.

Keywords

[silicon radiation detector, BJT, radon monitor, FPGA-based readout electronics]

List of publications

Conference Papers

- **V. Tyzhnevyyi**, G.-F. Dalla Betta, G. Verzellesi, L. Bosisio, G. Batignani, G. Giacomini, A. Picciotto “BJT detector for α -particle and Radon detection and monitoring,” *IEEE Nuclear Science Symposium Conference Record*, Valencia, 2011.
- D. Saguatti, **V. Tyzhnevyyi**, G. Giacomini, “Alpha-particle monitoring systems based on a BJT detector on high-resistivity silicon,” *7th Conference on PhD Research in Microelectronics and Electronics*, PRIME 2011 (Trento), 2011.
- L. Rovati, G. Verzellesi, M. Bonaiuti, L. Bidinelli, D. Saguatti, G.-F. Dalla Betta, **V. Tyzhnevyyi**, N. Zorzi, S. Bettarini, “A 2.4-GHz wireless alpha-ray sensor for remote monitoring and spectroscopy,” in *Proceedings of 2010 IEEE International Instrumentation and Measurement Technology Conference*, IM2TC 2010, Austin, TX, USA, 2010.
- L. Rovati, G. Verzellesi, M. Bonaiuti, L. Bidinelli, D. Saguatti, G.-F. Dalla Betta, **V. Tyzhnevyyi**, N. Zorzi, S. Bettarini, “Sensore wireless per il monitoraggio remoto di particelle alfa,” *GMEC Conference Proceedings, 2010. GMEC 2010*, pp. 1403 - 1406, 2010. (Title in English: “Wireless sensor for remote alpha-particle monitoring”).
- **V. Tyzhnevyyi**, G.-F. Dalla Betta, “ALPHADET - new FPGA-based readout electronics for alpha-particle detection by BJT-detector,” *Proceedings of the Junior Scientist Conference 2010*, 2010, pp. 153-154.
- **V. Tyzhnevyyi**, G. Batignani, L. Bosisio, G.-F. Dalla Betta, G. Verzellesi, and N. Zorzi, “Laser and alpha particle characterization of floating-base BJT detector,” *NIMA*, vol. 617, no. 1-3, pp. 593-595, 2010.

Journal Papers

- **V. Tyzhnevyy**, G.-F. Dalla Betta, L. Rovati, G. Verzellesi, N. Zorzi, “BJT detector with FPGA-based read-out for alpha particle monitoring,” *JINST*, vol. 6, p. C01051, 2011.
- L. Rovati, S. Bettarini, M. Bonaiuti, L. Bosisio, G.-F. Dalla Betta, **V. Tyzhnevyy**, G. Verzellesi, and N. Zorzi, “Alpha-particle detection based on the BJT detector and simple, IC-based readout electronics,” *JINST*, vol. 4, p. P11010, 2009.

Acknowledgements

During my PhD studies I met many people that influenced my personal and professional growth. I would like to express my sincere gratitude to all of them.

First of all, I would like to thank Prof. Gian-Franco Dalla Betta for his help, advice, motivation and guidance over the last five years, firstly, during my master studies and then during PhD studies. He introduced me to the exciting and interesting field of silicon radiation detectors and then successfully guided through it as a thesis advisor.

Thanks to Prof. Luciano Bosisio, Prof. Giovanni Verzellesi, and Dr. Gabriele Giacomini for their help in layout design of BJT detectors and expertise that they shared during that time. I am thankful to Prof. Giovanni Verzellesi also for the fruitful collaboration and discussions.

Thanks to Dr. Nicola Zorzi who works at FBK (Trento, Italy), he patiently taught me how to use a probe station and then how to make electrical tests using various test structures. Fabrication of the second batch of BJT detectors BD2 has been made at FBK and I am grateful to Dr. Antonino Picciotto for fabricating this batch.

Thanks to ICT Doctoral School that encourages PhD students to go abroad to visit top world universities. That allowed me to have an internship at the ID Lab (the University of Hawaii at Manoa), where I met Prof. Gary Varner and Dr. Michael Cooney. Thanks to them for their hospitality and help with the design and implementation of the FPGA-based electronics.

Thanks to my friends Alena Repchankova, David Macii, Julia Aysina, Jacopo Iannacci and Ekaterina Panina for their support and encouragement during these tough four years of my life. I would especially like to thank Ekaterina Panina for sharing interest in mountain sports, initiatives that kept my social life going and incredible patience during a hard time of thesis write up.

Finally, I would like to thank my family Sergii, Tetiana, and Olga for their love and support during all years of the studies.

Contents

Introduction	1
1 Radon detection methods and instrumentation	5
1.1 Radon gas	5
1.2 Radon health risks	6
1.3 Radon measuring techniques and monitors	8
1.3.1 Grab/Instantaneous sampling	9
1.3.2 Integrating measurement methods	9
1.3.3 Continuous radon measurement methods	12
1.3.4 Commercially available continuous radon monitoring systems	13
1.4 Silicon detectors for α -particle and radon detection and monitoring	14
1.4.1 BJT detector for α -particle detection	18
1.5 Summary	22
2 Functional characterization of the detectors from BD1 batch	23
2.1 Layout of the tested samples	23
2.2 Electrical characterization of the samples	25
2.3 Laser tests	26
2.4 Alpha-particle tests	30
2.4.1 Transimpedance readout	31
2.4.2 ALPHADET readout	33
2.5 Summary	37
3 ALPHADET	39
3.1 Design and layout	39
3.2 Electrical characterization	43
3.2.1 Testing ALPHADET using logic analyzer	43
3.2.2 Testing ALPHADET using ChipScope	48
3.2.3 Analysis of acquired data	50

3.3	Summary	52
4	Fabrication process flow and layout of BD2 batch	55
4.1	Fabrication process flow	55
4.2	Layout description of BD2 batch	61
4.3	Summary	67
5	Electrical characterization of BD2 batch	71
5.1	Planar test structures	71
5.1.1	Generation lifetimes, full depletion voltages, and substrate doping profiles (very large diode)	73
5.1.2	Surface recombination velocity	76
5.1.3	Oxide thickness, substrate doping profiles and charge oxide density (large MOS capacitor)	79
5.2	Test pixels	82
5.3	Arrays of pixels	92
5.4	Summary	96
6	Functional characterization of BD2	97
6.1	Pulsed laser light tests	97
6.2	Alpha-particle tests	105
6.2.1	Comparison of the detection properties of single pixels	106
6.2.2	Detection properties of the arrays	110
6.2.3	The tests with an array of pixels in the temperature range from 0 °C to 30 °C	119
6.3	Radon tests	123
6.4	Summary	124
	Conclusions	127
	Bibliography	129
A	Schematics and layout of ALPHADET board	137
B	Optical system for functional characterization of radiation detectors	149
B.1	APT system architecture	152

List of Tables

2.1	Summary results of functional characterization of DPIX4 and BPAD3 samples.	32
3.1	The structure of data that are written by software to a *.txt file.	45
4.1	Single test BJT pixels. Numeration of the layout cells corresponds to the numeration of the pixels shown in fig. 4.10.	68
5.1	Generation lifetimes for “poly” and “thinned” splittings.	75
5.2	Full depletion voltage values for “poly” and “thinned” splittings.	76
5.3	Surface recombination velocities measured on the wafers from the “poly” and “thinned” splittings.	78
5.4	Oxide thickness profiles for all wafers in BD2 batch. A variable Δ has been calculated as a difference between maximum and minimum value of oxide thickness.	80
5.5	Substrate doping profiles obtained by CV characterization of MOS structures and diodes. $\bar{N}_{d,MOS}$ and $\bar{N}_{d,diode}$ are mean values of doping concentration over a single wafer, for wafer W12 N_d values for every test structure were presented due to the large deviations in the values.	81
6.1	Summary results of functional characterization of die 43 (NCH20xNN14) and die 44 (NCH32xNN16). μ_{peak} , $FWHM_{peak}$, μ_{coll} , and $FWHM_{coll}$ are the mean values and FWHMs of Q_{peak} and Q_{coll} distributions correspondingly. The values in a bold font characterize device with leakage currents increased after dicing and bonding steps.	113
6.2	Summary results of functional characterization of die 45. μ_{peak} , $FWHM_{peak}$, μ_{coll} , and $FWHM_{coll}$ are the mean values and FWHMs of Q_{peak} and Q_{coll} distributions correspondingly. Emitter current values have been acquired at 10 V collector bias and 20 °C.	117

6.3	Summary results of functional characterization of die 24. μ_{peak} , $FWHM_{peak}$, μ_{coll} , and $FWHM_{coll}$ are the mean values and FWHMs of Q_{peak} and Q_{coll} distributions correspondingly. Emitter current values have been acquired at 10 V collector bias and 20 °C.	118
6.4	Summary results of functional and electrical characterization of the NCH32xNN20 array consisting of $1 \times 1 \text{ mm}^2$ pixels in a wide temperature range. The collector bias was 10 V, the distance between source and detector was 13 mm. The values of $Q_{peak,mean}$, $Q_{coll,mean}$, and $ I_e $ were measured, while τ , $\Delta I_e(0)$, β , and C_B were calculated.	122

List of Figures

1.1	^{238}U decay chain, taken from [1] via [2].	7
1.2	Radon measuring techniques. All of them can be based either on radon or radon progenies measurements and can feature either active or passive radon/radon progeny sampling.	8
1.3	Summary of Grab/Instantaneous sampling methods.	9
1.4	Summary of integrating radon detection methods	10
1.5	Summary of continuous radon monitoring methods.	12
1.6	Schematic cross-sections of CMOS monolithic active pixel sensor, [3] . . .	17
1.7	(a) - Schematic cross section of BJT pixel; (b) - Energy band diagram of BJT pixel in forward-active region of operation.	19
2.1	Layout of the tested BJT detectors: (a) - layout of DPIIX detector, consisting of 5x5 pixels ($1.4 \times 1.4 \text{ mm}^2$ each) with NCH32xNN20 emitter layout configuration. Top left corner pixels are bonded individually, while the other 21 pixels have emitters wired together (array configuration); (b) - layout of BPAD pixels having $0.5 \times 0.5 \text{ mm}^2$ base area and minimum size NCH18xNN11 emitter layout.	24
2.2	IV characterization of DPIIX pixels after the bonding: (a) - leakage currents of DPIIX1 - DPIIX4 pixels; (b) - gain curves for DPIIX4 pixel with indicated quiescent gain values for 10 V, 30 V, 50 V, and 70 V collector biases. . . .	25
2.3	Gain curve for the BPAD pixel acquired at 70 V collector bias with indicated quiescent gain values for 10 V, 30 V, 50 V, and 70 V collector biases.	26
2.4	Full depletion voltage V_{depl} measurements. The V_{depl} are 65 V, 101 V, 60 V, and 60 V measured by the test diodes from the TS 26, TS 44, TS 61, and TS 65 test structures respectively.	27
2.5	Schematic representation of the setup consisting of transimpedance amplifier and digital storage oscilloscope used to carry out laser tests of BJT detectors.	27

2.6	Transient response of DPIX3 pixel biased at different collector voltages to 1060 nm laser pulses emulating α -particle with $E_\alpha = 1.41$ MeV energy.	28
2.7	(a)- laser scan of DPIX3 pixels with an energy of light pulse corresponding to the energy of α -particle $E_\alpha = 1.41$ MeV. The step is $100 \mu\text{m}$, bias voltage is $V_{bias} = 70$ V. (b) - Gaussian fits of distribution of Q_{coll} corresponding to the laser scan. Solid line shows multi-peaks Gaussian fit with mean values for the peaks $\mu_1 = 25.0$ pC, $\mu_2 = 37.2$ pC, and $\mu_3 = 44.6$ pC.	29
2.8	laser scan of BPAD3 pixels with an energy of light pulse corresponding to the energy of α -particle $E_\alpha = 1.14$ MeV. The step is $10 \mu\text{m}$, bias voltage is $V_{bias} = 70$ V.	30
2.9	Laser pulsed light test of BPAD3 pixel: (a) - distribution of collected charge values that was built after the laser scan of one of the segments not covered by metal was performed; (b) - transient response of BPAD3 pixel biased at different collector voltages to 1060 nm laser pulses emulating α -particle with $E_\alpha = 1.14$ MeV energy.	31
2.10	Schematic representation of the setup used to test BJT detectors from the BD1 batch consisting of transimpedance amplifier and digital storage oscilloscope.	31
2.11	Functional characterization of DPIX 4 pixel from DPIX array, BD1 batch using transimpedance amplifier readout. The source was placed above the detector at $h_{ds} = 13$ mm height, the temperature was fixed at $T = 20$ °C, and resistance $R = 47$ k Ω : (a) - distributions of collected charge values Q_{coll} . (b) - single peaks, where Q_{coll} values correspond to $\mu_{peak,2}$ mean values of distributions shown in (a) (refer to Table 2.1). The offset level has been subtracted for all curves.	32
2.12	Functional characterization of BPAD3 pixel, BD1 batch using transimpedance amplifier readout. The source was placed above the detector at $h_{ds} = 13$ mm height, the temperature was fixed at $T = 20$ °C, and resistance $R = 47$ k Ω : (a) - distributions of collected charge values Q_{coll} . (b) - single peaks, where Q_{coll} values correspond to mean values of distributions reported in Table 2.1. The offset level has been subtracted for all curves.	33
2.13	A part of data file with an inset showing that just three points were taken into account during integration	34
2.14	Gain distribution for the array of DPIX pixels at 70 V collector bias (3 corner pixels with defects not included)	34

2.15	Spectra acquired by single pixels DPIX1 (a), DPIX2 (c), DPIX3 (b), and DPIX4 (d). The trigger was set to 10 pC; the acquisition time was fixed to 125 s; collector bias was set to 70 V.	35
2.16	Spectra acquired by four DPIX pixels (DPIX1, DPIX2, DPIX3, DPIX4) having emitters shorted together. The trigger was set to 10 pC; the acquisition time was fixed to 125 s; collector bias was set to 70 V.	36
2.17	Functional characterization of the array of DPIX pixels. Distribution of the collected charge values acquired by an array of 21 pixels wired together and read out with a transimpedance amplifier and an oscilloscope.	37
3.1	Power banks of XC2S400 Spartan-3 FPGA.	40
3.2	The block diagram of DDC114 component.	41
3.3	General scheme of ALPHADET electronics.	42
3.4	Implementation of the board (the size is 11×7.5 cm ²).	42
3.5	Block diagram of experimental setup.	44
3.6	Test1, picture of scope screen. The monitored signals are CONV (D2), EN (D5), DATA_CH3(15:8) (D15-D8 correspondingly, only D8, D9 and D11 are shown) and analog input A1.	46
3.7	Test2, picture of scope screen. The monitored signals are CONV (D2), EN (D5), DATA_CH3(15:8) (D15-D8 correspondingly, only D8, D9 and D11 are shown) and analog input A1.	47
3.8	Timing diagram of the Test Mode of the DDC114 [4] [datasheet of DDC114].	48
3.9	TEST signal.	49
3.10	TEST signal.	49
3.11	Typical representation of structure of saved data file. Collected charge is plotted with boxes (left y-axis), while analog input signal is plotted with a red line (right y-axis).	50
3.12	Linearity test of ALPHADET board: (a) - linearity test, (b) - charge occurrence diagram for 10 pC injected charge.	51
3.13	Noise characterization of ALPHADET boards: (a) - board A vs. board B in terms of noise properties, (b) - noise characterization of input channels of board B.	52
4.1	Step 1 and step 2 of fabrication process flow. Step 1 is a first part of substrate contact (collector) formation and preparation of wafers for the following lithography steps. Step 2 is a first part of p-well formation.	56

4.2	Fabrication process flow, step 3 and step 4. Step 3 is a second part of p-well formation, so-called, drive-in. Step 4 is a first part of n-channel formation (n-channel lithography and phosphorus implantation).	57
4.3	Fabrication process flow, step 5 and step 6. Step 5 is a completion of n-channel formation and a first step of shallow n^+ region formation. Step 6 is a completion of shallow n^+ region formation.	58
4.4	Fabrication process flow, step 7 and step 8. Step 7 is a shallow p^+ region formation and a completion of shallow n^+ region formation. Step 8 includes contact and metal lithographies.	59
4.5	Fabrication process flow, step 9 and step 10. Step 9 is an overglass deposition. Step 10 is a deposition of metal on the backside of the wafer and completion of overall fabrication process.	60
4.6	BD2 layout and numeration of the dies.	62
4.7	Layout of a single pixel forming STD_Pixels_400_NCH32xNN20 array. Pixel has “standard” layout configuration, i.e., it has NCH32xNN20 emitter layout and minimum p-well size. The base size of the pixel is $400 \times 400 \mu\text{m}^2$	63
4.8	Layout of the test dies 22, 27, 46, 76 containing test structures.	65
4.9	Layout of single pixels that form STD_pixels_1mm_PP_FR - (a), STD_pixels_1mm_PP_FR_small - (b) and STD_pixels_1mm_PWell_Extend - (c) arrays. Note that “PP over P-well” is not an actual layout layer, it was included into the legend just to ease understanding of the layout. All pixels have emitter layout same as it is shown in fig. 4.7, page 63.	67
4.10	Layout of the test dies 32, 53, 73. Labels in a blue color were actually made during the fabrication process, while labels in black color were made just for illustration purposes to indicate cell names and numerate pixels.	69
5.1	Snapshot of one of the wafers from BD2 batch of BJT detectors.	72
5.2	Snapshot of the die with test structures.	73
5.3	Generation lifetimes for “standard” splitting. (a) - typical plots that were acquired while testing one of the wafers from “standard” splitting; (b) - summarized data.	74
5.4	Full depletion voltage values for the “standard” splitting. (a) - $1/C^2$ plots obtained by testing W1 from the “standard” splitting; (b) - summarized data.	77
5.5	Finger gated-diode.	77
5.6	Surface recombination velocities measured on the wafers from the “standard” splitting. (a) - typical plots that were acquired while testing test structure TS22, wafer W4; (b) - summarized data.	78

5.7	CV characterization of MOS capacitor (a) - CV curve (b) - a schematic representation of a MOS capacitor.	80
5.8	Summarized results of charge oxide density Q_{ox} measurements over all wafers of BD2.	82
5.9	Electrical IV characterization of single test BJT pixels (a) - Gummel plots for three single test BJT pixels with different emitter layout; (b) - collector current I_c vs. collector bias V_{sub} ; (c) - gain curves corresponding to Gummel plots (a); (d) - base potential V_b vs. collector bias V_{sub} . The points, which have the same color as corresponding curve, show a quiescent states of the pixels.	84
5.10	Electrical IV characterization of single test BJT pixels with same emitter layout and base size of $1 \times 1mm^2$ but different base layout configuration. (a) - Gummel plots for four single test BJT pixels with different base layout; (c) - gain curves corresponding to Gummel plots; (b) - collector current I_c vs. collector bias V_{sub} ; (d) - base potential V_b vs. collector bias V_{sub} . The points, which have the same color as corresponding curve, show a quiescent states of the pixels.	85
5.11	Electrical IV characterization of single test BJT pixels with extended p-well base layout configuration and different emitter layouts. The base sizes were $400\mu m$ and $500\mu m$, while emitter layouts were NCH32xNN16 and NCH20xNN14. (a) - Gummel plots; (b) - collector current I_c vs. collector bias V_{sub} ; (c) - gain curves corresponding to Gummel plots; (d) - base potential V_b vs. collector bias V_{sub} . The points, which have the same color as corresponding curve, show a quiescent states of the pixels.	86
5.12	Electrical IV characterization of single test BJT pixels with "standard" emitter and base layout. The only difference between pixels is the base size ($800 \times 800\mu m^2$, $1 \times 1mm^2$, $1.1 \times 1.1mm^2$, and $1.4 \times 1.4mm^2$). (a) - Gummel plots; (b) - collector current I_c vs. collector bias V_{sub} ; (c) - gain curves corresponding to Gummel plots; (d) - base potential V_b vs. collector bias V_{sub} . The points, which have the same color as corresponding curve, show a quiescent states of the pixels.	87

5.13	Electrical IV characterization of single test BJT pixels that have p-well layout of “standard” pixel like in BD1 batch (pixel STD 1.4mm (BD1)) and p-well layout of “standard” pixel like in BD2 batch (pixel STD 1.4mm (BD2)). (a) - Gummel plots; (b) - collector current I_c vs. collector bias V_{sub} ; (c) - gain curves corresponding to Gummel plots; (d) - base potential V_b vs. collector bias V_{sub} . The points, which have the same color as corresponding curve, show a quiescent states of the pixels.	88
5.14	Uniformity test of gain properties of BJT pixels. (a) and (c) - very uniform Gummel plots and gain curves that were acquired while testing wafer W7 from the “poly” splitting; (b) and (d) - non-uniform Gummel plots and gain curves (W2, “standard” splitting).	89
5.15	(a) - one of the Van der Pauw structures. The central part that has a from of cross is an implant, the metal contacts are numerated. The arrows represent forced current flow between contact 1 and contact 2. (b) - a test structure designed to measure a contact resistance value.	90
5.16	Sheet resistance measurements. (a) - acquired IV plots for one of the pads of Van der Pauw structure, when the pad was used as a diode. The curve in a black color was acquired before oxide breakdown, while the curve in a red color was acquired after the oxide breakdown. (b) - sheet resistance plots for p^+ Van der Pauw test structure.	91
5.17	IV characterization of large $1 \times 1cm$ arrays from the wafer W7. Only those arrays that have emitters shorted together are shown in this figure.	92
5.18	IV characterization of large $1 \times 1cm$ arrays from the wafer W2 (“standard” splitting).	94
5.19	IV characterization of large $1 \times 1cm$ arrays from the wafer W11 (“thinned” splitting). Only those arrays that have emitters shorted together are shown in this figure.	95
6.1	Laser scan of NCH32xNN20 array, the step of scan is $100 \mu m$. Schematic sketch of the layout is to show positioning of the scanned detector and its boundaries.	98
6.2	(a) - Gaussian fit of distribution of Q_{coll} . $Q_{coll,mean} = 21.42$ pC; (b) - laser light calibration plot acquired by D400FC detector [5], amplified by THS4303 amplifier and then visualized and saved via TDS3052B oscilloscope [6]. The equivalent energy of α -particle corresponding to such laser pulse is ≈ 1.8 MeV.	99

6.3	Laser scan with an energy of light pulse corresponding to the energy of α -particle $E_\alpha \approx 4MeV$ (a) - NCH32xNN20 array; (b) - NCH32xNN11 array; (c) - NCH18xNN11 array. The step is $200\mu m$, bias voltage is $V_{bias} = 10V$. Note that the charge axes ranges are different.	100
6.4	Gaussian fits of the distributions corresponding to the laser scans plotted in fig. 6.3. Mean values are 48.5 pC, 62.6 pC, and 69.1 pC for NCH18xNN11 , NCH32xNN20 , and NCH32xNN11 arrays correspondingly.	101
6.5	Laser scan of die 45, w7 with an energy of light pulse corresponding to the energy of α -particle $E_\alpha \approx 4.1$ MeV. (a) - Standard array; (b) - PP FR array; (c) - PP FR small array; (d) - PW extend array. The step is $400 \mu m$, $V_{bias} = 10$ V. Note that the charge axes ranges are different.	102
6.6	Gaussian fits of the distributions corresponding to the laser scans of die 45, w7 plotted in fig. 6.5. The equivalent energy of α -particle corresponding to the laser pulse is ≈ 4.1 MeV.	103
6.7	Laser scans of: (a) - Pix200 , (b) - Pix400 from die 43, w7 and (c) - Pix200 , (d) - Pix400 from die 44, w7. The step is $50 \mu m$	104
6.8	Gaussian fits of distribution of Q_{coll} corresponding to the laser scan of Pix400 array from die 43, w7 plotted in fig. 6.7(b). Solid line shows multi-peaks Gaussian fit with mean values for the peaks $\mu_1 = 31.6$ pC and $\mu_2 = 37.0$ pC.	105
6.9	Setup used for α -particle characterization of BJT detectors.	106
6.10	A part of data file acquired during functional characterization of STD 1.4mm single test pixel. The dashed line represents 2.5 pC “soft” trigger.	107
6.11	(a) - family of I_e vs V_{sub} curves acquired at different temperatures, the tested device was Pix400 (w7, die 73); (b) - dependence on temperature of emitter current measured at 10 V bias after the dicing and bonding, the tested devices are Pix400 and STD 1.4mm, red points show emitter current values at 10 V bias acquired before dicing.	108
6.12	A comparison of the detection properties of two pixels that have the maximum and the minimum size of their bases. Emitter size is the same for both devices (NCH32xNN20). (a) - distributions of collected charge values; (b) - distributions of peak values.	109

6.13	Functional characterization of Die 43 using ^{241}Am source of α -particles. The plots correspond to the $5 \times 5\text{mm}^2$ arrays with NCH20xNN14 emitter layout and $200 \times 200\mu\text{m}^2$, $300 \times 300\mu\text{m}^2$, $400 \times 400\mu\text{m}^2$, and $500 \times 500\mu\text{m}^2$ base areas. The plots refer to the distributions of collected charge values Q_{coll} acquired at 10 V bias; the temperature was fixed at 20 °C and the distance between detector and source (h_{ds}) was 13 mm.	110
6.14	Functional characterization of Die 43 using ^{241}Am source of α -particles. The plots (a), (b), (c), and (d) correspond to the $5 \times 5\text{mm}^2$ arrays with NCH20xNN14 emitter layout and $200 \times 200\mu\text{m}^2$, $300 \times 300\mu\text{m}^2$, $400 \times 400\mu\text{m}^2$, and $500 \times 500\mu\text{m}^2$ base areas correspondingly (disposition of plots corresponds to the actual disposition of the arrays on the die). The plots refer to the distributions of collected charge peak values Q_{peak} acquired at $V_{bias} = 10\text{ V}$, $T = 20\text{ °C}$, and $h_{ds} = 13\text{ mm}$	112
6.15	IV characterization of die 43, w7. The leakage current plots show that one of the arrays (Pix200) has changed its properties after dicing and bonding steps while other arrays have not changed their leakage currents (note the much wider scale used for the currents in case of Pix200).	113
6.16	Functional characterization of Die 44 (W7) using ^{241}Am source of α -particles. The plots correspond to the $5 \times 5\text{mm}^2$ arrays with NCH32xNN16 emitter layout and $200 \times 200\mu\text{m}^2$, $300 \times 300\mu\text{m}^2$, $400 \times 400\mu\text{m}^2$, and $500 \times 500\mu\text{m}^2$ base areas. The plots refer to the distributions of collected charge peak values Q_{peak} acquired at $V_{bias} = 10\text{ V}$, $T = 20\text{ °C}$, and $h_{ds} = 13\text{ mm}$. (The leakage currents of all four arrays remained unchanged after the bonding step.)	114
6.17	Functional characterization of die 44, w7 using ^{241}Am source of α -particles. The plots (a), (b), (c), and (d) correspond to the $5 \times 5\text{mm}^2$ arrays with NCH32xNN16 emitter layout and $200 \times 200\mu\text{m}^2$, $300 \times 300\mu\text{m}^2$, $400 \times 400\mu\text{m}^2$, and $500 \times 500\mu\text{m}^2$ base areas correspondingly (disposition of plots corresponds to the actual disposition of the arrays on the die). The plots refer to the distributions of collected charge peak values Q_{peak} acquired at $V_{bias} = 10\text{ V}$, $T = 20\text{ °C}$, and $h_{ds} = 13\text{ mm}$. (The leakage currents of all four arrays remained unchanged after the bonding step.)	115
6.18	IV characterization of die 45, w7. (a) - leakage currents of the arrays after the bonding step; (b) - leakage currents of the arrays at 10 V collector bias measured versus temperature. The red symbols are I_e values acquired before the bonding was made.	116

6.19	Functional characterization of die 45, w7 using ^{241}Am source of α -particles. All arrays have same emitter layout but different base layout. For further details on layout refer to section 4.2, p. 67. (a) - shows distributions of collected charge values Q_{coll} ; (b) - shows distributions of collected charge peak values Q_{peak} . The data were acquired at $V_{bias} = 10\text{ V}$, $T = 20\text{ }^\circ\text{C}$, and $h_{ds} = 13\text{ mm}$	116
6.20	IV characterization of die 24 (w7) after dicing and bonding steps. (a) - leakage currents of the arrays; (b) - leakage currents of the arrays at 10 V collector bias measured versus temperature. The red symbols are I_e values acquired before the dicing and bonding were made.	117
6.21	Functional characterization of die 24 (w7) using ^{241}Am source of α -particles. All arrays have same base layout but different emitter layout. (a) - shows distributions of collected charge values Q_{coll} ; (b) - shows distributions of collected charge peak values Q_{peak} . The data were acquired at $V_{bias} = 10\text{ V}$, $T = 20\text{ }^\circ\text{C}$, and $h_{ds} = 13\text{ mm}$	118
6.22	Functional characterization of die 24 (W11) using ^{241}Am source of α -particles. All arrays have same base layout but different emitter layout. (a) - shows distributions of collected charge values Q_{coll} ; (b) - shows distributions of collected charge peak values Q_{peak} . The data were acquired at $V_{bias} = 10\text{ V}$, $T = 20\text{ }^\circ\text{C}$, and $h_{ds} = 13\text{ mm}$	119
6.23	Test of NCH32xNN20 array from die 24, w7 in a wide temperature range (the distance between source and the array was 13 mm): (a) - distribution of collected charge values; (b) - distribution of peak values.	120
6.24	Mean values of the gaussian fits of Q_{coll} (left y-axis) and Q_{peak} (right y-axis) distributions collected under different temperatures. The exponential fit of the peak mean values is $Q_{peak,mean} = 0.224 \cdot e^{T/10.298}$ and the exponential fit of the charge mean values is $Q_{coll,mean} = 4.253 \cdot e^{T/11.343}$	121
6.25	(a) Base-emitter capacitance of single NCH32xNN20 pixel with $800 \times 800\text{ }\mu\text{m}^2$ base size measured at different temperatures. (b) - summarized data. . . .	122
6.26	Radon test. (a) - data acquired using a STD_Pixels_400_NCH32xNN20 detector coupled to microcontroller based readout electronics [7]; (b) - data acquired using a calibrated continuous radon monitor; (c) - calibration curve for the developed system.	123
B.1	KT112, single mode and multimode fiber coupler: 5.6 mm and 9 mm laser diodes [8].	150
B.2	(a) light beam is projected from the fiber directly on the surface of the detector. The light spot has $560\text{ }\mu\text{m}$ diameter. (b) light beam is focused. . .	151

B.3	Schematic representation of the designed optical system. \longleftrightarrow - double headed arrows mean that communication between components can be done in both directions, while \longrightarrow single headed arrows mean that communication can be done only in the indicated direction.	152
B.4	APT system architecture diagram. The system comprises of APT software block (on the right) and of APT hardware unit blocks (two “TDC001” blocks on the left).	153
B.5	KT112, single mode and multimode fiber coupler: 5.6 mm and 9 mm laser diodes [8].	153

Introduction

The problem of radon exposure causing health damage is known since a very long time. Already in 15th century it was noticed that miners were dying from respiratory diseases [9]. The hypothesis that exposure to elevated levels of radon concentrations, which is usually present in mines, can cause lung cancer was advanced at the beginning of 20th century. The reported studies in 50s and 60s of 20th century concerning miners' health confirmed that radon exposure can cause lung cancer. Further studies of health risks related to indoor radon exposure showed that there is a linear relationship between lung cancer risk and exposure to even low radon concentrations, i.e., there is no a particular threshold after which radon becomes harmful. Thus, due to its ubiquitous presence in dwellings, it should be always monitored and prevented or mitigated. As radon detection problem has been approached since the middle of last century, nowadays this field of science is a very well established field. There are plenty of developed methods, techniques and, consequently, systems of radon monitoring. Almost all radon detection methods are based on the detection of either alpha or gamma radiation emitted during decay of radon itself and its short lived progeny.

The objective of our research was to develop a BJT detector optimized for radon monitoring and detection that can be done either indoor or outdoor. In this thesis we consider only those methods of radon monitoring and detection that rely on α -particle detection since the developed BJT detector is better suited for the detection of α -particles rather than for the detection of γ or β rays. Chapter 1 summarizes the field of radon detection and monitoring through a survey of already developed radon monitoring techniques, state of the art radon monitoring systems that are already present on the market or just being under the development and radon monitoring systems based on a silicon detector.

As it will be shown in Chapter 1, the niche for BJT detector use is integrating and continuous radon monitoring systems operated with battery power supply, i.e., low-power consumption should be considered as a primary goal. In order to show that the detector could satisfy requirement of low-power consumption, results of functional tests performed using BJT detectors from the BD1 batch, which were already available at the beginning of the studies, will be presented. These tests were carried out to verify how BJT detectors

would detect α -particles while being operated with floating base, i.e., being self-biased. This mode of operation is intrinsically low power consuming. In fact, the detector is always in the idle state consuming just the power dissipated due to the leakage current (usually it is a few nA) unless α -particle hits it. When particle hits the detector, it automatically turns BJT on. In other words, effective operation of BJT detector with floating base is a way to implement low power consuming and, hence, portable radon monitoring system with battery power supply. The first results of laser and alpha particle characterization of floating-base BJT detectors were published in our paper [10]. Chapter 2 presents extended description of these results.

One of the advantages that provides use of a BJT detector in a monitoring system is that it does not require high-performance and, hence, costly readout electronics. On the contrary, readout electronics can be made using only commercially available rather inexpensive off-the-shelf components. The microcontroller based version of this electronics was presented in [11]. In this work we will present a different type of readout electronics that was also presented in our paper [12]. The electronics was called ALPHADET (from ALPHA DETection). It is FPGA-based electronics, which is completely compatible with microcontroller based electronics. The choice of FPGA as a core of a readout system gives few relevant advantages at a prototyping stage. First of all, it is a possibility to implement good debugging facilities on the board that allow fast programming and reprogramming of FPGA. Another advantage of ALPHADET is a use of convenient USB connection between the board and user PC, so the option of on-the-fly processing of acquired data becomes available. As a result, this electronics has become very convenient for the laboratory use. Chapter 3 describes design and layout of the printed circuit board together with a concise explanation of the choice of components and their specific purpose on the board. The results of electrical characterization of this electronics are presented in this Chapter as well.

Basing on the available experience, results of functional tests, and layout design know-how, a new batch of BJT detectors with optimized layout has been designed and fabricated. Chapter 4 describes improved fabrication process flow developed at FBK, Trento. It establishes a connection between fabrication process and layout of new BD2 batch of BJT detectors. List and description of all relevant layout cells of single test BJT pixels, BJT arrays and test structures can be found in the Chapter 4.

After the fabrication of the second batch of BJT detectors (so-called BD2) was finalized a set of electrical tests was performed. These tests aimed at verifying fabrication process characteristics, i.e, extraction of process parameters that most influence BJT performance and also at estimation of such properties of BJT as gain, leakage current and base potential at particular collector bias. Summary data of all the tests will be presented in Chapter 5.

These data characterizes silicon properties, single BJT pixels, and BJT arrays. The difference between detectors from different splittings will be discussed. We will show that the detectors from “standard” and “poly” splittings can be safely used with designed readout electronics, while detectors from “thinned” splitting can not.

Finally, functional characterization of BJT detectors from the BD2 batch is discussed in Chapter 6. The characterization includes laser and α -particle tests. The performance of BJT detectors will be analyzed considering use of the detectors in radon monitoring system with implemented electrostatic collection of radon progeny on the surface of the detector, where quite high energies of α -particles are expected. At the end of the thesis conclusions about overall performance of newly fabricated BJT detectors will be drawn and suggestions for further layout modifications will be provided.

Chapter 1

Radon detection methods and instrumentation

In this Chapter we will discuss different radon detection and monitoring techniques and methods. As the problem of radon exposure causing health damage is known since a very long time, field of science dealing with radon monitoring is well established. There are plenty of developed radon monitoring systems but only the most widely used and those systems employing silicon radiation detectors for α -particle detection will be described here.

Section 1.1 shortly introduces properties of radon gas and ^{238}U decay chain that has radon as one of the descendants. Then section 1.2 describes health risks associated with exposure to radon. Finally, different techniques and methods of radon detection and monitoring together with description of some popular commercially available monitors will be presented in section 1.3. After that a BJT detector and its, so-called, floating base operation mode will be shortly introduced.

The main idea of this Chapter is to determine a niche for the use of novel BJT detector in the field of radon detection and monitoring. As it will be shown throughout this and next Chapters BJT detector operated with a floating base is well suited for being used in portable instrumentation like continuous radon monitors and dosimeters.

1.1 Radon gas

Radon is a chemically inert, radioactive, colorless and odorless gas that emanates from soil and rocks. Three radon isotopes ^{222}Rn , ^{220}Rn , and ^{219}Rn are known, which are called radon, thoron, and actinon, respectively. Radon is a descendant from the ^{238}U decay chain, while thoron is a descendant from the ^{232}Th decay chain and actinon is a

descendant from the ^{235}U decay chain. As thoron and actinon have very short half-lives of 55.6 s and 3.96 s, respectively, comparing to the radon that has half-life of 3.82 days, they are very rare gases in the atmosphere. Thus, later on we will discuss just the radon gas. Figure 1.1 shows ^{238}U decay chain. Radon has four short-lived progeny - ^{218}Po , ^{214}Pb , ^{214}Bi , and ^{214}Po . All methods of radon monitoring are based on the detection of either α -particles or γ -rays emitted during the decays both of ^{222}Rn and its progeny.

1.2 Radon health risks

Current concern about acceptable level of indoor radon concentration and actual need of indoor radon gas monitoring has initially been derived from a clear evidence that occupational lung cancer strongly correlates with exposures to elevated radon concentrations [13], [14], [15]. As it was found in 70s and 80s that radon gas was an ubiquitous air pollutant in homes, additional studies were made to estimate lung cancer risk in case of exposure to low, comparing to those in mines, radon gas concentrations. The results of the studies were summarized in the National Council report [9]. It was concluded by the report that around 4% death from lung cancer could be possibly avoided if indoor radon concentration was kept lower than 148 Bq/m^3 (action level guideline according to the Environmental Protection Agency, US). Further epidemiological studies and analyses, for example, presented in [16], [17], [18], confirmed again a clear evidence that lung cancer can be caused by exposure to radon gas. Finally, World Health Organization summarized all knowledge about radon health effects, radon measurements, and mitigation and prevention techniques in a handbook on indoor radon, [19].

Although Radon was initially considered as a main contributor to the delivered dose to the lungs, then it was found that the dose is mainly delivered by α -particles released during decays of short-lived radon progeny ^{218}Po and ^{214}Po (refer to the radon decay chain scheme shown in 1.1). During recoil movement of alpha-particle that has enough energy to strip off the orbital electrons of the parent atom radon progeny become positively charged. At the end of the recoil movement a parent ionized atom slows down to the thermal velocity and so probability to capture electrons considerably increases. Therefore, about 88% of all polonium atoms are positively charged and remaining 12% are neutral. Due to the fact that polonium ions are positively charged they can attach to the dust particles and penetrate lungs with inhaled air.

When polonium decays, emitted α -particles can disrupt DNA of the lung cells making major genomic changes in a cell that can become one of the steps in a chain of events leading to the lung cancer. Moreover, existing studies show that there is no any particular level after which radon exposure becomes harmful to the health; there is clear evidence

^{238}U Decay Scheme

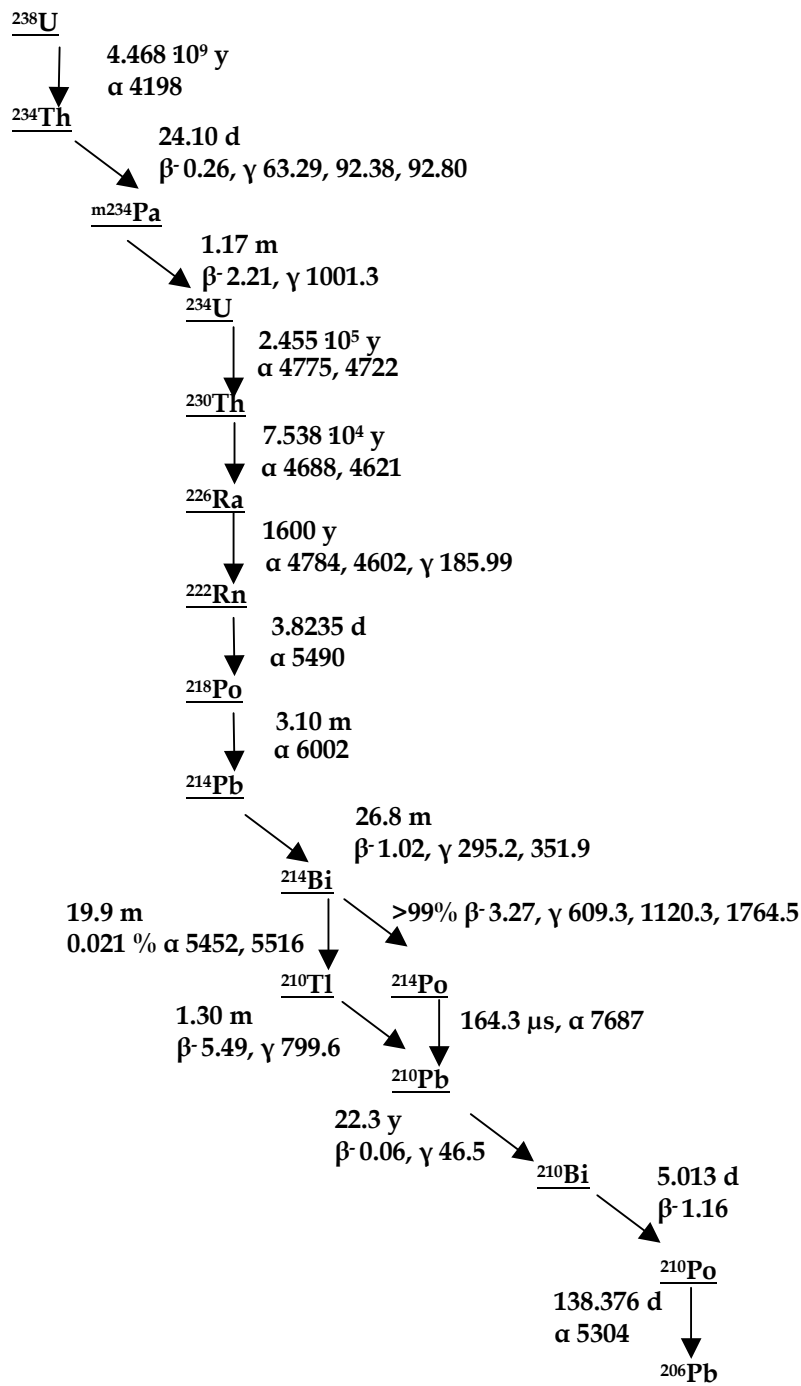


Figure 1.1: ^{238}U decay chain, taken from [1] via [2].

that any exposure to radon poses a risk for the health [13], in fact, the relation between cancer risk and radon exposure is linear. Taking into account that this relation is linear the

health risks can be greatly decreased by radon prevention (in case of newly built dwellings) or mitigation (in case of existing old dwellings). In other words, radon monitoring should continuously be done in order to: 1) identify dwellings with higher than acceptable level of radon gas concentration; 2) determine effectiveness of radon prevention or mitigation methods. Depending on the mechanism of radon gas contribution, e.g., pressure-driven gas infiltration from soils (typical concentrations of radon in soil vary from 10000 till 50000 Bq/m³), radon emanation from building materials and tap water [19], in some cases from outdoor air and domestic gas [20], different strategies for prevention and mitigation can be used. However, mainly all of them are based on establishing barriers for gas penetration and ventilation. In order to, firstly, determine if a dwelling or working place or a place where public is likely to stay a long time (for example, schools etc.) has elevated radon gas concentration and then to find gas entrance points, radon gas monitoring must be done. Overview of different radon detection/monitoring methods and systems will be presented in section 1.3.

1.3 Radon measuring techniques and monitors

Radon measuring techniques can be classified as those that are based on the detection of radon itself or radon progeny. Further classification can be done basing on sampling method. Figure 1.2 shows three main groups of radon measuring techniques: grab or instantaneous, integrating and continuous [21], [22]. Each technique has advantages and disadvantages that, mainly, depend on time needed to measure concentration, precision, easiness of use and cost-effectiveness of tests.

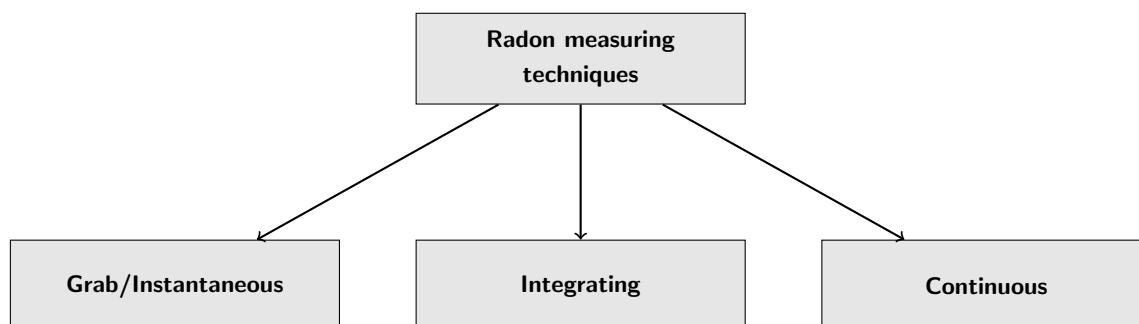


Figure 1.2: Radon measuring techniques. All of them can be based either on radon or radon progenies measurements and can feature either active or passive radon/radon progeny sampling.

1.3.1 Grab/Instantaneous sampling

Summary of grab sampling methods can be found in fig. 1.3. Samples are collected during short-time intervals using active sampling device, i.e., air pump, and then analyzed. Grab sampling method is used to localize radon entrance points. The instruments that rely on radon sampling are ionization chambers (for example, AlphaGUARD system [23]) and scintillation cells (for example, from Pylon models of Lucas scintillation cell¹ or scintillation flasks from ALGADE²). Another type of instrumentation used for instantaneous radon measurements relies on sampling of radon progenies on the filter, which is analyzed thereafter either by silicon detector or ZnS(Ag) scintillator plus photomultiplier tube based systems. The analysis of radon concentration can be done both by means of gross alpha counting and by means of spectrometry. Modern state-of-the art radon monitors allowing spectrometric analysis can combine instantaneous and continuous radon monitoring techniques³.

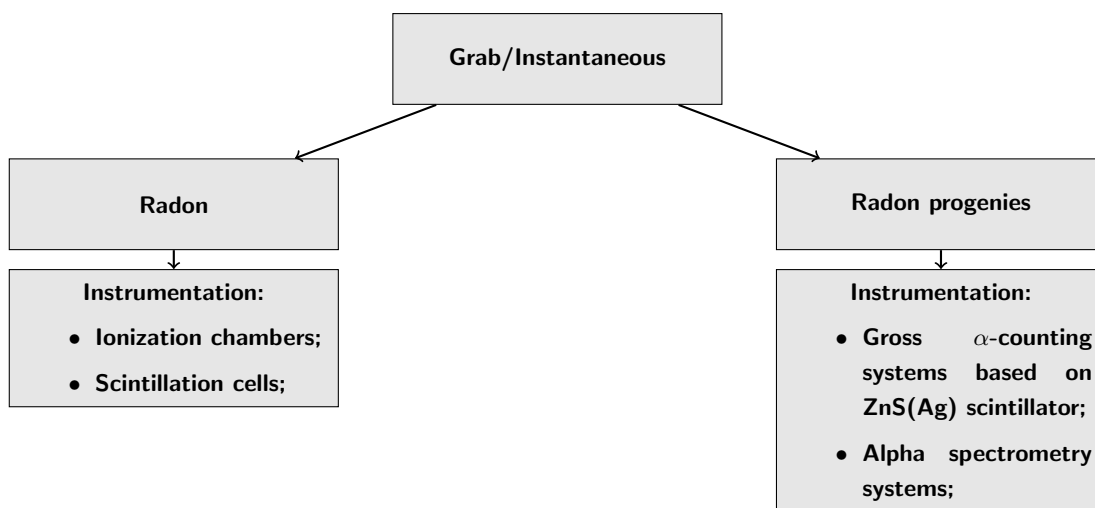


Figure 1.3: Summary of Grab/Instantaneous sampling methods.

1.3.2 Integrating measurement methods

Integrating radon monitoring methods are widely used methods due to their cost effectiveness and easiness of use. The most popular monitors are activated carbon monitors and solid state nuclear track detectors (SSNTD). While activated carbon monitors are used for short term sampling periods, SSNTDs are used for long term sampling periods

¹<http://www.pylonelectronics.com/pylonpdfs/DS126R2.pdf>

²<http://www.algade.com/index.php/english/Mesure-ponctuelle-du-radon/>

³http://www.durridge.com/documentation/R7MAN_v7.1.3.pdf (short explanation of instantaneous SNIFF mode of radon measurement by RAD7 can be also found on page 13)

(up to one year). Many large surveys were made using these detectors, e.g., [16], [18]. Summary of integrating radon monitoring methods is shown in fig. 1.4.

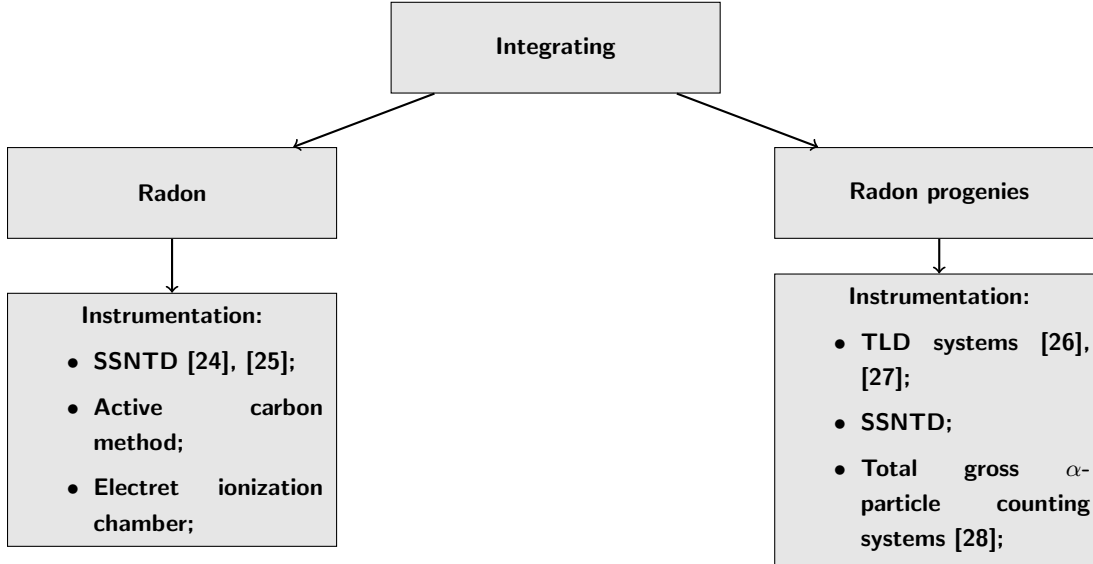


Figure 1.4: Summary of integrating radon detection methods

Solid state nuclear track detectors (SSNTD). SSNTDs are mainly used for integrating radon monitoring using passive sampling. The main types of SSNTD are CR39 and LR115 plastic films. These plastic films are sensitive to α -particles that leave tracks in the material. The tracks are etched afterwards in, usually, NaOH (or KOH) solution by chemical or electrochemical etching to make tracks visible under a low-power microscope. Then the tracks are counted and corresponding dose is calculated. For example, assuming that SSNTD is CR39 with a quite good sensitivity of 4 tracks/cm² per 1 kBq/m³/h [29], [30], then the exposure of this detector to 50 Bq/m³ for 90 days would result in 4 tracks/mm². SSNTD detectors are also used to measure response just from radon progeny, to that purpose electret or electrostatic collection methods are used that drastically increase response of the detectors, e.g., the response of CR-39 increases from upper theoretical limit of 14 tracks/cm² per 1 kBq/m³/h in case of passive collection of radon till 2486 and 5000 tracks/cm² per 1 kBq/m³/h for electret and electrostatic collection, respectively [25].

Active carbon method. Activated carbon monitor (also referred to as charcoal canister) is mainly used for passive and short term (few days) radon sampling. During sampling period radon adsorbs from the air onto activated carbon and its concentration then can be determined by gamma or alpha and beta spectroscopy [21]. In gamma spectroscopy usually areas under peaks from ²¹⁴Pb (242 keV, 295 keV and 352 keV) and ²¹⁴Bi (609 keV) are considered (refer to ²³⁸U decay chain shown in fig. 1.1). Gamma rays are

detected either by NaI(Tl)⁴ attached to photomultiplier tube that is fed to multichannel analyzer or by germanium detector. This method of radon monitoring is appreciated for the convenience of sampling. It was shown that even respirator filter can be used for the sampling [31]. The sensitivity of standard charcoal canister is 50 Bq/m³ with 50 % precision [29], thus, activated carbon monitors are better suited for screening purposes rather than for precise measurements. Although this method is mainly used for passive radon measurements, charcoal canisters are used as well for active radon collection.

Electret ionization chamber is mainly used for passive, integrating radon monitoring. Electret is a teflon disk that has a large (few hundred volts) voltage gradient maintained between the surfaces of the disk. Presence of voltage gradient is achieved by orienting dipoles present in original heated teflon material using electric field. After the material is cooled down it can keep the position of oriented dipoles [27]. When α -particle or γ -photon hits electret, the surface voltage of the electret drops down due to the partial neutralization of the charge of electret. For example, electret used for short-term radon measurements yields a voltage drop of 0.054 V per Bq/m³ per day, i.e., 2 V per pCi/l per day, [21]. To determine radon concentration the measured voltage drop should be divided by a calibration factor and duration of this measurement. One of the disadvantages of this device is that it is sensitive to γ radiation, which should be measured as well and then extracted.

The only commercially available radon monitoring system employing electret ion chamber is E-PERM; it is manufactured by Rad Elec Inc⁵. E-PERM systems were successfully used in a few recent studies, e.g., [32] and [33].

TLD systems. Systems employing thermoluminescent detectors (TLD) are still used for radon monitoring. TLD is made of solid-state crystalline dielectric materials⁶, which have two kinds of centers - traps and luminescent sites. When α -, β - particles or γ -photons generate charge the generated electrons are captured by trap centers while holes are trapped by luminescent sites. All thermoluminescent material have property to release the traps at elevated temperature, which is followed by recombination at luminescent center that, in turn, results in light emission proportional to the collected radioactivity [27]. The light emission can be measured by PMT or analogous silicon device. In order to measure dose related to α -particle emission it is necessary to use at least two TL detectors: one of them measures all radiation and another detector measures only background⁷, which is extracted afterwards. Although these devices are still used for radon detection,

⁴Sodium iodide activated with thallium.

⁵<http://radelec.com/>

⁶Summary of materials can be found in [27].

⁷In case of radon monitoring the background is caused by β and γ rays and it can be measured by shielding detector against α -particles.

for example, [34] (passive, integrating radon monitoring), [26] (active, integrating radon monitoring), it is better suited for gamma dosimetry combined with radon monitoring [35], [36]

1.3.3 Continuous radon measurement methods

In continuous radon monitoring methods sampling and analysis of radon concentration occur simultaneously. Thus real-time measurement results become available. Such instruments are used to monitor radon concentrations that are changing either rapidly or considerably from one place to another. Classification of instrumentation is shown in fig. 1.5.

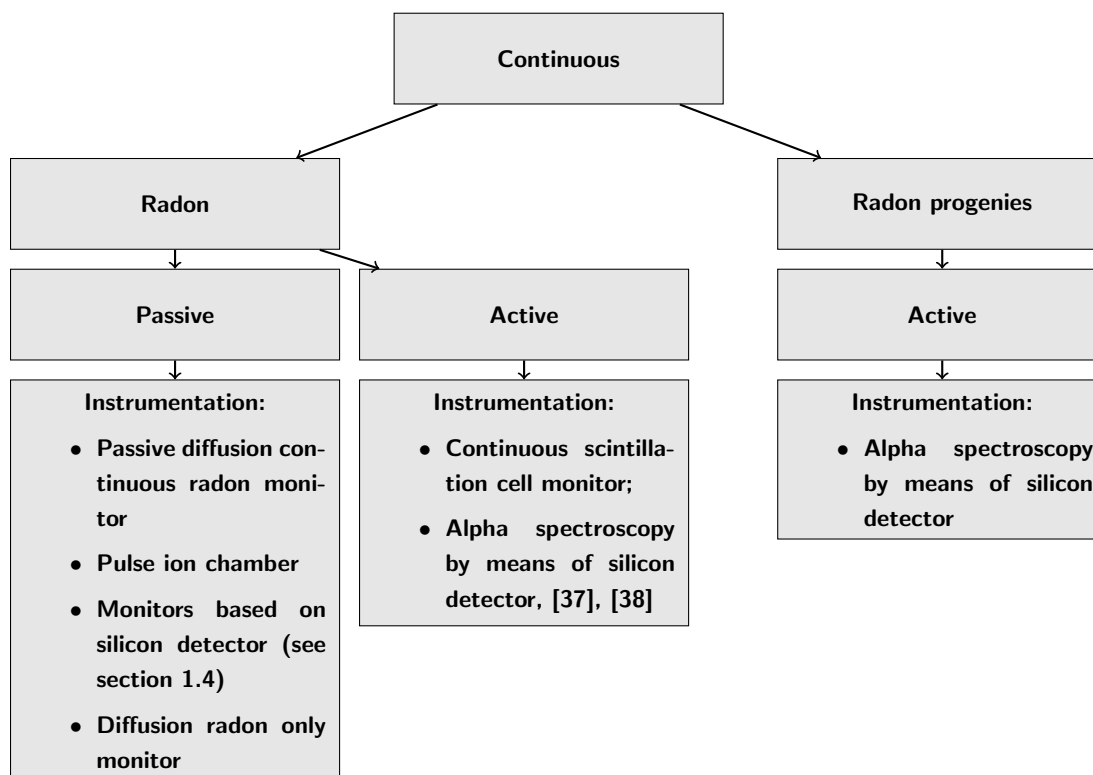


Figure 1.5: Summary of continuous radon monitoring methods.

Passive diffusion continuous radon monitors. All such monitors have a chamber with inlet opening covered by a filter excluding radon progeny from entering the chamber. Two types of chambers are usually used: **pulse ion chamber** and **chamber with a silicon detector** (see sections 1.3.4 and 1.4 for more detailed explanations). In pulse ion chamber radon progeny are removed electrostatically, so, pulses only from radon decay are counted. On the contrary, in the monitors employing silicon detector

radon progeny are electrostatically collected on the surface of the detector. Then, depending on the detector and its electronics, radon concentration is determined either by gross alpha counting or by alpha spectrometry.

Diffusion radon only monitor is a scintillation cell combined with an electret. Only radon diffuses in the cell, however, it does not reach equilibrium with its progeny. Positively charged ^{218}Po and ^{214}Po progeny are collected by the electret, so the only α -particles that hit scintillating walls of the cell are those emitted during radon decay [39]. However, this approach has not been used extensively.

Continuous radon monitors with active sampling work in a similar way as passive diffusion continuous radon monitors, however, with implemented active radon sampling, for example, using air pump.

1.3.4 Commercially available continuous radon monitoring systems

AlphaGUARD (Saphymo GmbH), [23] - is a radon concentration monitoring system based on pulse-counting ionization chamber. The system was developed for continuous radon monitoring using passive sampling. It has a good sensitivity of 5 cpm at 3 pCi/L or 100 Bq/m³ in a very wide range of concentrations from 2 up to 2×10^6 Bq/m³. Thus, AlphaGUARD is well suited for the calibration of existing or newly developed systems.

Radim system, as well as similar and simpler system Ramon 2.2, is based on electrostatic collection of short-lived radon decay progeny ^{218}Po on the surface of silicon α -particle detector. After the deposition, the activity of ^{218}Po is determined by means of alpha spectroscopy, so, the radon concentration can be calculated. The results acquired by Radim are automatically corrected according to the ambient conditions, i.e., temperature, pressure, and humidity [40]. The resolution of Radim system is 1 Bq/m³ and minimum measurable concentration is ~ 30 Bq/m³ for 1 hour measurement.

RAD7 radon monitor (DurrIDGE Inc., USA) - this instrument was developed for radon and thoron continuous monitoring. α -particle detection is done by silicon detector placed in the center of hemisphere coated with a conductor to make electrostatic collection of positively charged radon and thoron progenies on the surface of the detector. The instrument features few operation modes, two of them would be relevant to be mentioned here, those are SNIFF and NORMAL mode. In a SNIFF mode RAD7 looks only at ^{218}Po progeny if radon should be monitored or at ^{216}Po in case thoron is monitored. In a NORMAL mode decays from all progenies are taken into account. Such modes of operation were achieved by dividing energy range from 0 MeV till 10 MeV into 8 “windows”, so, only decays from a particular (e.g., ^{218}Po in a SNIFF mode) or all (e.g., ^{218}Po and ^{214}Po in a NORMAL mode) progenies are analyzed.

Electrostatic collection of short-lived radon progeny ^{218}Po on the surface of silicon

detector was used in the continuous radon monitoring **RADHOME** systems (Algade). The systems **RADHOME HR3, HR2, P** were developed for monitoring indoor radon concentrations and use passive radon sampling, i.e., radon diffuses into the chamber via filter that stops radon progenies but allows radon to enter the chamber. The system **RADHOME HRE** was developed for monitoring radon in mining industry that requires faster radon monitoring. Therefore, active sampling using air pump to force radon into the instrument was implemented.

Therefore, many commercially available continuous radon monitoring systems are employing silicon detectors together with electrostatic collection of radon daughters on the surface of the detector. These systems feature both passive and active radon collection methods depending on the measurement time demands and required precision. Availability of spectrometric analysis makes such systems more versatile and faster. On the other hand, spectrometric analysis requires elaborate silicon detector and readout and processing electronics that makes such instruments good for industrial and laboratory applications but rather cost ineffective for home use.

1.4 Silicon detectors for α -particle and radon detection and monitoring

Nowadays field of silicon radiation detectors is extremely wide; it has been growing from p-n junction detectors, p-i-n diodes, diode strip detectors, double-sided strip detectors, drift detectors, CCD detectors to 3d detectors and silicon photomultiplier. Every type of detector is well suited for some particular application, e.g. minimum ionizing particle detection or photon detection etc., which are still relevant and so the research about all mentioned detectors is going on. However, almost all silicon detectors can potentially be used for α -particle detection. This section will discuss how existing detectors are used for that purpose and how their performance and design inspired development of novel BJT detector with layout optimized for α -particle detection.

Effective and fast radon detection requires detectors with large areas that would allow monitoring system to collect a reliable statistics in a reasonably short time intervals. All silicon detectors specifically developed for radon detection were optimized to have a largest possible area, which, of course, depended on the fabrication process used for their production. The main challenge to design such detectors is to keep overall capacitance of the detector as small as possible. Electrode “segmentation” or “pixelation” of the detector is the way to reduce the capacitance.

Silicon strip detectors were often used to detect and track ionizing particles, [41]. These detectors provide information about energy of incoming particles and their position. How-

ever, strip detectors suffer from high capacitance. Taking into account that output signal depends on capacitance as $\Delta V = \frac{Q}{C}$, high strip capacitance drastically degrades output signal. Today's approach is to split detectors into pixels with much smaller capacitance and then to bump-bond each pixel to the readout chip. However, before bump-bonding became a mature technology, different approaches were suggested to decrease strip capacitance. The simplest approach would be to split strips onto pixels and then route signal out using metal lines. This approach was not viable as capacitance of metal lines is comparable to the capacitance of strips. Nevertheless, Horisberger was one of the first to propose slightly different solution that would overcome problem of high capacitance of metal lines [42]. He suggested to add another shallow implantation that would change pixel from a p-n junction to a BJT pixel. In other words, Horisberger suggested to include preamplification stage into the pixel and then deal with already amplified signal.

Signal preamplification was realized in different ways: i.e. with bipolar transistor detectors [42], [43], [44], pMOS pixel detectors [45], PIN detectors with JFET and MOS preamplification capabilities [46] or monolithic CMOS detectors⁸ [3], [47]. Analysis of mentioned detectors might be important in order to show all advantages that BJT-detector can have and also it can help us to avoid some possible pitfalls.

PIN diode with amplification by means of **pMOS** [45] consists of n-type silicon substrate with implanted n-well and p+ region on the backside of substrate (p-type implantation of PIN diode). The n-well contains source and drain of pMOS transistor. When particle impinges it generates electron-hole pairs due to the ionization. Charge cloud splits onto electrons (which move toward the n-well that contains source and drain) and holes, which move to p+ region of PIN diode. Collected electrons change potential and so transistor's bulk voltage is changed. It means that so called "front-side" and "back-side" transconductances of pMOS transistor change according to the n-well potential and, consequently, to the energy of the detected particle. The same idea was implemented in [46] using nMOS instead of pMOS transistor. Detectors of this type show very good noise behavior, e.g. it was calculated [45] that for the strip consisting of 256 pixels the noise is about 388 electrons. It was also shown that even if the noise behavior depends on the technology process it is still sufficiently low [46]. Gain for pMOS (nMOS) pixel detectors [45], [46] is not very large, i.e. theoretically 10 (or less). Despite the elegance of this approach, the detectors produced on high-resistivity substrates with added MOS transistor lose their radiation hardness due to a rapidly degrading MOS oxide. Thus, such detectors are not well suited for the applications with high fluences for which it was designed. However, it can be used for α -particle detection as a PIN diode with a preamplification,

⁸In this case "monolithic" means Monolithic Active Pixel Sensors that joins monolithically p-n junction and preamplifying readout electronics.

which would relax design constraints imposed by readout electronics.

AlphaRad. α -particle and radon detection monitoring can be also done using CMOS monolithic active pixel sensor (MAPS) [3], [47], which authors refer to as **MIMOSA** (Minimum Ionizing particle MOS active pixel). The chip was initially designed for vertex and tracking detectors in high-energy physics. The first prototype of **MIMOSA** was fabricated using standard submicron 0.6 μm CMOS process; it consists of four arrays each having 64×64 pixels⁹. Each pixel consists of photodetector monolithically integrated with 3T readout electronics. Although **MIMOSA** chip was designed for the detection of minimum ionizing particles, it was noticed that the chip could be efficiently used for α -particle detection [48].

The active pixel sensor shown in fig. 1.6 consists of (from bottom to top): p^{++} silicon substrate of a modest quality, p-type epitaxial layer, p^+ well implanted in epi-layer, and n^+ implantation in p^+ well, which is p-n junction that collects released charge. The detector has few considerable advantages over other similar or featuring same characteristics detectors due to use of a standard CMOS fabrication process and layout of the detector providing high fill factor value. The potential barriers on the edges of epi-layer confine produced charge in this layer. Thus, all charge generated by particle is collected by a photodiode with a high charge collection efficiency. The charge collection mechanism is a quite slow thermal diffusion, which is dominant due to just a partial depletion of epi-layer in vicinity to the p-n junction (N_{well}/P_{epi}), so, generated in epi-layer charge should diffuse to the N_{well} . However, due to the potential barriers on the edge of epi-layer, none of the charge is dispersed into the substrate. Recently, a CMOS MAPS (MIMOSA4 prototype) on nonepitaxial, high resistivity substrate was successfully implemented [49].

Paper [48] has shown the possibility to detect radon exposing already made **MIMOSA** system [47] to the ^{241}Am source and then to the radon gas. This experiment showed that after eliminating the noise, fake events, and photon hits α -particles emitted by radon and its progeny could be detected. Radon activity has been measured by 4 different types of detectors (AlphaGUARD, 6 films of LR115, 6 films of CR39, four E-PERM electret chambers) and then by use of Monte-Carlo simulation amount of particles was calculated and compared to the measured by **MIMOSA**, which showed that almost all particles reaching the detector were detected. Implemented continuous radon monitoring system relied on the detection of α -particles emitted both by radon and radon progeny.

Further investigations resulted in new **AlphaRad** system [50] specifically fit to α -particle detection. The basic element of the system is still a monolithic active pixel sensor. **AlphaRad** consists of two 32×64 matrices of pixels shorted together; each matrix covers a total sensitive area of $2.56 \times 5.12 \text{ mm}^2$. The readout is made by charge-to-voltage

⁹Each array has detection area of 1.64 mm^2 .

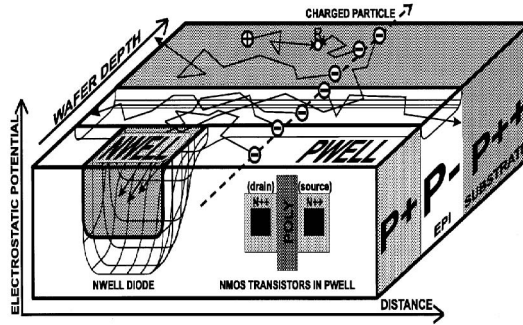


Figure 1.6: Schematic cross-sections of CMOS monolithic active pixel sensor, [3]

amplification chain put outside the sensitive area. Due to rather high capacitance of a single matrix (around 41 pC) a gain of ~ 700 is needed to provide an output signal with 1 V amplitude. Use of monolithic array of pixels has greatly simplified design of electronics. The results of field tests of **AlphaRad** system in a radon chamber were in detail discussed in [28]. Two types of measurements were done. The first one was passive measurement of radon by detection of particles emitted both by radon and radon progeny; the method is well suited for the detection of moderate radon concentrations (~ 1 kBq/m³) The second test was an active measurement of radon by detection of particle emitted just by radon progeny; it was implemented by collecting progeny attached on aerosols on the filter put in vicinity to the detector. Authors claim that this method can be used to monitor lowest possible indoor radon concentrations.

So, it is clear that CMOS system developed for radon detection has many advantages: firstly, partially integrated read-out electronics and then relatively fast charge collection times. However, applications where acquisition of 2d information about position of particle hit or tracks of charged particles (e.g., vertex or tracking detectors) is needed are still the main applications of CMOS systems.

α Ram. Operation principle of the developed detector is similar to the operation principle of DRAM memory. In fact, loses of information stored in a single cell of DRAM due to α -particle or heavy-ion hits indicated, on one hand, that this memory is vulnerable to such type of radiation and, on the other hand, that it can be used for α -particle and, hence, radon detection [51]. The first CMOS integrated α -particle counter similar to a DRAM was reported in [52]. Each pixel is a reverse biased p-n junction used as a precharged capacitor discharging when particle hits it. Next version of this detector was called α RAM; its description and results of radon tests can be found in [53], [54], [55]. The detector is a 16×16 array of $100 \mu\text{m}^2$ pixels with total chip area of $3.5 \times 3.5 \text{ mm}^2$. Due to such small area a collection mechanism of radon or radon progeny should necessarily be implemented in the radon monitor.

PIN silicon photodiode. The detector can be used both in continuous and integrating radon monitoring systems based on either α -counting [56] or α -spectrometry [38], [37], [57]. However, the main advantage that PIN detector provides is possibility to implement spectrometric analysis and, hence, implement a sensitive radon monitor. The readout chain is quite standard; it consists of charge sensitive amplifier, shaping amplifier and processing unit (e.g., microcontroller in case of simple α -particle counting or multichannel analyzer in case of spectrometric analysis).

Use of PIN detectors in radon monitor offer a number of significant benefits: 1) large detection areas¹⁰; 2) on-line and time-resolved monitoring; 3) good precision and lower measurement uncertainties can be achieved. On the other hand, PIN detector requires rather elaborated signal readout chain, especially when it is used for spectrometric analysis.

Silicon photomultiplier. The detector is used in the same way as photomultiplier tube in scintillation cell for radon measurement by grab sampling method. To the best of our knowledge, only RADIM 7 developed in frame of RAPSODI collaboration employs silicon photomultipliers (SiPM) for radon monitoring [58]. RADIM 7 uses electrostatic collection of ^{218}Po and ^{214}Po radon progeny on the large scintillating ZnS foil (wavelength of scintillation light 450 nm) coupled with WLS¹¹ fibers that deliver light to SiPM at wavelength shifted to the peak spectral sensitivity. Such system benefits from large detection area that is limited just by scintillator size. However, elaborated electronics should be developed to eliminate rather high dark count rates of SiPM and to deal with SiPM operation voltages higher than 20 V.

1.4.1 BJT detector for α -particle detection

We have already mentioned few silicon radiation detectors and systems developed for α -particle and radon detection and monitoring. All of them have pros and cons. The main constraints are simplicity and, consequently, cost-effectiveness of the design of detector, readout electronics and, finally, radon monitoring system. In this thesis we suggest another approach to implement radon detection system that is based on the use of BJT detector.

The idea to use bipolar junction transistor for α -particle detection firstly was proposed in the paper of Williams [43]. Later on, this approach was used as a starting point for the proposal of the bipolar silicon microstrip detector by Horisberger, [42] and new pixel detector relying on the BJT with floating base suggested by Ardelean, [44]. These

¹⁰ For example, papers [38] and [37] report on use of $18 \times 18 \text{ mm}^2$ Hamamatsu diodes, which in principle could be substituted by even larger $28 \times 28 \text{ mm}^2$ diodes.

¹¹Wavelength shifting.

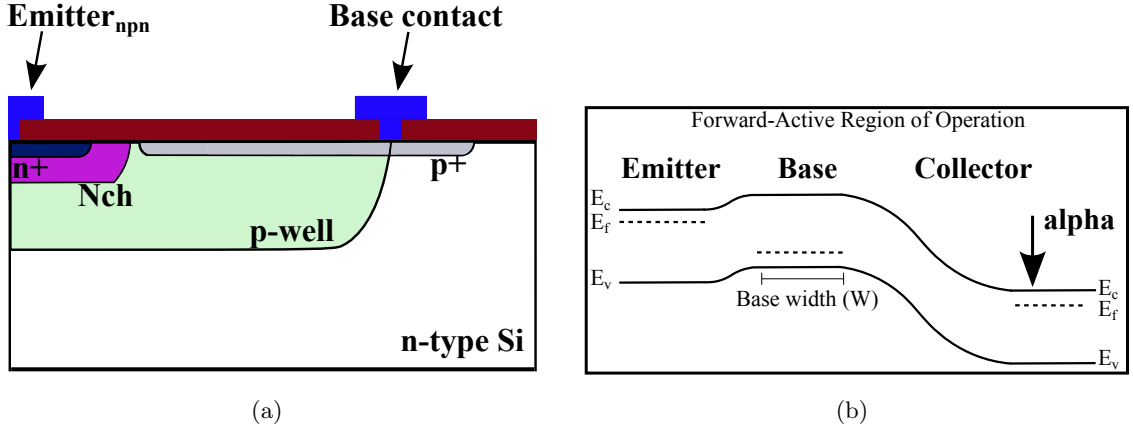


Figure 1.7: (a) - Schematic cross section of BJT pixel; (b) - Energy band diagram of BJT pixel in forward-active region of operation.

papers have presented the concept of minimum ionizing particle detection and then signal preamplification by means of pixel using BJT amplifying effect.

As it was mentioned above, one of the main concerns is a capacitance of a single pixel and, therefore, the overall capacitance of a whole detector matrix. The first and simple solution of this problem was presented in [42] where author suggested splitting up the strips onto pixels. Also it was suggested to make an additional n+ implant inside the p-well region. Accordingly, the obtained pixels are bipolar pixels with all the basic characteristics of BJT transistors. The subsequent work was continued by [44] where the basic pixel for the detector was BJT with floating base, which had to decrease the capacitance drastically. The base biasing is obtained by providing base current via lateral pnp-transistor.

Other alternative biasing methods exist as well: pnp-transistor as a current source [44] [49], punch-through from p+ region, biasing through a large polysilicon resistor connected to a base, biasing by current coming either from a breakdown structure or a Schottky diode. In case such types of biasing are used, BJT detector can be biased just by applying bias to a collector while base is left floating. Alternative biasing methods observe noticeable power consumption by BJT-detector; therefore making complicated if not impossible their application in low power consuming systems relying on battery power supply.

This thesis discusses performance of BJT detectors used for α -particle detection and operated with a floating base. The very first samples of BJT detectors were fabricated at former ITC-IRST¹² (Trento, Italy). Batignani et al. reported in their paper [59] on the

¹²now Fondazione Bruno Kessler, <http://www.fbk.eu/>

first results¹³ of electrical and functional tests of these BJT samples that were fabricated on high-resistivity silicon. That was one of the first implementations of BJT detectors on high-resistivity silicon. Therefore, the detectors could be used for the detection of ionizing radiation (β -, γ -, α -, minimum ionizing particles and X-rays) differently from phototransistors fabricated on low-resistivity silicon (low-resistivity silicon has very short recombination lifetimes, so charge generated by the radiation would recombine before reaching collecting electrodes).

A conceptual design of the device is similar to the design of BJT detectors reported in this work. Fig. 1.7(a) shows a schematic cross section of the device. It is fabricated on n-type high-resistivity Si wafers of different thickness (can be 300 or 600 μm depending on the application). Base of BJT is a p-well that is obtained by a high-energy boron implantation in order to make it sufficiently deep, so it could also host an emitter of BJT. Emitter is obtained by double implantation, first implantation is called n-channel, while second implantation is called n+. Batignani et al. refer to such emitter layout as to “double-implant emitter”. Finally, p+ shallow implantation is done to provide a contact to the base. A more detailed description of fabrication process flow can be found in Chapter 4 on page 55. Electrical characterization of the test BJT detectors showed good gain values of 700 for the detector with “double-implant” emitter¹⁴ and 60 for transistors with “single-implant” emitter. Functional characterization of the detector with higher gain was done using ⁹⁰Sr beta source. Base contact of the detector was left floating but proper operation current was chosen by illuminating detector with an LED light. Output signal was readout from the emitter connected to a 800 k Ω resistor using oscilloscope. Therefore, it was shown by the authors of this paper that even without any amplification the output signal induced by β -particle could be observed using an oscilloscope just due to the transistor effect.

Principle of particle detection by BJT detector operated with a floating base can be understood from the band energy diagram shown in fig. 1.7(b). The device is biased in a forward-active region of operation. When particle hits the detector it generates electron-hole pairs in the bulk due to the ionization. Electric field in the BJT is such that electrons are swept to the collector, while holes are collected in the base. Due to that, the energy barrier between base and emitter decreases so emitter-base electron current increases. This current is then amplified by an electric field created by the collector bias and current pulse corresponding to the particle can be readout from the emitter or collector electrodes.

Further research has been carried out to determine how device performance is influenced by different geometrical and technological parameters, Piemonte et al. [62]. Using

¹³These results were partially connected and derived from the results presented in [60] and [61].

¹⁴For instance, NCH32xNN20 emitter layout is “double-implant” emitter.

TCAD simulations and different experimental techniques¹⁵ doping profiles were extracted with a rather good precision. Apart from that, most of the attention was devoted to the TCAD simulation of BJT detector with “double-implant” emitter. Gummel plots were simulated and corresponding differential gain curves were extracted and compared to the measured gain curves. Fair correspondence of simulated IV characteristics to the measured data allowed simulations of the transient response of the detector to the ionizing particle. As a result, the device performance as a function of all relevant parameters (one of them was LED light biasing) was evaluated.

After that a dynamic performance of BJT detector was characterized using ^{239}Pu as a source of α -particles, ^{90}Sr as a beta source and shielded ^{241}Am as an X-ray source, Batignani et al. [63]. In order to figure out dependence of time decay constant τ ($\tau = R_B C_B + \beta R_L C_{BC}$) on base-to-collector capacitance C_{BC} , a BJT strip detector with non-negligible C_{BC} capacitance was used. To extract C_B from functional tests authors used a set of different load resistors R_L . Obtained agreement of measured C_B and C_{BC} values validated an adopted model for device dynamic performance, which was presented in [59].

A more detailed investigation of the performance of BJT detector was presented by Bosisio et al. in [64], focusing in particular on the noise properties, rate and performance limitations of the device. Noise properties of the device were investigated using ^{241}Am X-ray source and digital storage oscilloscope used for output signal integration. The extracted noise values corresponded to ENC as low as $\approx 390 e^-$ and rate limitations of the device were determined to be in the order of tens of kHz. Furthermore, careful analysis of limitations of BJT performance underlined best possible applications for the device, i.e., those that do not require high resolution and low noise but simplicity and cost considered of higher priority.

In parallel to the already described activity, a sufficient research has been done on the subject of alternative biasing methods for BJT detectors [65, 66]. Novel pnp-based biasing technique of BJT detector was developed by integrating pnp-transistor into the base of BJT detector. When pnp-transistor is driven into its forward active region of operation, all its hole collector current flows into the base of npn-transistor, therefore, biasing it. The method has a few advantages in comparison to other methods, e.g., it does not require additional silicon area as large polysilicon resistor, it has good uniformity parameters in comparison to the bias via “punch-through” effect. The performance of such biasing structure was tested both electrically and using pulsed laser light, which confirmed its effectiveness.

To conclude, a vast research experience, including variety of available samples, good theoretical background, and layout design know-how, was gained before 2007 when the

¹⁵Secondary Ion Mass Spectroscopy, Spreading Resistance, CV, and sheet resistance measurements

work on the subject of this thesis started. Apart from the mentioned achievements a microcontroller-based readout electronics for BJT detector was developed as one of the preliminary prototypes of radon monitoring system. Thus, all this work has become a good background for the development of BJT detector with optimized layout that is well suited for α -particle and, hence, radon detection and monitoring. The FPGA-based electronics presented in Chapter 3 has been designed taking into account all pros and cons of already existing readout electronics.

1.5 Summary

The advances in silicon detectors and readout electronics made silicon detectors attractive to the field of radon monitoring, which is well established field with plenty of developed techniques and methods. Modern instruments with silicon detectors are used for instantaneous, integrating, and continuous radon monitoring. They satisfy requirements imposed by all monitoring techniques, unless instrument should be developed for calibration purposes where very good sensitivity is needed¹⁶. Apart from that, some of the instruments can combine radon monitoring techniques. For example, instruments that have spectrometric analysis can perform both instantaneous and continuous measurements, instruments that rely on α -particle counting can perform both integrating and continuous measurements.

The developed BJT detector can successfully occupy a niche of integrating (dosimeters) and continuous radon monitoring systems due to a good detection efficiency, low power consumption, well established fabrication process at FBK (Trento, Italy), and possibility to be used with simple and, hence, low cost readout electronics. In principle, BJT detector might potentially be used for instantaneous radon measurements as well. However, it is still to be shown that BJT detector operated with floating base could be used for spectra acquisition, which is needed to distinguish “old” radon (the one related to ^{214}Po energy peak) from “new” radon (the one related to ^{218}Po energy peak), so, instantaneous measurement of radon concentrations could be done.

¹⁶For example, good sensitivity of 1 cpm at 20 Bq/m³ has AlphaGUARD instrument, which is used for calibration.

Chapter 2

Functional characterization of the detectors from BD1 batch

In this chapter, we investigate detection properties of BJT detectors from the first batch of such detectors - BD1. The detectors were operated with floating base. Firstly, the layout of the tested samples will be explained in section 2.1. Then the results of electrical characterization of the tested samples will be discussed in section 2.2. After that, section 2.3 reports about results of laser pulsed light tests that were performed to evaluate charge-collection properties of the detectors and show that floating base operation mode could be efficiently deployed for α -particle detection. Section 2.4 presents the results of α -particle functional characterization of BJT detectors. Subsection 2.4.1 describes the very first results of α -particle tests that were acquired using readout chain consisting of transimpedance operational amplifier and oscilloscope, while subsection 2.4.2 refers to the data acquired with custom designed FPGA-based readout electronics ALPHADET. Finally, section 2.5 summarizes and concludes the results of functional tests confirming that floating base operation mode of BJT detector can be efficiently used for α -particle detection even in spite of non-optimized layout of the detectors from BD1 batch.

2.1 Layout of the tested samples

BJT detectors from the BD1 batch were initially designed to be operated with a base being properly biased. So, among existing detectors only some of them could be operated with a base left floating. We have found two types of such detectors, which afterwards were characterized using laser and α -particle tests. One of the samples of BJT-detector that was used in the experiments was called DPIX (see the layout in Fig.2.1(a)); this is a 1×1 cm² die that includes a 5×5 array of single BJT-pixels, each one having a

$1.4 \times 1.4 \text{ mm}^2$ active area. All bonding pads for the 25 emitters are placed along the top of the layout. The bonding was made to obtain four single pixels and one array with the remaining 21 pixels, thus easing the analysis of the impact of single pixel properties on the behavior of the whole array of pixels.

Another sample that was also tested is so-called BPAD sample. The layout of BPAD can be seen in fig. 2.1(b). The tested pixels have minimum size NCH18xNN11 emitter layout with $0.5 \times 0.5 \text{ mm}^2$ base area, which is ~ 8 times smaller than DPIX pixel. Both indicated pixels BPAD3 and BPAD4 observed very similar detection properties. Thus, the results of BPAD3 characterization only are presented in the following.

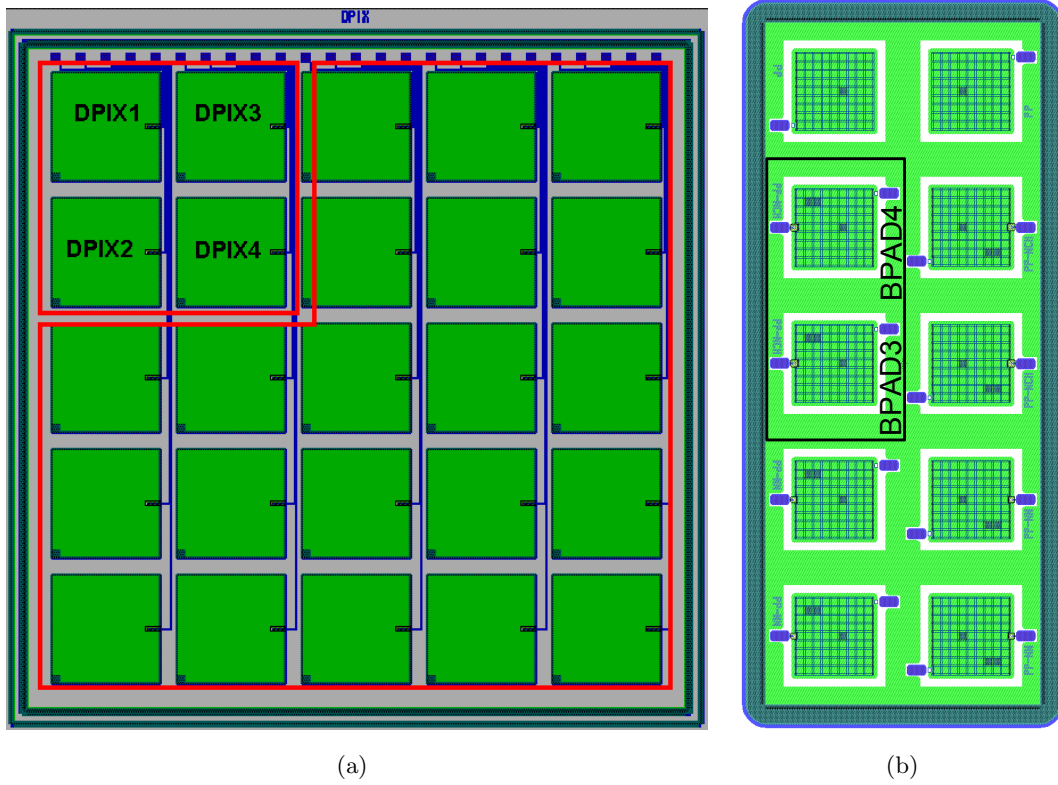


Figure 2.1: Layout of the tested BJT detectors: (a) - layout of DPIX detector, consisting of 5×5 pixels ($1.4 \times 1.4 \text{ mm}^2$ each) with NCH32xNN20 emitter layout configuration. Top left corner pixels are bonded individually, while the other 21 pixels have emitters wired together (array configuration); (b) - layout of BPAD pixels having $0.5 \times 0.5 \text{ mm}^2$ base area and minimum size NCH18xNN11 emitter layout.

2.2 Electrical characterization of the samples

Firstly, before starting functional characterization of the BJT detectors an electrical characterization of the samples has been done. The characterization of DPIX sample included measurements of collector (emitter) currents and Gummel plots. The results of these measurements are presented in fig. 2.2. As it can be seen from fig. 2.2(a), the pixels DPIX1-DPIX4 have drastically changed their collector currents after the bonding. This is due to the fact that these pixels had their emitter and base contacts bonded individually. So, as the base contact was not routed out of the pixel, which means that the bonding pad was in the “active” area region, the bonding caused considerable damage of the silicon bulk, thus, causing increase of leakage current I_L and emitter current $I_e = I_L \cdot \beta$, where β is a quiescent gain of a pixel. Figure 2.2(b) refers to the gain curve that was obtained from Gummel plots using $\frac{\partial I_c}{\partial I_b}$ formula, where I_c is a collector current and I_b is a base current. This gain curve is the same for all pixels in DPIX array. Apart from the gain curve, fig. 2.2(b) indicates also quiescent gain values for DPIX4 pixel (β_{quiesc}) that was tested using ^{241}Am source. These quiescent gain values are rather high comparing to the values that unbonded pixel would have. For example, the measured values of β_{quiesc} are 220, 270, 300, and 320 at 10 V, 30 V, 50 V and 70 V collector biases respectively, when for unbonded pixel β_{quiesc} would be 50, 80, 100, and 110 at the same collector biases.

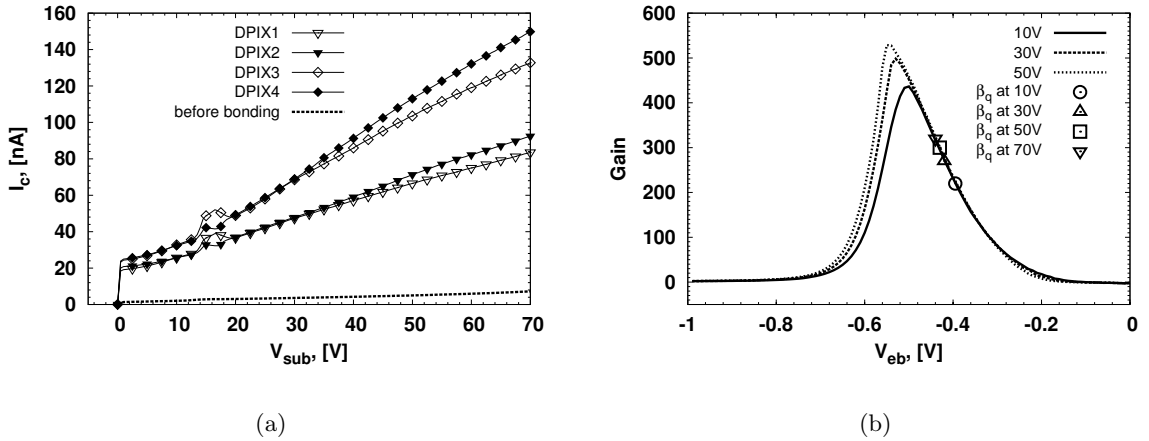


Figure 2.2: IV characterization of DPIX pixels after the bonding: (a) - leakage currents of DPIX1 - DPIX4 pixels; (b) - gain curves for DPIX4 pixel with indicated quiescent gain values for 10 V, 30 V, 50 V, and 70 V collector biases.

The results of electrical and functional characterization of BPAD3 sample are shown in fig. 2.3 and fig.2.12 respectively. The BPAD3 sample has different layout comparing to DPIX sample, the emitter layout of BPAD3 has NCH18xNN11 configuration. Due

to such emitter layout of BPAD3 sample the gain has a pronounced drop at low values of base-emitter potential (~ 0.46 V), i.e., at low values of base currents. This is why, BPAD3 pixel has much lower quiescent and, consequently, overall gain values. Partial explanation of this effect can be found in [64], it is related to the higher recombination rate in the base-emitter depletion region. Figure 2.3 includes a gain curve characterizing DPIX pixel for the reference purposes.

The gain curve measurements were carried out at 70 V collector bias, which is higher than a full depletion voltage. Figure 2.4 refers to the CV characterization of the test diodes, which showed that mainly all detectors on the wafer would be fully depleted at 70 V collector (i.e., substrate) bias. This is why, all following functional tests were done at collector biases corresponding to the full depletion voltage, i.e., 70 V, and at biases lower than full depletion voltages, i.e., 10 V, 30 V, and 50 V because operation of the detector at such biases can potentially decrease power consumption due to the lower collector and, consequently, emitter currents.

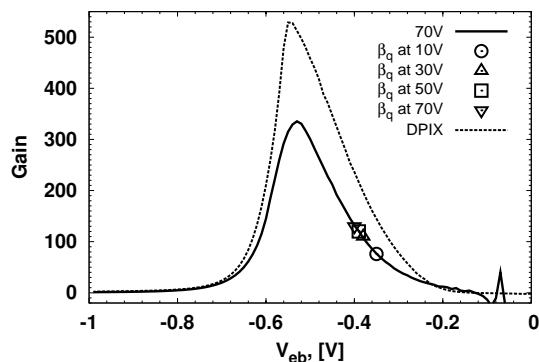


Figure 2.3: Gain curve for the BPAD pixel acquired at 70 V collector bias with indicated quiescent gain values for 10 V, 30 V, 50 V, and 70 V collector biases.

2.3 Laser tests

To carry out laser tests we have used a setup shown schematically in fig. 2.5. It consists of two parts, the main part consists of transimpedance amplifier and digital storage oscilloscope, the second part is responsible for the light calibration and it consists of wideband fixed-gain amplifier THS4303, TI [67] and calibrated D400FC InGaAs photodetector [5] connected to the digital storage oscilloscope. Generally speaking, the main purpose of laser tests is to verify detection properties, uniformity of the detection properties and gain of the tested detector. For that purpose it is necessary to measure energy of laser light

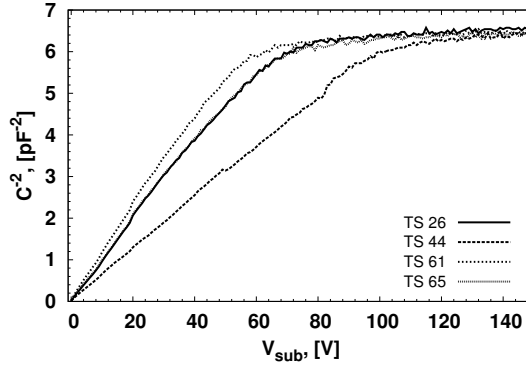


Figure 2.4: Full depletion voltage V_{depl} measurements. The V_{depl} are 65 V, 101 V, 60 V, and 60 V measured by the test diodes from the TS 26, TS 44, TS 61, and TS 65 test structures respectively.

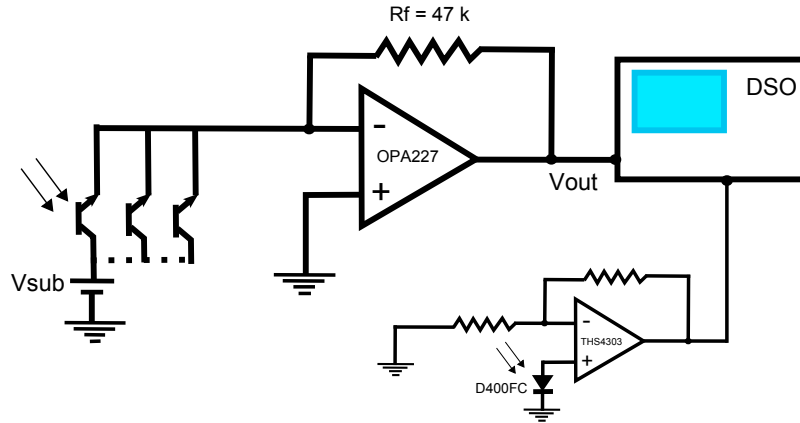


Figure 2.5: Schematic representation of the setup consisting of transimpedance amplifier and digital storage oscilloscope used to carry out laser tests of BJT detectors.

pulse as precise as possible. After that the energy of laser light pulse can be converted to the energy of α -particle equivalent to this pulse.

Firstly, DPIX3 pixel from the DPIX sample was tested. The results of the tests are shown in figures 2.6 and 2.7. The wavelength of laser light is 1060 nm¹ and energy of equivalent α -particle is $E_\alpha = 1.41$ MeV, assuming that the quantum efficiency of the

¹Actually, laser light with 1060 nm wavelength is not perfectly suited for α -particle emulation due to the large absorption depth. In fact, laser with, for instance, 780 nm wavelength would be more suitable for such tests. However, taking into account that responsivity of the D400FC detector used for the light calibration is ≈ 0.1 A/W at 780 nm, the light calibration could not be done reliably. On the contrary, the D400FC detector has high responsivity at 980 nm (0.65 A/W) and at 1060 nm (0.7 A/W) Therefore, in all experiments we have used lasers with either 980 nm or 1060 nm wavelengths to make light calibration step more reliable.

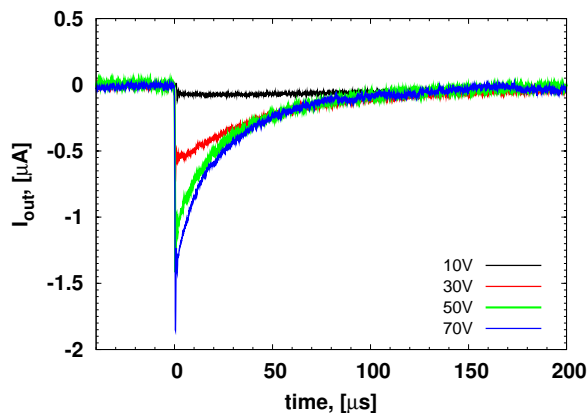


Figure 2.6: Transient response of DPIX3 pixel biased at different collector voltages to 1060 nm laser pulses emulating α -particle with $E_\alpha = 1.41$ MeV energy.

detector is $\eta = 0.7$. Fig. 2.6 refers to the transient response of the pixel to the laser light pulse at different collector biases. Measured charge values Q_{coll} are 13.7 pC, 36.4 pC, 37.5 pC, and 43.2 pC at 10 V, 30 V, 50 V, and 70 V collector biases respectively. These Q_{coll} correspond to the overall gain values $\beta_{10V} = 150$, $\beta_{30V} = 390$, $\beta_{50V} = 400$, and $\beta_{70V} = 460$. Comparing overall gain values to the quiescent gain values $\beta_{q,10V} = 190$, $\beta_{q,30V} = 230$, $\beta_{q,50V} = 250$, and $\beta_{q,70V} = 270$ we can conclude that the tested DPIX3 pixel operated with a floating base² is effectively biased by the laser light pulse equivalent to an α -particle with energy $E_\alpha = 1.41$ MeV.

Fig. 2.7 refers to the results of laser scanning of the DPIX3 pixel, where (a) shows three-dimensional representation of data of the laser scan, while (b) shows distribution of collected charge values Q_{coll} corresponding to the laser scan (a). There are three peaks in the distribution of Q_{coll} that have mean values at $\mu_1 = 25.0$ pC, $\mu_2 = 37.2$ pC, and $\mu_3 = 44.6$ pC. The third peak corresponds to the events collected in the central area of the pixel approximately equal to 1.2×1.2 mm², the second peak corresponds to the events collected on the edge of the pixel and the first peak corresponds to the events collected near the edge of the pixel in the interpixel area. These data explains low energy tails in the distributions of collected charge values that were collected during the α -particle tests (see, for example, fig. 2.15).

²These data confirms that the tested pixel is well biased by the laser light pulse when the collector is biased at 30 V, 50 V, and 70 V. However, as it can be seen the overall gain value of the pixel biased at 10 V is lower than the quiescent gain value. The explanation for this effect is twofold: firstly, the pixel may not be biased by the light pulse when it is operated with a floating base and, secondly, integration time of 340 μ s is not long enough to integrate all generated charge. Apart from that the resolution of waveform acquired at 10 V collector bias is quite poor that could as well influence precision of integration. Thus, it is unclear whether the pixel operated with floating base at 10 V is biased by the light pulse or not.

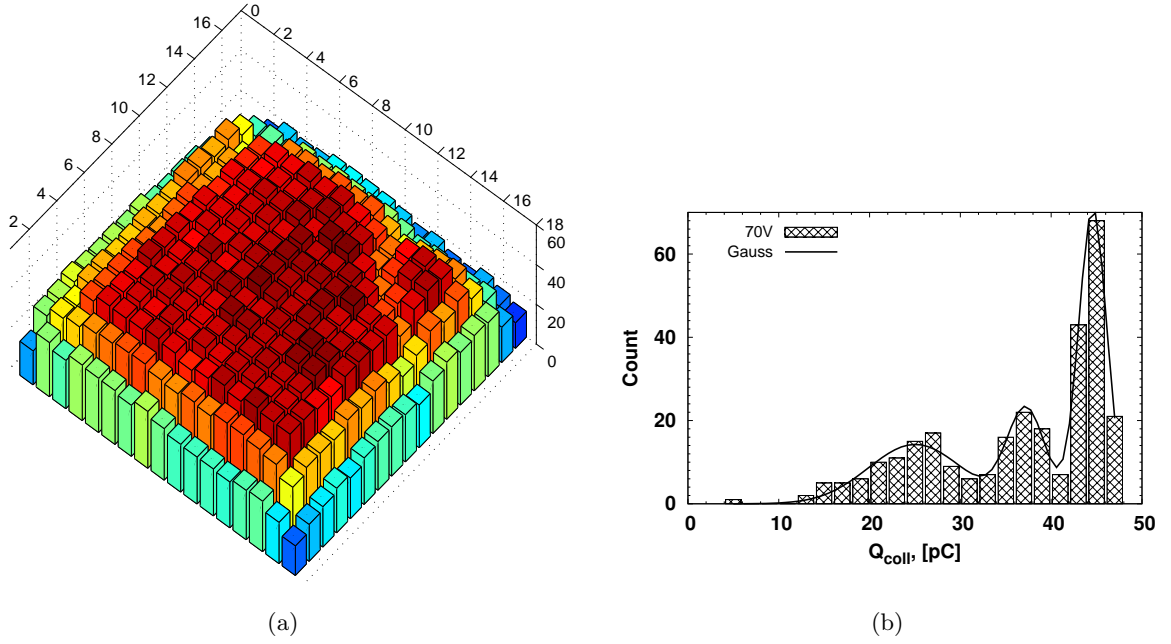


Figure 2.7: (a)- laser scan of DPIX3 pixels with an energy of light pulse corresponding to the energy of α -particle $E_\alpha = 1.41$ MeV. The step is $100 \mu\text{m}$, bias voltage is $V_{bias} = 70$ V. (b) - Gaussian fits of distribution of Q_{coll} corresponding to the laser scan. Solid line shows multi-peaks Gaussian fit with mean values for the peaks $\mu_1 = 25.0$ pC, $\mu_2 = 37.2$ pC, and $\mu_3 = 44.6$ pC.

The results of laser light characterization of BPAD3 pixel that has minimum size emitter (NCH18xNN11) are presented in fig. 2.8 and fig. 2.9. The light pulse had an energy equivalent to α -particle with $E_\alpha = 1.14$ MeV. The laser scan shown in fig. 2.8 was performed with a rather small step of $10 \mu\text{m}$ in order to take into account all peculiarities of the layout of pixel (see the layout in fig. 2.1(b)), such as a base contact metal grid over the active area of the pixel and three metal base contact pads. Moreover, due to the small step of the scan even bonding wire could be seen. However, presence of metal grid in active area prevents making a direct comparison between laser and α -particle tests as the light is reflected by the metal lines, so Q_{coll} values are ~ 0 pC or slightly larger³, while α -particle can penetrate the metal.

In order to acquire distribution of Q_{coll} a single $40 \times 40 \mu\text{m}^2$ segment of BPAD3 pixel not covered by metal has been scanned with a rather small step of $2.5 \mu\text{m}$. The collector of pixel was biased at 70 V. The distribution of Q_{coll} is shown in fig. 2.9(a); it has two peaks with mean values $\mu_1 = 2.3$ pC and $\mu_2 = 14$ pC. The first peak corresponds to the

³The collected charge values can be larger than 0 pC even when the light spot is positioned over the metal line due to rather large size of the spot. The spot was large because the focuser could not be put closer to the detector due to the peculiarities of the bonding PCB.

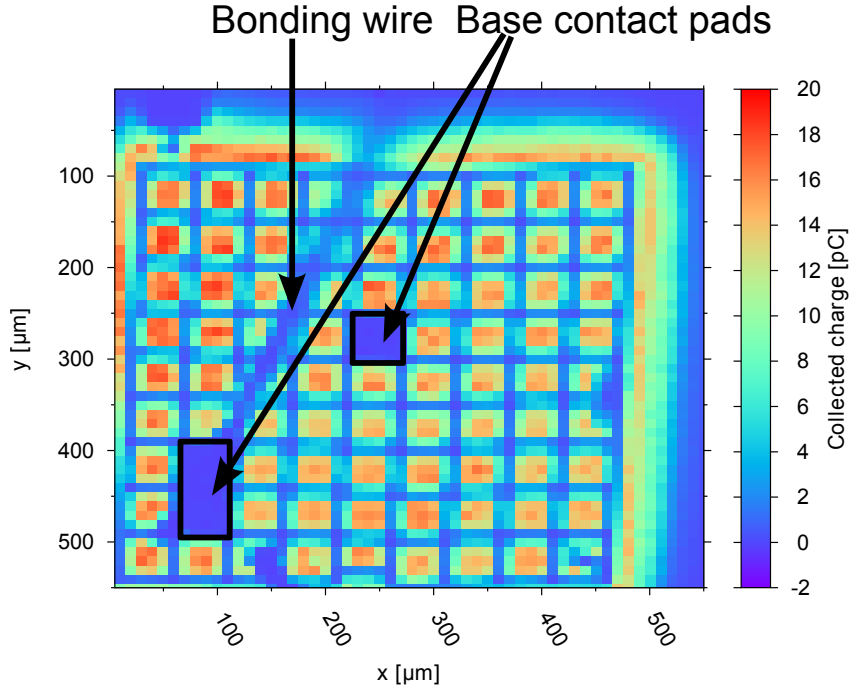


Figure 2.8: laser scan of BPAD3 pixels with an energy of light pulse corresponding to the energy of α -particle $E_\alpha = 1.14$ MeV. The step is $10 \mu\text{m}$, bias voltage is $V_{bias} = 70$ V.

edge of the active area of the segment and metal lines around active area, the second peak corresponds to the events collected within the active area. The transient response of BPAD3 pixel collected at different collector biases is shown in fig. 2.9(b). The data has been collected when the laser spot was put in the center of the tested segment. The overall gain values are 75, 150, 210 and 280 for 10 V, 30 V, 50 V, and 70 V collector biases correspondingly. Comparing these gain values to quiescent gain values shown in Table 2.1 we can conclude that also BPAD3 pixel with minimum emitter size can be biased by an α -particle, when the pixel is operated with a floating base.

2.4 Alpha-particle tests

To perform α -particle tests an ^{241}Am radioactive alpha-particle source (AMR01032, nominal activity ~ 3 kBq, active diameter ~ 2 cm²) was used. In both experiments employing either analog or digital readout electronics the distance between source and detector was 13 mm, while temperature conditions were slightly different, i.e., the experiments employing analog readout were carried out in a climatic chamber at 20 °C temperature, the experiments employing digital readout electronics were made at room temperature ≈ 23.5 °C.

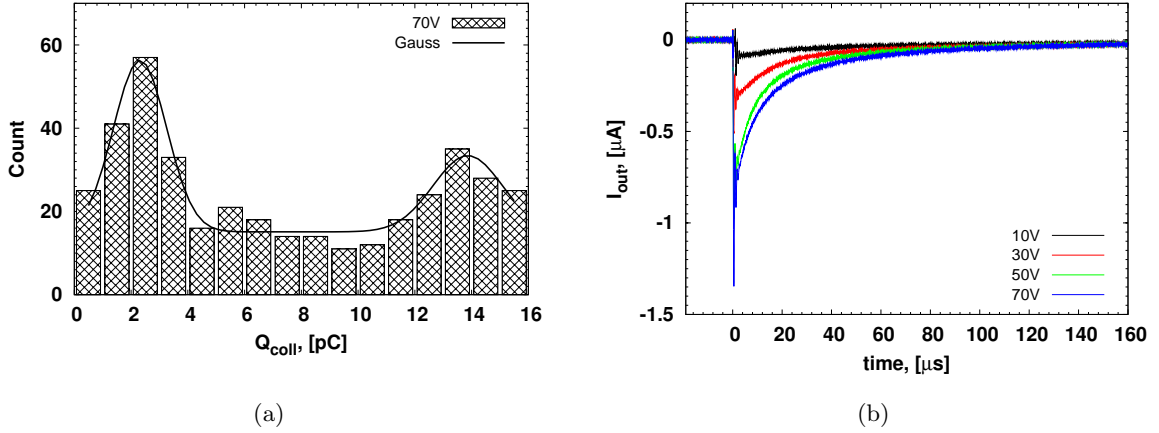


Figure 2.9: Laser pulsed light test of BPAD3 pixel: (a) - distribution of collected charge values that was built after the laser scan of one of the segments not covered by metal was performed; (b) - transient response of BPAD3 pixel biased at different collector voltages to 1060 nm laser pulses emulating α -particle with $E_{\alpha} = 1.14$ MeV energy.

2.4.1 Transimpedance readout

The readout scheme is very similar to the readout scheme used in laser pulsed light tests. A schematic representation of analog readout can be seen in fig. 2.10. It consists of high precision, low noise operational amplifier OPA227 with feedback resistor $R_f = 47$ k Ω and digital storage oscilloscope. Two types of oscilloscopes were used in this experiment TDS 3052B, [6] and ZTEC 4211, [68].

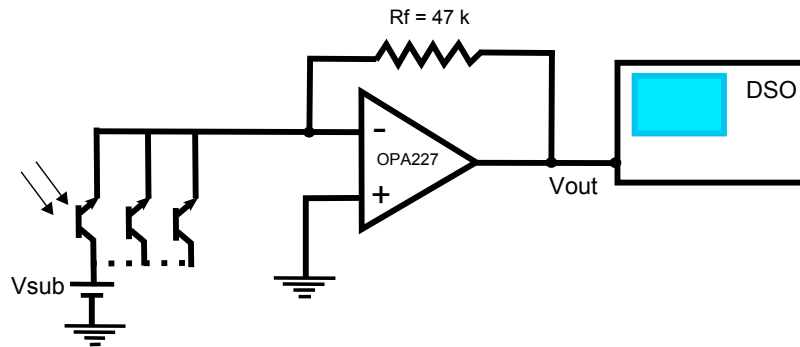


Figure 2.10: Schematic representation of the setup used to test BJT detectors from the BD1 batch consisting of transimpedance amplifier and digital storage oscilloscope.

The results of functional characterization of DPIX4 pixel are presented in fig. 2.11. The data were collected at different collector biases (10 V, 30 V, 50 V, and 70 V), in each case a thousand of events were acquired, integrated and after that distributions of collected

charge values were built. As it can be seen from figure 2.11(a) the distributions of collected charge acquired at 30 V, 50 V, and 70 V collector biases observe two peaks (corresponding mean values of Gaussain fits are presented in Table 2.1), while at $V_{sub} = 10$ V collector bias the distribution has only one peak. Presence of two peaks in the distribution can be explained by incomplete depletion of interpixel volume. So, part of charge generated by incoming α -particle is lost. In case of $V_{sub} = 10$ V the low charge peak disappears as all charge generated by α -particle in the interpixel volume is lost. Shift of the distributions to the higher values with increasing bias voltage is due to the increase of overall gain value that increases together with the bias (refer to fig. 2.2(b)). As the amount of collected events is the same in all cases, the data plotted in fig. 2.11(a) can not be used for the comparison of the rates, i.e., higher count values of the distribution acquired at 10 V bias do not mean that the detector has better detection properties at such bias voltage.

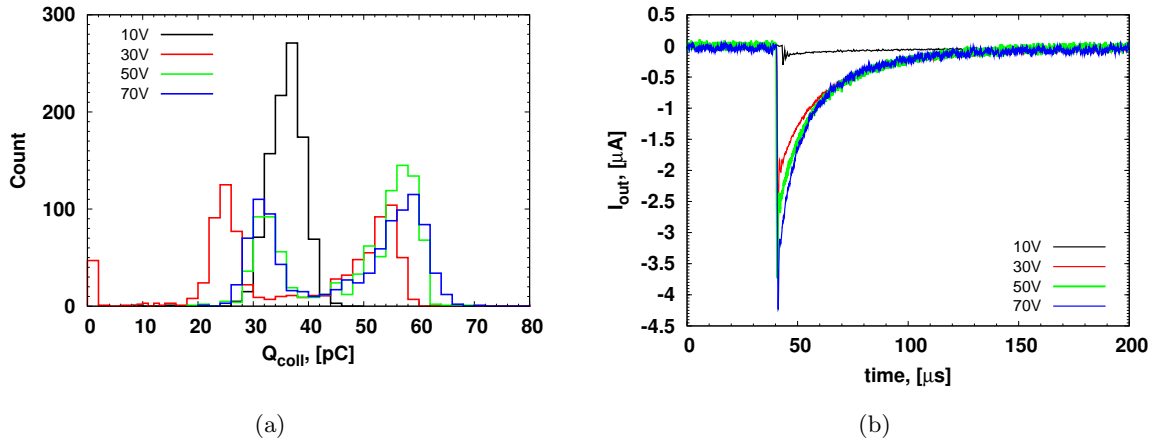


Figure 2.11: Functional characterization of DPIX 4 pixel from DPIX array, BD1 batch using transimpedance amplifier readout. The source was placed above the detector at $h_{ds} = 13$ mm height, the temperature was fixed at $T = 20$ °C, and resistance $R = 47$ k Ω : (a) - distributions of collected charge values Q_{coll} . (b) - single peaks, where Q_{coll} values correspond to $\mu_{peak,2}$ mean values of distributions shown in (a) (refer to Table 2.1). The offset level has been subtracted for all curves.

Bias, [V]	DPIX4			BPAD3	
	$\mu_{peak,1}$, [pC]	$\mu_{peak,2}$, [pC]	β_{quiesc}	μ_{peak} , [pC]	β_{quiesc}
10		36.2	220	3.52	76
30	24.8	53.2	270	6.42	110
50	32.4	56.8	300	13.1	120
70	31.5	57.4	320	19.4	130

Table 2.1: Summary results of functional characterization of DPIX4 and BPAD3 samples.

Distributions acquired during the characterization of BPAD3 are shown in fig. 2.12, the summary results are reported in Table 2.1. Obviously, due to the low gain values at low base currents the distributions are shifted to lower Q_{coll} values comparing to the similar distributions shown in fig. 2.11. In fact, assuming that energy of α -particle passing 13 mm distance in the air at 20 °C temperature is 2.44 MeV, BPAD3 pixel could maximally reach $Q_{coll} \approx 30\text{pC}$ (here we assumed that overall gain value reached its maximum value), while DPIX4 sample could reach $Q_{coll} \approx 58\text{pC}$.

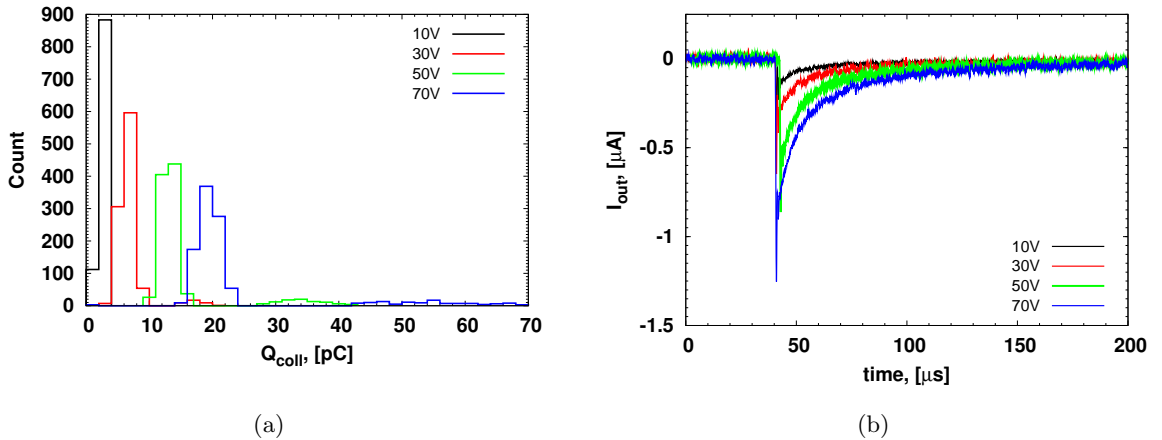


Figure 2.12: Functional characterization of BPAD3 pixel, BD1 batch using transimpedance amplifier readout. The source was placed above the detector at $h_{ds} = 13$ mm height, the temperature was fixed at $T = 20$ °C, and resistance $R = 47$ k Ω : (a) - distributions of collected charge values Q_{coll} . (b) - single peaks, where Q_{coll} values correspond to mean values of distributions reported in Table 2.1. The offset level has been subtracted for all curves.

Analysis of the data presented in fig. 2.12 confirms that the pixel with NCH18xNN11 emitter layout operated with floating base at 70 V is “turned on” by α -particles, so the overall gain is ~ 200 , while at lower biases (10 V, 30 V, and 50 V) the pixel was not “turned on” by α -particles. Therefore, the overall gain values were approximately equal to the quiescent gain values.

2.4.2 ALPHADET readout

After α -particle tests with analogue readout confirmed that DPIX sample had better detection properties than BPAD sample, similar α -particle tests were done using digital ALPHADET readout electronics⁴.

Firstly, single pixels (from DPIX1 to DPIX4) were tested individually. The data were acquired with a trigger set below 0 pC (-0.55 pC), so all data converted by ADC could

⁴Detailed description of ALPHADET electronics is presented in the next Chapter 3, page 39.

be swept into a *.txt file and then analyzed. The analysis was performed offline. Firstly, α -particle events were identified in a data file using a “peak detection” function. Any point in the data file is considered as a “peak” if the preceding point is smaller by a value of “soft”-trigger (soft - in this case states for software as the value of this trigger can be changed offline in the software used for the analysis of data). After that an integration of every event was performed. Fig. 2.13 shows a piece of data file which was used to build a distribution shown in fig. 2.15(a). The inset in fig. 2.13 is a zoom of one of the events every point of which represents a value of charge collected by DDC114 during a single integration period ($400 \mu\text{s}$). The integration of every event was made over 1.2 ms, i.e., just three points were taken into account (those are in red color in the inset).

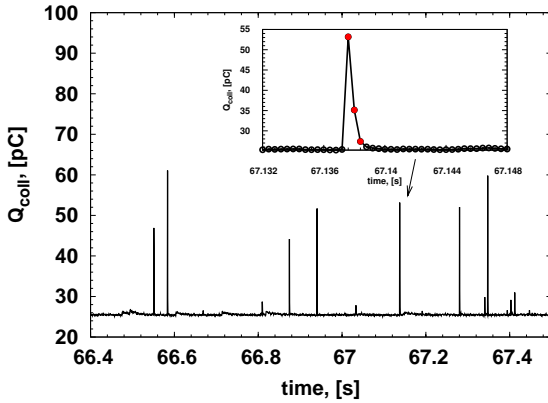


Figure 2.13: A part of data file with an inset showing that just three points were taken into account during integration

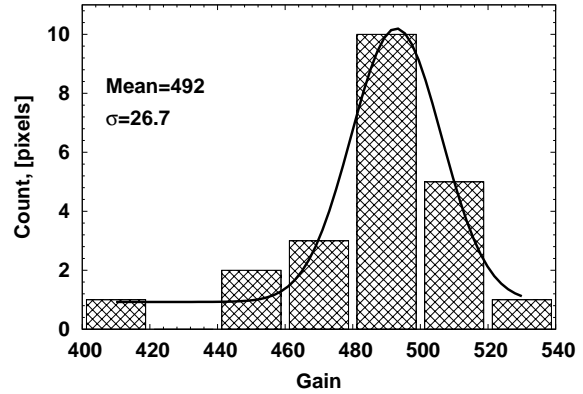


Figure 2.14: Gain distribution for the array of DPIX pixels at 70 V collector bias (3 corner pixels with defects not included)

The data were analyzed with a “soft”-trigger set to 10 pC and acquisition time fixed to 125 s. Pairs of pixels (DPIX1-DPIX2 and DPIX3-DPIX4) show similar distributions of collected charge (see fig. 2.15). The differences between pairs of pixels can be ascribed to the damage caused to the detector by the bonding: in fact, the contact pads were placed inside the active area, and bonding induced a large, and non uniform, leakage current degradation. DPIX1-DPIX2 were found to have lower leakage current ($\sim 70 \text{ nA}$ vs $\sim 120 \text{ nA}$ at 70 V collector bias, see fig. 2.2(a)) and so a lower base voltage value (V_b) in the quiescent state, thus reducing their gain. After that DPIX1-DPIX4 pixels were shorted together and characterized. Fig. 2.16 refers to the results of the characterization; naturally, spectrum acquired by an array of four DPIX pixels corresponds to the sum of spectra acquired individually.

Additional electrical measurements (e.g., Gummel plots, output characteristics, etc.)

were performed on other identical DPIX detector from the same wafer. These tests allowed confirming that the gain values at a given collector bias (e.g., 70 V in this case) are very uniform, with a spread in the order of 5% (see the distribution in fig. 2.14)⁵. Therefore, we could conclude that the gain non uniformity does not depend on the fabrication process itself but only on the bonding step, which of course should be improved in view of operating arrays of pixels.

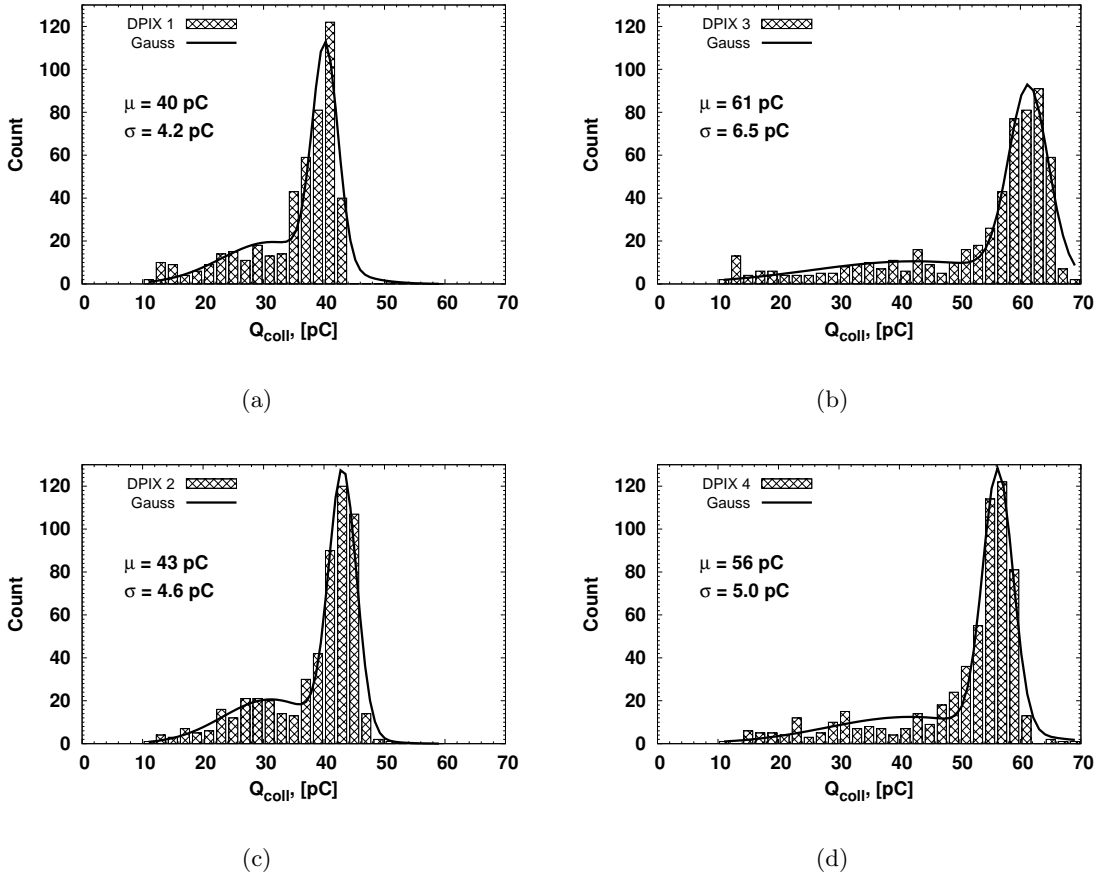


Figure 2.15: Spectra acquired by single pixels DPIX1 (a), DPIX2 (c), DPIX3 (b), and DPIX4 (d). The trigger was set to 10 pC; the acquisition time was fixed to 125 s; collector bias was set to 70 V.

Another reason for the observed differences in the distributions of collected charge is to be attributed to the different energies that impinging α -particles have when they reach the detector surface, as a result of the different solid angles within which particles hit pixels: in case of the 4 pixels so far considered and with the radioactive source placed above them at 10 mm height the solid angle is just ~ 0.1 steradian, whereas it is almost

⁵This conclusion is valid only if an array of pixels is considered and not a whole wafer.

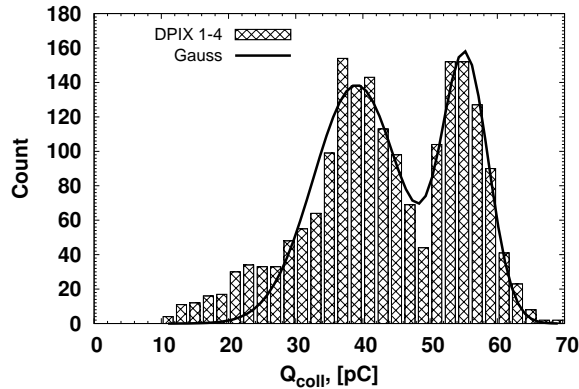


Figure 2.16: Spectra acquired by four DPIX pixels (DPIX1, DPIX2, DPIX3, DPIX4) having emitters shorted together. The trigger was set to 10 pC; the acquisition time was fixed to 125 s; collector bias was set to 70 V.

5 times higher for a 21 pixels array. Therefore, for the 21 pixels array most α -particles are expected to have smaller energies due to a longer path traveled in air while reaching the detectors. Hence, the peak of distribution should be shifted to lower energy values and only the tail should consist of high energy events. This prediction could be assessed with measurements on the 21 pixels read as one detector. However, as already mentioned, the bonding caused a large increase in the leakage current, from ~ 4 nA at 70 V collector bias before bonding to the values ranging from 40 nA to more than 120 nA, a fact that of course was not expected. Taking into account that the integration time of DDC114 is 400 μ s and the average leakage current is ~ 80 nA, we obtain a charge offset value of 32 pC per pixel. The maximum value of charge that DDC114 can convert is 350 pC, thus preventing from using the ALPHADET electronics to read out the signal from the array of 21 pixels. In order to verify the prediction about influence of solid angle on the distribution of collected charge, an additional test have been performed using the analogue readout. This readout consisted of a transimpedance amplifier and an ZTEC 4211 oscilloscope⁶ (see the schematic diagram of the setup on fig. 2.10). The distribution of the collected charge values is shown in fig. 2.17, and, as expected, is rather broad. However, taking into

⁶ZTEC 4211 is an 8-bit Digital Storage oscilloscope (DSO) [manual MClassDSO instrument]. The instrument digitizes analog input in the records the size of which is controlled by user. The DSO has an ethernet interface compliant with IEEE 802.3 Ethernet standard (this feature is particularly convenient when the measurements have to be done under the dark condition). The maximum record length for non-interleaved and normal mode acquisition is 128 MiSamples. If the record size is chosen by user to be smaller, then the overall amount of records saved in the internal memory of the DSO is 128 MiSamples/record size. Testing array of DPIX pixels the size of record was chosen as 4096 with 1 μ s time interval. It means that the maximum amount of events (i.e., records) that could be collected under such conditions was 32768, which is enough to acquire a good distribution.

account functional tests that were performed on the samples from the BD2 batch of BJT detectors (the second batch with a modified layout, which excluded a strong influence of the bonding step on the properties of detectors) we can conclude that the broadening of a spectrum appeared mainly due to the changes of detector’s detection properties after the bonding step.

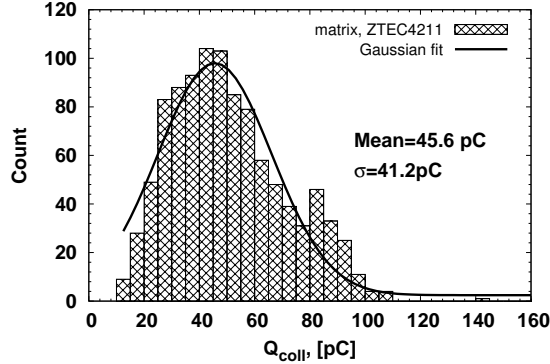


Figure 2.17: Functional characterization of the array of DPIX pixels. Distribution of the collected charge values acquired by an array of 21 pixels wired together and read out with a transimpedance amplifier and an oscilloscope.

2.5 Summary

Laser tests have confirmed that pixels with either “standard” emitter layout or minimum size emitter layout could be efficiently used for α -particle detection while being operated with a floating base. Acquired distributions of collected charge values explained low energy tails in the similar distributions acquired during α -particle functional tests.

Functional tests using ^{241}Am alpha-particle source were performed using different read-outs coupled to DPIX and BPAD pixels. The very first results acquired with analogue readout confirmed that pixels either with NCH32xNN20 (DPIX pixel) or NCH18xNN11 (BPAD) emitter layout can be “turned on” by an α -particle. However, DPIX pixel has shown better detection properties than BPAD pixel at collector biases lower than full-depletion voltage. Such effect has twofold explanation: firstly, the gain of DPIX pixel is much higher than the gain of BPAD pixel at low base currents; secondly, the quiescent gain value for DPIX pixel is higher than for BPAD pixel due to larger area and higher leakage current.

The following functional tests included characterization of only DPIX pixels. When DPIX pixels are read out individually using ALPHADET electronics, the collected charge

distributions are pretty good with clear peaks and standard deviations in the order of 10%. When several pixels are read out together as one detector, a much broader distribution is observed, which we could explain in terms of two concurrent effects: the different energies of α -particles reaching the detectors within different solid angles when large pixel arrays are considered, and the non uniformity of the gain of BJT pixels which was determined by the large and non uniform leakage current degradation induced by the bonding step.

Taking into account all relevant results of the functional tests, we could draw some important conclusions about possible layout of the pixel that would be a basic pixel in the BD2 batch. Such pixel has been called as a “standard” pixel. “Standard” pixel has a minimum size p-well implant in order to minimize base capacitance and NCH32xNN20 emitter layout configuration to ensure high gain values at low base currents.

Chapter 3

ALPHADET

In this chapter we will introduce a new FPGA-based readout electronics, so-called ALPHADET board, which was specifically designed for the operation with BJT detectors. Section 3.1 describes the design and layout of the printed circuit board. This includes a concise explanation of the choice of components and their specific purpose on the board. Section 3.2 describes a methodology of electrical characterization of FPGA-based electronics. A thorough explanation of all performed tests is provided in this section, so one could repeat these measurements. The results of the characterization are presented in this section as well. Finally, a short summary of the chapter is presented in section 3.3.

3.1 Design and layout

Design and layout of ALPHADET board was based on the same principle as our previous microcontroller based digital readout electronics for BJT-detector [69], [7]. Single module of such electronics coupled to BJT-detector was designed as a Wireless Sensor Network (WSN) node that could be operated in a star network [7]. Obviously, the power consumption was of primary importance for the choice of components, hence, a microcontroller was chosen in that case as a core for the electronics.

The Analog-to-Digital conversion in ALPHADET board is done by DDC114 component, while in a former microcontroller based readout the conversion was done by DDC112 component. DDC114 is a functionally equivalent component, which has a slightly higher sampling rate (3.125 kSPS instead of 3 kSPS) and, more relevant in our case, this component supports a +2.7 V to +5.25 V digital supply while DDC112 supports only +4.75 V to +5.25 V digital supply. V_{CCO} , the supply voltage for output drivers, for the banks of Spartan-3 FPGA may not exceed 3.75 V [70] (3.3 V is a recommended value). The power banks of XC2S400 FPGA used in the current design can be seen in fig. 3.1. It should be underlined that V_{CCO} , differently from V_{CCAUX} and V_{CCINT} , which are fixed to 2.5 V

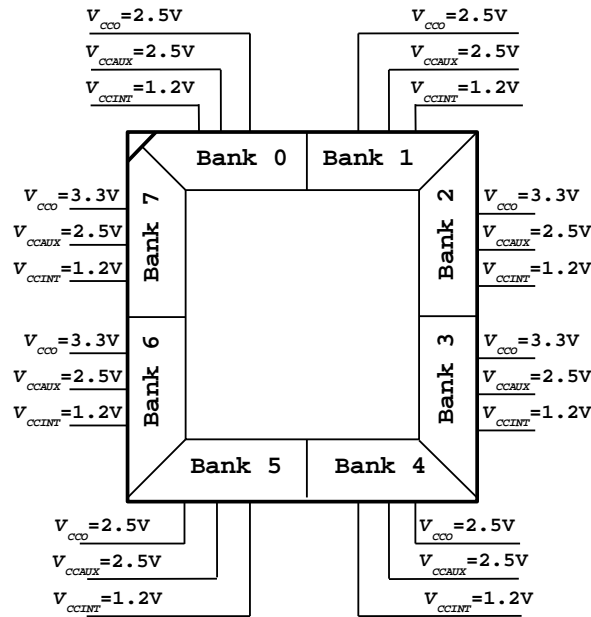


Figure 3.1: Power banks of XC2S400 Spartan-3 FPGA.

and 1.2 V correspondingly, can be either 3.3 V or 2.5 V. Thus just supplying $V_{CCO}=3.3$ V to the banks of FPGA, which are connected to the ADC (in this case the banks 6 and 7), the compatibility of two components may be achieved. The other banks have lower V_{CCO} , so the power consumption of FPGA becomes smaller. So, that was a reason why we have switched from DDC112 to DDC114 component that considerably simplified the design, i.e., allowed avoiding voltage-level shifters.

This ADC component (Texas Instruments) has been chosen due to few reasons. First of all, it has current input instead of voltage input, which is most suitable for the detector with strong current signal output, i.e., BJT detector. Another relevant advantage that provides use of DDC114 is a continuous current integration, while one integrator is being digitized another is integrating signal; therefore, no information about read-out signal is lost. In case an information about possible maximum value of a read-out charge is available, then an adjustable fullscale range becomes relevant and higher precision can be achieved. The block diagram of the DDC114 component is shown in fig. 3.2, [4]. This component has 4 input channels. Although, a BJT detector has a single output channel, we have designed the layout of the board and firmware for FPGA in such a way that any of those channels can be coupled to the BJT detector. This approach confirmed to be successful; due to some problems during a soldering step (it is quite problematic to solder manually VQFN type of component package) some channels were not working at first. However, after making first electrical tests with working channels, which confirmed that

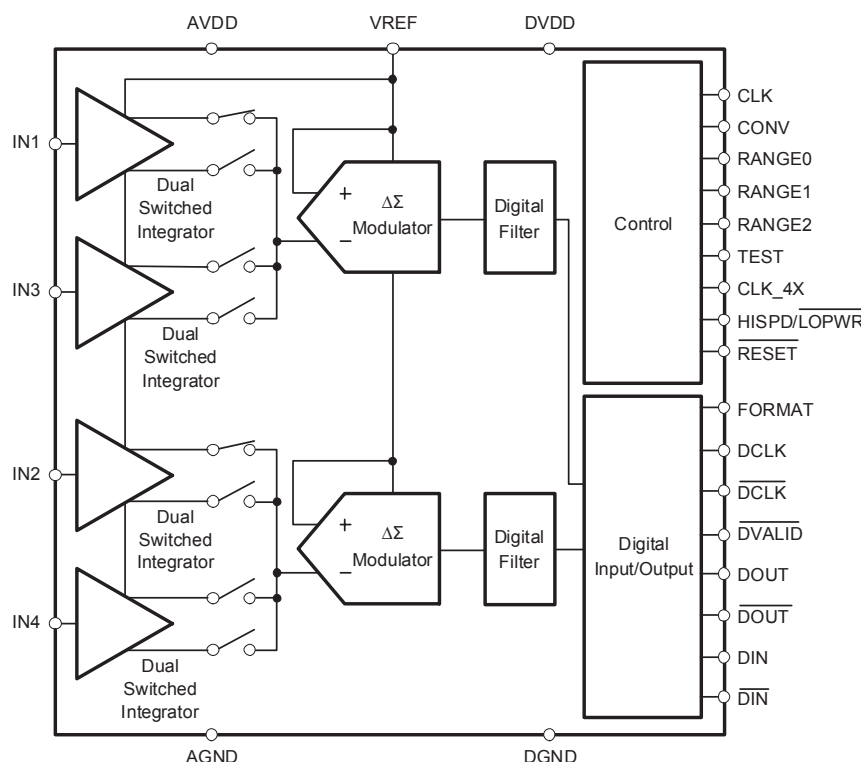


Figure 3.2: The block diagram of DDC114 component.

the design was correct, the missing channels were repaired. The right side of the block diagram contains all the pins that were connected to the banks 6 and 7 of the FPGA. The control pins establish working conditions for the DCC114 component, while input/output pins send to FPGA a digitized input current signal and define format of output data (16 or 20 Bits) etc.

As it has been already mentioned, the ALPHADET board has an XC2S400 from Spartan-3 FPGA-family as a main processing unit. The choice of FPGA as a core of readout electronics gives few relevant advantages at a prototyping stage. First of all, it is possible to implement good debugging facilities on the board, which allow fast programming and reprogramming of the board, and also monitoring all the signals. In principle, monitoring may be done either via hardware, i.e., using logic analyzer, or via software (ChipScope tool in case of Xilinx FPGA). Another advantage of ALPHADET is the use of convenient USB connection between the board and user PC, so the option of on-the-fly processing of acquired data becomes available.

The general scheme of the board is depicted in fig. 3.3. The current signal is digitized by DDC114, then digital signal is processed by FPGA, stored in the internal FIFO memory of FPGA, after that the packets of information are transferred to user PC via

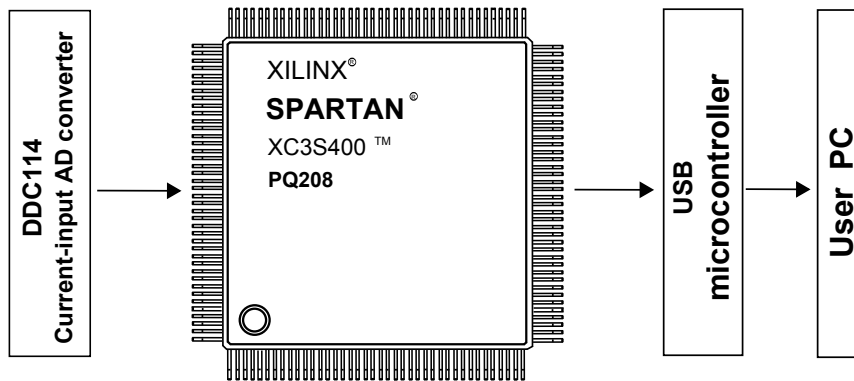


Figure 3.3: General scheme of ALPHADET electronics.

USB microcontroller (Cypress USB microcontroller - CY7C68013). The actual layout of the board includes four copper layers, aimed at routing a large amount of signals with proper ground and power planes. A picture of the board is shown in fig. 3.4. The design schematics and the layout of the ALPHADET board can be found in Appendix A. The layout of each copper layer is self-explanatory. However, a few details regarding layout of power and ground copper layers should be underlined. The ground plane was divided into two parts, i.e., digital and analog. These grounds are brought together via resistor and ferrite connected in parallel. The power plane has been also split onto two parts. The analog part is 5 V power supply for DDC114. The digital part includes 3.3 V and 2.5 V copper planes, which provide power supply for FPGA. The rightmost copper plane is 3.3 V power supply for the USB microcontroller.

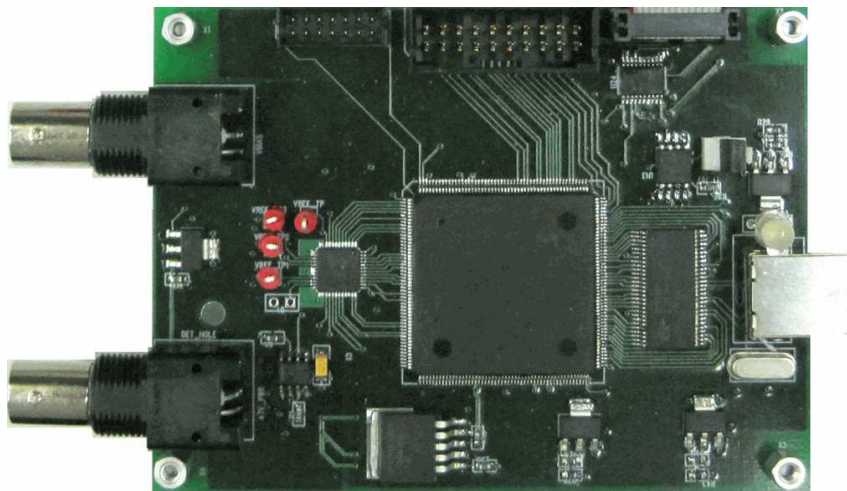


Figure 3.4: Implementation of the board (the size is $11 \times 7.5 \text{ cm}^2$).

3.2 Electrical characterization

In this section we present two independent testing strategies. The choice of the best strategy depends on possible limitations, e.g., it can be a lack of necessary hardware or software. The first strategy relies on the use of logic analyzer, while the second relies on the use of ChipScope software, so having access just to one of the tools provides a possibility to implement a proper electrical characterization of readout electronics. In case none of those options is available the ALPHADET could be tested by using firmware and software resources. A short description of the Test Mode of DDC114 is presented here as well.

3.2.1 Testing ALPHADET using logic analyzer

DDC114 has four analog inputs. The design of ALPHADET board was made in such a way that all analog inputs were connected to either so-called TP (test points) or detector header (see the Appendix A). Due to use of FPGA it is equally convenient to work either with single or multiple channels. However, we will only use one of the single channels for the subsequent testing; the option of choosing multiple channels for the simultaneous testing is not considered here (in fact, this option would be important in case the problem of crosstalk between the channels was relevant; however, as we are planning to use only a single channel in the final application there is no need to consider a crosstalk). This makes firmware and software simpler, so the debugging becomes easier. Among four available channels we have chosen channel N3 (AIN3¹) for the subsequent tests. Due to the peculiarities of the layout of the board, AIN3 is more convenient for the placement of external components, i.e., injection capacitor and 50 Ω resistor.

Four buses DATA_CH1, DATA_CH2, DATA_CH3, and DATA_CH4 corresponding to four input channels were implemented in firmware. DDC114 component digitizes an analog signal from all analog inputs AIN1-AIN4 and outputs it via DOUT pin as a serial data. The serial data is then parallelized and split onto four buses corresponding to each input channel. In principle, any data bus could be routed either to USB microcontroller or monitor header. The monitor header has been installed on the board only for testing and debugging purposes, because it provides a very convenient access to the internal FPGA signals. To test ALPHADET board and firmware the DATA_CH3(15:0) bus was routed directly to a monitor header². So, a logic analyzer could be used for the debugging. After the debugging and testing were finished the data bus DATA_CH3(15:0) was rerouted from the monitor header to the USB microcontroller and, hence, to a PC, where the digitized

¹AIN means Analog INput

²This header can be found in schematics as MON_b and in firmware as MonitorHeader block

data from AIN3 could be saved to a *.txt data file.

To make an electrical characterization of ALPHADET board we have used a setup suggested in [69], which can be observed on fig. 3.5. The charge is injected into the input channels via an injecting capacitor. The injected charge is proportional to the amplitude of a signal generated by SG (Signal Generator Agilent 33250A) and capacitance of a capacitor according to the formula $Q=C \cdot V$, where C equals to 200 pF in this particular test.

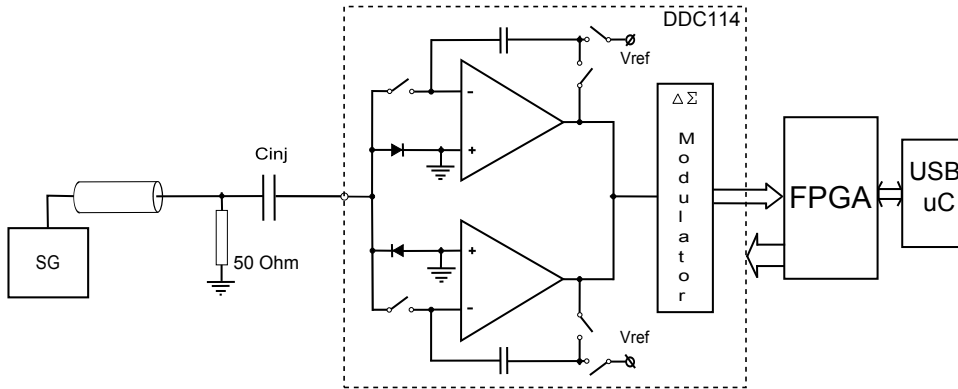


Figure 3.5: Block diagram of experimental setup.

For simplicity we call analog signal generated by SG as A1, the reason for that is because logic analyzer (mixed signal oscilloscope 54641D) has two analog inputs and A1 signal was monitored by the first input. A1 has the following properties: period - 220 μ s, amplitude - 100 mV, offset - 50 mV, pulse width 50 μ s. According to the above mentioned formula, the value of injected charge should be around 20 pC. However, due to the fact that the analog signal A1 was also monitored by the oscilloscope 54641D this signal was divided on the oscilloscope/(ALPHADET input resistance) voltage divider; thus, the actual amplitude of input signal was not 100 mV but 67.5 mV (Table 3.1 shows a part of the output data file, which corresponds to the input signal with an amplitude of 67.5 mV).

After known charge is injected into DDC114 it is possible to make a comparison of DDC114 output and data written to *.txt file. This approach aims at two purposes. Firstly, it is to make check that software writes to the output file exactly the same data that comes from DDC114 as DOUT signal. It can be made simply by monitoring data bus and comparing its decimal values with values in *.txt file. The second purpose is to test DDC114 with known injected charge, which can be made by comparing values of injected charge and values of charge in *.txt file.

The output data word consists of 16 bits. In principle, it is possible to connect at once all 16 bits to the monitor header. However, it is not convenient because we would

Timer	Timer (32:25)	Timer (24:16)	Timer (16:8)	Timer (7:0)	DATA (15:8)	DATA (0:7)	footer (15:8)	footer (7:8)	Charge, bit value	Charge, pC
1684874	219	25	181	138	10	210	43	43	2770	13.4791
1684875	219	25	181	139	1	22	43	43	278	0.117955
1684876	219	25	181	140	0	0	43	43	0	-1.4
1684877	219	25	181	141	1	22	43	43	278	0.117955
1684878	219	25	181	142	1	30	43	43	286	0.160848
1684879	219	25	181	143	1	24	43	43	280	0.128678
1684880	219	25	181	144	10	200	43	43	2760	13.4255
1684881	219	25	181	145	0	0	43	43	0	-1.4
1684882	219	25	181	146	1	12	43	43	268	0.064339
1684883	219	25	181	147	1	12	43	43	268	0.064339
1684884	219	25	181	148	1	16	43	43	272	0.085786
1684885	219	25	181	149	10	196	43	43	2756	13.404

Table 3.1: The structure of data that are written by software to a *.txt file.

lose the possibility to observe other relevant signals, e.g. enable (EN) signal or conversion (CONV) signal. These two signals give a general idea when the data is ready to be read out and which side of DDC114 is currently integrating. This is why only 8 bits of the data bus were monitored, those are DATA_CH3(15:8). These bits can show in a very reliable way the state of the data. In order to explain this idea a piece of data file is presented here in Table 3.1, which also shows the structure of the data generated by the firmware. The first column is a 24 bit counter (that is also called a timer) with a single increment of $400 \mu s$. The current version of the firmware has a counter with a maximum value corresponding to ~ 107 minutes. Thus, every 107 minutes the counting starts again from zero. This time period is enough for a regular laboratory experiment.

When the firmware takes the value of a timer it stores it into FIFO and then sends the data to the USB microcontroller. The microcontroller can read from FIFO only 16 bits at once. Since the counter has 24 bit dimension it has to be split onto two 16 bit words. So, there are 8 bits that can be used for other purposes. It would be convenient to know where the data packets start and end. This is why those 8 free bits were assigned as a mask; the mask shows that there are 3 bytes of timer information and 2 bytes of data information after it. It has the value of 219 in decimal representation and “11011011” in binary representation. Referring to Table 3.1, the mask is the second column in *.txt data file, while the next three columns are the actual bytes of the timer (3th, 4th, 5th columns). The data bytes DATA_CH3(15:8) and DATA_CH3(7:0) are represented in 6th

and 7th columns correspondingly. The remaining 8th and 9th columns are the “footer”, which signals when the data transfer is finished. “Charge_bit” column (10th) shows the decimal value of digitized charge collected by an integrator of DDC114, while “Charge” column (11th) shows actual value of charge in pC.

The first data byte DATA_CH3(15:8) corresponds to the decimal numbers from 256 to 65280 (65280 is $\sim 100\%$ FS value that is 350 pC), the second data byte DATA_CH3(7:0) corresponds to the numbers from 0 to 255 (from -0.3955% FS to 0% FS³). Thus, for testing purposes only DATA_CH3(15:8) signals can be connected to the monitor header. In that way the signals EN and CONV are monitored simultaneously with the data bus.

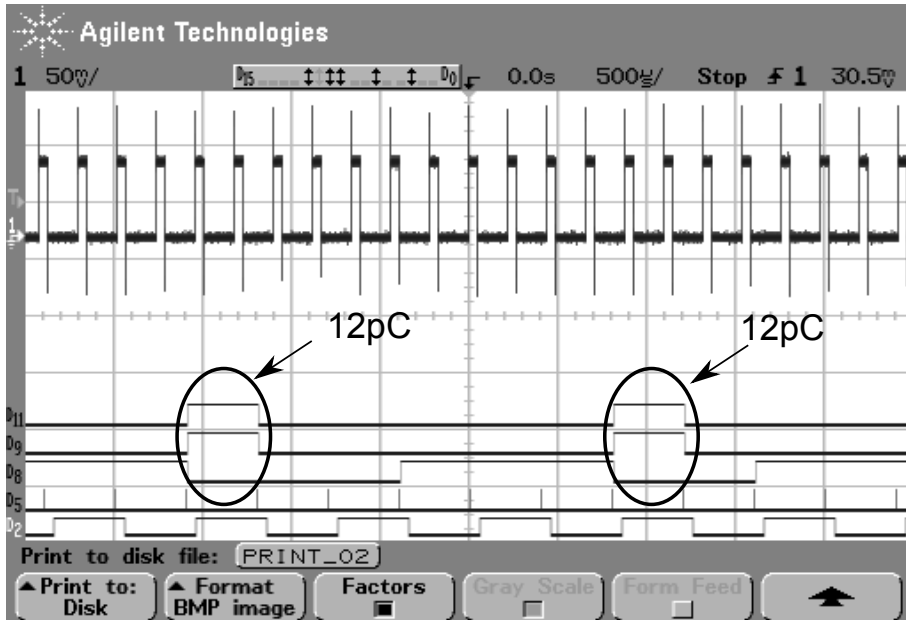


Figure 3.6: Test1, picture of scope screen. The monitored signals are CONV (D2), EN (D5), DATA_CH3(15:8) (D15-D8 correspondingly, only D8, D9 and D11 are shown) and analog input A1.

Fig.3.6 is a snapshot of a logic analyzer. Following signals from the bottom to the top of the picture we define them as: D2 - conversion signal CONV, D5 - enable signal EN, D8, D9, D11 are 8th, 9th and 11th bits in DATA_CH3(15:8) byte correspondingly.

Let’s consider a case when D8=0, D9=1, and D11=1 then DATA_CH(15:8)=“00001010”, (“00001010” byte is equal to 10 as a decimal number). Assuming that all not monitored bits are equal to “0”, the corresponding 16 bit word is “0000101000000000”; it is 2560 in decimal representation and it corresponds to ~ 12 pC charge. So, indeed, it is possible to monitor value of a Charge_bit by monitoring only (15:8) bits of DATA_CH3.

³decimal 256 is exactly 0% FS

The results of the test are presented in fig.3.6. The test A1 signal has a period of $220 \mu\text{s}$ that is smaller than integration period of $400 \mu\text{s}$. Therefore, the maximum value of collected charge should be observed during the entire test time. Nevertheless, fig. 3.6 confirms that there is no “saturation” and only every 5th value of “Charge_bit” corresponds to a charge injected into DDC114 instead of heaving all monitored data signals in a high state.

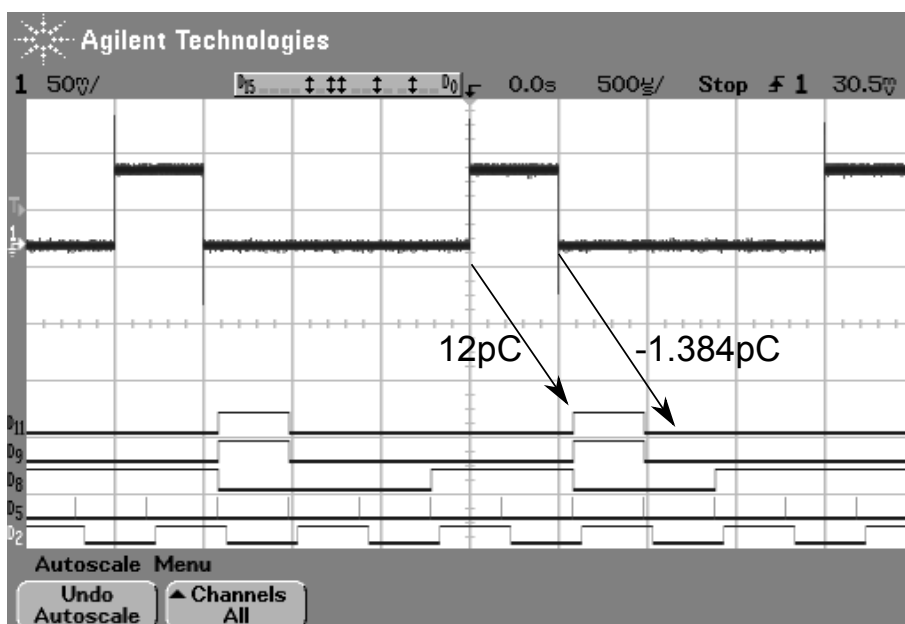


Figure 3.7: Test2, picture of scope screen. The monitored signals are CONV (D2), EN (D5), DATA_CH3(15:8) (D15-D8 correspondingly, only D8, D9 and D11 are shown) and analog input A1.

The observed phenomenon, when the charge is injected into the input channel constantly but detected only every 5th period of integration, can be explained by the fact that, due to a particular setup (fig.3.5), two current pulses are produced, which correspond to rising and falling edges of the voltage pulse. So, in case when the duration of voltage pulse is less than integration period of DDC114 ($400 \mu\text{s}$), the total injected charge is equal to 0 pC . Therefore, when the test signal has pulse width less than integration period the most of the voltage pulses will happen during a single integration period of DDC114 and only a few of the pulses are split between two integration periods. In that case we observe in the output data file that one of the strings corresponds to an injected charge with an expected value, i.e., 12 pC and the next string contains zero value, which corresponds to a negative charge (it means that the charge is extracted from the readout circuit).

Therefore, the results of this test should be correct, i.e., corresponding to the input

analog signal, if this signal has a pulse width larger than integration time of DDC114. Fig.3.7 shows a snapshot of logic analyzer screen for the experiment with an analog signal that has a pulse width of $500 \mu\text{s}$. The output digitized signal completely corresponds to the analog input signal, i.e., every 2 ms DDC114 collects 12 pC during one of the integration cycles and during the very next integration cycle DDC114 collects a negative charge, which corresponds to a falling edge of the test voltage pulse.

3.2.2 Testing ALPHADET using ChipScope

The Test Mode is the mode that was implemented on the hardware level in the DDC114 component. It is mainly used on the debugging stage. This mode can be entered if TEST signal is held high during CONV transition. It is possible to provide 11 pC charge packets to DDC114 simply by strobing TEST low and then high, each rising edge of the TEST signal provides 11 pC either to A or B side of the integrator. In order to quit Test Mode it is enough to take TEST low before transition of CONV. The timing diagram is presented on fig.3.8.

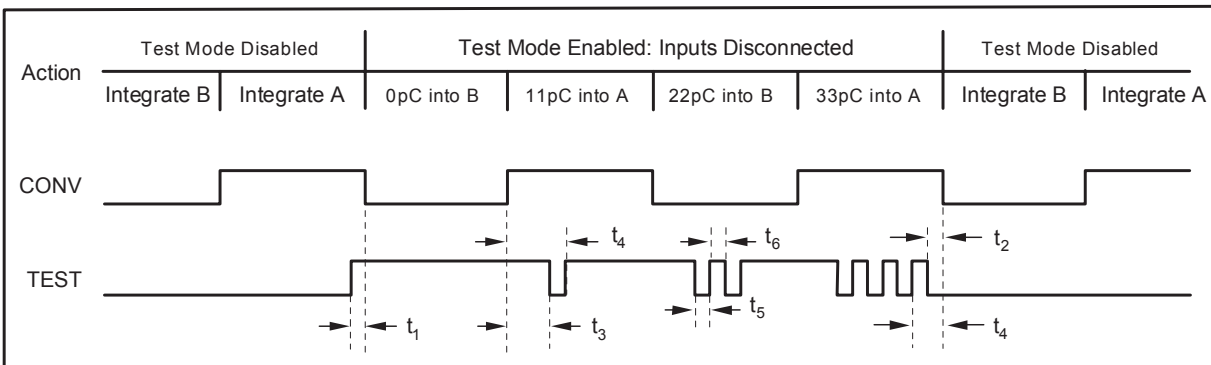


Figure 3.8: Timing diagram of the Test Mode of the DDC114 [4] [datasheet of DDC114].

The advantage of this method to test DDC114 is that there is no interaction with external environment. So there is no need to care about noise issues, connecting capacitor and resistor to an analog input of DDC114 etc.

There are few ways to monitor data bus, which are:

- Logic analyzer via Monitor header on ALPHADET board;
- ChipScope software provided by Xilinx;
- Software and firmware.

ChipScope is software from Xilinx that allows monitoring signal generated by FPGA via JTAG interface. While designing this board, the possibility of using ChipScope was

reserved by connecting JTAG connector to proper pins of FPGA.

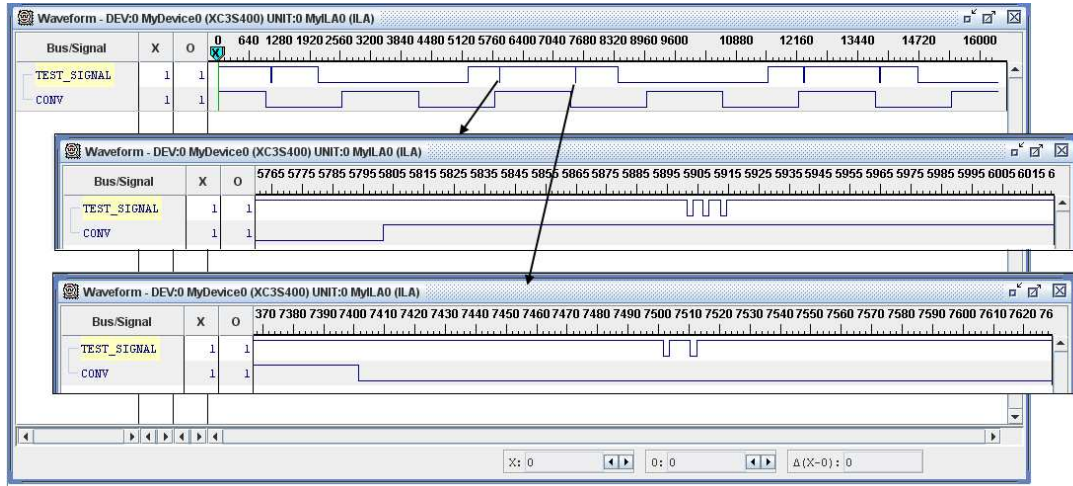


Figure 3.9: TEST signal.

The TEST signal was generated in a way that 33 pC are applied to A side and 22 pC to B side of integrator. The A side integrates when CONV is high, and the B side integrates when CONV is low. Fig. 3.9 is a snapshot of waveform window generated by ChipScope. The time diagram includes waveforms for two signals - TEST_SIGNAL and CONV. After 33 pC and 22 pC are applied to A and B sides, the TEST signal is taken low to quit Test Mode and two integration periods are just to integrate applied charge. The results of the test are shown on fig. 3.9.

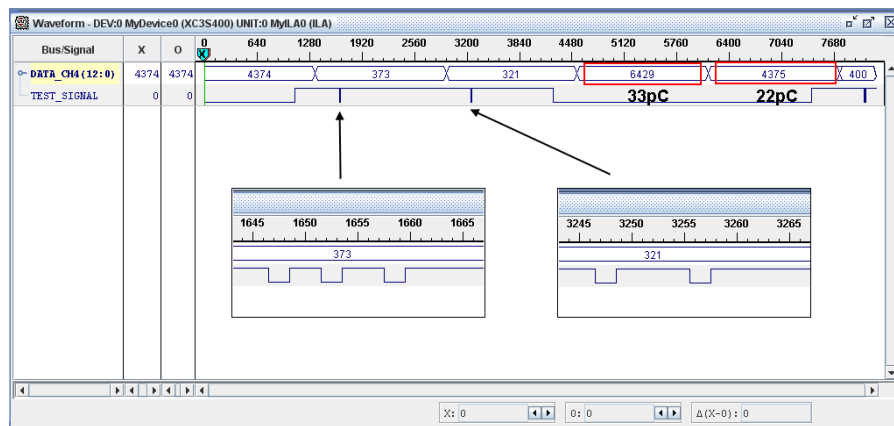


Figure 3.10: TEST signal.

We can see that there are a data bus DATA_CH4(12:0) consisting of 13 bits and TEST_SIGNAL. 13 bits are enough to represent decimal from 0 to 8191 that corresponds to a range from ~ 0 to 44 pC. So it is enough to have just 13 bits, as long as injected

charge is less than 44 pC. There are few reasons for such limits. Firstly, it is because RAM modules in FPGA are split between two implemented cores - ChipScope core and implemented FIFO core. The second reason is that CONV signal has frequency of 1.25 kHz while clock signal CLK has frequency of 4 MHz; simple calculation shows that for single transition of CONV (from rising to falling edge and vice versa) the CLK has 1600 cycles. So, in order to see just two periods of CONV signal CLK must have 6400 periods. This is why the minimum data depth in ChipScope core is 8192, which significantly limits amount of monitored signals (in this particular case it is 14).

The analysis of obtained data shows exactly what we would expect - two “packets” close to 0 pC, and then two consequent “packets” of 33 pC and 22 pC (see fig. 3.10). Also we can see that while DDC114 is in Test Mode the integrator is not integrating, this is why 33 pC and 22 pC “packets” are shifted. (It is worth mentioning that data bus is changing its state on falling edge of \overline{DVALID} signal.)

3.2.3 Analysis of acquired data

The first type of test has been performed using the setup shown in fig. 3.5. The data have been acquired with analog input signal of 2.4 ms period, with 500 μ s pulse width and different pulse amplitudes. Fig. 3.11 shows a case when the amplitude of the signal is \sim 33 mV, which corresponds to the injected charge of 6.6 pC. The plot of analog signal and plot of collected charge are overlapped in order to demonstrate how data file is analyzed. The plot of collected charge also includes noise data, which is cut off by a software trigger during the next experiments.

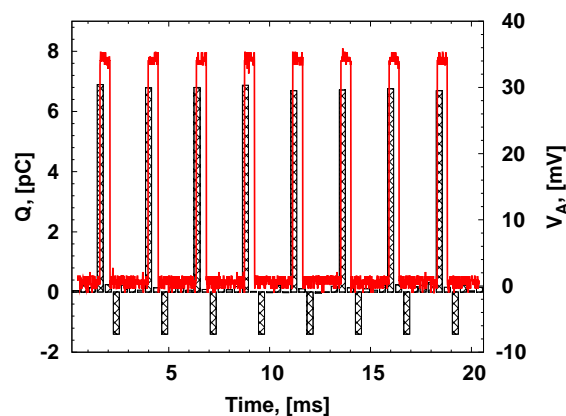


Figure 3.11: Typical representation of structure of saved data file. Collected charge is plotted with boxes (left y-axis), while analog input signal is plotted with a red line (right y-axis).

The value of injected charge depends on the amplitude of analog input signal. Making

few acquisitions with different amplitudes of analog input signal it is possible to make a so-called linearity test. This test shows if collected charge values depend linearly on the injected charge values. The data have been collected with a sufficiently high trigger value, so the acquisition would not be triggered by noise. After making acquisition for different injected charge values, the data were analyzed and distributions of collected charge values were built. These distributions are called charge occurrence diagrams, one of them is shown in fig.3.12(b). Due to large values of charge provided by the BJT detector, the range of input charge values is quite wide (for 5.5 MeV alpha-particle and gain of detector 500 the expected output charge is ~ 120 pC). The mean values of the Gaussian fits of charge occurrence diagrams are plotted with points in fig. 3.12(a); they show a very linear behavior, e.g., a standard deviation of the linear fit is $= 0.53$ pC, which is rather good value for the injected charge ranging from 10 pC to 150 pC.

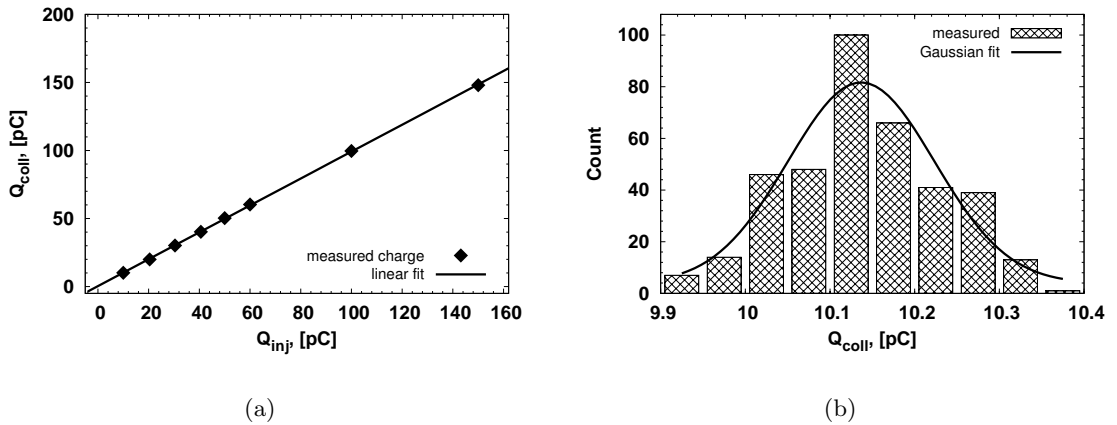


Figure 3.12: Linearity test of ALPHADET board: (a) - linearity test, (b) - charge occurrence diagram for 10 pC injected charge.

Two versions of ALPHADET board were designed and implemented (A and B). Performance of these boards was compared in terms of their noise properties. The comparison was carried out between the same channels of the boards. Fig.3.13(a) shows results that were acquired using the same channel 3 (Ch3) for both boards. It is clear that ENC values are much smaller for board B. The Equivalent Noise Charge (ENC) for Ch3 of board B is ~ 600 electrons rms, whereas for the corresponding channel of board A it is ~ 2400 electrons rms. The large difference in the ENC values may be ascribed to the fact that board B features better shielding of input channels and also that a thermal pad under DDC114 component is grounded in board B and left floating in board A. Due to its lower noise, board B was fully characterized and also used for the functional tests reported in the following. As for the channel uniformity within board B in terms of noise, test results

are shown in Fig.3.13(b), along with the linear fits of the data: as can be seen, channels 3 and 4 have smaller ENC values than channels 1 and 2. Again, this difference is due to a slightly different layout that improved shielding for channels 3 and 4, which should be preferred when precise measurements have to be done. It should be stressed that, assuming an alpha-particle energy of $\sim 5.5\text{MeV}$, the expected signal-to-noise ratio would be much higher than 500 for both boards, that is good enough for most applications.

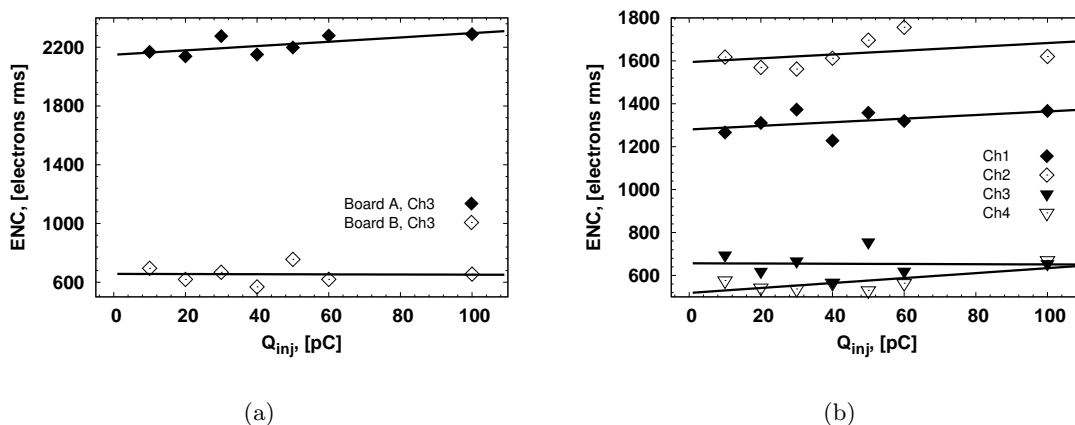


Figure 3.13: Noise characterization of ALPHADET boards: (a) - board A vs. board B in terms of noise properties, (b) - noise characterization of input channels of board B.

3.3 Summary

We have designed and implemented a new FPGA-based readout electronics specifically fit for BJT detectors. The system is completely compatible with previously designed microcontroller based readouts, which used ADC component from the same family as DDC114. This compatibility provides a convenient possibility to use ALPHADET readout for the laboratory tests (e.g., temperature dependence of detection properties of BJT detectors, efficiency of the detectors, etc.) and then to use microcontroller-based systems for the field tests.

Electrical characterization of ALPHADET board confirmed the expected performance with good linearity. The noise properties of all channels are rather good for α -particle detection; in case other prototypes have to be developed, the layout of board B would be preferable due to the better shielding of the channels, which provided optimized noise performance.

Functional tests using ^{241}Am alpha-particle source presented in Chapter 2 and Chapter 6 describing the results of functional characterization of the BJT detectors from BD1

and BD2 batches respectively confirmed that designed ALPHADET board can successfully be used for the readout of signal from the BJT detectors.

Chapter 4

Fabrication process flow and layout of BD2 batch

Based on the vast experience previously gained as during fabrication of BD1 batch of BJT detectors as during fabrication of other radiation detectors, a new and improved fabrication process flow has been developed in FBK, Trento. Section 4.1 shortly introduces overall fabrication process flow with conceptual renderings, explanations and listing of main steps. This section establishes a connection between layout and fabrication process.

Section 4.2 lists and describes all relevant layout cells of single test BJT pixels, BJT arrays and test structures. This section together with section 4.1 can be used as a guide through the layout of BD2 batch.

4.1 Fabrication process flow

Step 1 - a first part of collector contact formation and preparation of wafers for the following lithography steps (see fig.4.1(step 1))

- **Field oxide growing** - usually “wet” oxidation is used to grow this oxide. Field oxide has lower quality than oxide grown by “dry” oxidation method because of faster rate of silicon oxidation in atmosphere containing water vapor, which results in lower density oxide. On the other hand, quality of dielectric properties of field oxide are not so critical as the oxide is usually used for masking and, in this case, fast rate of oxidation is more relevant parameter;
- **Remove oxide on the back side** - this is done to provide a window for the following diffusion step;
- **Two-step diffusion**

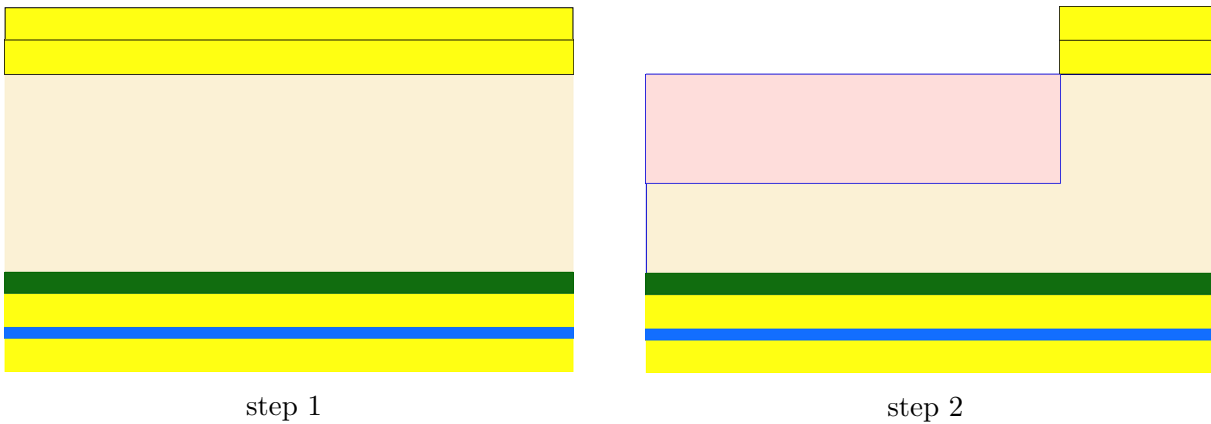


Figure 4.1: Step 1 and step 2 of fabrication process flow. Step 1 is a first part of substrate contact (collector) formation and preparation of wafers for the following lithography steps. Step 2 is a first part of p-well formation.

- Phosphorus doping of the back side of the wafer (ohmic contact) - the diffusion from solid source is done at quite high temperature ($\sim 1000^{\circ}C$), so the second, so-called, “drive-in” step, in principle, could be avoided. However, to form Gaussian diffusion profile “drive-in” step was performed as well;
- Phosphorus drive-in - in this case it is used to move diffusion front to a desired depth. Drive-in is done in a nitrogen (N_2) atmosphere;
- Oxide deposition from TEOS source ¹ - deposition of quite a thick oxide is done using low pressure chemical vapor deposition (LPCVD) method;
- **Silicon nitride deposition** - thin, comparing to the previously deposited TEOS layer, Si_3N_4 layer is deposited in order to provide a diffusion barrier for p-type dopants;
- **Dry etching of nitride** (on the front side of the wafers) - nitride deposition is made on the front- and back- sides of the wafers. As the diffusion barrier must be only on the backside of each wafer, the nitride layer should be etched away from the front side of the wafer.

¹TEOS is a chemical compound called tetraethylorthosilicate (TEOS). Chemical formula of this compound is $Si(OC_2H_5)_4$. Silicon oxide SiO_2 is deposited during decomposition of the TEOS vapor released from a liquid source. SiO_2 can be as well deposited in a LPCVD system at temperatures between $650^{\circ}C$ and $750^{\circ}C$ (in our particular case it was $720^{\circ}C$). Oxide deposited via decomposition of TEOS has good uniformity and step coverage. Reference [71] provides a table with a comparison of properties of oxides grown by different methods (the table is reprinted from M.Sze, VLSI Technology, 1983). Oxide deposited from TEOS source has only SiO_2 composition (instead, other oxides contained H and Cl elements in their composition), conformal step coverage, good dielectric strength of $10 \frac{MV}{cm}$, and slow etch rate of $30 \frac{\text{\AA}}{min}$.

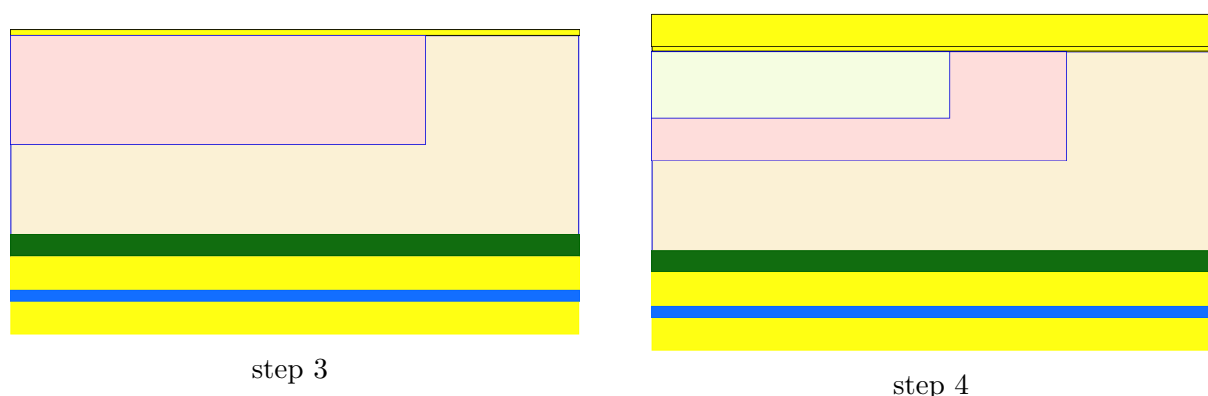


Figure 4.2: Fabrication process flow, step 3 and step 4. Step 3 is a second part of p-well formation, so-called, drive-in. Step 4 is a first part of n-channel formation (n-channel lithography and phosphorus implantation).

- **Oxide deposition from TEOS source** - second thick oxide layer was deposited for masking purposes, i.e., to provide a barrier to stop high-energy atoms of boron and phosphorus (p-well and n-channel ion implantations are done at rather high implantation energy of few hundreds of keV).

Step 2 - a first part of p-well formation (see fig.4.1(step 2))

- **P-well lithography** (P-WELL layer in the layout²) - lithography step includes few sub-steps: 1) coating wafer with a photoresist; 2) soft bake of photoresist; 3) photoexposure of pattern on a photoresist; 4) development of a photoresist; 5) hard baking; 6) oxide etching; 7) photoresist stripping;
- **Oxide etching** - open windows in the oxide for the following boron implantation;
- **Boron implantation** - boron with a high implantation energy of few hundred keV is implanted into the Si areas, which were designed in the layout as p-wells;
- **Wet photoresist stripping** - it is made in a bath of a mixture of sulfuric acid and hydrogen peroxide (H_2SO_4/H_2O_2), so-called, “piranha”. Wet stripping is usually used in case of unimplanted or lightly implanted photoresist.

Step 3 - a second part of p-well formation (see fig.4.2(step 3))

- **Wet oxide etching** - all oxide from the front side of the wafers is etched away;

²The layout of BD2 batch includes 8 layout layers. According to these layers eight lithography masks were fabricated. However, only 7 lithography steps were actually performed during the fabrication process. A lithography step corresponding to the backside local thinning of the wafers could not be performed due to the technical problems. This is why this lithography step that corresponds to the BACK-THIN layout layer is not described further.

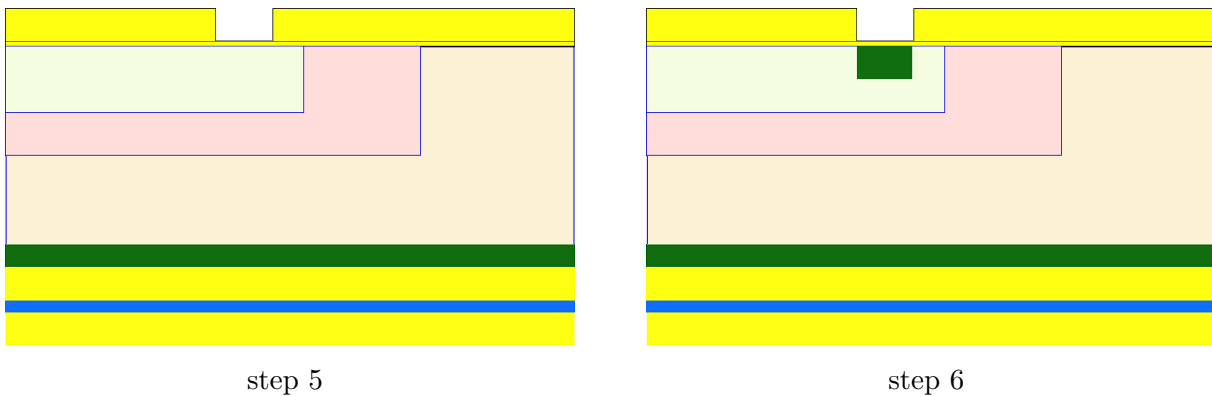


Figure 4.3: Fabrication process flow, step 5 and step 6. Step 5 is a completion of n-channel formation and a first step of shallow n^+ region formation. Step 6 is a completion of shallow n^+ region formation.

- **P-well “drive-in”** - a sufficient damage of silicon lattice develops during the implantation process. When the dose is high enough, the damaged silicon areas may become amorphous. In order to remove implantation damage and form proper doping profile, a short annealing in atmosphere of two gases $O_2 + N_2$ is done. This step is also called “drive-in” because dopants after this step diffuse deeper into silicon till they reach a desired depth and resistivity. During “drive-in” step a thin oxide is formed on the surface.

Step 4 - a first part of n-channel formation (see fig.4.2(step 4))

- **n-channel lithography** (N-CHANNEL layer in the layout) - this step includes photoresist deposition, photoresist development, and oxide etching over n-channel areas;
- **Phosphorus implantation** - double charged ions of phosphorus (P^{+2}) with final energy twice as much as initial energy due to the ionization are implanted into Si;
- **Dry and wet photoresist stripping**;
- **Oxide deposition from TEOS source** - fig. 4.2(step 4) schematically represents wafer after oxide deposition is already done.

Step 5 - a second part of n-channel (drive-in) and beginning of shallow n^+ region formation (see fig.4.3(step 5))

- **n^+ lithography** (NPLUS layer in the layout);
- **Oxide etching** - windows for the following n^+ implantation are opened;

- **n-channel drive-in** - formation of n-channel is finalized.

Step 6 - shallow n^+ region formation (drive-in) (see fig.4.3(step 6))

- **Arsenic implantation** - arsenic ions with 180keV energy are implanted into Si (it is shown in a green color on the upper part of fig. 4.3(step 6)).
- **Dry and wet photoresist stripping.**

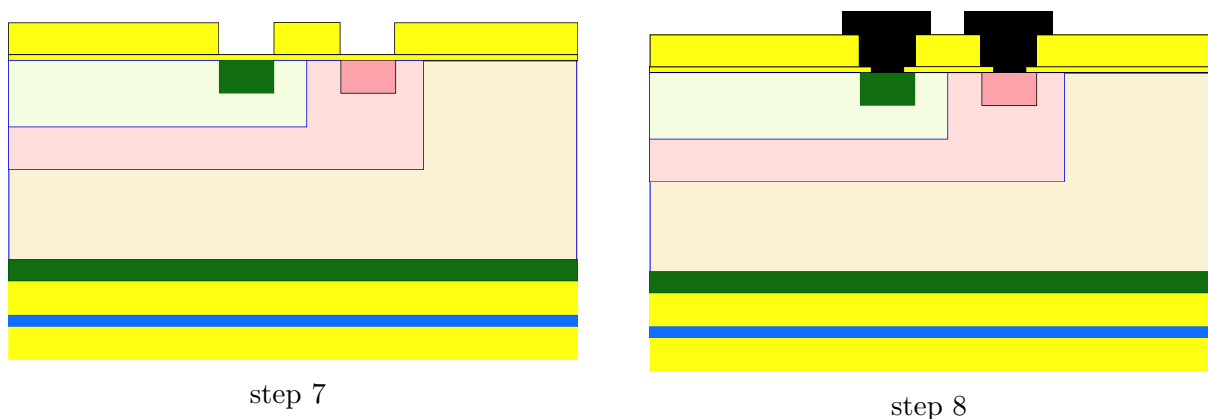


Figure 4.4: Fabrication process flow, step 7 and step 8. Step 7 is a shallow p^+ region formation and a completion of shallow n^+ region formation. Step 8 includes contact and metal lithographies.

Step 7 - shallow p^+ and n^+ (completion) regions formation (see fig.4.4(step 7))

- **p^+ lithography** (PPLUS layer in the layout);
- **Oxide etching** - windows for the following p^+ implantation are opened;
- **Boron implantation** - boron ions with energy much smaller than it was in case of p-well formation are implanted into Si.
- **Dry and wet photoresist stripping**
- **p^+ and n^+ drive-in.**

Step 8 - contact and metal lithography steps (see fig.4.4(step 8))

- **Contact opening lithography** (CONHO layer in the layout);
- **Oxide etching;**

- **Metal deposition** - it is done by sputter deposition of metal. Composition of deposited material is Aluminum with 1% of Silicon. Such composition improves adhesion of *Al* to *Si* and allows avoiding defects³. The thickness of deposited layer is 1.2 μm .
- Metal lithography (Metal layer in the layout);
- Oxide etching;
- Dry metal etching;
- Photoresist stripping.

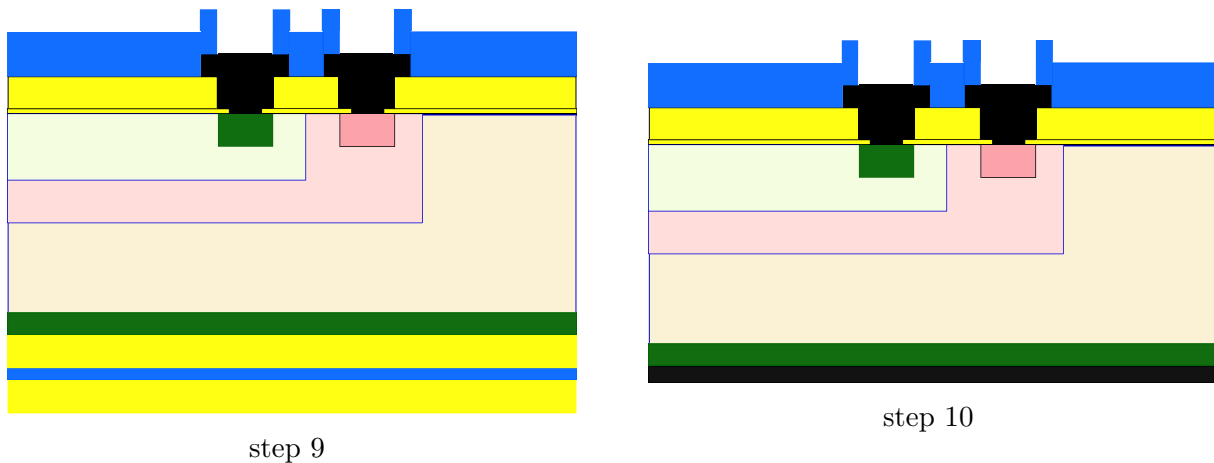


Figure 4.5: Fabrication process flow, step 9 and step 10. Step 9 is an overglass deposition. Step 10 is a deposition of metal on the backside of the wafer and completion of overall fabrication process.

Step 9 - overglass deposition (see fig.4.5(step 9))

- **Overglass deposition** - a thick layer of low temperature oxide (LTO) is deposited on the surface of the wafer for passivation purposes;

³One of the main defects is related to the solubility of *Si* in *Al*, which ranges from 0.25 to 1.5% at temperatures between 400°C and eutectic temperature⁴. Due to the solubility property *Si* migrates into deposited aluminum layer leaving “voids” that are then filled with an aluminum. Moreover, *Si* atoms do not migrate into aluminum uniformly but from a few points. Thus, aluminum spikes can form in *Si* causing a serious problem due to fact that metal lines contact heavily doped silicon areas, i.e., pn-junctions, so the spikes can shorten this junctions. To prevent spiking, some part of *Si* can be added to *Al* (a silicon concentration of 0.5% saturates aluminum at 425°C, and 1% *Si* saturates *Al* at 500°C). Adding *Si* into *Al* saturates *Al* with maximum soluble amount of *Si*; so, *Si* diffusion becomes unfavorable during subsequent annealing steps.

⁴This is a temperature at which an alloy of materials (eutectic composition) solidifies. The main property of eutectic composition is that this composition solidifies at temperature lower than any other composition of constituent elements.

- **Overglass lithography** (GLASS layer in the layout);
- **Dry oxide etching**;
- **Photoresist stripping**.

Step 10 - metal deposition on the backside of the wafer (completion of collector contact formation) see fig.4.5(step 10))

- **Dry etching of oxide and nitride that were deposited on the backside of the wafer**;
- **Sputter deposition of $Al + 1\%Si$** ;
- **Sintering** - this step is a sort of thermal annealing at $420^{\circ}C$ in N_2H_2 atmosphere. As sputtering is causing considerable damage of SiO_2 due to energetic ion bombardment, additional positive charge is trapped into oxide. In this case sintering can be used to passivate the interface states at Si/SiO_2 interface, remove positive charge from the oxide and prevent formation of spikes in Si (annealing improves quality of $Al + 1\%Si$ alloy, thus, it stops migration of Si into Al) [72].

4.2 Layout description of BD2 batch

Layout of the whole **wafer** cell is shown in fig. 4.6. The figure explains how the dies were numbered, the first digit of the die number is a row number, while the second digit is a column number. In the following section we are going to describe shortly a layout of all dies.

Die 12, 34, 47, the die is represented by **STD_DPIX_BD1** layout cell, which is a copy of array of DPIX pixels that was called in BD1 layout as **DPIX_out**, the layout of the cell was remade according to newly introduced p^+ and n^+ layers instead of p-select and n-select⁵. The cell is an array of pixels where all emitter and base contacts are routed separately. The base area of single pixel is $1.4 \times 1.4mm^2$, NChannel size is $32 \times 32\mu m$, n^+ - $20 \times 20\mu m$. This emitter layout configuration is further denoted as NCH32xNN20. The p-well area is minimized and emitter is shifted to the edge of the pixel.

⁵P-select and n-select layers were used in the layout of BD1 batch due to the additional “active area” layer that was used to define active regions (n and p). “Active area” layer is defined by oxide etching on the areas where p^+ and n^+ implantations should be done. Additionally introduced p-select and n-select layers had to account for the overetching effect; thus, p- and n-select layers were defined as p^+ , n^+ areas oversized by $3\mu m$. Fabrication process flow used to fabricate BD2 batch was designed without “active area” design layer. Therefore, p- and n-select layers were excluded from the layout.

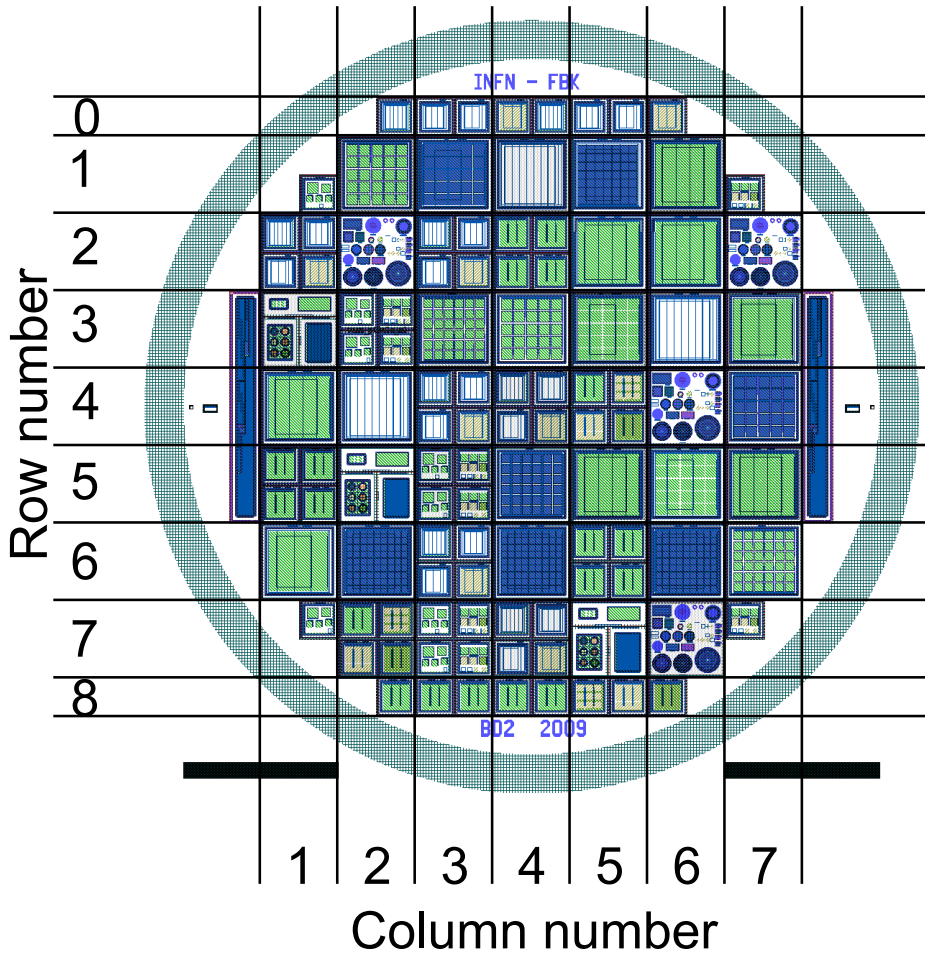


Figure 4.6: BD2 layout and numeration of the dies.

Dies 13, 35, 56, the dies are represented by `STD_DPIX_BD2_sh` layout cell. It is an array of $1.4 \times 1.4 \text{mm}^2$ NCH32xNN20 pixels, which are identical to DPIX pixels from the BD1 batch. The emitters of the pixels in the array are shorted together and routed to the periphery of the die. The metal grid has four metal pads placed at the corners of the die; it was done to ensure that all pixels in the array could be read out even in case metal lines would contain defects (one of the possible defects could be an overetching of metal during the last lithography step that could cause discontinuities in metal lines). Every pixel in the array is shielded by metal layer deposited over the base region.

Dies 14, 36, 42, the layout cell name is `STD_Pixels_400_NCH32xNN20`. Letters “**STD**” in the name of file mean “standard”, letters “**Pixels**” mean that this is a layout cell representing an array. Pixel with NCH32xNN20 emitter and minimized p-well is considered as a “standard” pixel. The base size of a single pixel in the array, which consists of 17×17 pixels, is $400 \times 400 \mu\text{m}^2$. The layout of a single pixel forming **STD-**

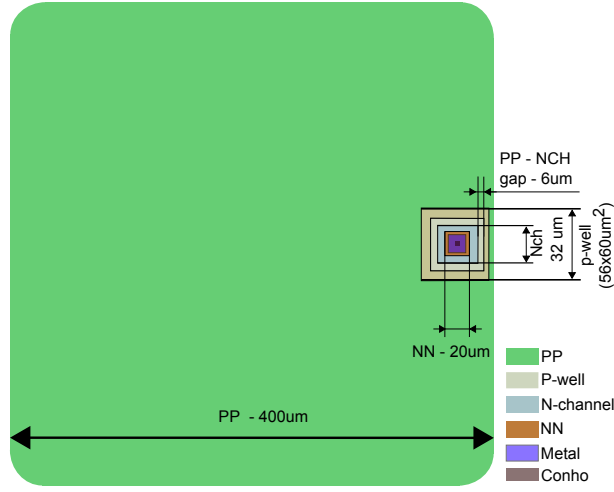


Figure 4.7: Layout of a single pixel forming **STD_Pixels_400_NCH32xNN20** array. Pixel has “standard” layout configuration, i.e., it has NCH32xNN20 emitter layout and minimum p-well size. The base size of the pixel is $400 \times 400 \mu\text{m}^2$.

Pixels_400_NCH32xNN20 array is shown in fig. 4.7. The pixel has the “standard” layout configuration, so other “standard” pixels have quite similar layout.

Dies 15 (shielded), **37**, **61**, the layout cell names are **STD_Pixels_1mm_NCH32xNN20_sh** (shielded) and **STD_Pixels_1mm_NCH32xNN20**. The basic pixel is a standard pixel with $1 \times 1 \text{ mm}^2$ base size. Each array contains 7×7 pixels. Every pixel in the “shielded” array is shielded by metal, letters “sh” in the name of cell mean that the array is shielded.

Dies 16, **41**, **62** (shielded), corresponding cell is **STD_Pixels_800_NCH32xNN20**, the basic pixel is a standard pixel with $800 \times 800 \mu\text{m}^2$ base size. Each array contains 9×9 pixels. The design of BD2 layout included a set of arrays that had single pixels forming those arrays with same emitter size (NCH32xNN20) but different base size. The purpose for that was to design arrays of BJT pixels that would have different bias points, i.e., different leakage currents and, consequently, different base voltages V_b and quiescent gain values.

Dies 21, **44**, corresponding cell is **Pixels_200_to_500_NCH32xNN16** cell. The overall size of this structure is $1 \times 1 \text{ cm}$, it includes 4 smaller $5 \times 5 \text{ mm}^2$ structures, which, in principle, can be diced apart. Every array has a basic pixel with emitter size NCH32xNN16. P-well implant has been extended almost as much as p^+ implant (p^+ oversizes p-well by $4 \mu\text{m}$). The base areas of single BJT pixels are:

- $200 \times 200 \mu\text{m}^2$ - layout cell **Pixels_200_NCH32xNN16_q**;
- $300 \times 300 \mu\text{m}^2$ - layout cell **Pixels_300_NCH32xNN16_q**;

- $400 \times 400 \mu\text{m}^2$ - layout cell **Pixels_400_NCH32xNN16_q**;
- $500 \times 500 \mu\text{m}^2$ - layout cell **Pixels_500_NCH32xNN16_q**.

None of the dies with $5 \times 5 \text{ mm}^2$ test arrays did not have metal shielding.

Dies 22, 27, 46, 76, the layout cell name is **test_standard**, each wafer contains 4 dies with test structures. They were named as TS22, TS27, TS46 and TS76 correspondingly to the numeration of the dies. Each test structure (see the layout of test dies in fig. 4.8) contains a set of large diodes, MOS structures, finger gated-diodes, Van der Pauw structures, cross Kelvin structures and n- and p-type MOSFETs. The largest guarded p^+ diode (labeled as **GRD-PP**), metal over substrate MOS structure (**C-MET-SUB**) and finger gated-diode in substrate (**GCD-SUB**) were tested on all test dies and all wafers. Other test structures were tested only in case some unusual effects were observed (one of such effects was explained in the section 5.2 of Chapter 5).

Dies 23, 43, **Pixels_200_to_500_NCH20xNN14** cell. The layout of this cell is similar to the layout of **Pixels_200_to_500_NCH32xNN16** cell. However, emitter layout is different, it is NCH20xNN14. Using these two layouts it is possible to derive dependence of BJT detector properties on emitter layout and base size. The base areas of single BJT pixels are:

- $200 \times 200 \mu\text{m}^2$ - layout cell **Pixels_200_NCH20xNN14_q**;
- $300 \times 300 \mu\text{m}^2$ - layout cell **Pixels_300_NCH20xNN14_q**;
- $400 \times 400 \mu\text{m}^2$ - layout cell **Pixels_400_NCH20xNN14_q**;
- $500 \times 500 \mu\text{m}^2$ - layout cell **Pixels_500_NCH20xNN14_q**.

Dies 24, 51, 65, layout cell is **STD_Pixels_quarters_m**. The large $1 \times 1 \text{ cm}^2$ die contains four smaller $5 \times 5 \text{ mm}^2$ arrays that have different emitter layouts but exactly the same base layout. Therefore, these four arrays can be used to evaluate how gain properties of BJT detector depend on the emitter layout. The subcells of main **STD_Pixels_quarters_m** cell are:

- **STD_Pixels_1mm_NCH32xNN20_q** (upper left array), it is a 3×3 array of pixels with $1 \times 1 \text{ mm}^2$ base area and NCH32xNN20 emitter layout;
- **STD_Pixels_1mm_NCH18xNN11_q** (upper right array), it is an array of pixels that have NCH18xNN11 emitter layout;
- **STD_Pixels_1mm_NCH32xNN11_q** (bottom right) it is an array of pixels that have NCH32xNN11 emitter layout;

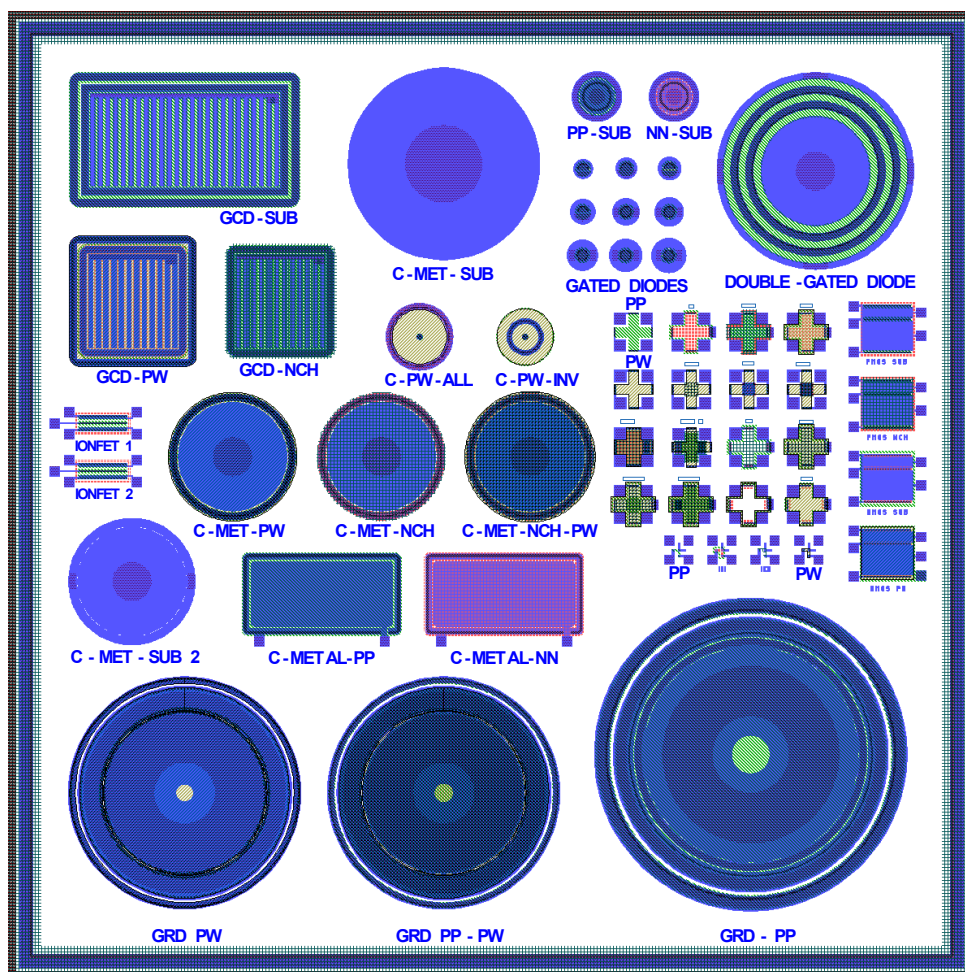


Figure 4.8: Layout of the test dies 22, 27, 46, 76 containing test structures.

- **STD_Pixels_1mm_NCH32xNN15_q** (bottom left) it is an array of pixels that have NCH32xNN15 emitter layout.

Dies 25, 55, 64, layout cell is **STD_Pixels_800_NCH18xNN11**. Single pixel has $800 \times 800 \mu\text{m}^2$ base size and NCH18xNN11 emitter.

Dies 26, 57, 66, layout cell is **STD_Pixels_800_NCH32xNN11**. Single pixel has $800 \times 800 \mu\text{m}^2$ base size and NCH32xNN11 emitter. This array together with the arrays represented by **STD_Pixels_800_NCH18xNN11** and **STD_Pixels_800_NCH32xNN20** layout cells make all possible configurations of emitter layouts that were represented not only by the arrays but also by test single BJT pixels ⁶.

Dies 45, 72, layout cell is **std_pixels_variations**. The large $1 \times 1 \text{ cm}^2$ die contains

⁶A test die with test single BJT pixels contains pixels corresponding to all arrays apart from the array **STD-Pixels_1mm_NCH32xNN15_q**.

four smaller $5 \times 5 \text{ mm}^2$ arrays that have different base layout but exactly the same emitter layout (NCH32xNN20). The subcells of main cell are:

- **STD_Pixels_1mm_NCH32xNN20_q** (upper left), it is a 3×3 array of “standard” pixels with $1 \times 1 \text{ mm}^2$ base area that was included into layout of the die for the reference purposes (see fig. 4.7 that shows layout of a similar pixel that differs from a single pixel forming **STD_Pixels_1mm_NCH32xNN20_q** array only by its base area, i.e., shown pixel has $400 \times 400 \mu\text{m}^2$ base area instead of $1 \times 1 \text{ mm}^2$);
- **STD_pixels_1mm_PP_FR** (upper right), it is an array where basic pixel has extended $1 \times 1 \text{ mm}^2$ p-well implant and a thin p^+ implant around edge of the base and emitter (the layout of a single pixel can be seen in fig. 4.9(a));
- **STD_pixels_1mm_PWell_Extend** (bottom right), single pixel has an extended $1 \times 1 \text{ mm}^2$ p-well implant and a p^+ implant spreading over all area of the pixel (the layout of a single pixel can be seen in fig. 4.9(c));
- **STD_pixels_1mm_PP_FR_small** (bottom left), single pixel has an extended $1 \times 1 \text{ mm}^2$ p-well implant and a thin p^+ implant just around an emitter (the layout of a single pixel can be seen in fig. 4.9(b)).

Dies 31, 75, layout cell is **mjd_bjt**. The cell is a replica of **mjd_bjt** from BD1 layout. Originally it was designed in the University of Trieste. The current design was changed according to the updated fabrication process. The main cell includes three subcells: a subcell with **bpix** pixels, a subcell with strip detector **bstrip** and a subcell with **mjd** pixels.

Dies 32, 53, 73, layout cell is **test_pixels_m1** (see the layout in fig. 4.10). The main cell is divided onto four $5 \times 5 \text{ mm}^2$ subcells, each subcell is filled with single test BJT pixels. Two upper subcells contain pixels that were designed according to the rules used for the design of BD1 batch layout and two bottom cells contain pixels designed according to the new layout rules, i.e., emitters were shifted to the edge of the pixels in order to minimize emitter-base capacitance and capacitance of metal lines. All layout cells corresponding to the test pixels included in the layout of large $1 \times 1 \text{ cm}^2$ die were summarized in Table 4.1, where numeration of the cells corresponds to the numeration of the pixels shown in fig. 4.10.

Dies 33, 54 (shielded), **67**, layout cell is **STD_Pixels_1_1mm_NCH32xNN20**. This is an array of pixels that is similar to **DPIX_out** array but differs by the size of a single pixel base. The base size is $1.1 \times 1.1 \text{ mm}^2$, amount of pixels is 6×6 . NChannel size is $32 \times 32 \text{ mm}^2$, Nplus - $20 \times 20 \text{ mm}^2$. The emitter pads are distributed on the top and on the bottom of a cell with fixed pitch, so automatic bonding can be applied.

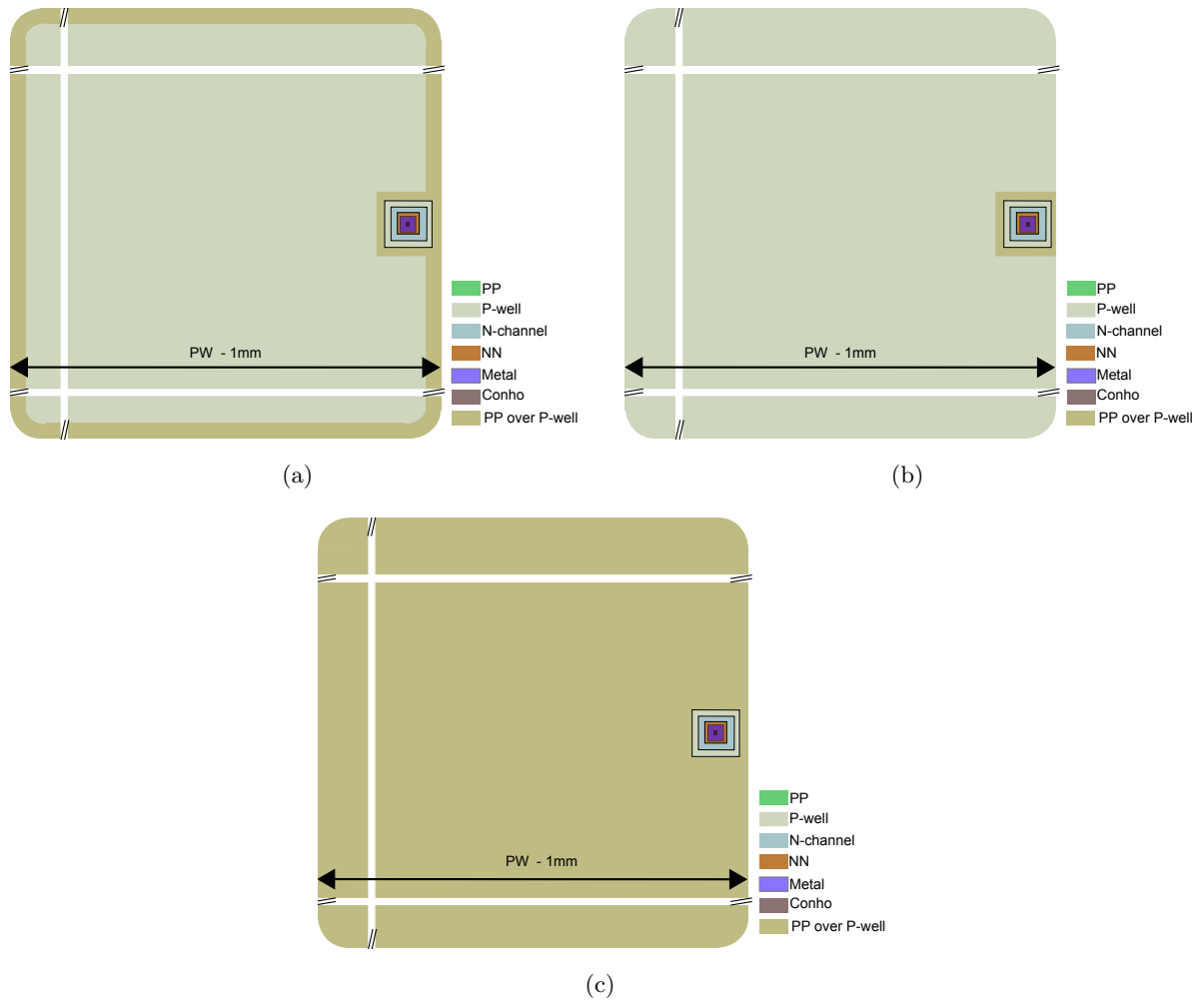


Figure 4.9: Layout of single pixels that form **STD_pixels_1mm_PP_FR** - (a), **STD_pixels_1mm_PP_FR_small** - (b) and **STD_pixels_1mm_PWell_Extend** - (c) arrays. Note that “PP over P-well” is not an actual layout layer, it was included into the legend just to ease understanding of the layout. All pixels have emitter layout same as it is shown in fig. 4.7, page 63.

4.3 Summary

In this chapter we have described a technology that was used to fabricate BJT detectors. This technology has shown to be effective, i.e., both batches of BJT detectors resulted in good quality α -particle detectors. Although, the devices from the second BD2 batch that were produced using new fabrication process flow observed better properties.

In addition, we have also presented in this chapter a description of relevant layout cells, i.e., single test pixels, arrays etc. with short explanations of their intended use.

Upper left subcell (test_pixels_1_4mm_quart)	Upper right subcell (test_pixels_quart)
1) Test_STD_Pix1_4_NCH32xNN20;	1) Test_STD_Pix1mm_NCH32xNN11;
2) Test_STD_Pix1_1mm_NCH32xNN20;	2) Test_STD_Pix1mm_NCH18xNN11;
3) Test_STD_Pix800_NCH18xNN11;	3) Test_STD_Pix1mm_NCH32xNN20;
4) Test_STD_Pix800_NCH32xNN11;	4) Test_STD_Pix1mm_PP_FR;
5) Test_STD_Pix800_NCH32xNN20;	5) Test_STD_Pix1mm_PP_FR_small;
6) Test_Pix300_NCH32xNN16;	6) Test_STD_Pix1mm_PWell_Extend;
7) Test_Pix300_NCH20xNN14;	7) Test_Pix400_NCH32xNN16;
8) Test_STD_Pix400_NCH32xNN20;	8) Test_Pix400_NCH20xNN14;
9) Test_Pix200_NCH32xNN16;	9) Test_Pix500_NCH32xNN16;
10) Test_Pix200_NCH20xNN14;	10) Test_Pix500_NCH20xNN14;
Bottom left subcell (test_pixels_1_4mm_quart_edg_m1)	Bottom right subcell (test_pixels_quart_edg_m1)
1) Test_STD_Pix1_4_NCH32xNN20_Edg;	1) Test_STD_Pix1mm_NCH32xNN11_Edg;
2) Test_STD_Pix1mm_NCH32xNN20_Edg;	2) Test_STD_Pix1mm_NCH18xNN11_Edg;
3) Test_STD_Pix800_NCH18xNN11_Edg;	3) Test_STD_Pix1mm_NCH32xNN20_Edg;
4) Test_STD_Pix800_NCH32xNN11_Edg;	4) Test_STD_Pix1mm_PP_FR_Edg;
5) Test_STD_Pix800_NCH32xNN20_Edg;	5) Test_STD_Pix1mm_PP_FR_small_Edg;
6) Test_Pix300_NCH32xNN16_Edg;	6) Test_STD_Pix1mm_PWell_Extend_Edg;
7) Test_Pix300_NCH20xNN14_Edg;	7) Test_Pix400_NCH32xNN16_Edg;
8) Test_Pix200_NCH32xNN16_Edg;	8) Test_Pix400_NCH20xNN14_Edg;
9) Test_Pix200_NCH20xNN14_Edg;	9) Test_Pix500_NCH32xNN16_Edg;
10) Test_STD_Pix400_NCH32xNN20_Edg;	10) Test_Pix500_NCH20xNN14_Edg.

Table 4.1: Single test BJT pixels. Numeration of the layout cells corresponds to the numeration of the pixels shown in fig. 4.10.

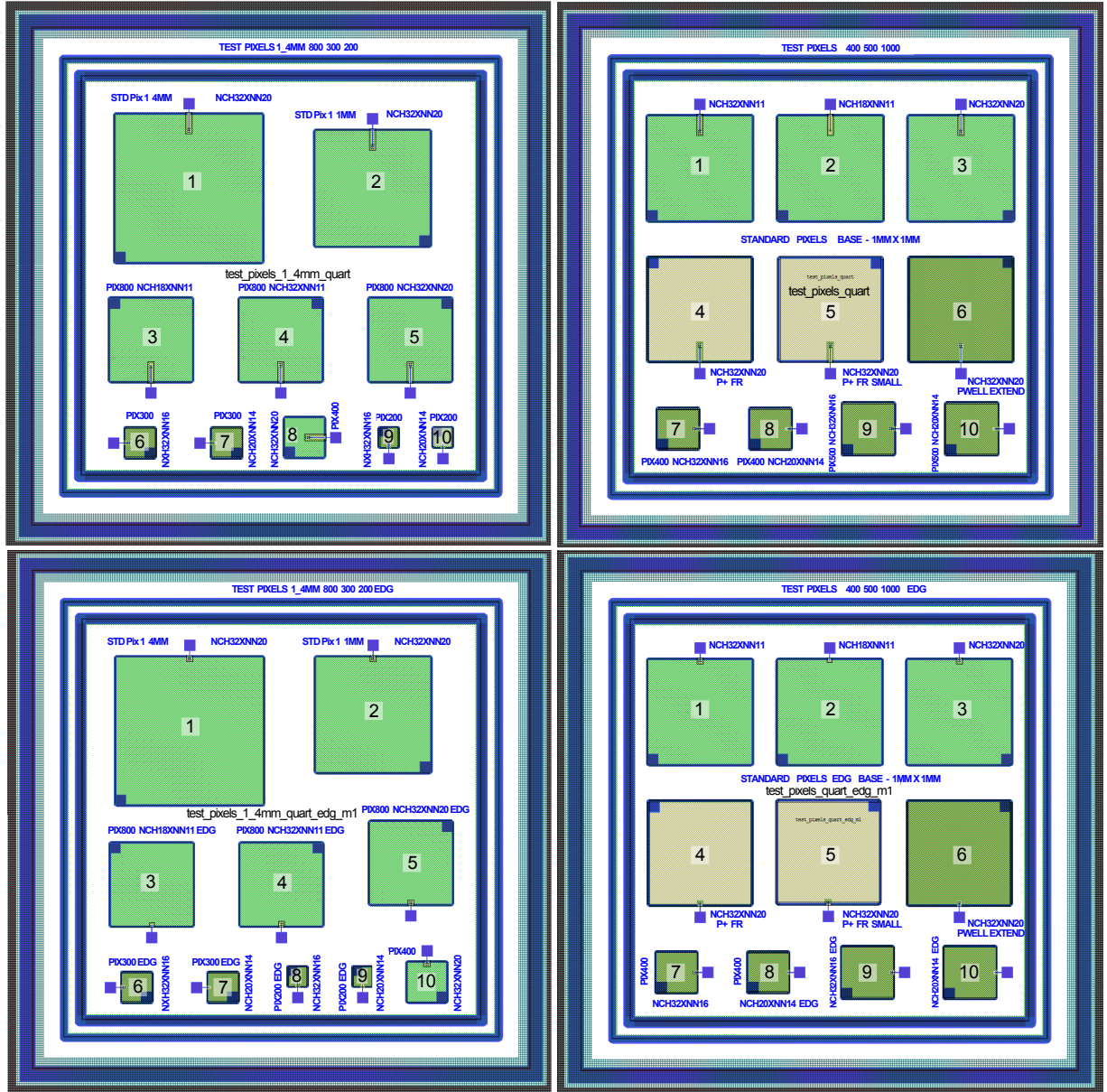


Figure 4.10: Layout of the test dies 32, 53, 73. Labels in a blue color were actually made during the fabrication process, while labels in black color were made just for illustration purposes to indicate cell names and numerate pixels.

Chapter 5

Electrical characterization of BD2 batch

After the fabrication of the second batch of BJT detectors (so-called BD2) was finalized a set of electrical tests was performed. These tests aimed at verifying fabrication process characteristics, i.e, extraction of process parameters that influence BJT performance the most and also at estimation of such properties of BJT as gain, leakage current and base potential at particular collector bias.

Section 5.1 describes characterization of the test structures and contains summary data about all extracted parameters that characterize silicon and, partially, device properties after the fabrication, i.e, full depletion voltage, doping concentration, generation lifetime, oxide thickness, charge oxide density, and surface recombination velocity. Then, section 5.2 presents results of characterization of test single BJT pixels. Here we analyze influence of emitter and base layout on properties of BJT detectors. This section introduces as well a “remaining oxide” effect that partially deteriorates Gummel plots of the test single BJT pixels but does not influence operation of the arrays of BJT pixels. The following section 5.3 discusses the results of electrical characterization of the arrays of pixels. It will be shown that detectors from “standard” and “poly” splittings can be safely used with designed readout electronics, while detectors from “thinned” splitting can not. And, finally, section 5.4 provides a short summary of this chapter.

5.1 Planar test structures

After the batch was released it had to be characterized in order to analyze silicon and BJT detectors’ properties, and, of course, quality of fabrication process. A photograph of one of the wafers from newly fabricated batch is shown in fig.5.1. Each wafer contains

4 types of the dies: large $1 \times 1 \text{ cm}^2$ arrays of BJT pixels, smaller $5 \times 5 \text{ mm}^2$ test arrays of BJT pixels, other dies with single BJT pixels for testing purposes, and the dies with planar test structures (fig.5.2). The planar test structures aimed at characterization of all relevant parameters and, in case of some disastrous problems during the fabrication process, at revealing the cause of the problem. The test dies are distributed on the wafer almost uniformly. TS46 and TS76 are particularly interesting due to their placement near the edge of wafer. As it will be shown, due to some peculiarities of the fabrication process the edge region has observed different treatment during fabrication and, consequently, this region has slightly different properties.

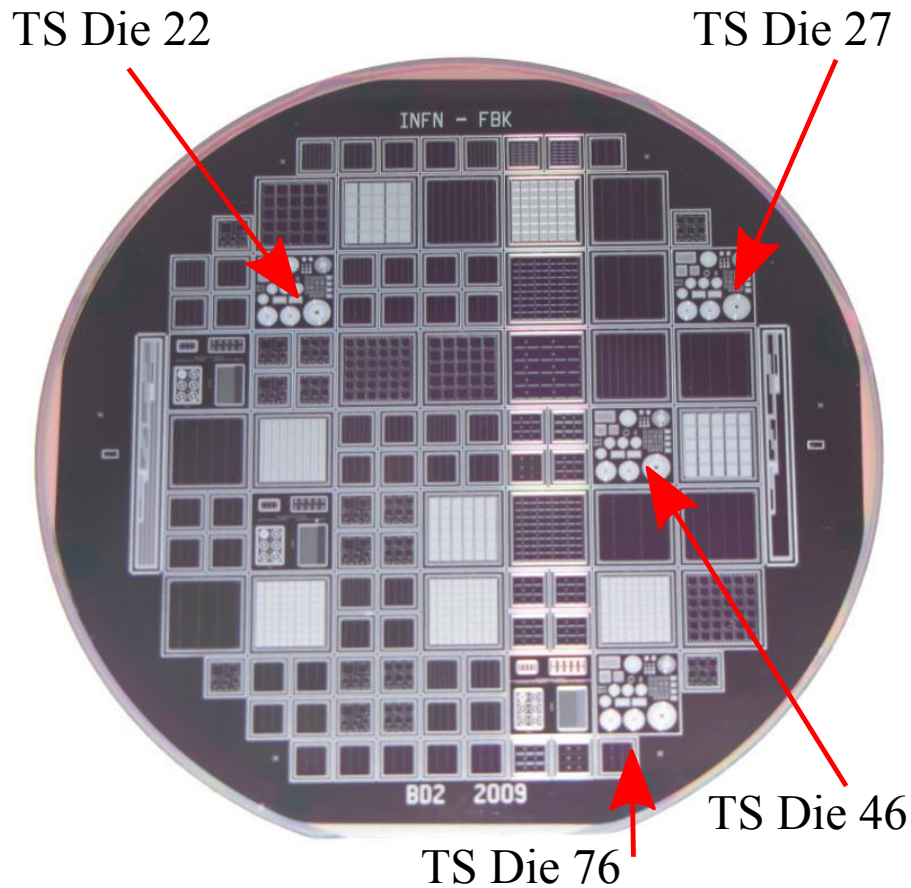


Figure 5.1: Snapshot of one of the wafers from BD2 batch of BJT detectors.

Usually, three test structures are tested, those are very large diode, MOS capacitor and finger gated-diode. In case some specific and detrimental features were observed then other test structures would be tested as well, for example, Van der Pauw or cross Kelvin structures.

IV characterization of very large diode allows extracting generation lifetimes of minor-

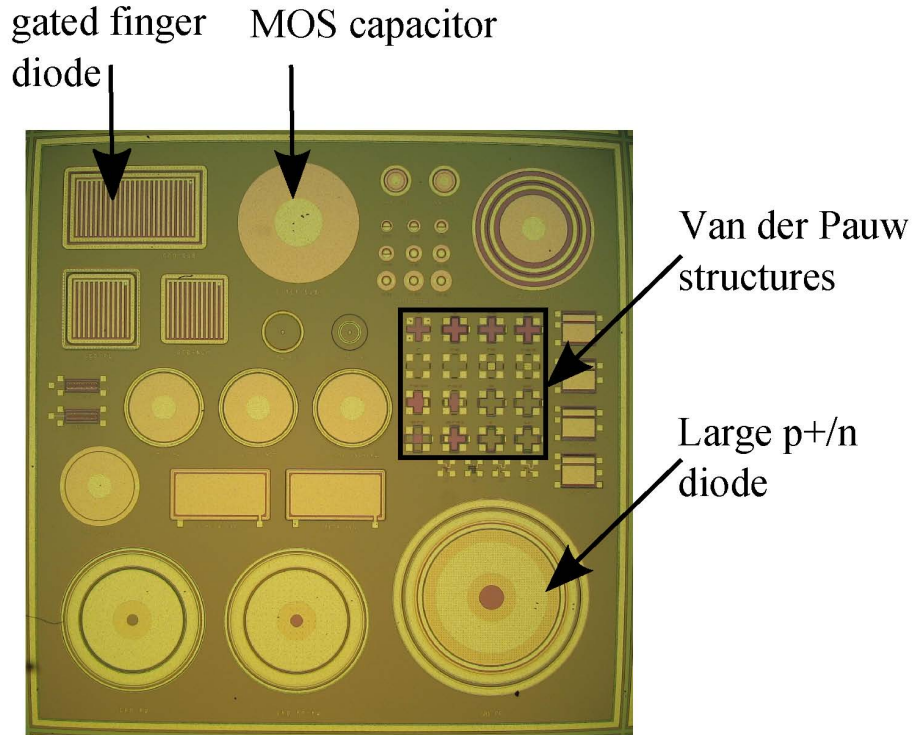


Figure 5.2: Snapshot of the die with test structures.

ity carriers (long lifetimes are preferable), while CV characterization of the same diode provides values of full depletion voltage V_{depl} and substrate doping concentration N_d (to calculate those values we assumed that the wafers from “standard” and “poly” splitting were $300\mu m$ thick, while wafers from “thinned” splitting were $200\mu m$ thick) ¹. CV characterization of large MOS capacitor was used to measure charge oxide density Q_{ox} , oxide thickness t_{ox} , and substrate doping N_d . Surface recombination velocity s_0 was measured using finger gated-diode. Sheet resistance was measured by Van der Pauw structures.

5.1.1 Generation lifetimes, full depletion voltages, and substrate doping profiles (very large diode)

Generation lifetimes can be measured using different techniques, some of them are well described in [73]. We have used an IV characterization of very large diode in order

¹The fabrication process flow included three types of splittings. Firstly, it was the splitting that had the same sequence of fabrication process steps as the previous batch BD1; therefore, we called it as a “standard” splitting. Then, the next splitting included some steps related to the gettering, this splitting was called a “poly” splitting. And, finally, there was a splitting that included backside substrate deep reactive ion etching (DRIE), which was called as a “thinned” splitting.

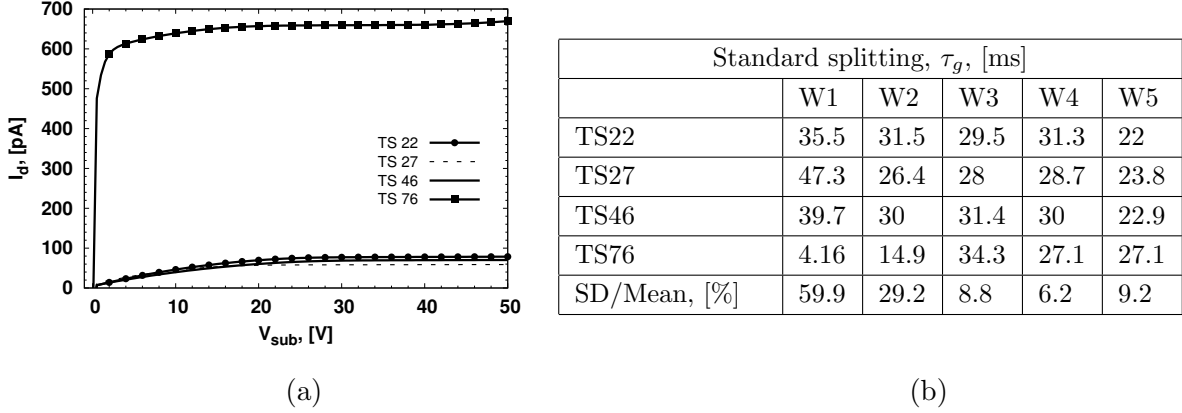


Figure 5.3: Generation lifetimes for “standard” splitting. (a) - typical plots that were acquired while testing one of the wafers from “standard” splitting; (b) - summarized data.

to extract generation lifetimes. Diode current density of a diode in reverse regime J_{rev} can be described as $J_{rev} = J_g + J_{diff} + J_{surf}$, where J_g represents generation current in the depleted region, J_{diff} - diffusion current from the quasi-neutral region and J_{surf} - generation current in the lateral depleted surface region (5.1):

$$\begin{aligned}
 J_g &= q \frac{n_i}{\tau_g} W_{depl} \\
 J_{diff} &= q \frac{n_i^2}{N_d} \sqrt{\frac{D_p}{\tau_p}} \\
 J_{surf} &= q n_i s_0
 \end{aligned} \tag{5.1}$$

where q is elementary charge, n_i - silicon intrinsic carrier density, τ_g - generation lifetime, W_{depl} - depletion width, N_d - substrate doping concentration, D_p - minority carrier diffusion constant, τ_p - minority carrier generation lifetime, s_0 - surface recombination velocity.

Taking into account that the diffusion current from quasi-neutral region is negligible under the full depletion and surface component of the current is also negligible due to the fact that it appears only at the edge of the diode that is surrounded by the guard ring we can assume that $J_{rev} = J_g$ and generation lifetime can be defined then as (5.2).

$$\tau_g = q \frac{n_i}{J_{rev}} W_{depl} \tag{5.2}$$

Fig.5.3 presents results of lifetime measurements on the wafers from “standard” splitting. Fig.5.3(a) shows that the lifetime profile is non-uniform, i.e., test structure TS76

showed much lower lifetime value, which means higher diode current. In order to compare different wafers and different splittings in terms of their lifetime uniformity a simple procedure was used. Mean value and standard deviation were calculated and then a ratio between them was taken. Small ratio means that the lifetime profile is uniform, while large ratio means non-uniform lifetime profile. For instance, wafer W4 has the most uniform profile in this splitting while W1 has the most non-uniform profile.

	Poly splitting, τ_g , [ms]				Thinned splitting, τ_g , [ms]		
	W6	W7	W8	W9	W10	W11	W12
TS22	88	109	83.3	93.1	29.40	32.10	3.35
TS27	90.2	105	83.1	95.4	0.75	0.64	0.04
TS46	91.4	113	81.1	92.7	3.89	1.96	0.13
TS76	91.5	97.3	79.6	87	0.33	0.42	0.03
SD/Mean, [%]	1.79	6.32	2.14	3.88	162.95	177.23	185.11

Table 5.1: Generation lifetimes for “poly” and “thinned” splittings.

Table 5.1 summarizes results of the lifetime measurements, which were carried out on the wafers from the “poly” and “thinned” splittings. Analysis of these data leads to an obvious conclusion that the lifetime profiles are very uniform for the wafers W6-W9, while wafers W10-W12 have non-uniform profiles. Taking into account that all wafers were observing similar properties before fabrication, it is most probable that the observed non-uniformity is related to the possible defects or contamination introduced into the silicon substrate during the deep reactive-ion etching.

It is possible to extract additional parameters, e.g., V_{depl} and N_d , by making CV characterization of the test diodes. The depletion width w_{depl} of reverse biased diode can be expressed as (5.3), where V_{rev} is applied reverse bias and N_d is substrate doping concentration.

$$w_{depl} = \sqrt{\frac{2\epsilon_0\epsilon_{Si}(V_{rev} + V_{bi})}{qN_d}} \quad (5.3)$$

On the other hand, diode capacitance C_d can be expressed as (5.4) and it should reach its minimum value when the depletion width is highest possible, i.e, equal to the thickness of the wafer. Combining (5.3) and (5.4) a dependence (5.5) can be derived, which shows that the depletion voltage value can be calculated as a point where $1/C^2$ curve reaches its “saturation” and substrate doping can be calculated from a slope of $1/C^2$ curve before it reaches “saturation”.

$$C_d = A_d \frac{\epsilon_0 \epsilon_{Si}}{w_{depl}} \quad (5.4)$$

$$\frac{1}{C_d^2} = \frac{2(V_{rev} + V_{bi})}{A_d^2 q \epsilon_0 \epsilon_{Si} N_d} \quad (5.5)$$

Fig.5.4 contains two sub figures which characterize “standard” splitting, the plot shows the results of characterization where two of the test structures of W1 (TS27 and TS76) have smaller depletion voltages and this effect is easily observed when the data is represented graphically.

The values of full depletion voltages are strictly related to the wafer thickness and to the values of substrate doping concentration N_d (see the table 5.5 with the results of N_d measurements). Tables 5.4(b) and 5.2 confirm it, “poly” splitting has smaller than “standard” splitting values of full depletion voltages, the mean value $\overline{V_{depl}}$ for “poly” splitting is 9.4V and standard deviation is $\sigma \approx 1.4V$, while “standard” splitting has $\overline{V_{depl}}=29.6V$ and $\sigma \approx 4.3V$. The “thinned” splitting has wider range of V_{depl} values; however, excluding W12 from the calculations due to the test structures that were in the area that was possibly damaged or contaminated during the DRIE step, the mean value $\overline{V_{depl}}=6.0V$ and $\sigma \approx 0.74V$.

Thus, from the point of view of V_{depl} values devices from both “poly” and partially “thinned” splittings are suitable for the applications where low voltage power supply, i.e., battery should be used. However, considering lifetimes profiles the devices from “standard” and “poly” splittings would consume much less power due to the lower generation lifetimes, and so, should be preferable for being used in the final radon monitoring/detection system.

	Poly splitting, V_{depl} , [V]				Thinned splitting, V_{depl} , [V]		
	W6	W7	W8	W9	W10	W11	W12
TS22	10.5	10.6	8.4	8.3	5.3	5.5	5.7
TS27	12.3	9.0	8.1	8.6	6.3	6.1	37.0
TS46	8.8	10.1	8.4	8.3	5.6	5.8	12.8
TS76	12.6	9.1	9.3	8.7	7.8	6.0	59.0

Table 5.2: Full depletion voltage values for “poly” and “thinned” splittings.

5.1.2 Surface recombination velocity

Surface recombination velocity was measured using finger gated-diode test structure, fig.5.6 shows a schematic sketch of its cross-section. The method was originally developed

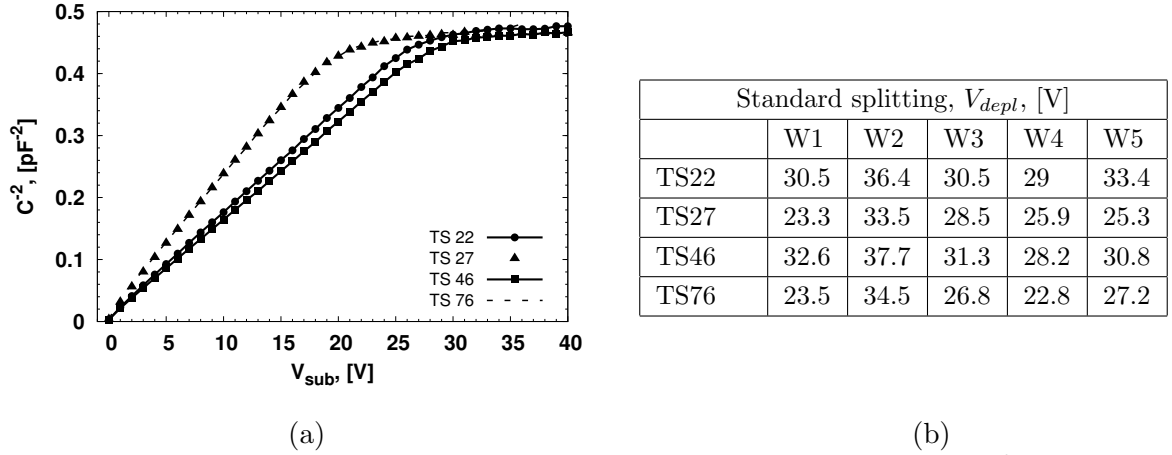


Figure 5.4: Full depletion voltage values for the “standard” splitting. (a) - $1/C^2$ plots obtained by testing W1 from the “standard” splitting; (b) - summarized data.

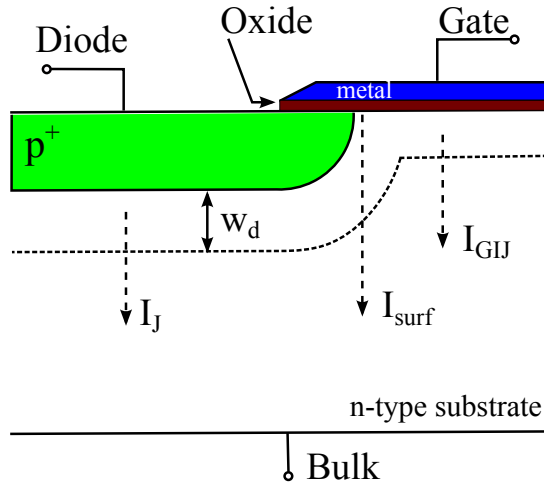


Figure 5.5: Finger-gated-diode.

by Grove and Fitzgerald [74]. Normally the diode is reverse biased to create a depletion region around it. The gate voltage V_g is swept from 0V to a sufficiently large negative bias values, so the undergate region goes through accumulation, depletion and inverse regimes. In accumulation regime the majority carriers (electrons in this case) are attracted to the oxide/Si interface. Accumulated layer of electrons efficiently suppresses the surface current; so, only current from the gate-induced space charge region (I_{GIJ}) and diode current I_J can be observed. When the gate voltage V_g decreases more the depletion region is entered and surface current component I_{surf} starts playing a significant role due to the fact that the surface recombination processes are not anymore suppressed. In inversion regime the surface recombination is again suppressed because of hole prevalence, so only I_J is observed. Using this procedure it was possible to extract surface current component

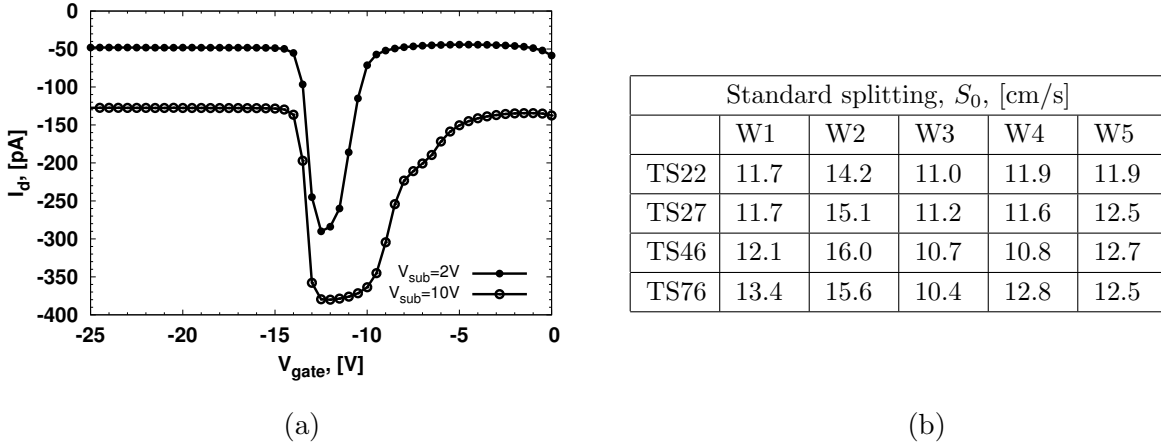


Figure 5.6: Surface recombination velocities measured on the wafers from the “standard” splitting. (a) - typical plots that were acquired while testing test structure TS22, wafer W4; (b) - summarized data.

I_{surf} and then calculate surface recombination velocity s_0 . The relationship between s_0 and I_{surf} is described by formula (5.6), where q - is elementary charge, n_i - intrinsic concentration of carriers, A_{SD} - is the area of the surface region of the diode that is depleted (SD states for surface diode), or it is just area of the gate electrode A_G .

$$I_{surf} = qn_i A_{SD} s_0 \quad (5.6)$$

	Poly splitting, s_0 , [cm/s]				Thinned splitting, s_0 , [cm/s]		
	W6	W7	W8	W9	W10	W11	W12
TS22	10.7	8.66	8.32	8.0	12.1	12.2	damaged
TS27	10.1	8.63	9.65	8.26	10.9	12.3	damaged
TS46	12.1	8.04	10.5	9.39	damaged	12.7	damaged
TS76	damaged	8.02	9.75	8.98	9.39	13.2	damaged

Table 5.3: Surface recombination velocities measured on the wafers from the “poly” and “thinned” splittings.

After the IV curves of finger gated-diodes were acquired the surface current component I_{surf} has been obtained by subtracting the minimum value of the curve from the maximum value of this curve in the accumulation regime. Characterization of all wafers from BD2 batch has shown that surface recombination velocity values are rather uniform and do not depend much on the type of splitting. The mean value of surface recombination velocity s_0 is 11.24cm/s, which is almost 4 times smaller than it was in the BD1 batch of BJT detectors ($s_0 \approx 44cm/s$). Tables 5.6(b) 5.3 present summary results of these tests.

It is interesting to note that one of the wafers in the “thinned” splitting could not be characterized in terms of surface recombination velocity due to unknown facts. Instead of going through accumulation, depletion and inversion regimes of operation the finger gated-diodes always remained in accumulation regime until their breakdown.

5.1.3 Oxide thickness, substrate doping profiles and charge oxide density (large MOS capacitor)

CV characterization of a large MOS capacitor allows extracting many useful parameters that describe fabrication process, for example, oxide thickness t_{ox} and charge oxide density Q_{ox} , and silicon properties, i.e., substrate doping N_d . All CV curves were acquired with Agilent 4278A 1kHz/1MHz capacitance meter at 10kHz frequency and 50mV amplitude of AC signal amplitude; fig.5.7(a) shows a typical CV curve that was obtained while testing one of the test MOS capacitors (TS22, W2).

The overall MOS capacitance can be expressed as (5.7), where C_{ox} is capacitance of the oxide and C_s is semiconductor capacitance. The semiconductor capacitance can be described as $C_s = A_M \cdot \epsilon_0 \epsilon_{Si} / w_{Si}$, where A_M is the area of metal electrode, w_{Si} is the width of semiconductor space charge region.

$$C_M = \frac{C_{ox} C_s}{C_{ox} + C_s} \quad (5.7)$$

When the bias applied to the MOS is 0V the semiconductor capacitance C_s is zero, and so, $C_M = C_{ox} = C_{max}$. Taking into account that the oxide capacitance C_{ox} is $C_{ox} = A_M \cdot \epsilon_0 \epsilon_{ox} / t_{ox}$, the oxide thickness t_{ox} can be calculated. For the given example (fig.5.7(a)) the oxide thickness is $t_{ox} = 518nm$, which corresponds to $C_{ox} = 209pF$.

Given that CV curves were acquired at high frequency for such analysis, the minimum capacitance value corresponds to inversion capacitance C_{inv} that is defined by width of space charge region under a strong inversion regime (5.8). Using eq. (5.8) substrate doping concentration N_d can be easily calculated, for example, the N_d measured by test structure TS22, W2 (fig.5.7(a)) was $4 \times 10^{11} cm^{-3}$.

$$w_{inv} = \sqrt{\frac{2\epsilon_s \epsilon_0 \phi_{s,inv}}{qN_d}} \approx \sqrt{\frac{4\epsilon_s \epsilon_0 kT \ln(N_d/n_i)}{q^2 N_d}} \quad (5.8)$$

The above described technique is called *maximum-minimum capacitance* technique; slightly extended explanation of this technique can be found here [73].

We have acquired CV curves for all test structures in the BD2 batch and then extracted t_{ox} and N_d . Summarized results of oxide thickness measurements are presented in Table

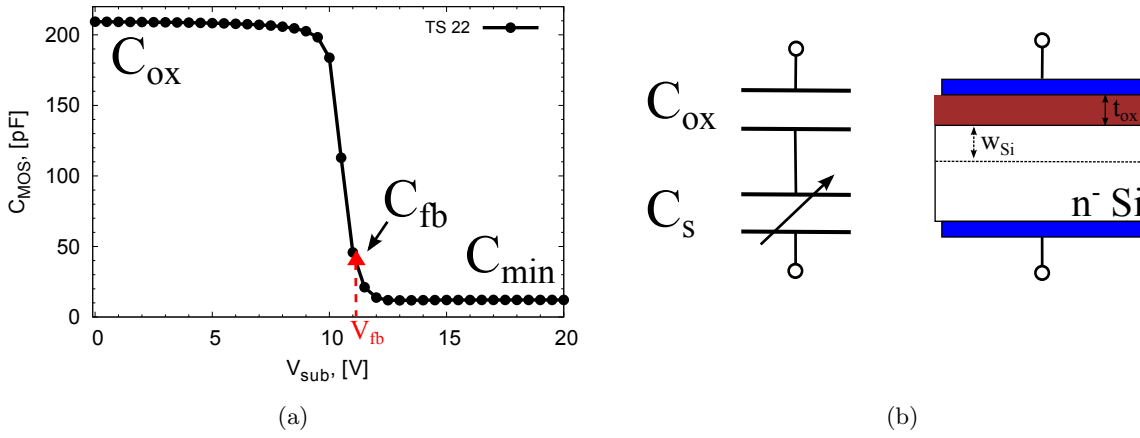


Figure 5.7: CV characterization of MOS capacitor (a) - CV curve (b) - a schematic representation of a MOS capacitor.

5.4, where $\overline{t_{ox}}$ is a mean value that was calculated on the basis of t_{ox} values measured over all wafers from a single splitting, SD is a standard deviation, Δ is a difference between maximum and minimum values of oxide thickness. As we can see, the wafers from the “poly” splitting have the most uniform oxide, which is confirmed by the smallest standard deviation value, though with rather large value of Δ . It will be shown in section 5.2 that observed variations in oxide thickness could be one of the possible reasons for so-called “remaining oxide” type of effect that partially deteriorated some of the base contacts of single BJT pixels.

Splitting	$\overline{t_{ox}}$, [nm]	SD, [nm]	min, [nm]	max, [nm]	Δ , [nm]
Standard	517.1	8.38	500	528	28
Poly	516.6	5.76	505	525	20
Thinned	512.2	6.39	502	521	19

Table 5.4: Oxide thickness profiles for all wafers in BD2 batch. A variable Δ has been calculated as a difference between maximum and minimum value of oxide thickness.

The values of substrate doping concentration N_d were extracted in a way that has been already explained. After that for every wafer, apart from W12 that showed high non-uniformity of the doping profile, a mean value of N_d was calculated. Table 5.5 contains the results of N_d measurements obtained by two different methods, i.e., by making analysis of CV curves acquired using either test MOS structure or large test diode. The observed difference between $\overline{N}_{d,MOS}$ and $\overline{N}_{d,diode}$ values is not large and is mainly defined by the precision of calculations, especially this effect is pronounced when the doping concentration is very low like it is in case of the wafers from “poly” and “thinned” splittings.

It is obvious that the wafers W1-W5 have ~ 2.5 times higher doping concentration than remaining W6-W12 wafers. This difference could not be explained by the peculiarities of fabrication process; however, it might be explained by variations of longitudinal resistivity of original ingot from which were taken the wafers for the BD2 batch. The observed variations of N_d values of W12 can be explained by a contamination of this wafer during the fabrication.

Splitting	Wafer	$\bar{N}_{d,MOS}, [cm^{-3}]$	$\bar{N}_{d,diode}, [cm^{-3}]$	
Standard	W2	$4.40 \cdot 10^{11}$	$5.16 \cdot 10^{11}$	
	W3	$4.28 \cdot 10^{11}$	$4.25 \cdot 10^{11}$	
	W4	$3.46 \cdot 10^{11}$	$3.84 \cdot 10^{11}$	
	W5	$4.05 \cdot 10^{11}$	$4.23 \cdot 10^{11}$	
Poly	W6	$1.45 \cdot 10^{11}$	$1.60 \cdot 10^{11}$	
	W7	$1.72 \cdot 10^{11}$	$1.41 \cdot 10^{11}$	
	W8	$1.51 \cdot 10^{11}$	$1.24 \cdot 10^{11}$	
	W9	$1.68 \cdot 10^{11}$	$1.23 \cdot 10^{11}$	
Thinned	W10	$1.39 \cdot 10^{11}$	$2.05 \cdot 10^{11}$	
	W11	$1.45 \cdot 10^{11}$	$1.91 \cdot 10^{11}$	
	W12	TS22	$1.61 \cdot 10^{11}$	$1.87 \cdot 10^{11}$
		TS27	$1.48 \cdot 10^{12}$	$1.21 \cdot 10^{11}$
		TS46	$3.37 \cdot 10^{11}$	$3.62 \cdot 10^{11}$
		TS76	$3.59 \cdot 10^{12}$	$1.68 \cdot 10^{12}$

Table 5.5: Substrate doping profiles obtained by CV characterization of MOS structures and diodes. $\bar{N}_{d,MOS}$ and $\bar{N}_{d,diode}$ are mean values of doping concentration over a single wafer, for wafer W12 N_d values for every test structure were presented due to the large deviations in the values.

Charge oxide density Q_{ox} has been calculated by comparing the flat band voltage V_{FB} shift of the experimental CV curve with a theoretical CV [73]. The fig.5.7(a) shows one of the CV curves with calculated value of the V_{FB} shift, which was $V_{FB} = 11.15V$. The relationship between Q_{ox} and V_{FB} is

$$Q_{ox} = \frac{C_{ox}}{qA}(\phi_{ms} - V_{FB}) \quad (5.9)$$

where, A is the area of the MOS test structure and ϕ_{ms} is a metal-semiconductor work-function difference, which can be calculated as

$$\phi_{ms} = \phi_{ms,0} + \frac{kT}{q} \ln\left(\frac{N_d}{n_i}\right) \quad (5.10)$$

The workfunction difference $\phi_{ms,0}$ is constant for the given fabrication process and temperature conditions.

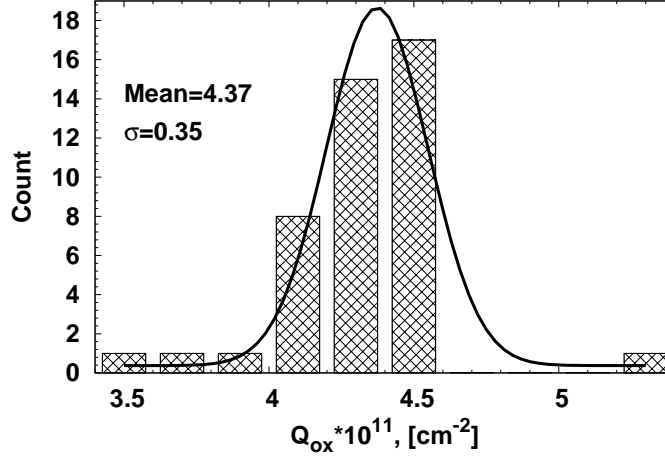


Figure 5.8: Summarized results of charge oxide density Q_{ox} measurements over all wafers of BD2.

Fig.5.8 presents summarized results of charge oxide density measurements. The values of Q_{ox} were rather uniform over a single wafer and over the whole BD2 batch as well. The mean value of Q_{ox} is $4.37 \cdot 10^{11} cm^{-2}$, while for the BD1 batch the mean value of Q_{ox} was $\sim 5.3 \cdot 10^{11} cm^{-2}$. Combination of such decrease of charge oxide density Q_{ox} together with a decrease of surface recombination velocity s_0 resulted in the higher gain properties of newly fabricated BJT detectors (refer to the next section 5.2, in particular, to fig.5.9(c)).

5.2 Test pixels

After the electrical characterization of the test structures confirmed good properties of silicon and Si/SiO_2 interface, a set of electrical tests was performed to obtain relevant information about performance of BJT detector. Usually, the most relevant information can be extracted from Gummel plots, base potential and collector current behavior versus collector bias. Gummel plots are collector and base currents plotted in log scale that are acquired by sweeping base-emitter junction into a forward regime at constant positive collector bias, i.e., biasing BJT into a forward-active regime of operation (in all performed tests the base contact was swept from 0V to 1V with emitter contact kept at ground potential and the collector bias was fixed at 10V). Using Gummel plots a differential gain of the detector can be calculated as $\beta = \frac{\partial I_c}{\partial I_b}$. Fig.5.9(a) and fig.5.9(c) show typical Gummel plots and corresponding gain curves respectively.

It should be stressed here that the design of the BD2 batch was made according to a “floating base” concept, where all arrays of BJT pixels were designed with a floating base contact, i.e., without base contact. It means that the base potential is not controlled and is dependent only on a leakage current of the pixel flowing through the base, hence, the quiescent base potential and gain values are not controlled as well. So, even BJT pixels with same emitter and base layout configurations but different base size would observe different quiescent gain values due to different quiescent V_b values. This is why, another IV test was routinely performed in order to obtain dependence of base potential V_b on collector bias V_{sub} (see fig.5.9(d), the symbols are to show base potential at 10V bias, two pixels NCH32xNN20 and NCH32xNN11 have almost the same $V_b \approx 0.355V$ value, which correspond to the quiescent gain value $\beta_{quies} \approx 200$ (fig.5.9(c)), pixel NCH18xNN11 has larger $V_b \approx 0.37V$ value, which, however, corresponds to the lower $\beta_{quies} \approx 130$). Fig.5.9 contains the plot of collector current I_c versus collector bias I_{sub} (fig.5.9(b)), these data are needed for the calculations and also to evaluate dynamic base resistance and power consumption of the detector.

In order to perform an analysis of how emitter and base layout influence amplification properties of the detectors, we have included various single test BJT pixels into layout of the BD2 batch. These pixels were used for electrical characterization, while arrays corresponding to these pixels were used for functional tests. Analysis of emitter layout influence on gain of the detector can be done using fig. 5.9. So, from the point of view of maximum quiescent and overall gain values ² pixel with NCH32xNN11 emitter layout would be the best. However, pixel with NCH32xNN20 emitter layout still has good quiescent gain value but lower overall gain value.

Then we analyzed how base layout influences performance of BJT detector. Layout of the die with test BJT pixels included pixels that had the same emitter layout and same base size ($1 \times 1cm^2$) but different configuration of the base layout. Fig.5.10 presents the results of electrical characterization of these pixels. The data for the pixel “NCH32xNN20” was included for the reference as this pixel had a standard emitter and base layout. Pixel “P+ FR” had an extended $1 \times 1mm^2$ p-well implant with a thin p^+ implant around emitter and the edge of the p-well, pixel “P+ FR Small” had an extended $1 \times 1mm^2$ p-well implant with a thin p^+ implant just around the emitter, pixel “PWell EXT” had an extended $1 \times 1mm^2$ p-well implant with a p^+ implant spreading over all area of the pixel. As it can be seen, there is a little difference between pixels “NCH32xNN20” and “PWell EXT”, which means that the size of p-well does not influence much the electrical properties of the pixel, i.e., the values of gain, base potential V_b and collector current

²Overall gain can be calculated after functional tests as a ratio between collected charge value and generated charge value, $\beta = \frac{Q_{coll}}{Q_{gen}}$.

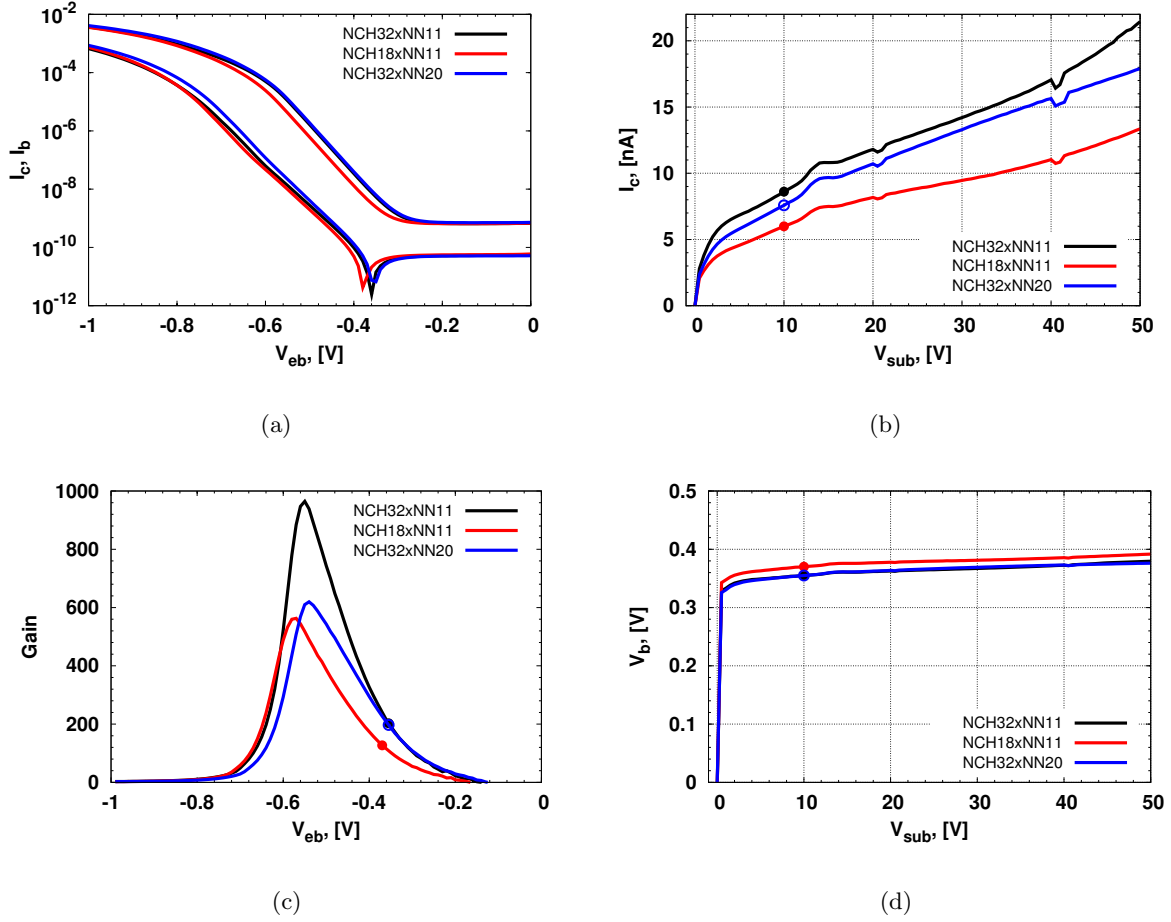


Figure 5.9: Electrical IV characterization of single test BJT pixels (a) - Gummel plots for three single test BJT pixels with different emitter layout; (b) - collector current I_c vs. collector bias V_{sub} ; (c) - gain curves corresponding to Gummel plots (a); (d) - base potential V_b vs. collector bias V_{sub} . The points, which have the same color as corresponding curve, show a quiescent states of the pixels.

I_c are very similar. Pixels “P+ FR” and “P+ FR Small” observe higher gain, V_b and I_c values because of the increase of base current that appeared due to the fact that the surface current component in the base of BJT pixel was not suppressed by a p^+ implant.

Pixels with exactly the same emitter and base layout but different base size were compared as well. Fig. 5.12 presents the results of electrical characterization of such pixels. Pixels with $800 \times 800 \mu m^2$, $1 \times 1 mm^2$, $1.1 \times 1.1 mm^2$ and $1.4 \times 1.4 mm^2$ base areas were tested. As it can be seen, usually, the larger pixel the higher is leakage current, base potential and, hence, quiescent gain values (as it in the case of Pix800 NCH32xNN20, STD 1.1mm and STD1.4mm pixels). However, pixel NCH32xNN20 has smaller leakage

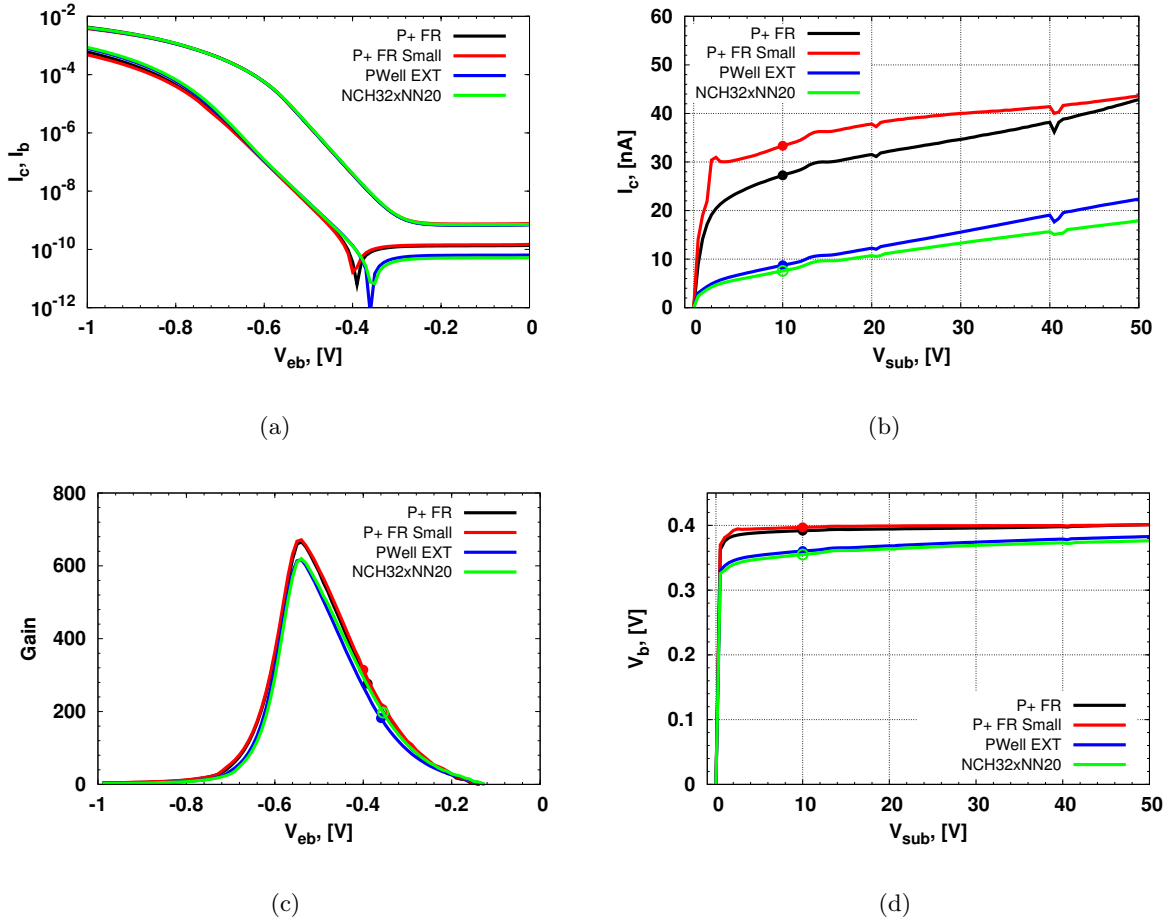


Figure 5.10: Electrical IV characterization of single test BJT pixels with same emitter layout and base size of $1 \times 1 \text{ mm}^2$ but different base layout configuration. (a) - Gummel plots for four single test BJT pixels with different base layout; (c) - gain curves corresponding to Gummel plots; (b) - collector current I_c vs. collector bias V_{sub} ; (d) - base potential V_b vs. collector bias V_{sub} . The points, which have the same color as corresponding curve, show a quiescent states of the pixels.

current than Pix800 NCH32xNN20 pixel, which has a smaller base area. Considering that the tested pixels belong to different subcells of the test **die 32** and that lifetime profile for the wafer W11 is rather non-uniform due to the performed DRIE the observed discrepancy can be explained by the differences in lifetimes.

Finally, we compared a performance of “standard” pixels that have p-well layout like it was implemented in BD1 batch with a performance of pixels having modified p-well layout implemented in BD2 batch ³. Fig. 5.13 shows the results of IV characterization

³ In a new BD2 batch of the detectors a p-well implant of “standard” pixels was minimized and, hence, the

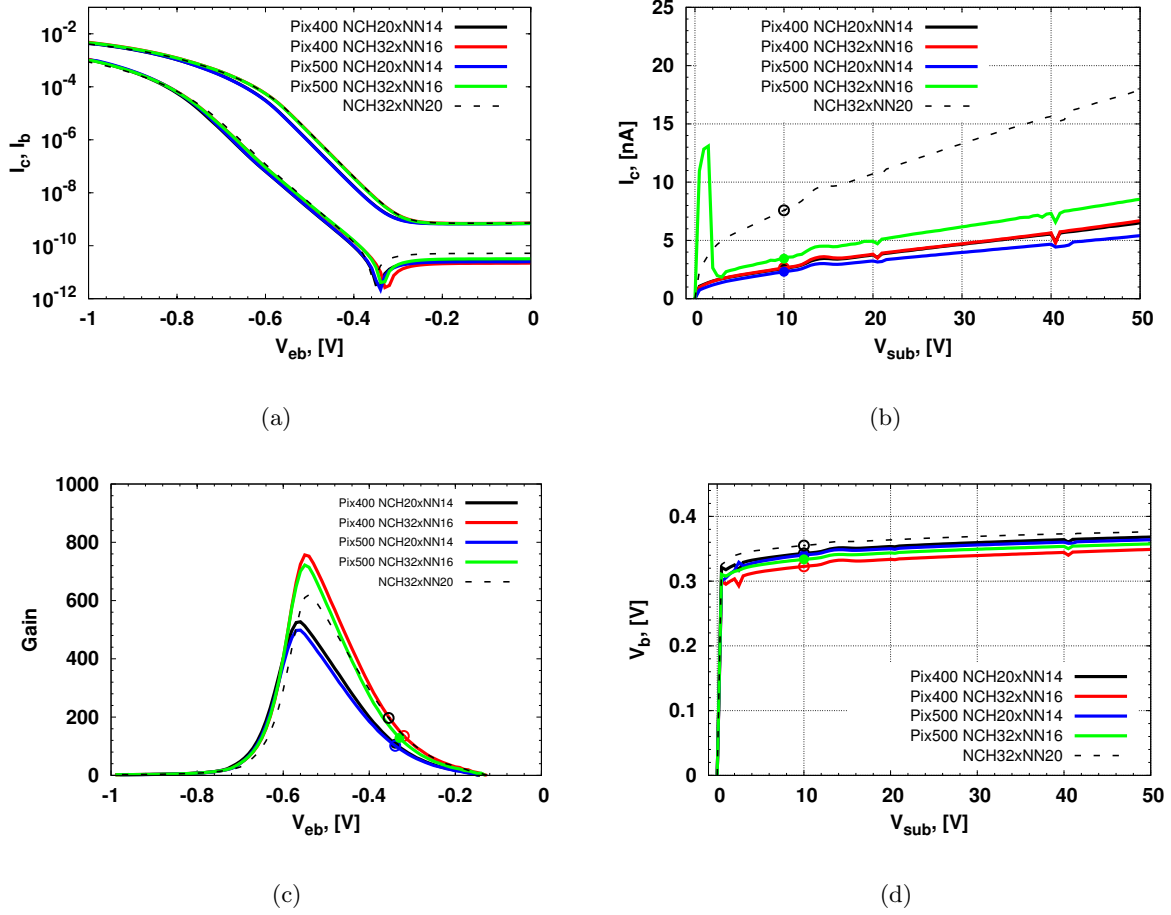


Figure 5.11: Electrical IV characterization of single test BJT pixels with extended p-well base layout configuration and different emitter layouts. The base sizes were $400\mu m$ and $500\mu m$, while emitter layouts were NCH32xNN16 and NCH20xNN14. (a) - Gummel plots; (b) - collector current I_c vs. collector bias V_{sub} ; (c) - gain curves corresponding to Gummel plots; (d) - base potential V_b vs. collector bias V_{sub} . The points, which have the same color as corresponding curve, show a quiescent states of the pixels.

of two identical pixels. The leakage currents, base potentials and Gummel plots observe very similar values. The gain values are the same till $V_{eb} = -0.49V$ and then the pixel with modified p-well layout (**STD 1.4mm (BD2)**) has higher gain values due to slightly lower base current.

Thus, the first electrical tests of single test BJT pixels showed that the designed detectors have very good amplification properties, e.g., the maximum gain values vary from ~ 500 to ~ 1000 . Comparison of new BJT pixels from BD2 batch that had modified capacitance of the pixel was minimized as well.

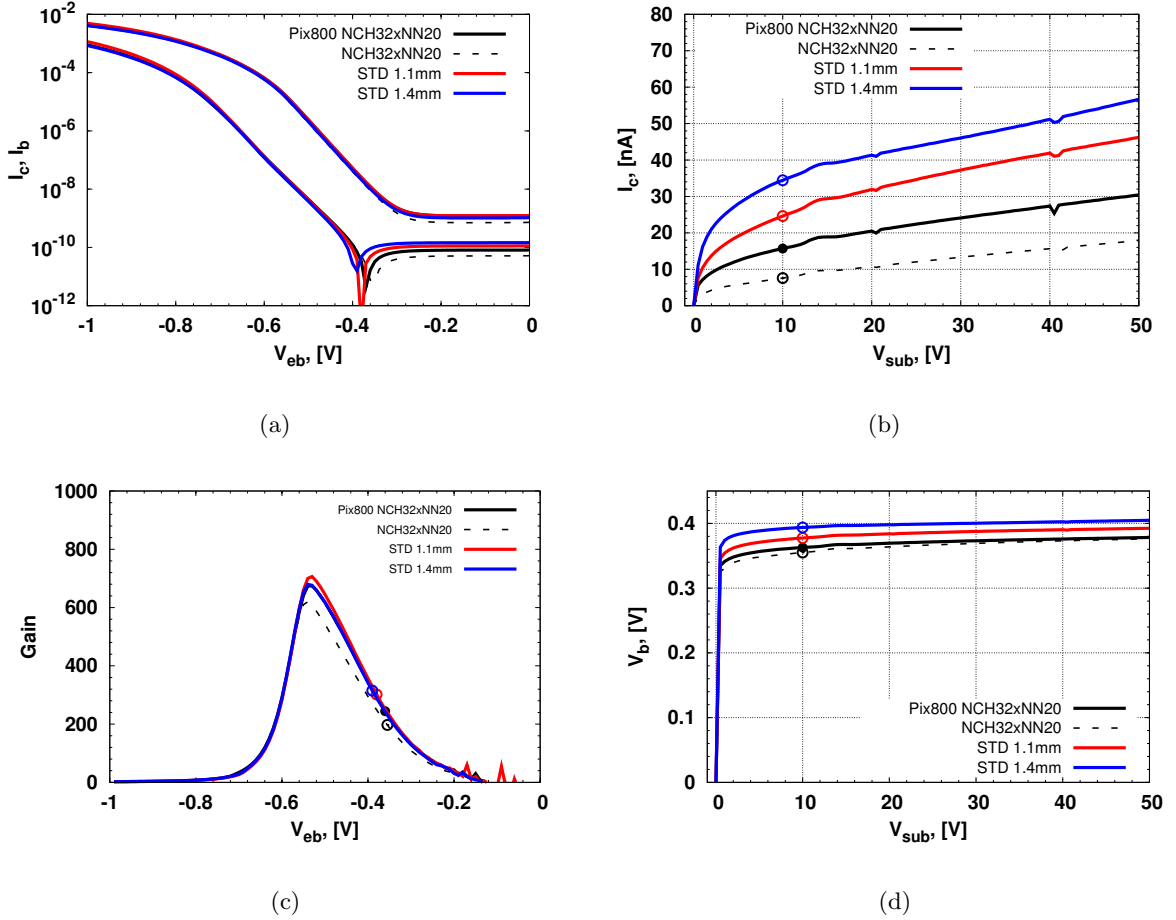


Figure 5.12: Electrical IV characterization of single test BJT pixels with “standard” emitter and base layout. The only difference between pixels is the base size ($800 \times 800 \mu\text{m}^2$, $1 \times 1 \text{mm}^2$, $1.1 \times 1.1 \text{mm}^2$, and $1.4 \times 1.4 \text{mm}^2$). (a) - Gummel plots; (b) - collector current I_c vs. collector bias V_{sub} ; (c) - gain curves corresponding to Gummel plots; (d) - base potential V_b vs. collector bias V_{sub} . The points, which have the same color as corresponding curve, show a quiescent states of the pixels.

layout of p-well to the pixels that had a layout of p-well as in BD1 batch confirmed that recently fabricated BJT detectors have at least the same amplification properties as they would have in BD1 batch. However, previously it was noticed that BJT detectors from BD1 batch were observing rather large variations of their gain properties depending on the position of detector on the wafer. Thus, we have made additional tests to verify uniformity of gain properties. The results of uniformity test are presented in fig.5.14; all tested pixels had the very same layout and the same relative position in the test die. As it can be seen the detectors from wafer W7 (fig.5.14(a),(c)) observe very uniform gain properties while

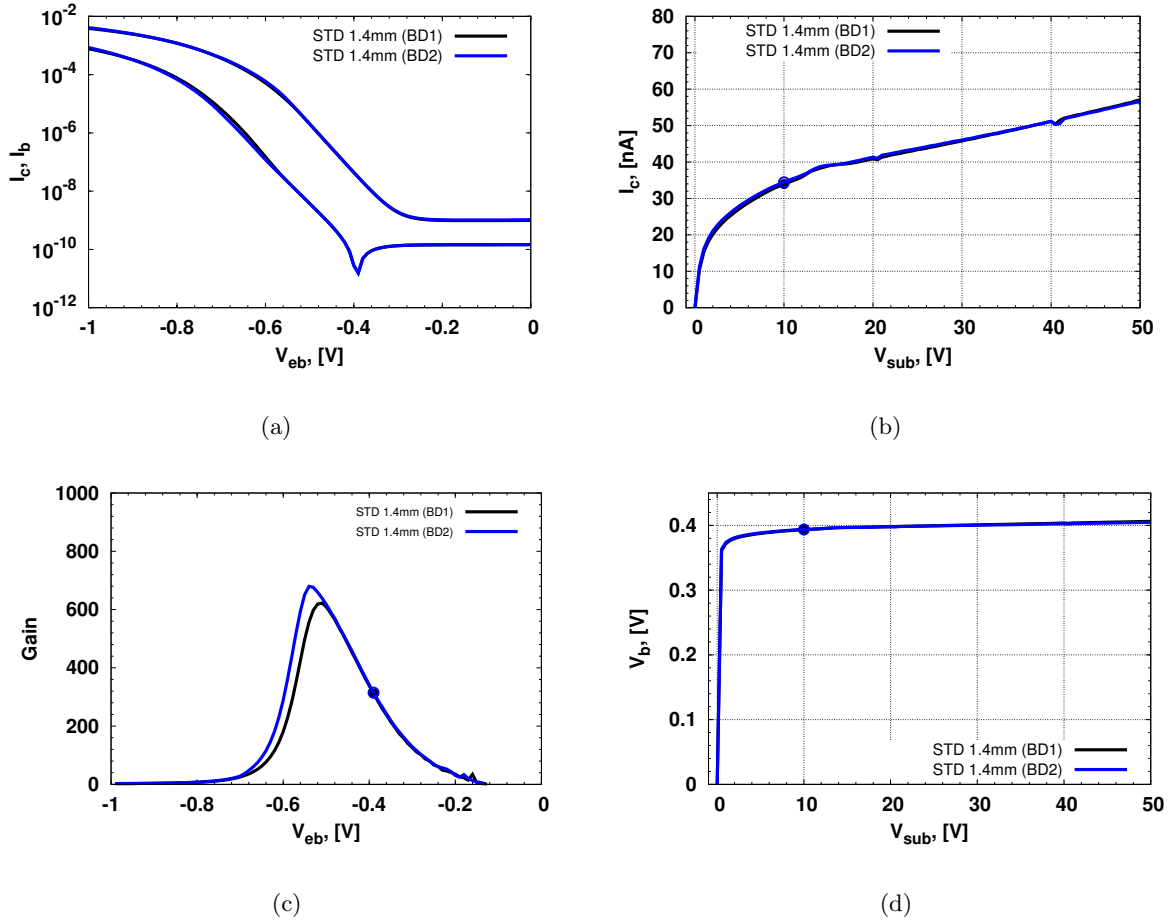


Figure 5.13: Electrical IV characterization of single test BJT pixels that have p-well layout of “standard” pixel like in BD1 batch (pixel **STD 1.4mm (BD1)**) and p-well layout of “standard” pixel like in BD2 batch (pixel **STD 1.4mm (BD2)**). (a) - Gummel plots; (b) - collector current I_c vs. collector bias V_{sub} ; (c) - gain curves corresponding to Gummel plots; (d) - base potential V_b vs. collector bias V_{sub} . The points, which have the same color as corresponding curve, show a quiescent states of the pixels.

the detectors from wafer W2 (fig.5.14(b),(d)) observe large non-uniformity of their gain properties. Such behavior was observed on almost every wafer of the BD2 batch, the observed non-uniformity was especially pronounced near the edge of the wafer while the central part of the wafer usually observed a good uniformity.

The very first assumption why such non-uniformity existed was that one of the implantation steps was not done properly, for example, p^+ implantation that has the largest area over the wafer. In order to confirm this assumption we tried to measure sheet resistance of the implants using Van der Pauw test structures. One of such test structures is

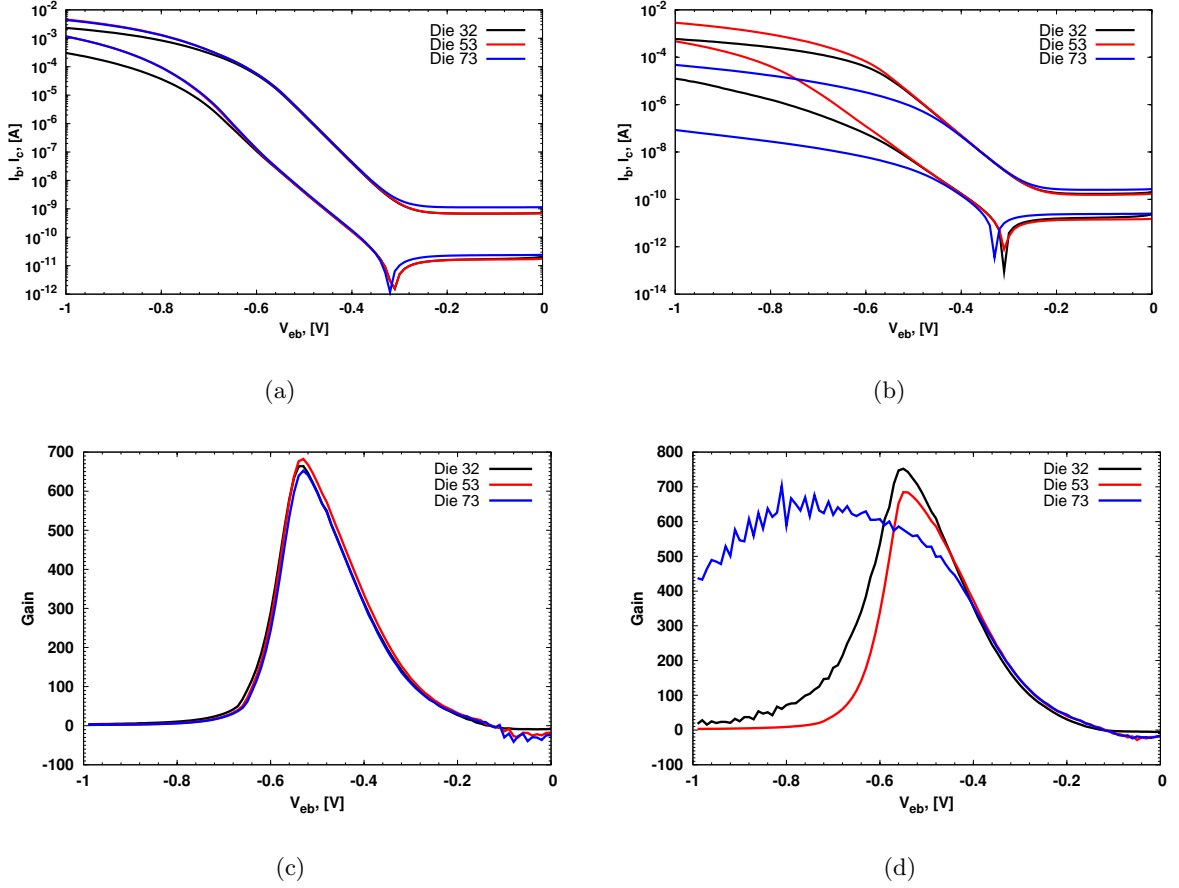


Figure 5.14: Uniformity test of gain properties of BJT pixels. (a) and (c) - very uniform Gummel plots and gain curves that were acquired while testing wafer W7 from the “poly” splitting; (b) and (d) - non-uniform Gummel plots and gain curves (W2, “standard” splitting).

shown in fig.5.15(a), the central part is an implant, which is made in form of a cross, the metal contacts are placed on the vertices of the cross. Sheet resistance R_{sh} is measured by forcing current between two adjacent nodes and measuring voltage potential between two other left nodes. For example, if the current is forced between contacts 1 and 2 and the potential is measured between contacts 3 and 4 then sheet resistance R_{sh} can be expressed as (5.11). Making tests using different configurations of the contacts through which current is forced an average value of R_{sh} can be calculated.

$$R_{sh} = \frac{\pi}{\ln 2} \frac{V_3 - V_4}{I_{12}} \quad (5.11)$$

The test dies 27 and 76 (wafer W2) were tested the first due to their proximity to the edge of the wafer, which observed non-uniform amplification properties of single test

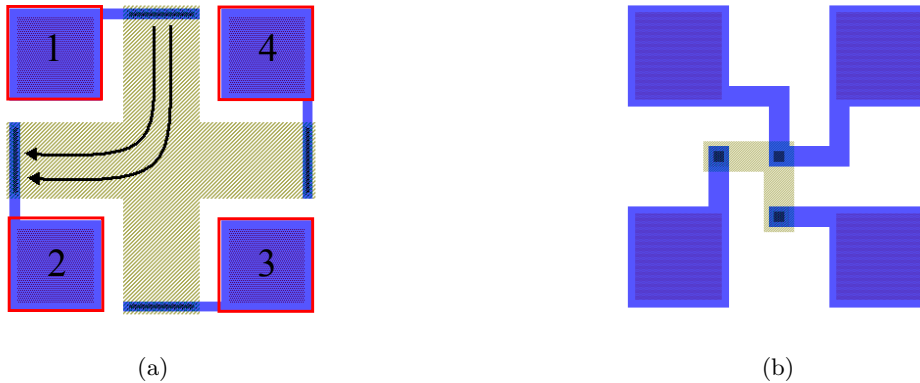


Figure 5.15: (a) - one of the Van der Pauw structures. The central part that has a form of cross is an implant, the metal contacts are numerated. The arrows represent forced current flow between contact 1 and contact 2. (b) - a test structure designed to measure a contact resistance value.

pixels (fig.5.14(b)(d)). The current was forced between contact pads 1 and 2 and the potential difference was measured between pads 3 and 4. The current sweep had to be done from -1mA to 1mA ; however, the voltage compliance of the source measurement unit 1 (SMU1) that forced current was immediately reached regardless of the value. Taking into account that $V = R \cdot I$, it means that there is an infinite resistance between contacts 1 and 2 of the test structure. The infinite resistance value means that either the implant or the contacts contain defects. The contact resistance could be verified using a specific test structure that was included in the layout, which, also has implants (see fig.(b)), so it is impossible to determine whether the problem is caused by the bad implant or bad contact. However, it is possible to disentangle two effects by considering Van der Pauw structure as a diode with four diode contacts, then the IV characterization of the diode should show values of V_{on} close to 1V .

The fig.5.16 shows a result of IV characterization of Van der Pauw test structure when one of the contact pads was used as a diode contact. Two sweeps were made, the first sweep showed very high $V_{on} \approx 14\text{V}$ of the diode, while the second sweep showed rather low $V_{on} \approx 1 \div 2\text{V}$. This effect has been observed previously on other wafers processed in the same clean room and it can be assigned to the oxide in a contact opening that remained there after the lithography step preceding metal deposition and, though, prevented a good contact between p^+ and metal. When the forward bias applied to the diode becomes high enough to breakdown a thin oxide, the contact becomes functional. Using values of bias at which a thin oxide between p^+ and metal breaks down, it was possible to calculate a thickness of that oxide. Assuming that field of an oxide breakdown is 10MV/cm , the

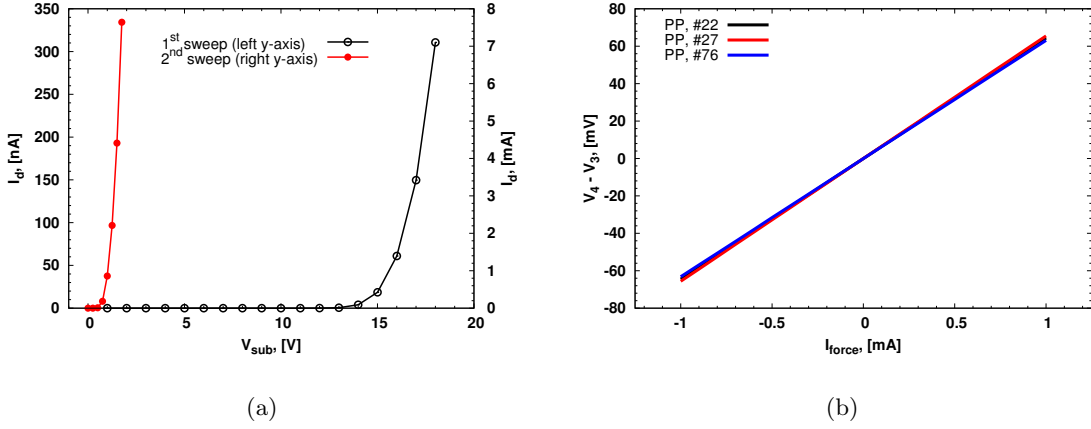


Figure 5.16: Sheet resistance measurements. (a) - acquired IV plots for one of the pads of Van der Pauw structure, when the pad was used as a diode. The curve in a black color was acquired before oxide breakdown, while the curve in a red color was acquired after the oxide breakdown. (b) - sheet resistance plots for p^+ Van der Pauw test structure.

oxide thicknesses vary from 12nm to 16.5nm. These values are very close to the values of oxide thickness deviation that was measured using MOS test structures (refer to the subsection 5.1.3).

Thus, before making measurements of sheet resistance of p^+ implants, the remaining thin oxide left in the contact openings of p^+ Van der Pauw test structures on all test dies was broken down using the explained technique. Figure 5.16(b) presents the results of the measurements of sheet resistance R_{sh} ; as it can be seen the slopes of the curves have very similar values, hence, the sheet resistance values are also similar - $R_{sh,22} = 292\Omega/sq$. $R_{sh,27} = 297\Omega/sq$. $R_{sh,76} = 286\Omega/sq$.

The “remaining oxide” effect has been observed on every wafer of BD2 batch (the edge areas of the wafers had thicker remaining oxide while central part of the wafer either had very thin remaining oxide or no oxide at all). However, the oxide remained only in the contact openings made on the areas with p^+ implantation, i.e., in the base contact openings, the emitter contact openings did not observe the “remaining oxide” effect. Taking into account that the arrays of pixels are designed to be operated with floating base, i.e., they do not have base contact, the problem of the “remaining oxide” can be neglected. Considering test single BJT pixels which have remaining oxide in the contact opening, the Gummel plots would observe some bending to the lower values of the base and collector currents due to the additional equivalent resistance attached to the base contact. Thus, during the next measurements relating to the analysis of amplification properties of the BJT detectors we, firstly, checked the base contact and then if the

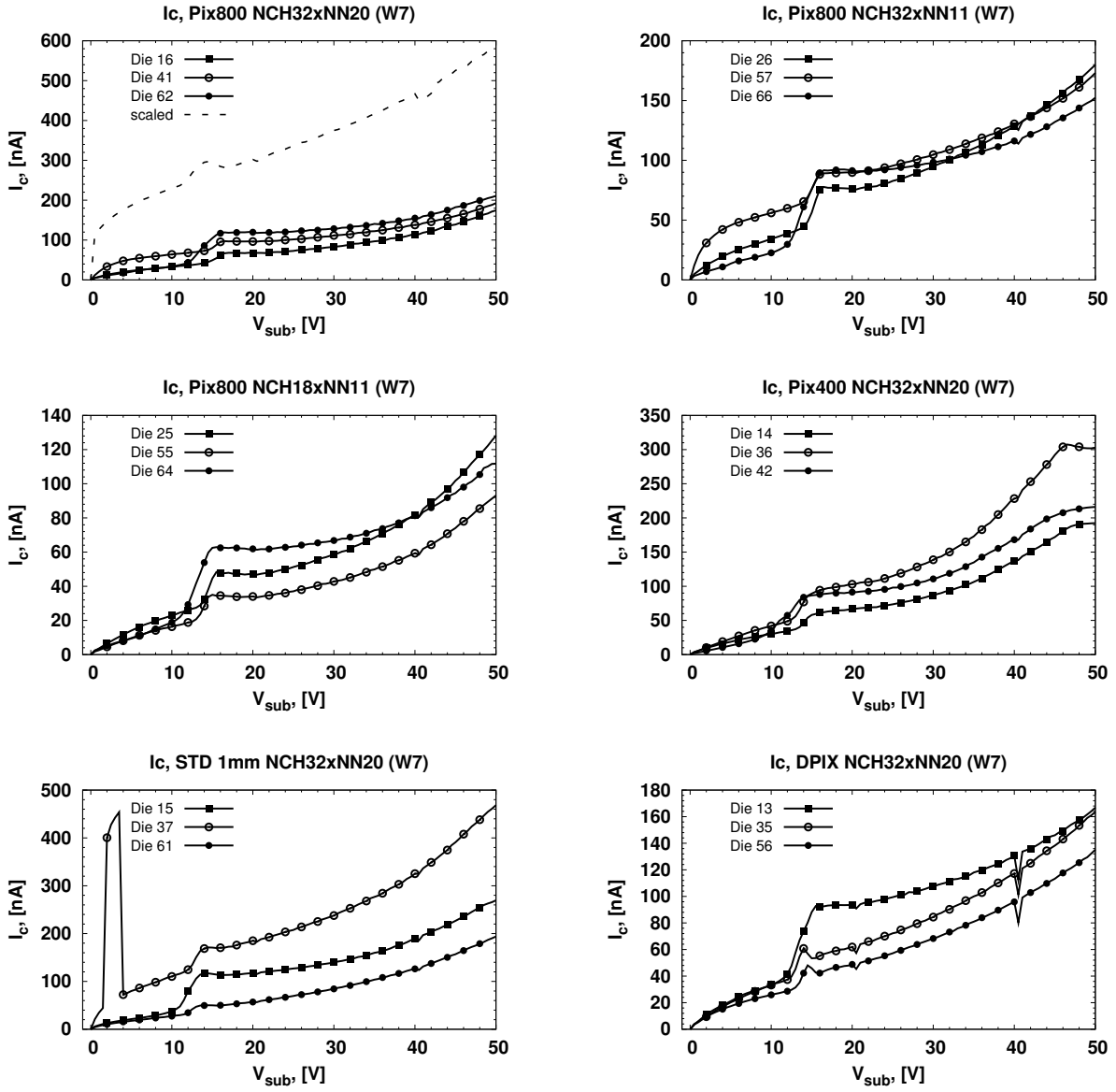


Figure 5.17: IV characterization of large $1 \times 1 \text{ cm}$ arrays from the wafer W7. Only those arrays that have emitters shorted together are shown in this figure.

contact was working properly we acquired the data.

5.3 Arrays of pixels

After single BJT pixels were tested the arrays of BJT pixels were tested as well. The layout included few types of arrays: large $1 \times 1 \text{ cm}^2$ arrays and smaller $5 \times 5 \text{ mm}^2$ arrays. The large $1 \times 1 \text{ cm}^2$ arrays were intended to be used in a radon monitoring/detection

system, while smaller arrays were included in the layout for testing purposes. Figure 5.17 shows the results of measurements carried out on the samples from the wafer W7 that was from “poly” slitting. The arrays from the “poly” splitting usually observed quite low and rather uniform leakage currents. Leakage current of one of the large large arrays was compared to the leakage current of identical single pixel (see the first plot on fig.5.17). As it can be seen, the dashed line showing scaled value of a leakage current that was calculated as a product of leakage current of single pixel and amount of pixels in the array confirms that this value of leakage current is much higher than actually observed. That is because of the proximity of the pixels in the array due to which appears a confinement of pixels’ actual area and active volume, while a test single pixel that is not surrounded by a guard ring does not have such confinement and, hence, has higher leakage current. On the other hand, such confinement of active volume of pixels did not appear in the arrays from “standard” splitting. The first plot on fig.5.18 shows that a scaled value of leakage current corresponds to the leakage current of the array **die 41**.

Plots representing leakage currents of the arrays consisting of $1 \times 1mm^2$ “standard” pixels bring up an interesting effect of drastic increase of collector current under low collector bias (see the data related to the **die 37**, fig. 5.17), which then returns to the expected leakage current values. This effect does not have any influence on the performance of BJT detector in case operation voltage for the identical arrays (for example, **dies 15, 37, 61**) is chosen in such a way that all arrays have “expected” leakage current values. In case collector bias is low, e.g., 3V, the leakage current of the **die 37** is similar to the leakage current of this detector at high $V_{sub} = 50V$ bias and it is considerably higher than corresponding currents for the **dies 15, 61** under the same bias conditions. It means that the **die 37** has higher base potential and quiescent gain value at low $V_{sub} = 3V$ bias; so, under this bias condition the detector observes much better amplification and operation speed properties. The effect can be explained by a diffusion current from outer regions of the detector that can reach a depletion region. Under low collector bias the detector and guard ring region is just partially depleted; so, the diffusion current can flow into a depletion region without being stopped by a guard ring. Such behavior could not be explained by peculiarities of the layout and it was attributed to the faults introduced during fabrication step. Almost always the “diffusion current” effect disappeared after the detectors and guard rings were bonded.

Another interesting effect that was observed during these tests is related to the “kink” present in the IV curves at $V_{sub} \approx 15V$ (see, for example, fig. 5.17). It is, so-called, “MOS” or “gated-diode” effect. Metal grid that routes out emitters acts as a gate in a gated-diode test structure and base of a BJT pixel acts as a diode. When the collector is swept from 0 V to 50 V, the base becomes reverse biased (in a gated-diode test structure

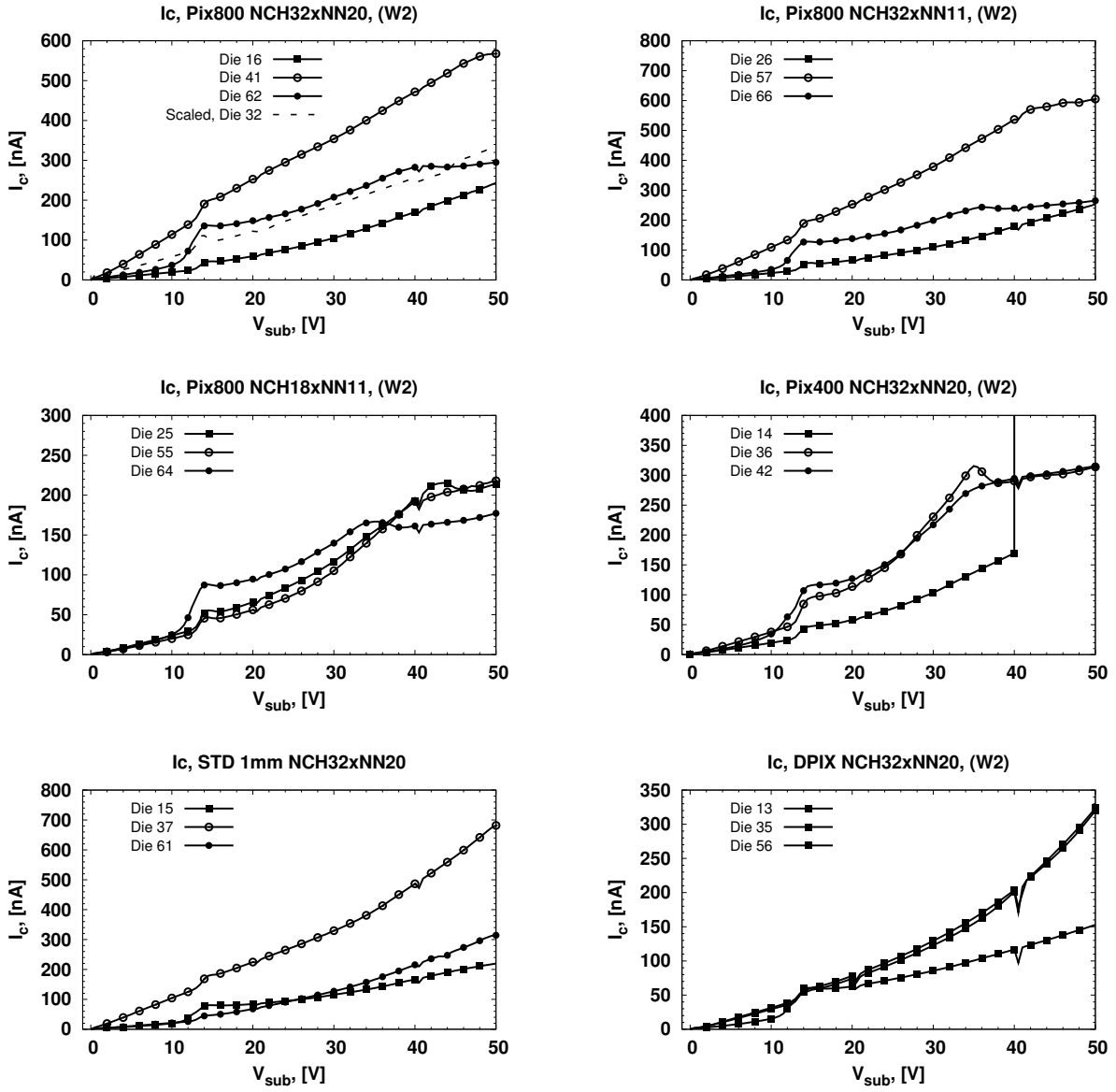


Figure 5.18: IV characterization of large $1 \times 1 \text{ cm}$ arrays from the wafer W2 (“standard” splitting).

the diode is also reverse biased) and the region under routing metal grid goes through accumulation, depletion and inversion regimes. In accumulation and inversion regimes surface recombination is suppressed⁴. However, in a depletion regime surface recombination is not suppressed; so, it contributes to the diode, i.e., base current⁵, which is then amplified by a transistor effect. Thus, a “kink” appears in the collector current curves.

Different results were acquired from the IV characterization of the arrays from the

⁴For more details refer to sub-section 5.1.2, page 76

⁵Fig. 5.6 shows how diode current depends on a gate sweep in a gated-diode test structure.

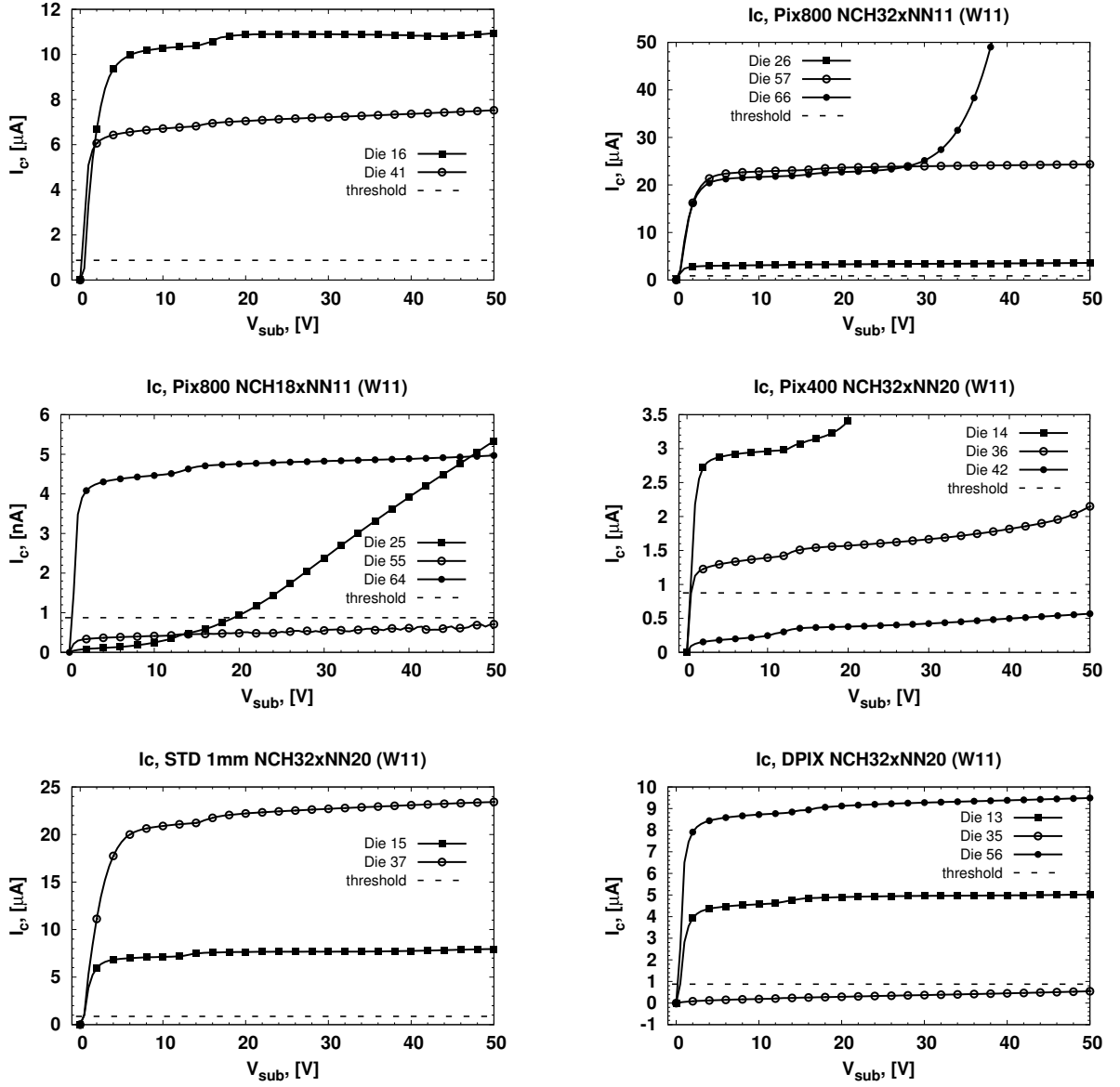


Figure 5.19: IV characterization of large $1 \times 1 \text{ cm}$ arrays from the wafer W11 (“thinned” splitting). Only those arrays that have emitters shorted together are shown in this figure.

“thinned” splitting (see fig.5.19⁶) - due to the small generation lifetimes and, hence, high leakage currents almost all large $1 \times 1 \text{ cm}^2$ arrays from this splitting had collector and emitter currents higher than acceptable threshold of $0.875 \mu\text{A}$, which corresponds to the charge of 350 pC integrated during $400 \mu\text{s}$ by DDC112/DDC114. As a result, large $1 \times 1 \text{ cm}^2$ arrays from the thinned splitting cannot be used with already designed ALPHADET or

⁶Data for two the dies 62, 61 is not presented here due to the crack in the wafer, which has appeared after fabrication and destroyed these arrays. Apart from that, the wafer W7 observed rather good properties.

microcontroller based electronics.

5.4 Summary

Current BJT fabrication process confirmed at least those characteristics that were observed in the previous BD1 batch. Moreover, some of the silicon characteristics observed even better properties, e.g., longer generation lifetimes, lower substrate doping concentration, lower full depletion voltages, smaller surface recombination velocity, smaller charge oxide density and good uniformity of these properties.

The BD2 batch was divided onto three splittings, which had rather different properties of silicon. The best properties had the “poly” splitting, which observed low leakage currents, high gain values and good uniformity of amplification properties of the pixels. The “thinned” splitting had good gain properties of single BJT pixels but the pixels observed modest uniformity properties. The large 1×1 cm arrays from the “thinned” splitting observed high leakage currents preventing use of this arrays with already designed electronics.

Thus, the detectors from the wafers with polysilicon gettering might be considered for the applications where power consumption is of primary concern, e.g., portable instrumentation. Further electrical characterization (Gummel plots, base potential and collector current vs. collector bias, base-emitter and emitter-collector capacitances) confirmed that all fabricated BJT detectors indeed feature good gain properties (low quiescent gain values and high maximum gain values).

So-called, “remaining oxide” effect has been observed during the electrical characterization of the BD2 batch; however, this effect does not influence a performance of the arrays and all of them can be used for α -particle detection.

Chapter 6

Functional characterization of BD2

This chapter discusses functional characterization of BJT detectors from the BD2 batch. The characterization included laser and α -particle tests. In principle, due to the permanent availability of radioactive ^{241}Am α -particle source it would be enough to carry out only α -particle tests as BJT detectors are expected to be used mainly for radon, i.e., α -particle detection. However, laser tests considerably extend range of information about detection properties of the detectors. For example, laser scanning of BJT arrays can provide an information about dependence of detection properties of BJT arrays on the position of charge generated by the flux of photons. Thus, laser scanning of the detectors can as well explain why some of the tested arrays or single pixels observed two energy peaks in the acquired distributions of collected charge values. Apart from that, pulsed laser light test is a very fast way to make initial tests in order to verify functionality of the detectors and to estimate overall gain of the detector.

So, section 6.1 describes the results of pulsed laser light tests. Then section 6.2 presents all results of α -particle tests. This section is divided onto two logical parts. The first part analyzes performance of single test BJT pixels, while the remaining part describes results of the characterization of different BJT arrays.

Finally, section 6.4 draws conclusions about overall performance of newly fabricated BJT detectors and provides some suggestions for further layout modifications.

6.1 Pulsed laser light tests

We have started pulsed laser light tests with characterization of **NCH32xNN20** array from die 24, w7, which was the first tested, and thus, the most studied and characterized sample. Two laser tests were done: one with quite small light energy (equivalent energy of α -particle $E_\alpha \approx 1.8$ MeV) and another with higher light energy (equivalent energy of α -particle $E_\alpha \approx 4$ MeV).

The results of first laser scan of **NCH32xNN20** array are shown in fig.6.1. Each bar represents a mean value of charge in pC collected at that point. Note that the units of figure axes are not microns, in order to obtain coordinates of the bars in microns simply multiply current axes units by value of step of the laser scan (100 μm in this case). Schematic sketch of layout of the array was put above the scan to show how the tested array was positioned. As it can be seen, the first three scanned rows showed slightly higher values of Q_{coll} , that is due to the fact that the laser needs some time to stabilize its performance.

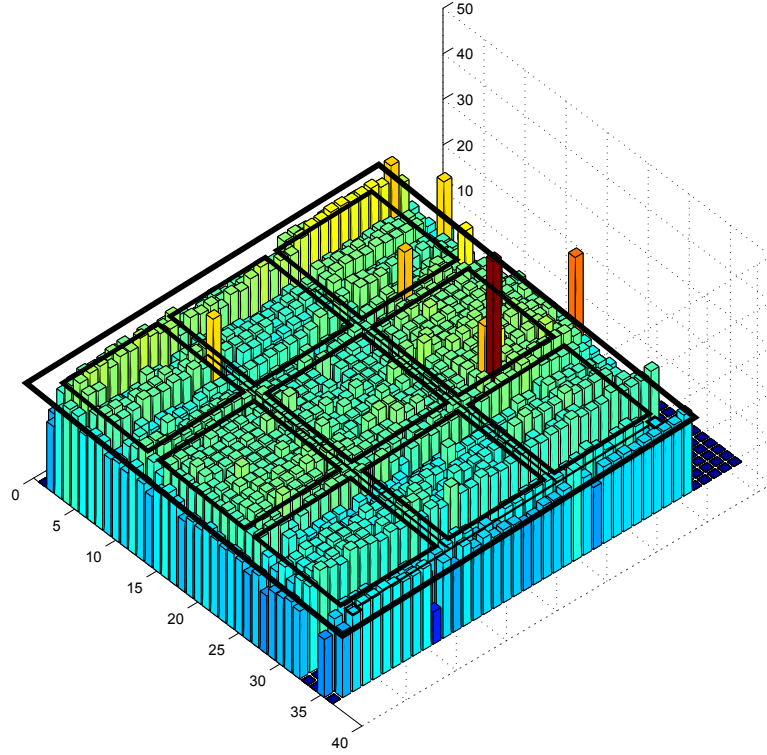


Figure 6.1: Laser scan of **NCH32xNN20** array, the step of scan is 100 μm . Schematic sketch of the layout is to show positioning of the scanned detector and its boundaries.

Figure 6.2(a) refers to the Gaussian fit of distribution of Q_{coll} . Mean value of this distribution $Q_{coll,mean}$ could be used to extract gain value of the detector. In this case gain is defined as a ratio between collected charge and charge generated in Si (6.1).

$$\beta = \frac{Q_{coll,mean}}{Q_{generated}} \quad (6.1)$$

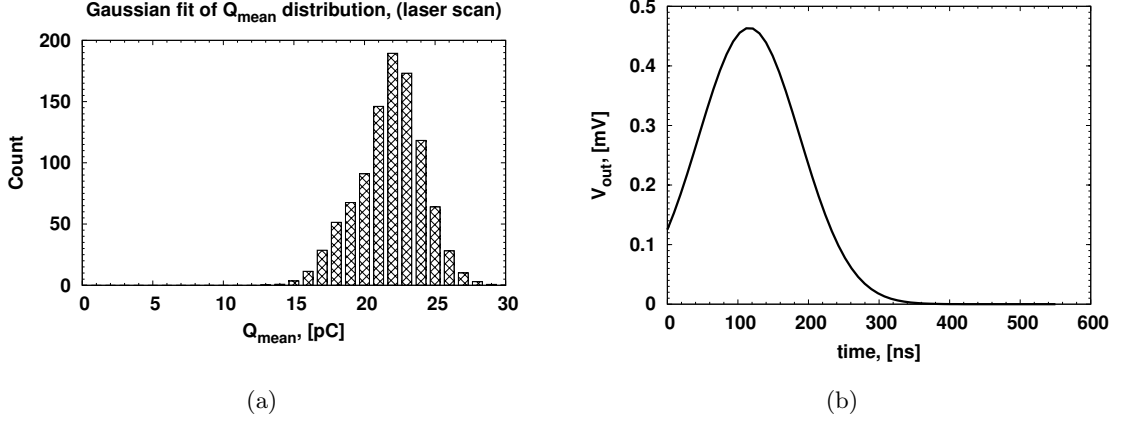


Figure 6.2: (a) - Gaussian fit of distribution of Q_{coll} . $Q_{\text{coll,mean}} = 21.42$ pC; (b) - laser light calibration plot acquired by D400FC detector [5], amplified by THS4303 amplifier and then visualized and saved via TDS3052B oscilloscope [6]. The equivalent energy of α -particle corresponding to such laser pulse is ≈ 1.8 MeV.

Generated charge can be calculated when the light pulse characteristics are known. The laser light wavelength was 980nm. Laser light pulse was registered by an oscilloscope connected to D400FC InGaAs photodetector through wideband THS4303 TI amplifier. After the laser pulse was acquired (fig.6.2(b)) generated charge and equivalent α -particle energy were calculated. The equivalent α -particle energy would be $E_{\alpha} \approx 1.8$ MeV, i.e., charge generated in Si would be $Q_{\text{generated}} \approx 0.08$ pC. Given that $Q_{\text{coll,mean}} = 21.43$ pC we could calculate that the gain was $\beta \approx 270$. This gain value corresponds to base potential $V_b = 0.43$ V, which corresponds to $C_{BE} = 2.5$ pF.

While fig. 6.1 presents the results of laser scan of **NCH32xNN20** array by laser light pulse with quite small energy of equivalent α -particle, figure 6.3 extends characterization of this sample by increasing laser light power in order to make energy of equivalent α -particle larger. Three arrays with different emitter layout configurations were tested at collector bias $V_{\text{bias}} = 10$ V. The laser scan was made with a step of $200 \mu\text{m}$, which turned out to be a very good trade-off between data acquisition duration and reliability of the data. For example, assuming that at least ~ 100 events should be acquired at each position of laser spot and taking into account that due to the long time decay constant τ_d of the detector acceptable frequency of the laser pulse is ~ 5 -10 Hz, just data acquisition time is 20 seconds. Adding time for the motor repositioning, data transfer and data processing the time of data acquisition for each point becomes ~ 30 s. So, for the scans showed on fig. 6.3, where the amount of acquired points was 361, overall duration of a single test is 3 hours. Decreasing step by factor of 2 (till $100 \mu\text{m}$) would increase overall duration of the test by factor of 4 (till 12 hours) without providing any additional relevant information.

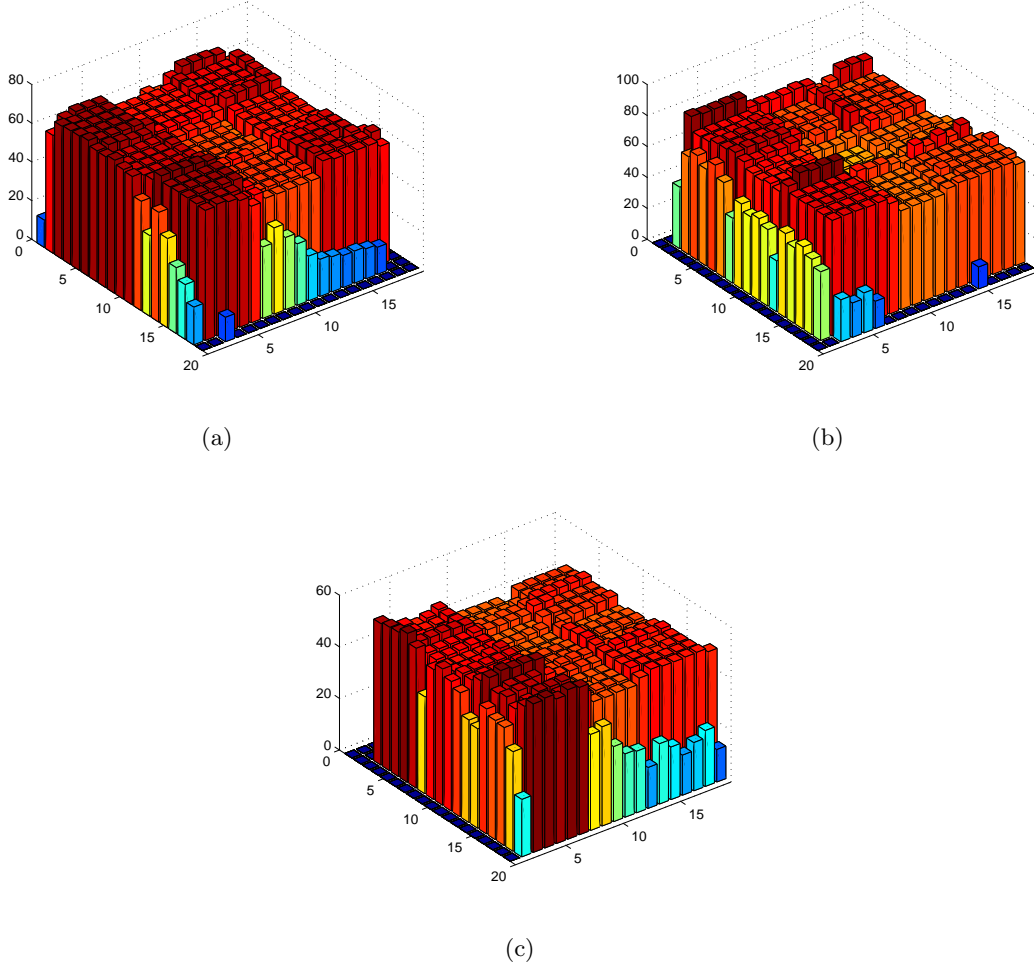


Figure 6.3: Laser scan with an energy of light pulse corresponding to the energy of α -particle $E_\alpha \approx 4\text{MeV}$ (a) - **NCH32xNN20** array; (b) - **NCH32xNN11** array; (c) - **NCH18xNN11** array. The step is $200\mu\text{m}$, bias voltage is $V_{bias} = 10\text{V}$. Note that the charge axes ranges are different.

This is why, $200\mu\text{m}$ step was considered as a good trade-off for the testing of such large arrays ($3.6 \times 3.6\text{mm}^2$).

After the laser scanning of the arrays was completed, the Gaussian fits of distributions of Q_{coll} were done in order to obtain mean values $Q_{coll,mean}$. The Gaussian fits are shown in fig. 6.4. The $Q_{coll,mean}$ values are 48.5 pC, 62.6 pC, and 69.1 pC for **NCH18xNN11**, **NCH32xNN20**, and **NCH32xNN11** arrays, respectively. So, taking into account that the conditions of the tests were exactly the same for all arrays, i.e., the power of laser light pulse was kept constant, a direct comparison between arrays with different emitter layout could be made.

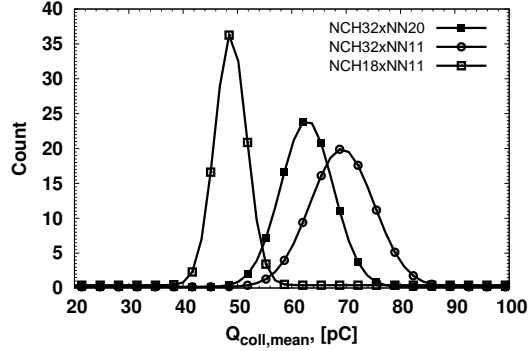


Figure 6.4: Gaussian fits of the distributions corresponding to the laser scans plotted in fig. 6.3. Mean values are 48.5 pC, 62.6 pC, and 69.1 pC for **NCH18xNN11**, **NCH32xNN20**, and **NCH32xNN11** arrays correspondingly.

Measured energy of laser light pulse corresponded to the α -particle with 4 MeV energy, which corresponded to generated charge $Q_{generated} = 177$ fC. Thus, overall gain values for the tested arrays **NCH18xNN11**, **NCH32xNN20**, and **NCH32xNN11** are 275, 350, and 390 correspondingly. This trend is in very good agreement with the results of electrical characterization of single pixels, i.e., Gummel plots. The reported overall gain values are the average dynamic gain values of the tested detectors that, obviously, differ from the quiescent gain values. The laser light biases the detectors, so, the gain changes dynamically from its quiescent value till some higher value, which at the end can be measured as an average (or overall) gain value.

After die 24, w7 was tested, we tested die 45, w7 which included 4 arrays with different configurations of base layout¹. One of these arrays is **NCH32xNN20**, which was included for reference purposes. As electrical characterization of these dies (refer to figures 6.18 and 6.20) showed that die 24, w7 has increased its leakage current after the bonding step and die 65, w7 has not changed its properties after the bonding, a significant difference in the detection properties of these dies should be observed. In fact, figures 6.5(a) and 6.6 confirm that **NCH32xNN20** from die 24, w7 has higher overall gain value comparing to the overall gain of **NCH32xNN20** from die 45, w7, e.g., mean value $\mu_{coll,24}$ of Gaussian fit of Q_{coll} distribution for **NCH32xNN20** from die 24, w7 is 62.6 pC while for **NCH32xNN20** from die 45, w7 it is $\mu_{coll,45} = 39.9$ pC. Such difference can be explained by different quiescent gain values for the tested arrays. For example, assuming that temperatures in the laboratory is 25 °C the quiescent gain for **NCH32xNN20** from die 24, w7 is $\beta_{quiesc,24} = 135$, while for **NCH32xNN20** from die 45, w7 it is $\beta_{quiesc,45} = 100$. Another factor that could increase or decrease β_{quiesc} is temperature variations in the lab-

¹More detailed explanation on layout details can be found in section 4.2 and on page 112.

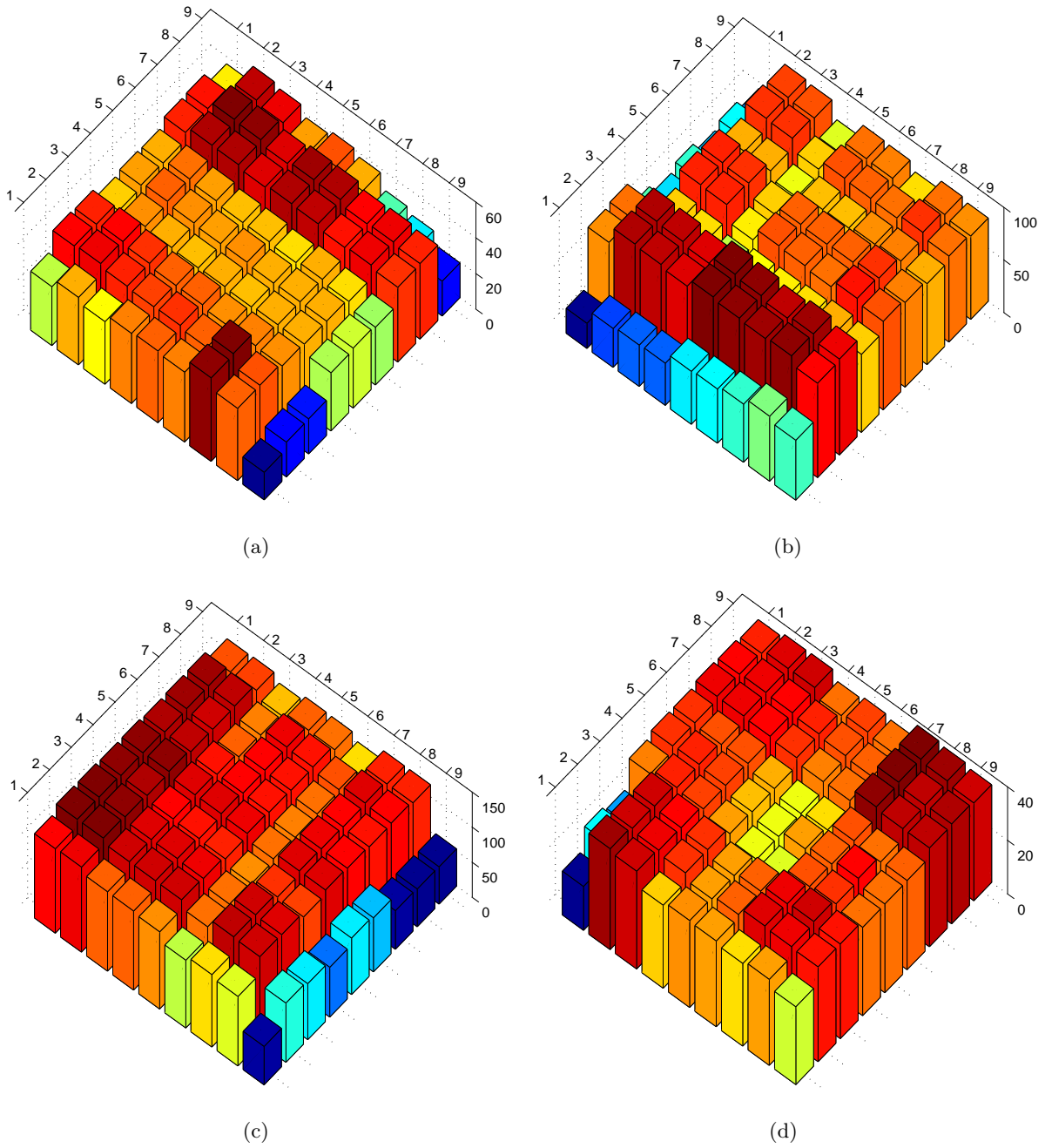


Figure 6.5: Laser scan of die 45, w7 with an energy of light pulse corresponding to the energy of α -particle $E_\alpha \approx 4.1$ MeV. (a) - **Standard** array; (b) - **PP FR** array; (c) - **PP FR small** array; (d) - **PW extend** array. The step is $400 \mu\text{m}$, $V_{bias} = 10$ V. Note that the charge axes ranges are different.

oratory, which could reach few degrees (approximately from 23°C till 27°C); the rate for the change of β_{quiesc} is $\sim 8.0/1^\circ\text{C}$. However, even though the reference **NCH32xNN20**

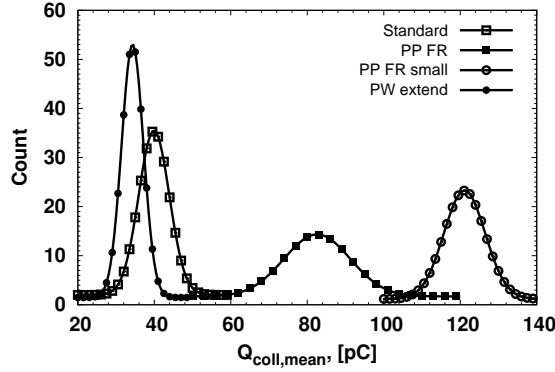


Figure 6.6: Gaussian fits of the distributions corresponding to the laser scans of die 45, w7 plotted in fig. 6.5. The equivalent energy of α -particle corresponding to the laser pulse is ≈ 4.1 MeV.

arrays observe different detection properties the arrays from die 45, w7 can be safely compared as they preserved their initial properties after the bonding step.

The results of characterization of the arrays from die 45, w7 are shown in fig. 6.5 and in fig. 6.6. Mean values of distributions acquired by characterization of **STD**², **PP FR**, **PP FR small**, and **PW extend** arrays are $\mu_{coll,STD} = 39.9$ pC, $\mu_{coll,PP FR} = 82.6$ pC, $\mu_{coll,PP FR small} = 121.1$ pC, and $\mu_{coll,PW extend} = 34.3$ pC respectively. Overall gain values for these arrays are $\beta_{STD} = 220$, $\beta_{PP FR} = 460$, $\beta_{PP FR small} = 700$, and $\beta_{PW extend} = 190$. Considering these gain values we can conclude that for all tested arrays from die 45, w7 the overall gain values are much higher than quiescent gain values ($\beta_{quiesc,STD} \approx 100$, $\beta_{quiesc,PP FR} \approx 170$, $\beta_{quiesc,PP FR small} \approx 240$, and $\beta_{quiesc,PW extend} \approx 90$, assuming that the temperature is $T = 25$ °C). It means that the arrays were biased by light pulse to a point with higher gain values and all of them were “woken up” by light pulse. Hence, charge generated in BJT bulk was amplified by a gain value higher than β_{quiesc} value.

After that all arrays from die 43, w7 and die 44. w7 were scanned as well. The results of these tests are shown in fig. 6.7. It should be stressed here that this characterization of the arrays from die 43, w7 and die 44, w7 was not intended for obtaining overall gain values but for verification of uniformity of detection properties of the arrays consisting of rather small pixels. It is obvious that all tested arrays have higher Q_{coll} values closer to the center of pixels, while on the boundaries of pixels and in between Q_{coll} values are significantly lower. Such effect can be explained by incomplete depletion of interpixel volume, so part of the charge generated in non-depleted region is lost. Histogram and Gaussian fit of Q_{coll} distribution for **Pix400** array from die 43, w7 are shown in fig. 6.8.

²STD states for “standard”, i.e., the array has NHC32xNN20 emitter layout.

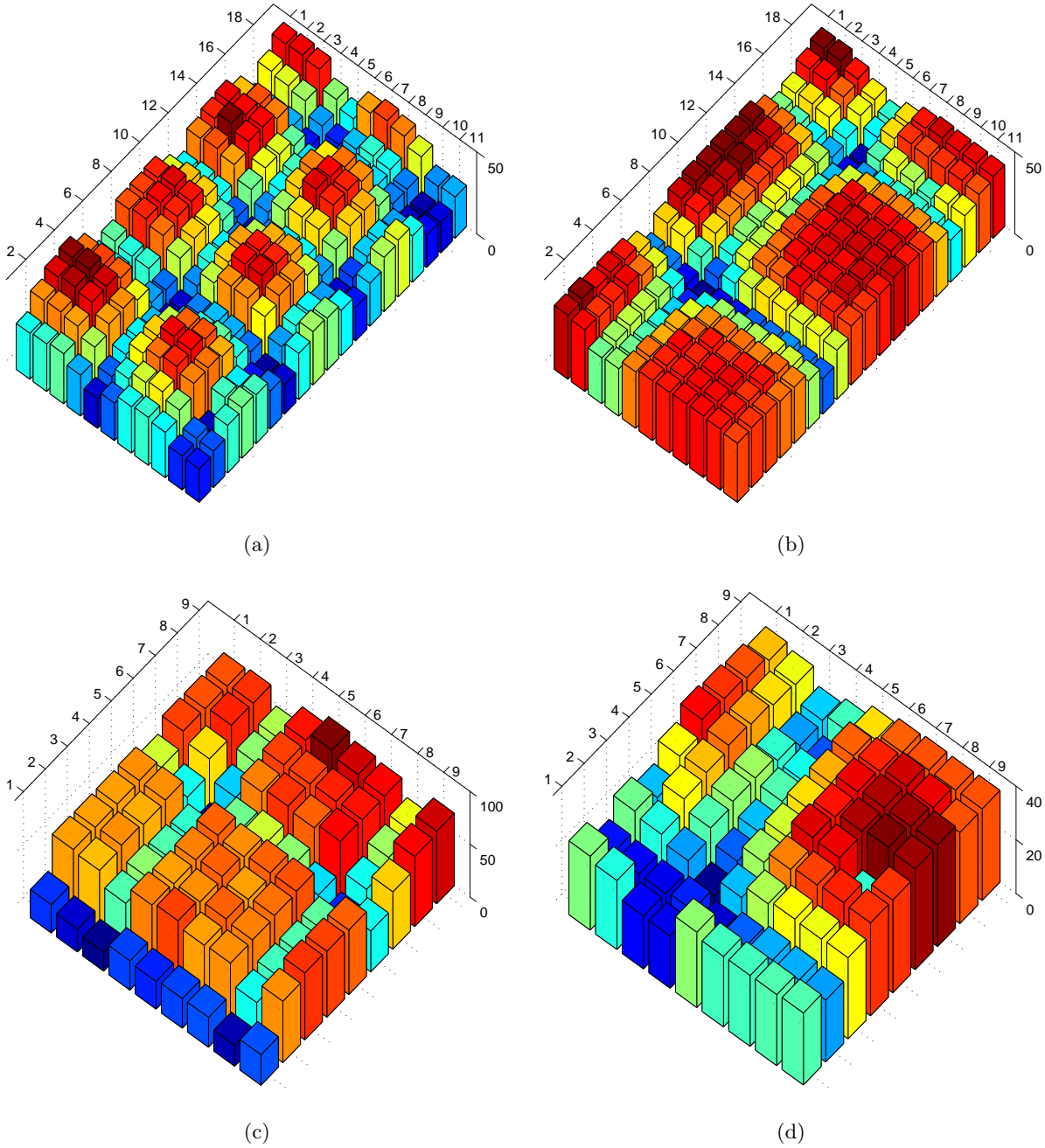


Figure 6.7: Laser scans of: (a) - **Pix200**, (b) - **Pix400** from die 43, w7 and (c) - **Pix200**, (d) - **Pix400** from die 44, w7. The step is $50 \mu\text{m}$

The Gaussian fit has two peaks with mean values at $\mu_1 = 31.6 \text{ pC}$ and $\mu_2 = 37.0 \text{ pC}$. The peak shifted to the higher values of Q_{coll} corresponds to the events registered at the center of pixels, while the other peak, shifted to lower values of Q_{coll} , corresponds to the events registered on the boundaries of pixels and in between them. Similar effect was observed

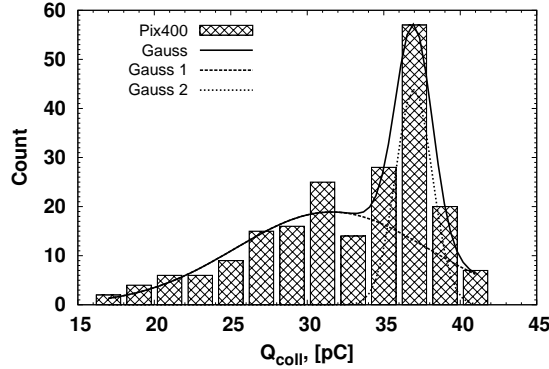


Figure 6.8: Gaussian fits of distribution of Q_{coll} corresponding to the laser scan of **Pix400** array from die 43, w7 plotted in fig. 6.7(b). Solid line shows multi-peaks Gaussian fit with mean values for the peaks $\mu_1 = 31.6$ pC and $\mu_2 = 37.0$ pC.

during functional characterization of single DPIX pixels from the BD1 batch (refer to fig. 2.15 on page 35); all of the pixels had low energy “tails” in the distributions of Q_{coll} .

6.2 Alpha-particle tests

Alpha-particle tests are the main functional tests usually implemented to test performance of Si radiation detectors intended for the use in radon monitoring/detection systems. For example, calibrated ^{241}Am source of α -particles was used to test CMOS α -particle counter and α RAM system for radon monitoring application [52], [54], AlphaRad system [28] and other systems that are based on Si radiation detectors.

The setup for α -particle functional characterization of BJT detectors is rather simple and, hence, reliable. It consists of the tested detector, ALPHADET readout electronics, ^{241}Am source of α -particles (AMR01032, $\sim 3\text{kBq}$ nominal activity, $\sim 2\text{ cm}^2$ active area), climatic chamber (mini test chamber VT 4002, [75]), two power supplies (Keithley 6487 picoammeter/voltage source to bias the detector [76] and Agilent E3631A to bias ALPHADET readout [77]) and PC to acquire and process data. It is important to control the temperature at which data acquisition is done as leakage currents of BJT detectors exponentially depend on temperature and, hence, bias point of the detector has similar dependence on temperature. So, a comparison of performance of different detectors should be done at the same temperature.

Figure 6.9 shows a part of the whole setup for the functional characterization of the detectors. It shows ALPHADET system with connected BJT detector and aluminum holder for the alpha-source. There is a paper mask with an opening in form of a slit

($2 \times 10\text{mm}^2$) that is put closely to the source and centered just above the array. The mask is needed to limit the rate of source in order to avoid pile-ups in data files, which would appear due to the high rate and long integration times of the detector; the rate drops approximately by factor of 7 (for example, from 13.36 s^{-1} to 1.96 s^{-1} at $20\text{ }^\circ\text{C}$ for tested array **NCH32xNN20**, die 24, w7).

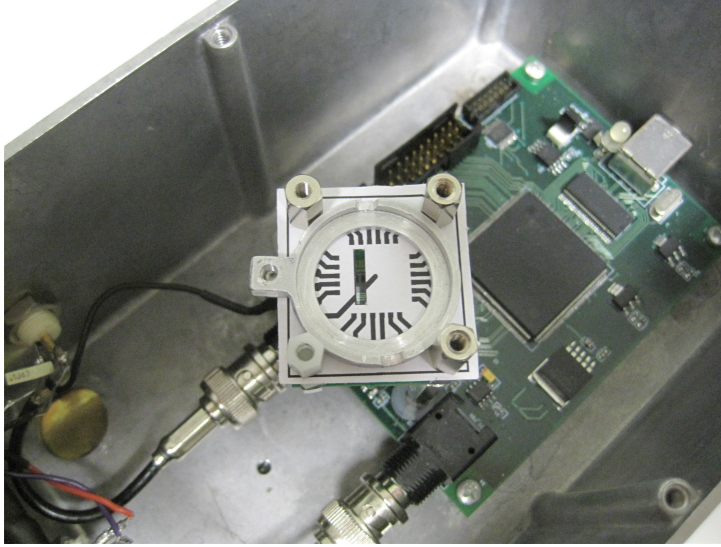


Figure 6.9: Setup used for α -particle characterization of BJT detectors.

6.2.1 Comparison of the detection properties of single pixels

As it has been already shown in Chapter 5 the detectors from “poly” splitting observe good uniformity of their properties. This is why, the detectors from “poly” splitting, namely, detectors from wafer w7 were tested first and then detectors from “thinned splitting” were tested as well.

Firstly, single BJT pixels were tested using ^{241}Am source. The data have been collected with a threshold put to a very small value (bit value for DDC114 is 100, which is -0.55 pC , i.e, all charge values larger than -0.55 pC are swept to the PC). The reason for that was that the data could be swept from DDC114 to the PC and then analyzed off-line. In that way it was possible to apply different techniques to process data and find out the best one. The events corresponding to α -particle hit were called “peaks”. In order to identify peaks in the acquired file a simple algorithm was used. This algorithm uses, so-called, “soft” trigger (“soft” states for software as it is implemented on the software stage of data processing); all the points in the file were considered as peaks corresponding to alpha-particle hits if their values were larger than the preceding points by a “soft” trigger value.

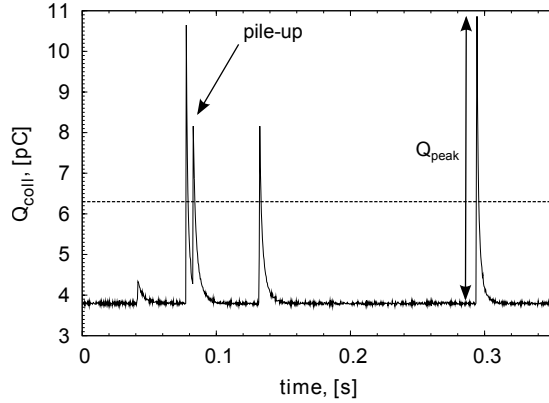


Figure 6.10: A part of data file acquired during functional characterization of STD 1.4mm single test pixel. The dashed line represents 2.5 pC “soft” trigger.

Fig. 6.10 refers to the signal acquired by STD 1.4mm (die 73, w7) pixel with a dashed line representing 2.5 pC “soft” trigger. Due to the collection of complete data an off-line data processing can be made. It provides all relevant information about BJT detector. Firstly, this is distributions of collected charge values Q_{coll} , which are built after all detected events excluding events in pile-ups (one of pile-ups is shown in fig. 6.10) are integrated over certain period of time. Pile-ups are excluded by means of moving window, which checks that only one event happens during the time window; it was set to 100 ms in all experiments. The mean value of such distributions $Q_{coll,mean}$ represents mean value of charge generated by the particles in the silicon bulk and then amplified due to the BJT effect by a factor β (the differential gain of BJT detector). Having mean value of energies of α -particles the average gain by which BJT detectors amplify generated charge can be calculated.

Apart from the distributions of Q_{coll} another relevant characteristic can be obtained off-line. That is distribution of peak values Q_{peak} . Availability of information about mean value $Q_{peak,mean}$ allows developing better triggering algorithm for the radon monitoring/detection system, i.e., it might be necessary to lower acquisition trigger level for some of the detectors in order to increase count of the events.

The results of off-line processing of data acquired by two single test pixels are shown in fig. 6.12. One of the pixels is STD 1.4mm and it is the largest pixel in the BD2 design that has “standard” NCH32xNN20 emitter layout configuration, another pixel is Pix400 and it is the smallest pixel in the design that has the same emitter layout as a former pixel. The measurements were done at 20 °C temperature with the source placed above the detectors at 13 mm height. The results were analyzed with a trigger fixed at 2.5 pC.

Before comparing these two pixels in terms of their performance it is necessary to

understand if the pixels preserved their electrical characteristics after the dicing and bonding steps. To that purpose we acquired a set of IV curves (emitter current vs. substrate voltage) under different temperatures like it is shown on fig. 6.11(a) and then made a comparison of I_e currents before and after dicing and bonding steps at 20 °C temperature. Figure 6.11(b) refers to the same data as fig. 6.11(a) but it shows I_e dependence vs. T just at 10 V collector bias. Such representation of data allows a convenient comparison of I_e before and after dicing and bonding, e.g., red points in fig. 6.11(b) are the emitter current values at 10 V bias acquired before wafer was diced, these values coincide with emitter current values acquired after bonding. Thus, a conclusion that the analyzed samples preserved their initial electrical characteristics can be done. It is important to make such tests before starting functional tests due to the strict dependence of BJT bias point on emitter current, and so, a proper comparison of samples in terms of their detection properties can be done only in case if their emitter currents did not change (or at least changed by the same factor).

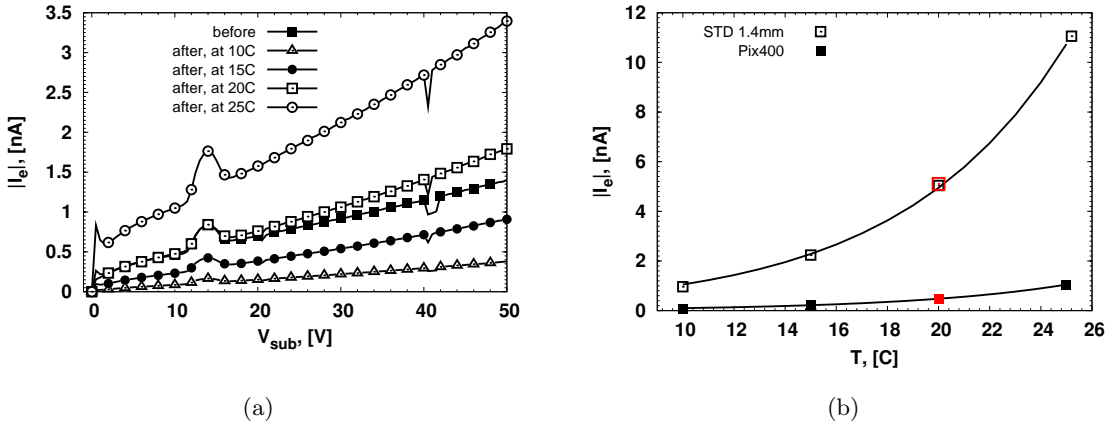


Figure 6.11: (a) - family of I_e vs V_{sub} curves acquired at different temperatures, the tested device was Pix400 (w7, die 73); (b) - dependence on temperature of emitter current measured at 10 V bias after the dicing and bonding, the tested devices are Pix400 and STD 1.4mm, red points show emitter current values at 10 V bias acquired before dicing.

Figure 6.12 shows the results of functional characterization of Pix400 and STD 1.4mm single test pixels. The distribution of Q_{coll} for STD 1.4mm device is shifted to higher values comparing to the distribution of Q_{coll} for Pix400 (the mean values of Gaussian fits are 26.8 pC and 35.7 pC for Pix400 and STD 1.4mm pixels correspondingly). That can be explained by higher overall gain for STD 1.4mm pixel comparing to the Pix400. It was found from the IV tests of these pixels that the quiescent gain value for STD 1.4mm is $\beta_{quiesc} = 195$ and for Pix400 $\beta_{quiesc} = 95$. Taking into account that the gain curves

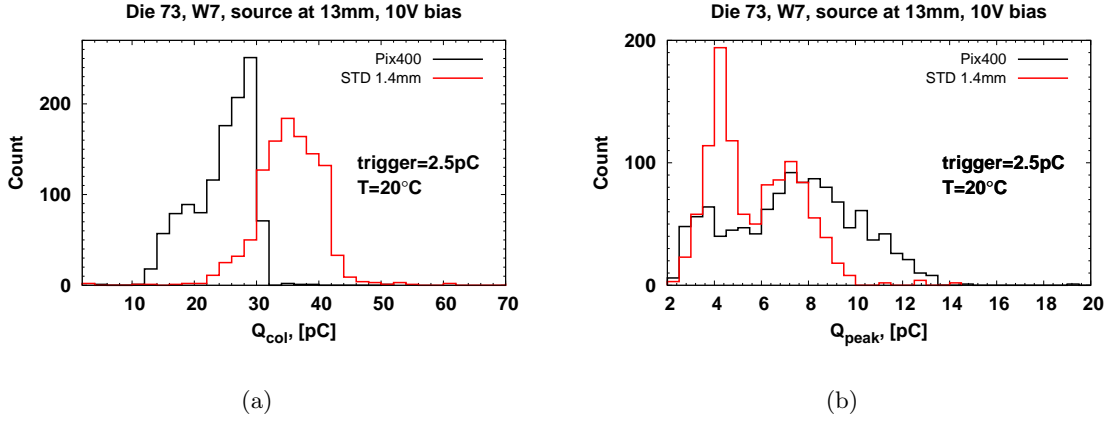


Figure 6.12: A comparison of the detection properties of two pixels that have the maximum and the minimum size of their bases. Emitter size is the same for both devices (NCH32xNN20). (a) - distributions of collected charge values; (b) - distributions of peak values.

for the devices with the same emitter and base layout³ but different base size practically coincide (refer, for example, to section 5.2 of Chapter 5) we may conclude that the overall gain of STD 1.4mm device is higher than the gain of Pix400 at least by 100; however, it can be even larger.

Figure 6.12(b) shows distributions of peak values Q_{peak} for the Pix400 and STD 1.4mm pixels. Differently from the distributions of Q_{coll} , pixel Pix400 has a shift of the distribution to the higher values comparing to the STD 1.4mm pixel. The explanation for that is rather obvious and is related to the base-collector capacitance C_{BC} of the pixels. Pixels that have same emitter and base layout but different base size have their C_{BC} proportional to the base size, i.e., larger pixel has larger C_{BC} and vice versa. Unfortunately, such dependence could not be derived using CV tests because of particularities of layout of single test BJT pixels that did not include individual guard rings around every single pixel but just a common guard ring for all pixels in the die. However, the results of functional tests shown in figures 6.12(b), 6.14, and 6.17 confirm that the capacitance of pixel is the main factor responsible for the Q_{peak} distributions.

This shift of mean value to higher Q_{peak} values influences choice of trigger value, for example, comparing charge values of the peaks that are higher than 8 pC for both pixels, we can find out that in the range from 8 to 14 pC Pix400 detects 361 particles more than STD 1.4mm pixel, which is 30% of overall amount of the events detected by STD 1.4mm during the time of the measurement. The second very interesting thing that was observed during this test is the presence of two types of events. The distributions contain two

³Same base layout means that two pixels have same p-well size and same overlap of p-plus and p-well implants.

peaks, this effect is strongly manifested for STD 1.4mm pixel and slightly less for Pix400 pixel. As it has been shown by laser tests the peak of lower charge can be assigned to the events happening on the periphery of the pixel and outside the pixel but within pixel's depletion region, while second peak is related to the events happening just within the boundaries of pixel.

6.2.2 Detection properties of the arrays

The previous section has described the results of functional characterization of single pixels. However, as it was shown in section 5.3 of Chapter 5 the IV characteristics of arrays of pixels are quite different from the characteristics of single test pixels, e.g., leakage current of single pixel Pix400 is 3 to 4 times higher than the leakage currents of array divided by number of pixels forming this array ($I_{e,single} = 0.46$ nA, for die 14 $I_{e/pix} = 0.11$ nA, for die 36 $I_{e/pix} = 0.145$ nA and for die 42 $I_{e/pix} = 0.12$ nA⁴). Thus, it is important to make as well a functional characterization of the arrays.

All arrays in the layout of BD2 batch can be divided onto two parts - large $1 \times 1 \text{ cm}^2$ and small $5 \times 5 \text{ mm}^2$ arrays (see section 4.2 for further details). The large arrays are intended to be used in radon monitoring/detection system, while small arrays were designed for the test purposes. The layout of the BD2 batch includes 16 test arrays. The results of characterization of each of these arrays will be presented in the current section.

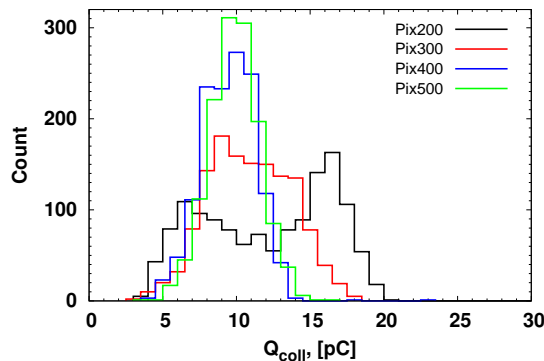


Figure 6.13: Functional characterization of Die 43 using ^{241}Am source of α -particles. The plots correspond to the $5 \times 5 \text{ mm}^2$ arrays with NCH20xNN14 emitter layout and $200 \times 200 \mu\text{m}^2$, $300 \times 300 \mu\text{m}^2$, $400 \times 400 \mu\text{m}^2$, and $500 \times 500 \mu\text{m}^2$ base areas. The plots refer to the distributions of collected charge values Q_{coll} acquired at 10 V bias; the temperature was fixed at 20 °C and the distance between detector and source (h_{ds}) was 13 mm.

Firstly test arrays with same emitter and base layout but different base size were

⁴It is still wafer w7.

tested. Fig. 6.13 and fig. 6.14 show the results of functional characterization of die 43, w7, which includes arrays with single pixels having NCH20xNN14 emitter layout and $200 \times 200 \mu\text{m}^2$, $300 \times 300 \mu\text{m}^2$, $400 \times 400 \mu\text{m}^2$, and $500 \times 500 \mu\text{m}^2$ (they are called **Pix200**, **Pix300**, **Pix400**, and **Pix500** correspondingly) base areas. The distributions of Q_{coll} are similar for **Pix300**, **Pix400** and **Pix500** arrays and mean values are ~ 10 pC, which is due to the similar values of quiescent gain, and so, the overall gain values are similar as well. Array **Pix200** has two peaks in the distribution with mean values ~ 6 pC and ~ 17 pC. Such properties of Pix200 could be explained only by higher overall gain. The IV tests shown in fig. 6.15 confirm that all arrays apart from **Pix200** preserved their initial IV characteristics after dicing and bonding. The leakage current of **Pix200** measured at 10 V collector bias has increased from 56 nA till 140 nA; therefore, the overall gain value increased and distribution of Q_{coll} has shifted to the higher values.

Fig. 6.14 refers to the distributions of peak values. Excluding array **Pix200** from the analysis, it is obvious that the mean value of every distribution shifts to the lower values while base size increases. These data directly confirm that the pixel with smaller base size, i.e., smaller base-collector capacitance C_{BC} have mean value of Q_{peak} distribution shifted to the higher values. Such behavior is desirable as it simplifies design of radon monitoring/detection system due to better signal-to-noise ratio, so trigger can be set to rather high value and system can be designed with rather relaxed requirements in terms of noise. The presence of two peaks in the distributions can be explained by incomplete depletion of interpixel volume; thus, a fraction of charge generated by α -particle is lost and total collected charge becomes smaller.

The results of functional characterization of die 44 (the die similar to previously tested die 43 but with NCH32xNN16 emitter layout instead of NCH20xNN14) are shown in fig. 6.16 and fig. 6.17. The leakage currents of all four arrays remained unchanged after the bonding step. So, a direct comparison of the arrays consisting of different base size pixels can be made. As it can be seen these arrays show similar properties as the arrays from die 43, i.e., with decreasing base size the mean value of Q_{peak} distribution is shifting to higher values and the mean values of Q_{coll} remain almost constant due to small difference in quiescent gain values. Hence, overall gain values as gain curves practically coincide for the pixels with same layout but different base size.

The obtained results are summarized in Table 6.1. Using this table a direct comparison of the arrays can be done. The arrays with smaller base size show larger μ_{peak} and FWHM_{peak} , μ_{coll} and FWHM_{coll} did not show dependence on the base size but on emitter layout, i.e., the devices NCH32xNN16 showed a shift of μ_{coll} to higher values comparing to the NCH20xNN14 devices, although, this dependence is not strongly manifested.

Quite interesting and unexpected results were acquired during functional characteri-

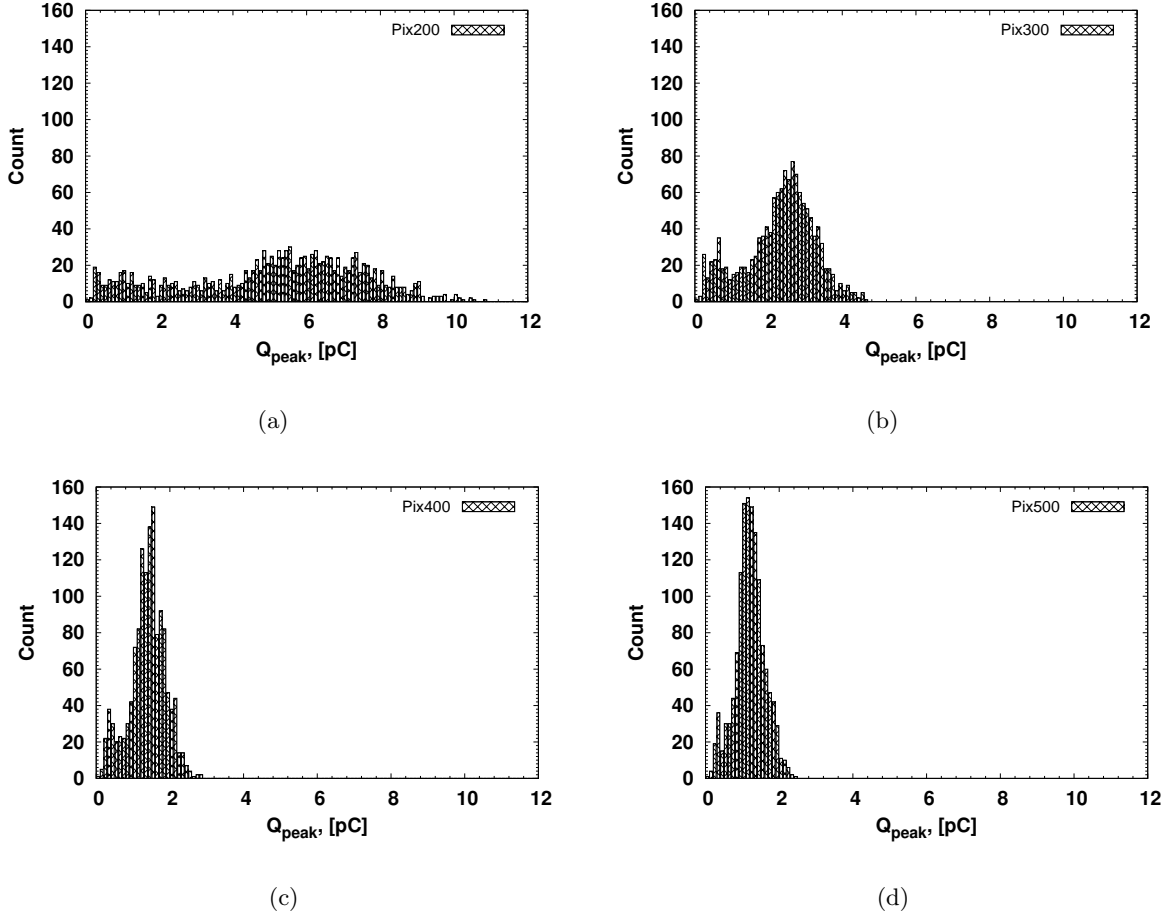


Figure 6.14: Functional characterization of Die 43 using ^{241}Am source of α -particles. The plots (a), (b), (c), and (d) correspond to the $5 \times 5 \text{ mm}^2$ arrays with NCH20xNN14 emitter layout and $200 \times 200 \mu\text{m}^2$, $300 \times 300 \mu\text{m}^2$, $400 \times 400 \mu\text{m}^2$, and $500 \times 500 \mu\text{m}^2$ base areas correspondingly (disposition of plots corresponds to the actual disposition of the arrays on the die). The plots refer to the distributions of collected charge peak values Q_{peak} acquired at $V_{bias} = 10 \text{ V}$, $T = 20 \text{ }^\circ\text{C}$, and $h_{ds} = 13 \text{ mm}$.

zation of die 45, w7. Fig. 6.18 presents the results of IV characterization of the samples versus temperature. The die includes four arrays with same NCH32xNN20 emitter layout. The **NCH32xNN20** arrays is an array consisting of “standard” pixels and it was included into layout for the reference purposes, the **NCH32xNN20 PW extend** is an array similar to **NCH32xNN20** but with p-well implant extended to the edge of the pixel. Fig. 6.18(a) shows emitter currents of the arrays vs. collector bias. As it can be seen, the arrays **NCH32xNN20** and **NCH32xNN20 PW extend** have similar emitter current values (-5.3 nA and -4.8 nA at 10 V collector bias and $20 \text{ }^\circ\text{C}$ temperature). Two

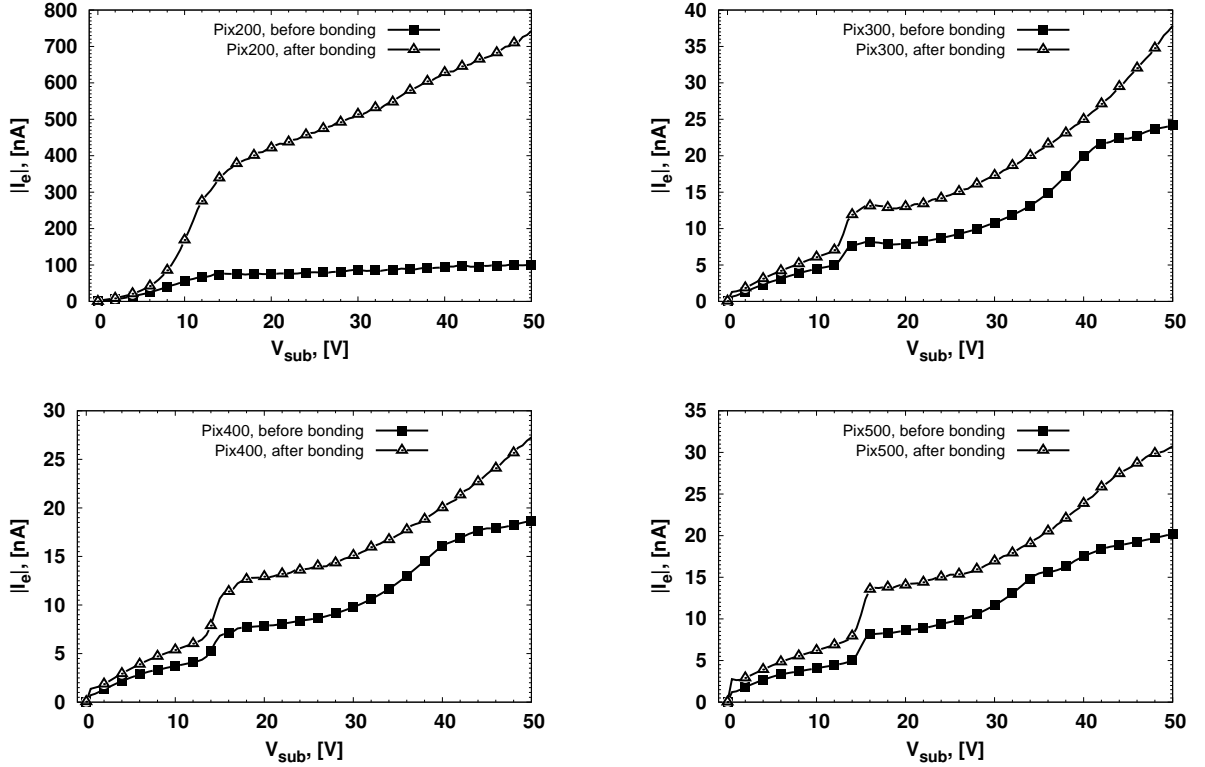


Figure 6.15: IV characterization of die 43, w7. The leakage current plots show that one of the arrays (Pix200) has changed its properties after dicing and bonding steps while other arrays have not changed their leakage currents (note the much wider scale used for the currents in case of Pix200).

	μ_{peak} , [pC]		FWHM $_{peak}$, [pC]		μ_{coll} , [pC]		FWHM $_{peak}$, [pC]	
	NCH20x	NCH32x	NCH20x	NCH32x	NCH20x	NCH32x	NCH20x	NCH32x
	NN14	NN16	NN14	NN16	NN14	NN16	NN14	NN16
Pix200	5.95	1.51	2.92	1.23	21.11	11.62	12.46	4.96
Pix300	2.58	1.23	1.06	1.01	10.83	11.42	7.30	4.19
Pix400	1.46	1.12	0.78	0.68	9.57	11.19	3.88	4.38
Pix500	1.21	1.02	0.65	0.59	9.89	11.46	3.26	3.49

Table 6.1: Summary results of functional characterization of die 43 (NCH20xNN14) and die 44 (NCH32xNN16). μ_{peak} , FWHM $_{peak}$, μ_{coll} , and FWHM $_{coll}$ are the mean values and FWHMs of Q_{peak} and Q_{coll} distributions correspondingly. The values in a bold font characterize device with leakage currents increased after dicing and bonding steps.

other arrays **NCH32xNN20 PP FR** and **NCH32xNN20 PP FR small** have a maximum $1 \times 1mm^2$ size of p-well but p-plus implant is either around emitter and p-well or just around emitter. The **NCH32xNN20 PP FR** array has the emitter current $I_e@10V$

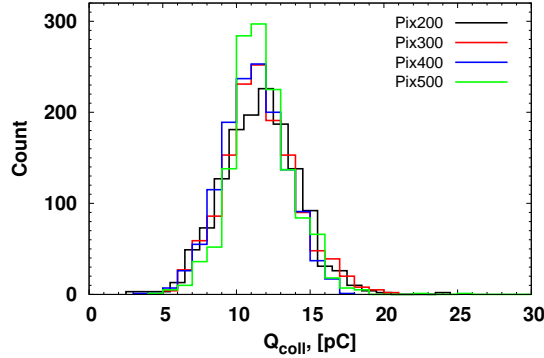


Figure 6.16: Functional characterization of Die 44 (W7) using ^{241}Am source of α -particles. The plots correspond to the $5 \times 5 \text{ mm}^2$ arrays with NCH32xNN16 emitter layout and $200 \times 200 \mu\text{m}^2$, $300 \times 300 \mu\text{m}^2$, $400 \times 400 \mu\text{m}^2$, and $500 \times 500 \mu\text{m}^2$ base areas. The plots refer to the distributions of collected charge peak values Q_{peak} acquired at $V_{bias} = 10 \text{ V}$, $T = 20 \text{ }^\circ\text{C}$, and $h_{ds} = 13 \text{ mm}$. (The leakage currents of all four arrays remained unchanged after the bonding step.)

= -16.5 nA and the **NCH32xNN20 PP FR small** array has the largest value of emitter current, $I_e@10V = -60.3 \text{ nA}$. All these arrays preserved their IV properties after the dicing and bonding steps were done (refer to fig. 6.18).

The results of α -particle tests are presented in fig. 6.19. The “standard” **NCH32xNN20** array is the reference array for this test die and also for this wafer as the IV characteristics of the array did not degrade unlike a similar array from die 24. As it was already mentioned in section 5.2 of Chapter 5 (see fig. 5.10), due to the fact that the surface current component in the base of BJT pixel is not suppressed by a p+ implant the leakage current of **NCH32xNN20 PP FR** and **NCH32xNN20 PP FR Small** arrays is higher and, hence, the quiescent and overall gain values are much higher than for **NCH32xNN20** and **NCH32xNN20 PW extend** arrays as well. This is why, the arrays with a p-plus frame have shown noticeably larger mean values both for distributions of collected charge values and for distributions of peak charge values. The data has been summarized into Table 6.2. Therefore, we can conclude that absence of p+ surface current suppressing implant inside the pixel causes increase of current flowing through the base, and so, it causes increase of emitter current, quiescent and overall gain values. Thus, this layout configuration can be considered as another method of BJT biasing⁵. The method can be used to move μ_{coll} and μ_{peak} to higher values. Simple calculations show that if arrays **NCH32xNN20 PP FR** and **NCH32xNN20 PP FR Small** were $1 \times 1 \text{ cm}^2$ large (7×7 array of pixels) the emitter currents would be 90 nA and 328 nA respectively, which is

⁵In fact, it is a self-biasing method.

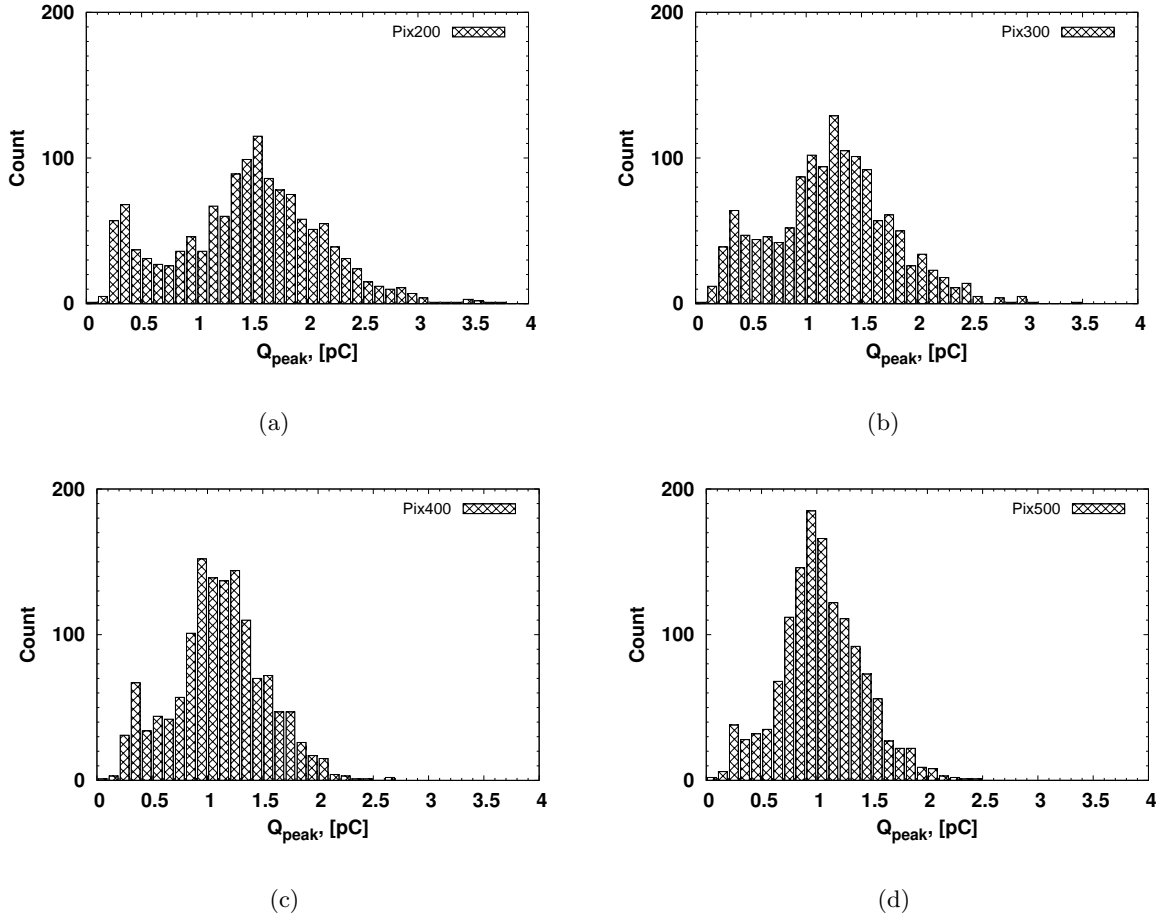


Figure 6.17: Functional characterization of die 44, w7 using ^{241}Am source of α -particles. The plots (a), (b), (c), and (d) correspond to the $5 \times 5\text{mm}^2$ arrays with NCH32xNN16 emitter layout and $200 \times 200\mu\text{m}^2$, $300 \times 300\mu\text{m}^2$, $400 \times 400\mu\text{m}^2$, and $500 \times 500\mu\text{m}^2$ base areas correspondingly (disposition of plots corresponds to the actual disposition of the arrays on the die). The plots refer to the distributions of collected charge peak values Q_{peak} acquired at $V_{bias} = 10\text{ V}$, $T = 20\text{ }^\circ\text{C}$, and $h_{ds} = 13\text{ mm}$. (The leakage currents of all four arrays remained unchanged after the bonding step.)

still much smaller than the range of DDC114 - 875 nA (350 pC range, 400 μs integration time).

After we found a dependence of detection properties of BJT arrays on the base size of a single pixel a set of tests was implemented in order to find how detection properties of BJT arrays depend on emitter layout of a single pixel. The die 24 (or die 65⁶) contains

⁶There are four $5 \times 5\text{mm}^2$ additional test dies on the edge of the wafer (dies 81, 82, 83, 84) that correspond to NCH32xNN20, NCH18xNN11, NCH32xNN15, and NCH32xNN11 arrays. However, these dies were

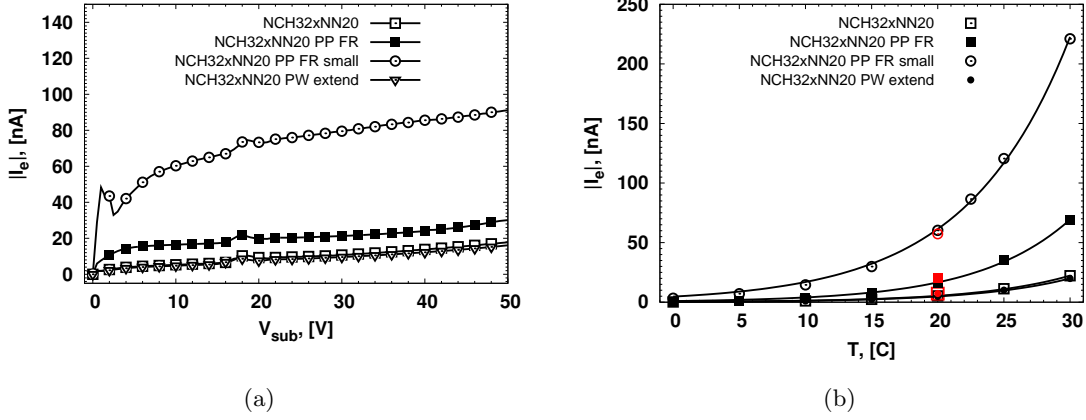


Figure 6.18: IV characterization of die 45, w7. (a) - leakage currents of the arrays after the bonding step; (b) - leakage currents of the arrays at 10 V collector bias measured versus temperature. The red symbols are I_e values acquired before the bonding was made.

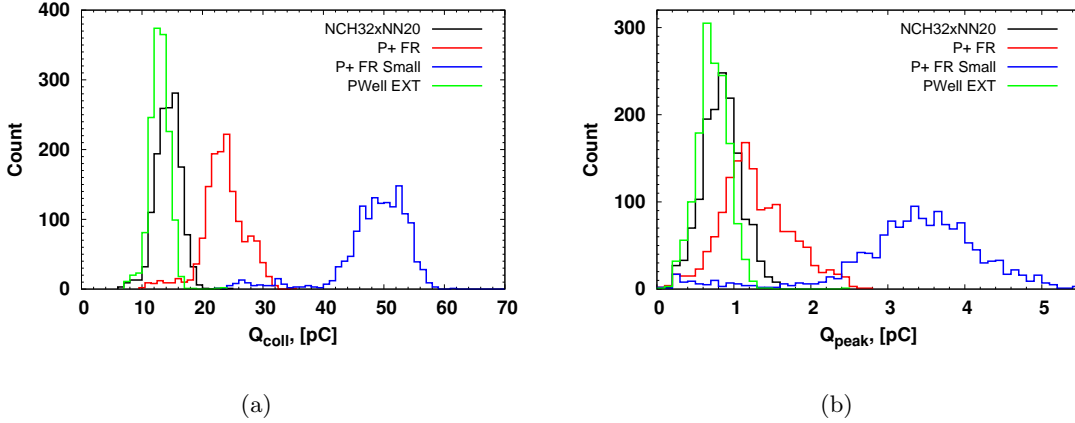


Figure 6.19: Functional characterization of die 45, w7 using ^{241}Am source of α -particles. All arrays have same emitter layout but different base layout. For further details on layout refer to section 4.2, p. 67. (a) - shows distributions of collected charge values Q_{coll} ; (b) - shows distributions of collected charge peak values Q_{peak} . The data were acquired at $V_{bias} = 10$ V, $T = 20$ C, and $h_{ds} = 13$ mm.

four arrays with NCH32xNN20, NCH18xNN11, NCH32xNN15 and NCH32xNN11 emitter layout configurations. The electrical properties of corresponding single pixels have been already presented in fig. 5.9. Unfortunately, a single NCH32xNN15 pixel forming the NCH32xNN15 array has not been included into the layout of a test die with single

not diced as it required different from existing dicing pattern.

Array	μ_{peak} , [pC]	$FWHM_{peak}$, [pC]	μ_{coll} , [pC]	$FWHM_{peak}$, [pC]	$ I_e@10V $, [nA]
NCH32xNN20	0.84	0.47	14.43	4.05	5.3
NCH32xNN20 PP FR	1.20	0.73	22.32	4.82	16.5
NCH32xNN20 PP FR Small	3.78	1.19	50.00	7.94	60.3
NCH32xNN20 PW extend	0.73	0.40	12.97	2.91	4.8

Table 6.2: Summary results of functional characterization of die 45. μ_{peak} , $FWHM_{peak}$, μ_{coll} , and $FWHM_{coll}$ are the mean values and FWHMs of Q_{peak} and Q_{coll} distributions correspondingly. Emitter current values have been acquired at 10 V collector bias and 20 °C.

test BJT pixels. So, in this case no direct comparison between performance of a single pixel and array can be done; however, the data acquired while testing NCH32xNN20 and NCH32xNN11 single pixels can be used to predict approximate electrical properties of NCH32xNN15 single pixel and, finally, compared to the performance of the array.

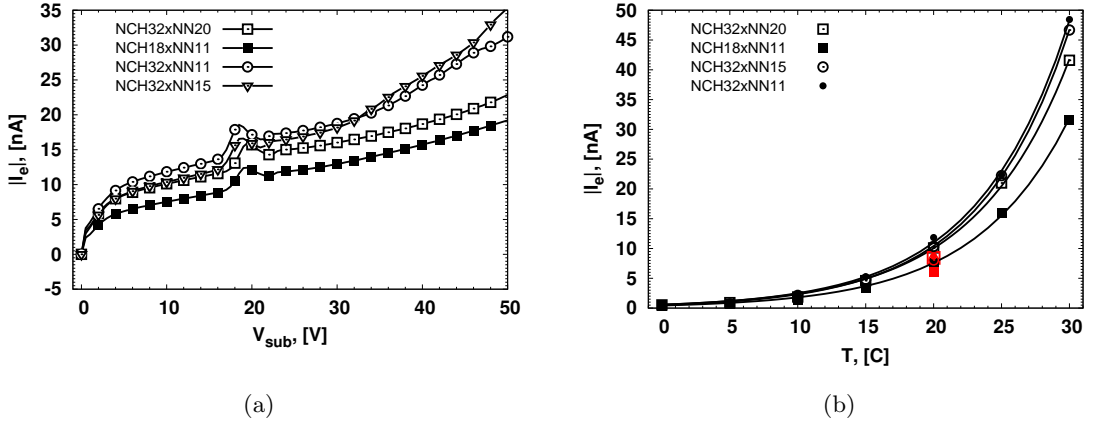


Figure 6.20: IV characterization of die 24 (w7) after dicing and bonding steps. (a) - leakage currents of the arrays; (b) - leakage currents of the arrays at 10 V collector bias measured versus temperature. The red symbols are I_e values acquired before the dicing and bonding were made.

The IV characterization of die 24 after the dicing and bonding were done showed that all four arrays increased their emitter current values. The emitter current of **NCH32xNN20** array increased by factor 1.19 and I_e currents of **NCH18xNN11**, **NCH32xNN15**, and **NCH32xNN11** increased by the same factor ~ 1.26 . Such increase of emitter currents caused increase of quiescent gain values from $\beta_{quiesc} = 50$ till $\beta_{quiesc} = 75$ for **NCH32xNN20**, from $\beta_{quiesc} = 20$ till $\beta_{quiesc} = 50$ for **NCH18xNN11** and from $\beta_{quiesc} = 90$ till $\beta_{quiesc} = 110$ for **NCH32xNN11**. That means that overall gain values before

and after the dicing and bonding steps will not differ much, and so, the arrays can be compared in terms of their detection properties despite the fact that the samples changed their emitter currents.

The results of functional characterization of die 24 are shown in fig. 6.21 and the summary results are presented in Table 6.3. There is no much difference between detection properties of **NCH32xNN20**, **NCH32xNN15**, and **NCH32xNN11**, which have almost coinciding gain curves in the range of base potentials from 0 V to ~ 0.36 V (refer to fig. 5.9). However, there is an obvious difference between **NCH18xNN11** and other arrays, single pixel NCH18xNN11 has lower gain, hence, the distribution of Q_{coll} is shifted to lower charge values. Similar behavior has the distribution of Q_{peak} that confirms that lower gain of NCH18xNN11 pixel prevails over low base-emitter capacitance of the pixel.

Array	μ_{peak} , [pC]	$FWHM_{peak}$, [pC]	μ_{coll} , [pC]	$FWHM_{coll}$, [pC]	$ I_e@10V $, [nA]
NCH32xNN20	1.58	0.68	24.75	5.12	10.1
NCH18xNN11	1.24	0.52	18.33	3.88	7.54
NCH32xNN15	1.45	0.75	23.08	6.26	10.4
NCH32xNN11	1.50	0.69	24.81	6.29	11.8

Table 6.3: Summary results of functional characterization of die 24. μ_{peak} , $FWHM_{peak}$, μ_{coll} , and $FWHM_{coll}$ are the mean values and FWHMs of Q_{peak} and Q_{coll} distributions correspondingly. Emitter current values have been acquired at 10 V collector bias and 20 °C.

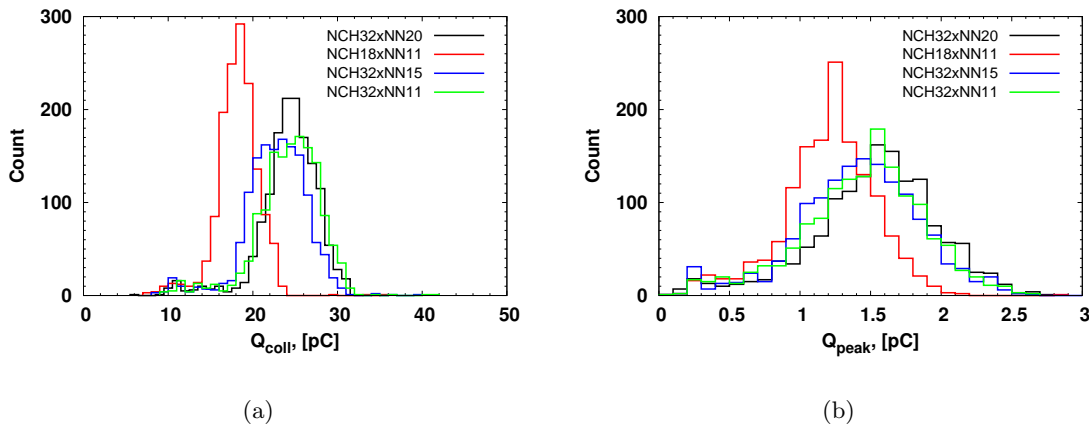


Figure 6.21: Functional characterization of die 24 (w7) using ^{241}Am source of α -particles. All arrays have same base layout but different emitter layout. (a) - shows distributions of collected charge values Q_{coll} ; (b) - shows distributions of collected charge peak values Q_{peak} . The data were acquired at $V_{bias} = 10$ V, $T = 20$ °C, and $h_{ds} = 13$ mm.

As it has been already mentioned, wafers from the “thinned” splitting observed quite non-uniform lifetime profiles; the lifetimes for w11, which showed good electrical properties of the detectors, varied from 0.42 ms till 32.10 ms (refer to Table 5.1 for additional data). Functional tests of die 24, w11, presented in fig. 6.22 have shown that there is no dependence on emitter layout. All arrays have high quiescent gains due to high emitter currents and, hence, the arrays have high quiescent and overall gain values. This is why the mean values of the Q_{coll} and Q_{peak} distributions acquired while testing die 24, w11, are shifted to much higher charge values in comparison to the analogous values acquired while testing die 24, w7.

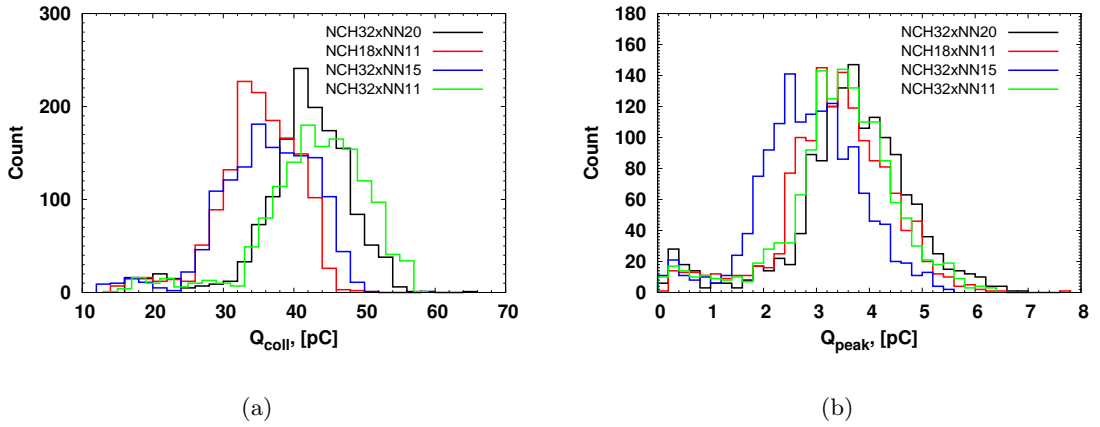


Figure 6.22: Functional characterization of die 24 (W11) using ^{241}Am source of α -particles. All arrays have same base layout but different emitter layout. (a) - shows distributions of collected charge values Q_{coll} ; (b) - shows distributions of collected charge peak values Q_{peak} . The data were acquired at $V_{bias} = 10$ V, $T = 20$ °C, and $h_{ds} = 13$ mm.

6.2.3 The tests with an array of pixels in the temperature range from 0 °C to 30 °C

All previously presented results and data were acquired at a constant temperature $T = 20$ °C. This temperature is very close to the lowest boundary of thermal comfort zone, which for office environment in the summer is between 23.5 and 25.5 °C and in the winter is between 21.0 and 23.0 °C [78]. In order to verify how detection properties of BJT detectors depend on temperature and which characteristics of the detectors (leakage currents, gain, C_{BE}) change most when the ambient temperature changes in rather wide range we have carried out a set of functional tests using **NCH32xNN20** array from the die 24, w7.

The ^{241}Am source was placed at the same height $h_{sd} = 13$ mm. Energy of α -particles

hitting the detector can be calculated according to the algorithm presented in [79]. According to the calculations the initial energy of particle with 5.49MeV should drop till 2.44 MeV after passing 13 mm in air at 20 °C temperature. The results of functional characterization are presented in fig. 6.23. Fig. 6.23(a) refers to the distributions of collected charge values Q_{coll} acquired at different temperatures in a range from 0 °C till 30 °C with 5 °C step. Fig. 6.23(b) refers to the distributions of Q_{peak} , which were acquired under the same conditions as Q_{coll} .

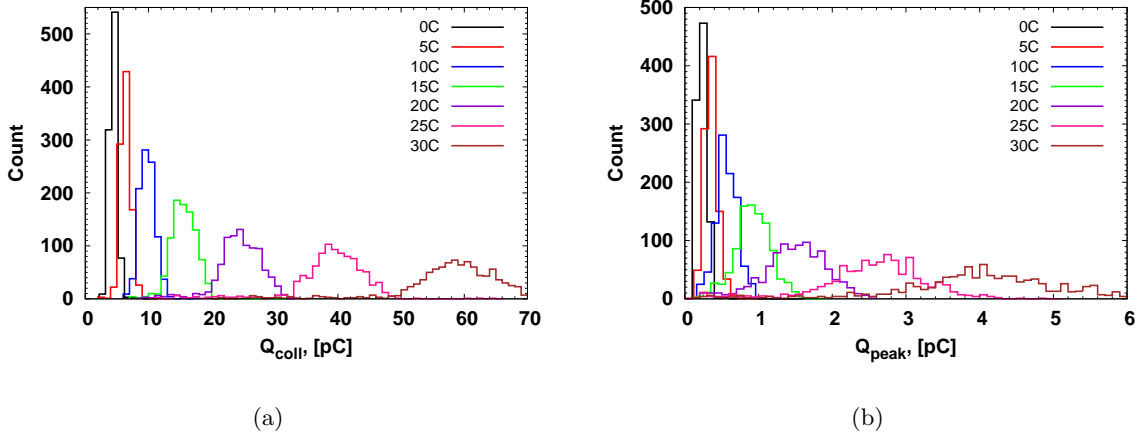


Figure 6.23: Test of **NCH32xNN20** array from die 24, w7 in a wide temperature range (the distance between source and the array was 13 mm): (a) - distribution of collected charge values; (b) - distribution of peak values.

After the Q_{coll} and Q_{peak} distributions were acquired and built the gaussian fits of them were made. The mean values of the gaussian fits are shown in fig.6.24. Along with the original data exponential fits of these data are presented as well. At least two factors can influence such exponential behavior: leakage current that depends exponentially on temperature (thus, base potential has similar dependence on temperature) and base-emitter capacitance.

In order to disentangle these effects we elaborated theoretical results presented in [59]; thus, an approximate evaluation of how I_e and C_B depend on temperature could be done. So, according to [59], the total collected charge S can be expressed as:

$$\begin{aligned}
 \Delta I_e(t) &= (\beta Q_0 / \tau) e^{-t/\tau} \\
 S &= \int_0^t (\beta Q_0 / \tau) e^{-t/\tau} dt = \left(\frac{\beta Q_0}{\tau} \right) (-\tau) e^{-t/\tau} \Big|_0^t \\
 S &= -\beta Q_0 e^{-t/\tau} + \beta Q_0 = \beta Q_0 (1 - e^{-t/\tau})
 \end{aligned} \tag{6.2}$$

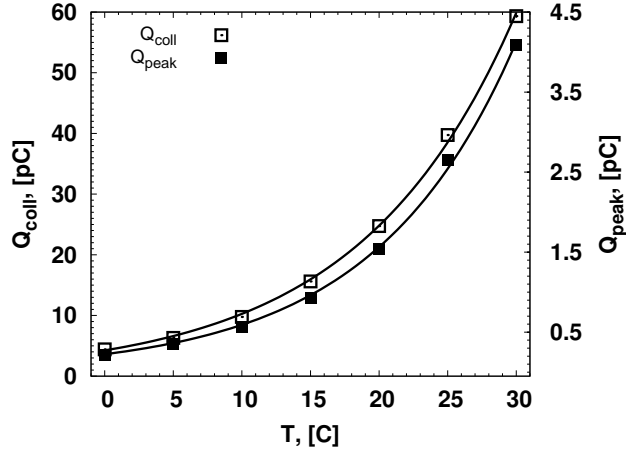


Figure 6.24: Mean values of the gaussian fits of Q_{coll} (left y-axis) and Q_{peak} (right y-axis) distributions collected under different temperatures. The exponential fit of the peak mean values is $Q_{peak,mean} = 0.224 \cdot e^{T/10.298}$ and the exponential fit of the charge mean values is $Q_{coll,mean} = 4.253 \cdot e^{T/11.343}$.

where βQ_0 is an overall collected charge that is equal to S when t is large, the value of βQ_0 is known from the experiment (it is mean value of Q_{coll}). If the charge collected during a shorter time was also known the time delay constant τ could be calculated. Q_{peak} distributions can be used to that purpose. Q_{peak} is a charge collected by DDC114 during a single and first after α -particle hit integration period of $400\mu s$. Using this definition of Q_{peak} we can derive time delay constant τ and base capacitance C_B .

$$\begin{aligned}
 Q_{peak} &= \beta Q_0 (1 - e^{-\frac{0.4ms}{\tau}}), Q_{coll} = \beta Q_0 \\
 \tau &= -\frac{0.4}{\ln(1 - \frac{Q_{peak}}{Q_{coll}})} \\
 C_B &= \frac{\tau \cdot I_L}{kT/q} = \frac{\tau}{kT/q} \cdot \frac{I_e}{\beta}
 \end{aligned} \tag{6.3}$$

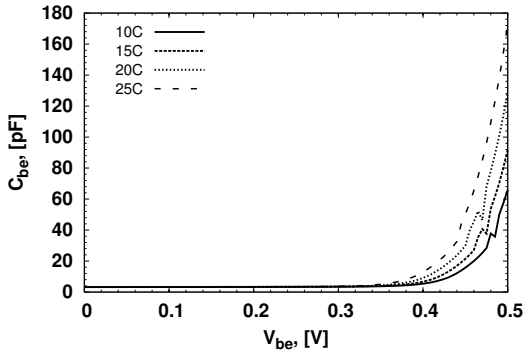
Equations (6.3) show relationships for the time delay constant τ and base capacitance C_B . Obviously, in order to calculate C_B the overall gain of the detector should be known. The β values can be, in principle, calculated as a ratio between charge generated in Si Q_0 and collected charge Q_{coll} , where Q_0 can approximately be estimated for the known distance between the source and the detector ($h_{ds} = 13$ mm). The summary results are presented in Table 6.4.

Thus, considering summary data presented in Table 6.4 we could conclude which parameter of the detector changes faster than other parameters when the temperature

T, [°C]	$Q_{peak,mean}$, [pC]	$Q_{coll,mean}$, [pC]	τ , [ms]	$ I_e $, [nA]	$\Delta I_e(0)$, [nA]	Q_0 , [pC]	β	C_B , [pF]
0	0.22035	4.413	7.81	0.539	0.565	0.1026	43	4.15
5	0.34633	6.309	7.08	9.08	0.890	0.1041	60	4.42
10	0.56327	9.762	6.73	1.86	1.450	0.1055	92	5.55
15	0.93116	15.611	6.5	4.61	2.400	0.1069	146	8.25
20	1.5354	24.731	6.24	10.1	3.963	0.1083	228	10.9
25	2.652	39.748	5.79	21.0	6.862	0.1096	363	13.0
30	4.0836	59.335	5.61	41.6	10.577	0.1109	535	16.7

Table 6.4: Summary results of functional and electrical characterization of the **NCH32xNN20** array consisting of $1 \times 1 \text{ mm}^2$ pixels in a wide temperature range. The collector bias was 10 V, the distance between source and detector was 13 mm. The values of $Q_{peak,mean}$, $Q_{coll,mean}$, and $|I_e|$ were measured, while τ , $\Delta I_e(0)$, β , and C_B were calculated.

conditions change. As we can see, the emitter current of the array at 30 °C is ~ 70 times larger than I_e at 0 °C, while calculated capacitance changes just by factor of ~ 4 under the same test conditions.



(a)

V_{sub} , [V]	V_b , [V]	β_{quiesc}	C_B , [pF]
10	0.295	53	3.45
15	0.304	80	3.52
20	0.308	120	3.63
25	0.314	155	3.87

(b)

Figure 6.25: (a) Base-emitter capacitance of single NCH32xNN20 pixel with $800 \times 800 \text{ }\mu\text{m}^2$ base size measured at different temperatures. (b) - summarized data.

Additional electrical characterization of similar test pixels (see fig. 6.25) with bonded emitter and base contacts has shown that the base-emitter capacitance changes much less (it is less than 1pF for the given temperature range). Thus, taking into account results of functional tests, calculations and CV measurements we can conclude that the most relevant parameter that most influences detection properties of the detector, while temperature changes, is emitter current (or collector current) of the detector.

6.3 Radon tests

Finally, after functional tests confirmed that BJT detectors from the BD2 batch properly detected α -particles, we tested a complete monitoring system in the radon chamber available at ENEA Radioprotection Institute (Italy). The system consisted of an **STD_Pixels_400_NCH32xNN20** detectors and a microcontroller based electronics, one of the versions of this readout has been presented in [7].

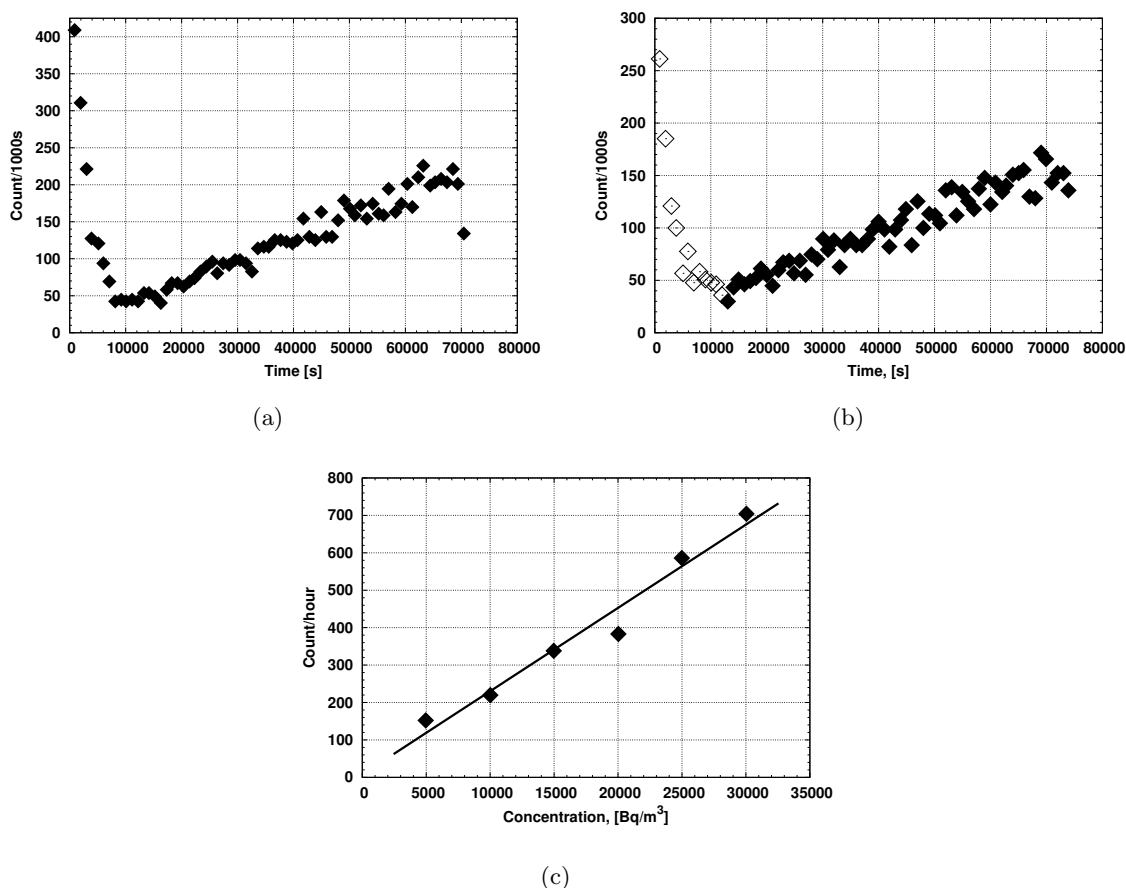


Figure 6.26: Radon test. (a) - data acquired using a **STD_Pixels_400_NCH32xNN20** detector coupled to microcontroller based readout electronics [7]; (b) - data acquired using a calibrated continuous radon monitor; (c) - calibration curve for the developed system.

Figure 6.26 shows the results of radon test [80] that was carried out at ENEA-IRP. The radon concentration varied over the time. Plot 6.26(a) refers to the data acquired by the developed system on the base of BJT detector, while plot 6.26(b) refers to the data acquired by the calibrated radon monitor. As it can be seen, the developed radon monitoring system shows very similar behavior to the calibrated radon monitor confirming

that it can be successfully used for the monitoring. Fig. 6.26(c) shows a calibration curve that was extracted from the plots 6.26(a) and 6.26(b). Using this curve, behavior of the developed radon monitor can be predicted even for very low radon concentrations.

6.4 Summary

In this chapter we have presented and discussed the results of functional characterization of BJT detectors, which included laser and α -particle tests.

Laser tests allowed us to verify functionality of BJT detectors and their detection properties. It has been shown that the detectors amplify charge generated by α -particles by overall gain value much higher than quiescent gain value. It means that detectors are properly biased by incoming particles, when the detector is operated with floating base. Also laser characterization of the arrays consisting of rather small pixels (**Pix200**, **Pix300**, **Pix400** and **Pix500**) has explained low energy “tails” in some of the collected distributions of Q_{coll} . The effect appears due to incomplete depletion of interpixel volume. Thus, boundaries of the pixels and interpixel areas observed a decrease of Q_{coll} values due to the partial losses of generated charge in incompletely depleted regions.

Alpha-particle tests were used to test performance of single BJT pixels and BJT arrays as well. Characterization of single pixels confirmed that pixels with larger base area have higher quiescent, and so, overall gain values. Thus distributions of collected charge values Q_{coll} are shifted to higher charge values, while distributions of peak values Q_{peak} are shifted to lower charge values comparing to the same distributions acquired using smaller single pixels. Therefore, if the algorithm used for the calculation of radon concentration is based on α -particle counting instead of α -rays spectrometry it is better to have arrays of BJT pixels with smaller base size due to the higher Q_{peak} values allowing use of trigger with higher value. Also due to the spread of depletion region of single pixel farther than it would be in case of an array of pixels, the leakage current and, hence, quiescent and overall gain value are much higher than in case of an array of pixels. This is why new versions of layout should have a modified layout of test dies with single BJT pixels. Each test single BJT pixel should be surrounded by a guard ring.

Alpha-particle characterization of BJT arrays allowed extracting dependence of detection properties of the tested arrays on layout of a single pixel. This characterization showed that arrays **NCH32xNN20** and **NCH32xNN20 PW extend** observed similar Q_{coll} and Q_{peak} distributions, which means that the size of p-well implant does not influence strongly the detection properties of BJT arrays. Functional characterization of the arrays **Pix200**, **Pix300**, **Pix400**, and **Pix500** from dies 43 and 44 has confirmed that the arrays with smaller pixel size would be preferable to be included into the next

layouts due to the higher mean values of Q_{peak} distributions and almost the same mean values of Q_{coll} distributions. Such effect has been explained by smaller base-collector C_{BC} capacitance of smaller pixels. C_{BC} is a constituent of overall base capacitance C_B ; thus, due to smaller C_B pixels with smaller base size have mean values of Q_{peak} distributions shifted to the higher values. Another method of shifting μ_{coll} and μ_{peak} (mean values of Q_{coll} and Q_{peak} distributions) to much higher values was discovered during testing of the arrays from die 45, w7. Absence of p+ implant in single pixels forming **NCH32xNN20 PP FR** and **NCH32xNN20 PP FR small** causes increase of current flowing through the base, thus, emitter current, quiescent and overall gain values considerably increase as well. So, μ_{coll} and μ_{peak} shift to the higher charge values. The layout configuration of these arrays can be considered as another method of BJT biasing.

The arrays from die 24, w7 have been extensively characterized. Firstly, we concluded that preferable emitter layout configurations are NCH32xNN20, NCH32xNN15 or NCH32xNN11 due to the high gain values. Testing **NCH32xNN20** array in a wide range of temperatures allowed us to conclude that emitter current among few parameters that influence detection properties of the detector when temperature changes is the most relevant parameter.

Finally, radon tests using an **STD_Pixels_400_NCH32xNN20** detector coupled to microcontroller based electronics were performed at ENEA Radioprotection Institute (Italy). The data acquired by the developed radon monitor were similar to the data acquired by the calibrated monitor confirming that the developed system works properly. However, even better performance of the developed radon monitor can be achieved by additional improvement of collection of radon progeny.

Conclusions

This work has been devoted to the development, design and implementation of BJT detector and its readout electronics specifically suited for α -particle detection and radon monitoring. Experimental and theoretical analysis of samples of non-optimized BJT detectors available at the beginning of this research activity underlined advantages and limitations of BJT detectors. On one hand, these detectors have high dynamic gain, can operate in self-biasing mode (floating base operation mode) if being used for α -particle detection, hence, they do not require complicated readout electronics. On the other hand, BJT detectors have limitations considering rate and noise performance. Thus, we concluded that best possible applications for the device were those that do not require high resolution and low noise but for which simplicity and cost are rather considered of higher priority, i.e., radon monitoring/detection systems. Survey of existing radon monitoring techniques indicated possible niches for the use of BJT detector in integrating (dosimeters) and continuous radon monitoring systems due to a good detection efficiency, low power consumption, well established fabrication process at FBK (Trento, Italy), and possibility to be used with simple and, hence, low cost readout electronics.

Using samples of non-optimized detectors from the BD1 batch we have performed laser and α -particle functional tests. Laser tests have confirmed that pixels with either “standard” NCH32xNN20 emitter layout or minimum size NCH18xNN11 emitter layout can efficiently be used for α -particle detection while being operated with a floating base. Functional α -particle tests were performed using analog and digital (ALPHADET) readouts. The acquired results confirmed that pixels both with NCH32xNN20 (DPIX pixel) and NCH18xNN11 (BPAD pixel) emitter layout are “turned on” by an α -particle. Therefore, taking into account all results of the tests, we drew some important conclusions about layout of the pixel that became a basic pixel in the next, so-called, BD2 batch of the detectors. The pixel has been called as a “standard”; it has minimum size p-well implant to obtain minimum base capacitance and NCH32xNN20 emitter layout configuration to ensure high gain values at low base currents.

In parallel to the layout design of BD2 batch, we have designed and implemented a new FPGA-based readout electronics specifically fit for BJT detectors. The system

is completely compatible with previously designed microcontroller based readouts. This compatibility provided a convenient possibility to use ALPHADET readout for the laboratory tests (e.g., temperature dependence of detection properties of BJT detectors, efficiency of the detectors, etc.) and then to use microcontroller-based systems for the field tests in a radon chamber. Electrical characterization of ALPHADET board showed good linearity and good noise performance. Finally, functional tests of the detectors from BD1 and BD2 batches coupled to ALPHADET confirmed effectiveness of this electronics.

After the fabrication of the new batch of BJT detectors was finalized a set of electrical tests was performed. These tests aimed at verifying fabrication process characteristics, i.e, extraction of process parameters that most influence BJT performance and also at estimation of such properties of BJT as gain, leakage current and base potential at particular collector bias etc. Data acquired using test structures basically confirmed those characteristics of the fabrication process that were observed in the previous BD1 batch. Moreover, some properties were even better, e.g., longer generation lifetimes, lower substrate doping concentration, lower full depletion voltages, smaller surface recombination velocity, smaller charge oxide density and good uniformity of these properties.

The BD2 batch was divided onto three splittings, which had rather different properties of silicon. The “poly” splitting had the best properties in terms of low leakage currents, high gain values and good uniformity of amplification properties of the pixels. Thus, we concluded that detectors from these wafers could be considered for the use in radon monitoring systems. Further electrical characterization (Gummel plots, base potential and collector current vs. collector bias, base-emitter) confirmed that all fabricated BJT detectors feature good gain properties (low quiescent gain values and high maximum gain values).

Finally, the detectors from the new BD2 batch were functionally characterized using laser and α -particle tests. These tests were used to test performance of both single BJT pixels and BJT arrays. We concluded that pixels with smaller base size would be preferred to be included into the layout of next batches due to smaller C_{BC} capacitance that preserves higher signal amplitudes. Dependence of the detection properties of the arrays on the pixel layout has been tested as well. NCH32xNN20 and NCH32xNN11 emitter layouts resulted in the detectors with high gain values. The arrays with different p-well size observed similar properties indicating that the detection properties of BJT arrays were not strongly influenced by the size of p-well implant but by the size of p+ implant. The results of radon tests performed at ENEA Radioprotection Institute (Italy) that were acquired using an **STD_Pixels_400_NCH32xNN20** detector confirmed that it can be successfully used in systems for radon monitoring.

Bibliography

- [1] R. Firestone, *Table of Isotopes CD-ROM Edition, Version 1.0. (Ed V.S. Shirley, CD-ROM Ed S.Y. Frank Chu)*. Wiley-Interscience, 1996.
- [2] H. ERNBO, *Minimum Detectable Amount of Radon Progeny in Outdoor Air*. PhD thesis, KTH Royal Institute of Technology, 2006.
- [3] R. Turchetta, J. Berst, B. Casadei, G. Claus, C. Colledani, W. Dulinski, Y. Hu, D. Husson, J. L. Normand, J. Riester, G. Deptuch, U. Goerlach, S. Higuere, and M. Winter, “A monolithic active pixel sensor for charged particle tracking and imaging using standard VLSI CMOS technology,” *Nuclear Instruments and Methods in Physics Research Section A: Accelerators, Spectrometers, Detectors and Associated Equipment*, vol. 458, no. 3, pp. 677 – 689, 2001.
- [4] “Quad Current Input, 20-bit Analog-To-Digital Converter, DDC114 datasheet.” <http://www.ti.com/product/ddc114>.
- [5] “D400FC InGaAs Fiber Optic Photo Detector.” <http://www.thorlabs.de/Thorcat/2100/2121-s01.pdf>.
- [6] “TDS3000B Series Digital Phosphor Oscilloscopes.” <http://www.tek.com/>.
- [7] L. Rovati, G. Verzellesi, M. Bonaiuti, L. Bidinelli, D. Saguatti, G.-F. Dalla Betta, V. Tyzhnevyyi, N. Zorzi, and S. Bettarini, “A 2.4-GHz wireless alpha-ray sensor for remote monitoring and spectroscopy,” in *Instrumentation and Measurement Technology Conference (I2MTC), 2010 IEEE*, pp. 821 –824, May 2010.
- [8] “Thorlabs.” <http://www.thorlabs.com>.
- [9] NRC (National Research Council), *Health effects of exposure to radon*. National Academic Press, Washington, D.C., 1999.
- [10] V. Tyzhnevyyi, G. Batignani, L. Bosisio, G.-F. Dalla Betta, G. Verzellesi, and N. Zorzi, “Laser and alpha particle characterization of floating-base BJT detector,” *Nuclear*

Instruments and Methods in Physics Research Section A: Accelerators, Spectrometers, Detectors and Associated Equipment, vol. 617, no. 1-3, pp. 593 – 595, 2010.

- [11] L. Rovati, G. Verzellesi, M. Bonaiuti, G. Batignani, L. Bosisio, G.-F. Dalla Betta, G. Giacomini, C. Piemonte, and N. Zorzi, “Radon alpha-ray detector based on a high-resistivity-silicon bjt and a low-cost readout electronics,” in *Instrumentation and Measurement Technology Conference Proceedings, 2008. IMTC 2008. IEEE*, pp. 1403 –1406, may 2008.
- [12] V. Tyzhnevyyi, G.-F. Dalla Betta, L. Rovati, G. Verzellesi, and N. Zorzi, “BJT detector with FPGA-based read-out for alpha particle monitoring,” *Journal of Instrumentation*, vol. 6, no. 01, p. C01051, 2011.
- [13] S. Darby, D. Hill, and R. Doll, “Radon: A likely carcinogen at all exposures,” *Annals of oncology*, vol. 12, pp. 1341 – 1351, 2001.
- [14] B. Grosche, M. Kreuzer, M. Kreisheimer, M. Schnelzer, and A. Tschense, “Lung cancer risk among german male uranium miners: a cohort study, 1946–1998,” *British Journal of Cancer*, vol. 95, no. 9, pp. 1280 – 1287, 2006.
- [15] J. Samet and G. Eradze, “Radon and lung cancer risk: taking stock at the millenium,” *Environmental Health Perspectives*, vol. 108, no. 4, pp. 635 – 641, 2000.
- [16] J. H. Lubin, “Studies of radon and lung cancer in North America and China,” *Radiation Protection Dosimetry*, vol. 104, no. 4, pp. 315–319, 2003.
- [17] S. Darby, D. Hill, A. Auvinen, J. Barros-Dios, H. Baysson, F. Bochicchio, H. Deo, R. Falk, F. Forastiere, M. Hakama, I. Heid, L. Kreienbrock, M. Kreuzer, F. Lagarde, I. Mkelinen, C. Muirhead, W. Oberaigner, G. Pershagen, A. Ruano-Ravina, E. Ruosteenoja, A. Rosario, M. Tirmarche, L. Tomsek, E. Whitley, H. Wichmann, and R. Doll, “Radon in homes and risk of lung cancer: collaborative analysis of individual data from 13 European case-control studies,” *BMJ*, vol. 330, no. 7485, p. 223–228, 2005.
- [18] D. Krewski, J. Lubin, J. Zielinski, M. Alavanja, V. Catalan, R. Field, J. Klotz, E. Ltourneau, C. Lynch, J. Lyon, D. Sandler, J. Schoenberg, D. Steck, J. Stolwijk, C. Weinberg, and H. Wilcox, “Residential radon and risk of lung cancer: a combined analysis of 7 North American case-control studies,” *Epidemiology*, vol. 16, no. 2, 2005.
- [19] H. Zeeb and F. Shannoun, *WHO handbook on indoor radon: a public health perspective*. WHO Press, 2009.

BIBLIOGRAPHY

- [20] F. Bochicchio, J. McLaughling, and S. Piermattei, “Radon in indoor air,” Tech. Rep. 15, European Commission Directorate-General for Science, Research and Development Joint Research Centre-Environment Institute, 1995.
- [21] A. George, “An overview of instrumentation for measuring environmental radon and radon progeny,” *Nuclear Science, IEEE Transactions on*, vol. 37, pp. 892–901, apr 1990.
- [22] N. L. Nagda, *Radon: Prevalence, Measurements, Health Risks and Control*. Astm Intl, 1994.
- [23] AlphaGUARD, “Radon Monitoring with AlphaGUARD.” http://www.genitron.de/download/ag_fb_gb_01_a4.pdf.
- [24] K. Amgarou, L. Font, and C. Baixeras, “A novel approach for long-term determination of indoor ^{222}Rn progeny equilibrium factor using nuclear track detectors,” *Nuclear Instruments and Methods in Physics Research Section A: Accelerators, Spectrometers, Detectors and Associated Equipment*, vol. 506, no. 1-2, pp. 186–198, 2003.
- [25] V. Nikolaev and R. Ilic, “Etched track radiometers in radon measurements: a review,” *Radiation Measurements*, vol. 30, no. 1, pp. 1–13, 1999.
- [26] S. Chalupnik, O. Meisenberg, L. Bi, J. Wang, K. Skubacz, and J. Tschiersch, “Application of LSC and TLD methods for the measurements of radon and thoron decay products in air,” *Radiation Protection Dosimetry*, vol. 141, no. 4, pp. 390–394, 2010.
- [27] M. F. L’Annunziata, *Handbook of Radioactivity Analysis*. Academic press, 2003.
- [28] S. Higuere, D. Husson, M. Trocme, A. Nourreddine, T. Le, and N. Michielsen, “Measurement of ^{222}Rn at the Bq m^{-3} level with the AlphaRad chip,” *Radiation Measurements*, vol. 43, no. 2-6, pp. 1059–1062, 2008.
- [29] J. Harley, “Measurement of ^{222}Rn : A brief history,” *Radiation Protection Dosimetry*, vol. 113, no. 4, pp. 438–441, 1992.
- [30] C. Howarth and J. Miles, “Results of the 2000 NRPB intercomparison of passive radon detectors,” tech. rep., National Radiological Protection Board (NRPB), 2002.
- [31] G. Espinosa and R. Silva, “Industrial commercial respirator filter as indoor radon monitor,” *Journal of Radioanalytical and Nuclear Chemistry*, vol. 282, pp. 405–408, 2009.

- [32] S. Righi and L. Bruzzi, “Natural radioactivity and radon exhalation in building materials used in Italian dwellings,” *Journal of Environmental Radioactivity*, vol. 88, no. 2, pp. 158 – 170, 2006.
- [33] C. Papachristodoulou, D. Patiris, and K. Ioannides, “Exposure to indoor radon and natural gamma radiation in public workplaces in north-western Greece,” *Radiation Measurements*, vol. 45, no. 7, pp. 865 – 871, 2010.
- [34] K. Turek, M. Gelev, and I. Dimov, “Comparative measurements of soil gas radon concentration using thermoluminescent and track detectors,” *Radiation Measurements*, vol. 38, no. 4-6, pp. 843 – 846, 2004.
- [35] R. Anjos, N. Umisedo, A. da Silva, L. Estellita, M. Rizzotto, E. Yoshimura, H. Velasco, and A. Santos, “Occupational exposure to radon and natural gamma radiation in the La Carolina, a former gold mine in San Luis Province, Argentina,” *Journal of Environmental Radioactivity*, vol. 101, no. 2, pp. 153 – 158, 2010.
- [36] R. Trevisi, A. Caricato, M. D’Alessandro, M. Fernandez, F. Leonardi, A. Luches, S. Tonnarini, and M. Veschetti, “A pilot study on natural radioactivity in schools of south-east Italy,” *Environment International*, vol. 36, no. 3, pp. 276 – 280, 2010.
- [37] A. Martin-Martin, J. Gutierrez-Villanueva, J. Munoz, M. GarciaTalavera, G. Adamiec, and M. Iniguez, “Radon measurements with a PIN photodiode,” *Applied Radiation and Isotopes*, vol. 64, no. 10-11, pp. 1287 – 1290, 2006.
- [38] Y. Takeuchi, K. Okumura, T. Kajita, S. Tasaka, H. Hori, M. Nemoto, and H. Okazawa, “Development of high sensitivity radon detectors,” *Nuclear Instruments and Methods in Physics Research Section A: Accelerators, Spectrometers, Detectors and Associated Equipment*, vol. 421, no. 1-2, pp. 334 – 341, 1999.
- [39] P. Chittaporn, M. Eisenbud, and N. Harley, “A continuous monitor for the measurement of environmental radon,” *Health Physics*, vol. 41, pp. 405 – 410, 1981.
- [40] Radim 3A Radon Monitor. http://www.radon.at/downloads_en/Radim3Atechnicaldescription.pdf.
- [41] G. Lutz, *Semiconductor Radiation Detectors*. Springer, 1999.
- [42] R. Horisberger, “The bipolar silicon microstrip detector: A proposal for a novel precision tracking device,” *Nuclear Instruments and Methods in Physics Research Section A*, vol. 288, pp. 97–91, 1990.

BIBLIOGRAPHY

- [43] R. L. Williams and P. P. Webb, "Transistor form of nuclear particle detector," *Nuclear Science, IRE Transactions on*, vol. 8, no. 1, pp. 35 –42, 1961.
- [44] J. Ardelean, R. Chase, and A. Hrisoho, "A proposed pixel detector based on floating base transistors," *Nuclear Instruments and Methods in Physics Research Section A: Accelerators, Spectrometers, Detectors and Associated Equipment*, vol. 305, no. 3, pp. 549 – 552, 1991.
- [45] S. Avrillon, H. Ikeda, T. Matsuda, Y. Saitoh, and M. Inoue, "Design considerations for mos pixel for single-sided two-dimensional detector," *Nuclear Instruments and Methods in Physics Research Section A: Accelerators, Spectrometers, Detectors and Associated Equipment*, vol. 355, no. 2-3, pp. 406 – 413, 1995.
- [46] S. Kavadias, K. Misiakos, and D. Loukas, "A novel radiation imaging sensor based on self-activated pixels," *Nuclear Science, IEEE Transactions on*, vol. 42, pp. 155 –162, jun 1995.
- [47] G. Deptuch, J.-D. Berst, G. Claus, C. Colledani, W. Dulinski, Y. Gornushkin, D. Husson, J.-L. Riester, and M. Winter, "Design and testing of monolithic active pixel sensors for charged particle tracking," *Nuclear Science, IEEE Transactions on*, vol. 49, pp. 601 –610, apr 2002.
- [48] A. Nachab, D. Husson, A. Nourreddine, and S. Higuere, "First measurement of ^{222}Rn activity with a CMOS active pixel sensor," *Nuclear Instruments and Methods in Physics Research Section B: Beam Interactions with Materials and Atoms*, vol. 225, no. 3, pp. 418 – 422, 2004.
- [49] W. Dulinski, J.-D. Berst, A. Besson, G. Claus, C. Colledani, G. Deptuch, M. Deveaux, A. Gay, D. Grandjean, Y. Gornushkin, A. Himmi, C. Hu, J.-L. Riester, I. Valin, and M. Winter, "CMOS monolithic active pixel sensors for minimum ionizing particle tracking using non-epitaxial silicon substrate," *Nuclear Science, IEEE Transactions on*, vol. 51, pp. 1613 – 1617, aug. 2004.
- [50] D. Husson, A. Bozier, S. Higuere, T. Le, and A. Nourreddine, "AlphaRad, a new integrated CMOS System-on-Chip for high efficiency alpha particles counting," *Nuclear Instruments and Methods in Physics Research Section A: Accelerators, Spectrometers, Detectors and Associated Equipment*, vol. 569, no. 3, pp. 845 – 852, 2006.
- [51] I. Thomson, "Radon detector." United states patent, US 4,983,843, 1991.

-
- [52] A. Ahmed, D. Walkey, and N. Tarr, "A CMOS integrated pulse mode alpha-particle counter for application in radon monitoring," *Nuclear Science, IEEE Transactions on*, vol. 44, pp. 1425–1430, jun 1997.
- [53] R. Griffin, H. Le, D. Jack, A. Kochermin, and N. Tarr, "Radon monitor using custom α -detecting MOS IC," in *Sensors, 2008 IEEE*, pp. 906–909, oct. 2008.
- [54] R. Griffin, H. Le, D. Jack, and N. Tarr, "aram: An α particle detecting MOS IC for radon monitoring," in *Microsystems and Nanoelectronics Research Conference, 2008. MNRC 2008. 1st*, pp. 73–76, oct. 2008.
- [55] A. Miles, R. Griffin, Y. Shen, and N. Tarr, "A wireless solution for radon gas detection," in *Microsystems and Nanoelectronics Research Conference, 2009. MNRC 2009. 2nd*, pp. 88–91, oct. 2009.
- [56] F. Karinda, B. Haider, and W. Ruhm, "A new electronic personal exposure meter for radon gas," *Radiation Measurements*, vol. 43, no. 2-6, pp. 1170–1174, 2008.
- [57] V. Drndarevic, "A very low-cost alpha-particle spectrometer," *Measurement Science and Technology*, vol. 19, no. 5, p. 057001, 2008.
- [58] M. Ramilli, *Silicon photomultipliers: characterization and application to fluorescence fluctuation spectroscopy*. PhD thesis, Universita degli Studi dellInsubria, 2011.
- [59] G. Batignani, C. Angelini, M. Bisogni, M. Boscardin, S. Bettarini, M. Bondioli, L. Bosisio, F. Bucci, G. Calderini, M. Carpinelli, M. Ciacchi, G.-F. Dalla Betta, S. Dittongo, F. Forti, M. Giorgi, P. Gregori, D. Han, P. Manfredi, M. Manghisoni, G. Marchiori, N. Neri, M. Novelli, E. Paoloni, C. Piemonte, I. Rachevskaia, M. Rama, L. Ratti, V. Re, G. Rizzo, S. Ronchin, V. Rosso, G. Simi, V. Speziali, A. Stefanini, and N. Zorzi, "A study for the detection of ionizing particles with phototransistors on thick high-resistivity silicon substrates," *Nucl. Instr. and Meth. A*, vol. 530, no. 1-2, pp. 98–104, 2004. Proceedings of the 6th International Conference on Large Scale Applications and Radiation Hardness of Semiconductor Detectors.
- [60] D. Han, G. Batignani, A. Guerra, G.-F. Dalla Betta, M. Boscardin, L. Bosisio, M. Giorgi, and F. Forti, "High-gain bipolar detector on float-zone silicon," *Nuclear Instruments and Methods in Physics Research Section A: Accelerators, Spectrometers, Detectors and Associated Equipment*, vol. 512, no. 3, pp. 572–577, 2003.
- [61] G. Batignani, M. Bisogni, M. Boscardin, L. Bosisio, G.-F. Dalla Betta, A. D. Guerra, S. Dittongo, F. Forti, M. Giorgi, D. Han, S. Linsalata, G. Marchiori, C. Piemonte,

- I. Rachevskaia, and S. Ronchin, "High-gain phototransistors on high-resistivity silicon substrate," *Nuclear Instruments and Methods in Physics Research Section A: Accelerators, Spectrometers, Detectors and Associated Equipment*, vol. 518, no. 1-2, pp. 569 – 570, 2004.
- [62] C. Piemonte, G. Batignani, S. Bettarini, M. Bondioli, M. Boscardin, L. Bosisio, G.-F. Dalla Betta, S. Dittongo, F. Forti, M. Giorgi, P. Gregori, I. Rachevskaia, S. Ronchin, and N. Zorzi, "Characterization of BJT-based particle detectors," *Nuclear Instruments and Methods in Physics Research Section A: Accelerators, Spectrometers, Detectors and Associated Equipment*, vol. 535, no. 1-2, pp. 433 – 437, 2004.
- [63] G. Batignani, S. Bettarini, M. Bondioli, M. Boscardin, L. Bosisio, G.-F. Dalla Betta, S. Dittongo, F. Forti, G. Giacomini, M. Giorgi, P. Gregori, C. Piemonte, I. Rachevskaia, S. Ronchin, and N. Zorzi, "Functional characterization of a high-gain BJT radiation detector," *Nuclear Science, IEEE Transactions on*, vol. 52, pp. 1882 – 1886, oct. 2005.
- [64] L. Bosisio, G. Batignani, S. Bettarini, M. Boscardin, G.-F. Dalla Betta, G. Giacomini, C. Piemonte, G. Verzellesi, and N. Zorzi, "Performance evaluation of radiation sensors with internal signal amplification based on the BJT effect," *Nuclear Instruments and Methods in Physics Research Section A: Accelerators, Spectrometers, Detectors and Associated Equipment*, vol. 568, no. 1, pp. 217 – 223, 2006.
- [65] G. Verzellesi, G. Batignani, S. Bettarini, M. Boscardin, L. Bosisio, G.-F. Dalla Betta, G. Giacomini, and C. Piemonte, "BJT-based detector on high-resistivity silicon with integrated biasing structure," *Nuclear Instruments and Methods in Physics Research Section A: Accelerators, Spectrometers, Detectors and Associated Equipment*, vol. 567, no. 1, pp. 285 – 289, 2006.
- [66] G. Verzellesi, D. Bergamini, G.-F. Dalla Betta, C. Piemonte, M. Boscardin, L. Bosisio, S. Bettarini, and G. Batignani, "N-p-n bipolar-junction-transistor detector with integrated p-n-p biasing transistor - feasibility study, design and first experimental results," *Semiconductor Science and Technology*, vol. 21, no. 2, p. 194, 2006.
- [67] "THS4303 Wideband Evaluation Module." <http://www.ti.com/tool/ths4303evm>.
- [68] "ZTEC Instruments." <http://www.ztecinstruments.com/>.
- [69] L. Rovati, S. Bettarini, M. Bonaiuti, L. Bosisio, G.-F. Dalla Betta, V. Tyzhnevyi, G. Verzellesi, and N. Zorzi, "Alpha-particle detection based on the BJT detector and simple, IC-based readout electronics," *JINST*, vol. 4, p. 11010, 2009.

- [70] Spartan-3 FPGA Family Data Sheet. http://www.xilinx.com/support/documentation/data_sheets/ds099.pdf.
- [71] R. C. Jaeger, *Introduction to Microelectronic Fabrication (Modular series on solid state devices; V.5)*. Prentice Hall, 2002.
- [72] W. Chen, Z. Li, and H. Kraner, "Application of the rapid thermal process: sintering the sputtered aluminum/silicon contact in silicon detector fabrication," *Nuclear Science, IEEE Transactions on*, vol. 39, pp. 558–562, aug 1992.
- [73] D. Schroder, *Semiconductor material and device characterization*. John Wiley and Sons, Inc., 2006.
- [74] A. Grove and D. Fitzgerald, "Surface effects on pn junctions: characteristics of surface space-charge regions under non-equilibrium conditions," *Solid-State Electron.*, vol. 9, pp. 783–806, August 1966.
- [75] "Votsch Industrietechnik." <http://www.v-it.com/en/vit/start>.
- [76] "Keithley 6487 Picoammeter/Voltage source." <http://www.keithley.com/products/dcac/voltagesource/application/?mn=6487>.
- [77] "Agilent E3631A 80W Triple Output Power Supply, 6V, 5A and 25V, 1A." <http://www.home.agilent.com/agilent/product.jsp?pn=e3631a&cc=IT&lc=ita>.
- [78] B. Olesen, "International standards for the indoor environment," *Indoor Air*, vol. 14, no. 7, pp. 18–26, 2004.
- [79] D. Andrews, "A novel experiment to investigate the attenuation of alpha particle in air," *Eur. J. Phys.*, vol. 29, pp. 1077 – 1083, 2008.
- [80] L. Rovati, G. Verzellesi, L. Bidinelli, A. Bosi, G.-F. Dalla Betta, V. Tyzhnevyy, M. Calamosca, and S. Penzo, "Sensore wireless per la rivelazione del gas radon," in *GMEC Conference Proceedings, 2011. GMEC 2011*, pp. 95 – 96, 2011.
- [81] "OFR Division of Thorlabs Inc.." http://www.ofr.com/fo-47_fiberfocuser.htm.

Appendix A

Schematics and layout of ALPHADET board

1

2

3

4

5

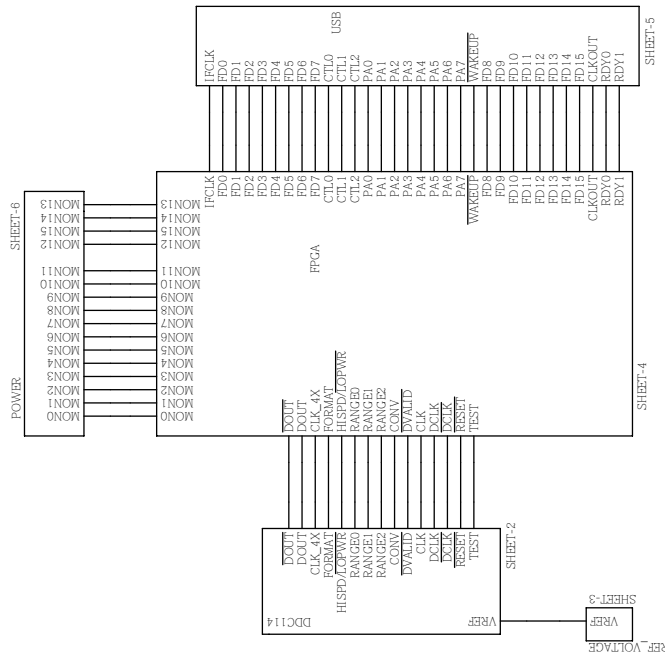
6

D

C

B

A

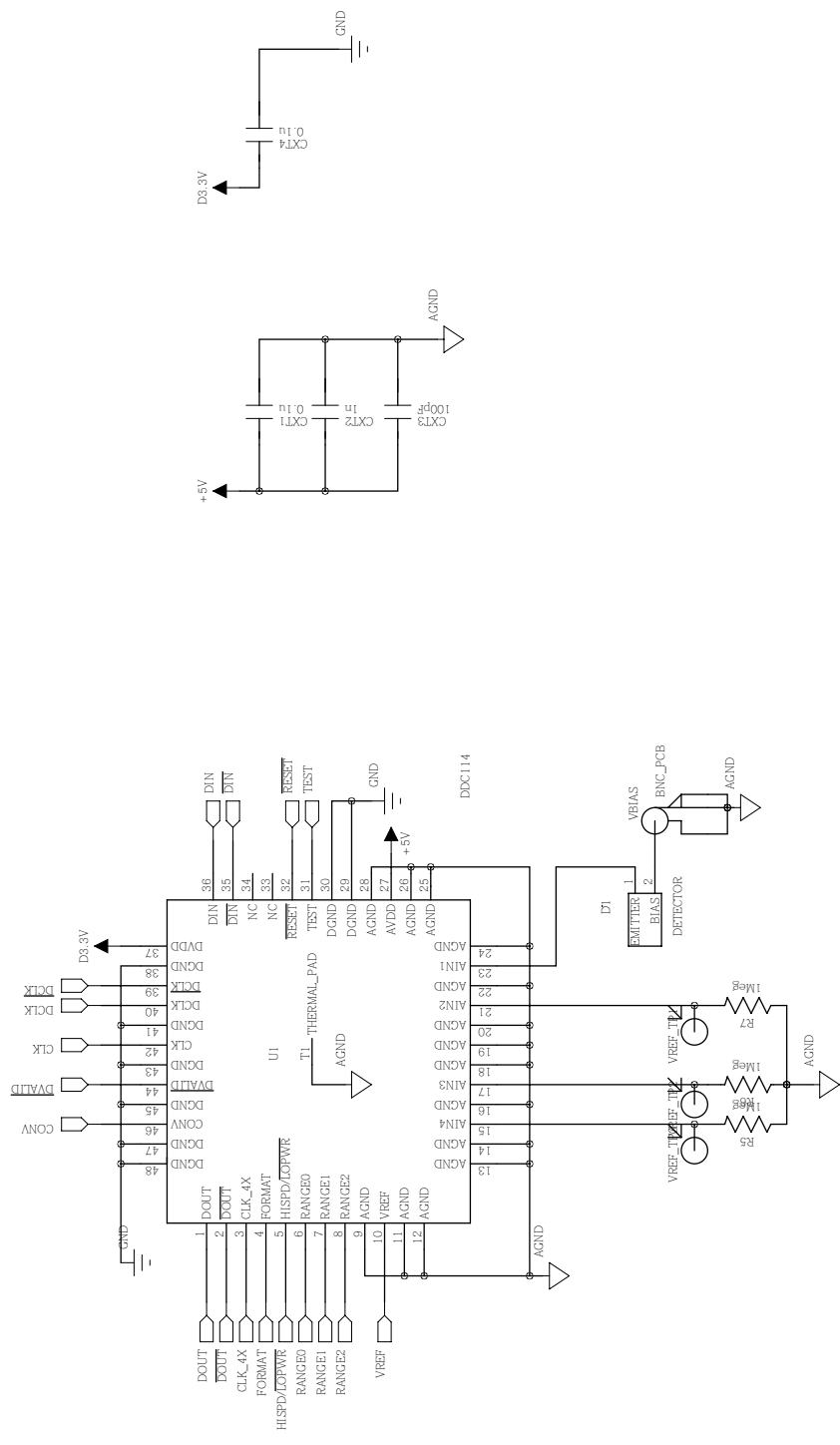


UNIVERSITA' DEGLI STUDI
DI TRENTO
Dipartimento di Ingegneria
e Scienze dell'Informazione

Univ. of Trento, Univ. of Hawaii Instr. Dev. Lab.	
TITLE: ALPHADET	Page Description Top Block
DESIGN: TYZHNEVYI V.	REV: B
DATED: November 2009	SHEET: 1 OF 6

6 5 4 3 2 1

D C B A



Univ. of Trento, Univ. of Hawaii Instr. Dev. Lab.	
TITLE: ALPHADET	DESIGN: TYZHNEVYI V.
UNIVERSITÀ DEGLI STUDI DI TRENTO	Page Description: DDC114 Block
Dipartimento di Ingegneria e Scienza dell'Informazione	REV: B
DATED: November 2009	SHEET: 2 OF 6

1

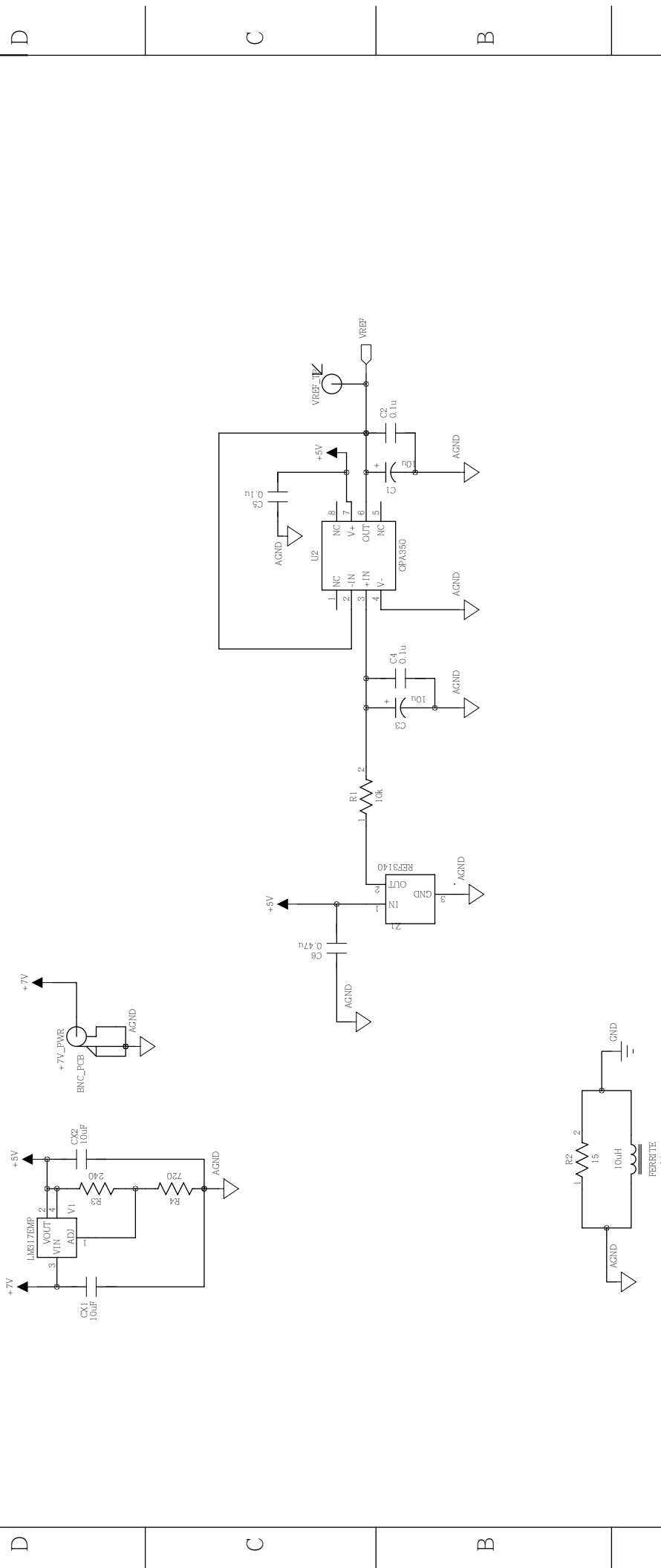
2

3

4

5

6



D

C

B

A



UNIVERSITÀ DEGLI STUDI
DI TRENTO
Dipartimento di Ingegneria
e Scienza dell'Informazione

Univ. of Trento, Univ. of Hawaii's Instr. Dev. Lab.

TITLE: ALPHADET

DESIGN: TYZHNEVYI V.

Page Description: REF_Voltage

DATE: November 2009

REV: B

SHEET: 3 OF 6

1

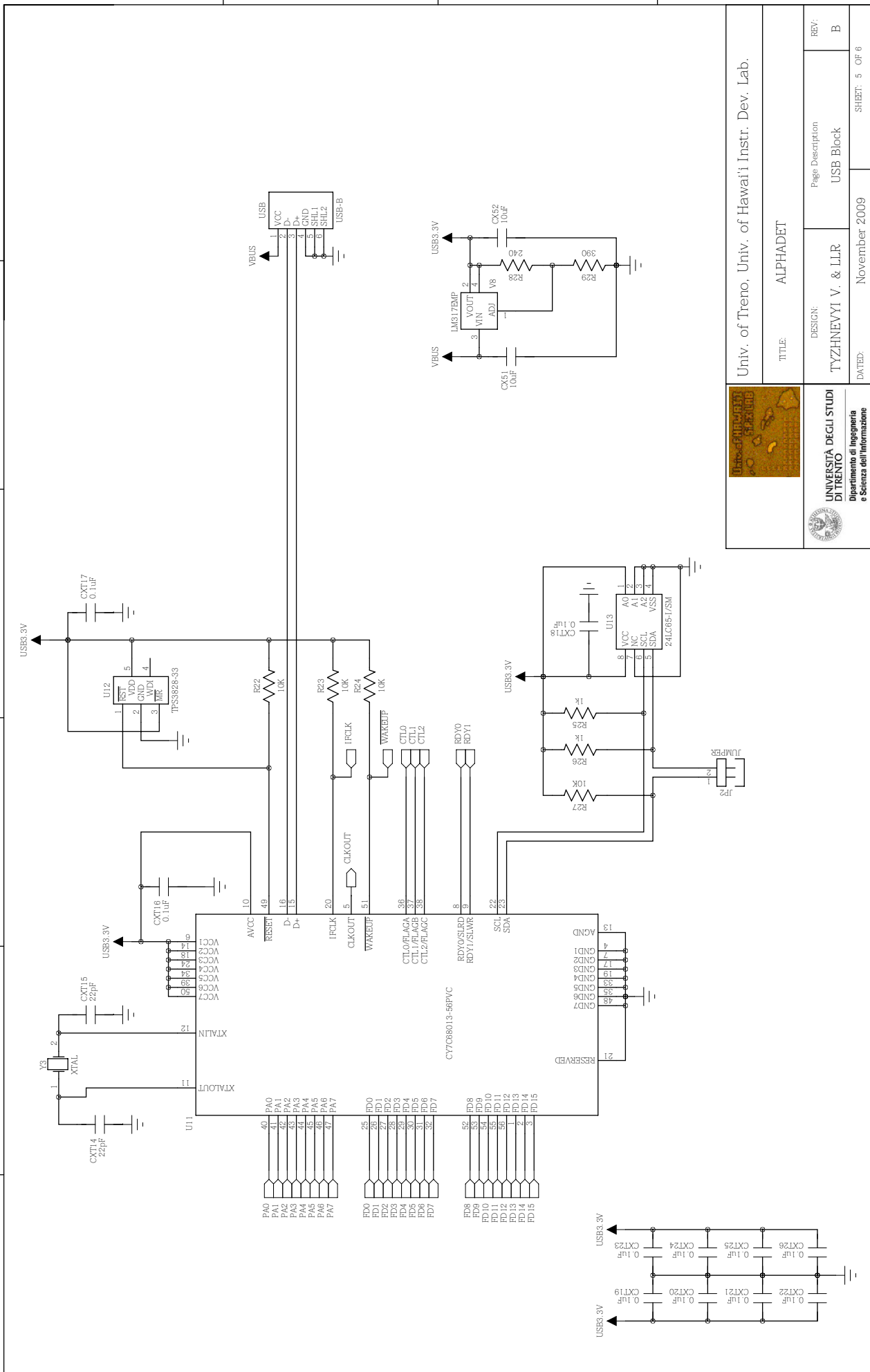
2

3

4

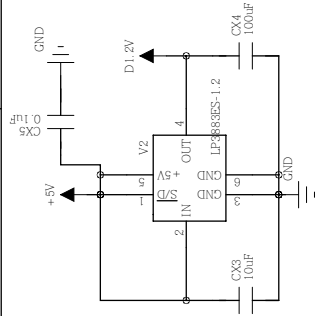
5

6

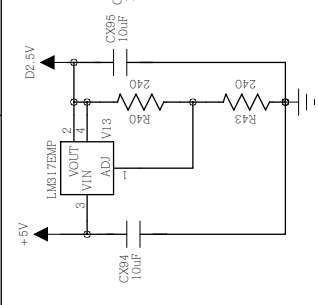


 UNIVERSITÀ DEGLI STUDI DI TRENTO Dipartimento di Ingegneria e Scienza dell'Informazione		TITLE: ALPHADET	Page Description: USB Block	REV: B
Univ. of Trento, Univ. of Hawai'i Instr. Dev. Lab.		DESIGN: TYZHNEVYI V. & LLR	DATED: November 2009	SHEET: 5 OF 6

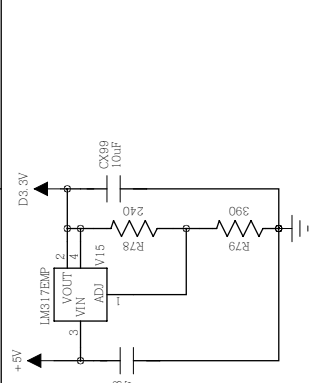
6



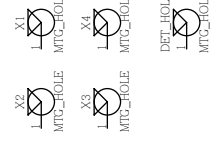
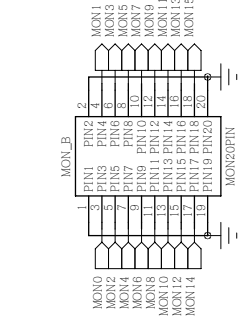
5



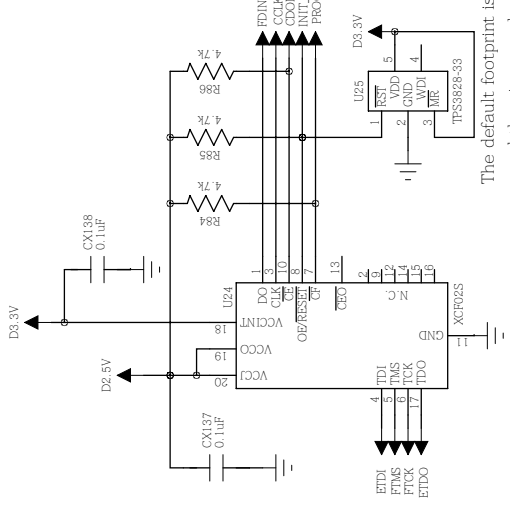
4



3



2



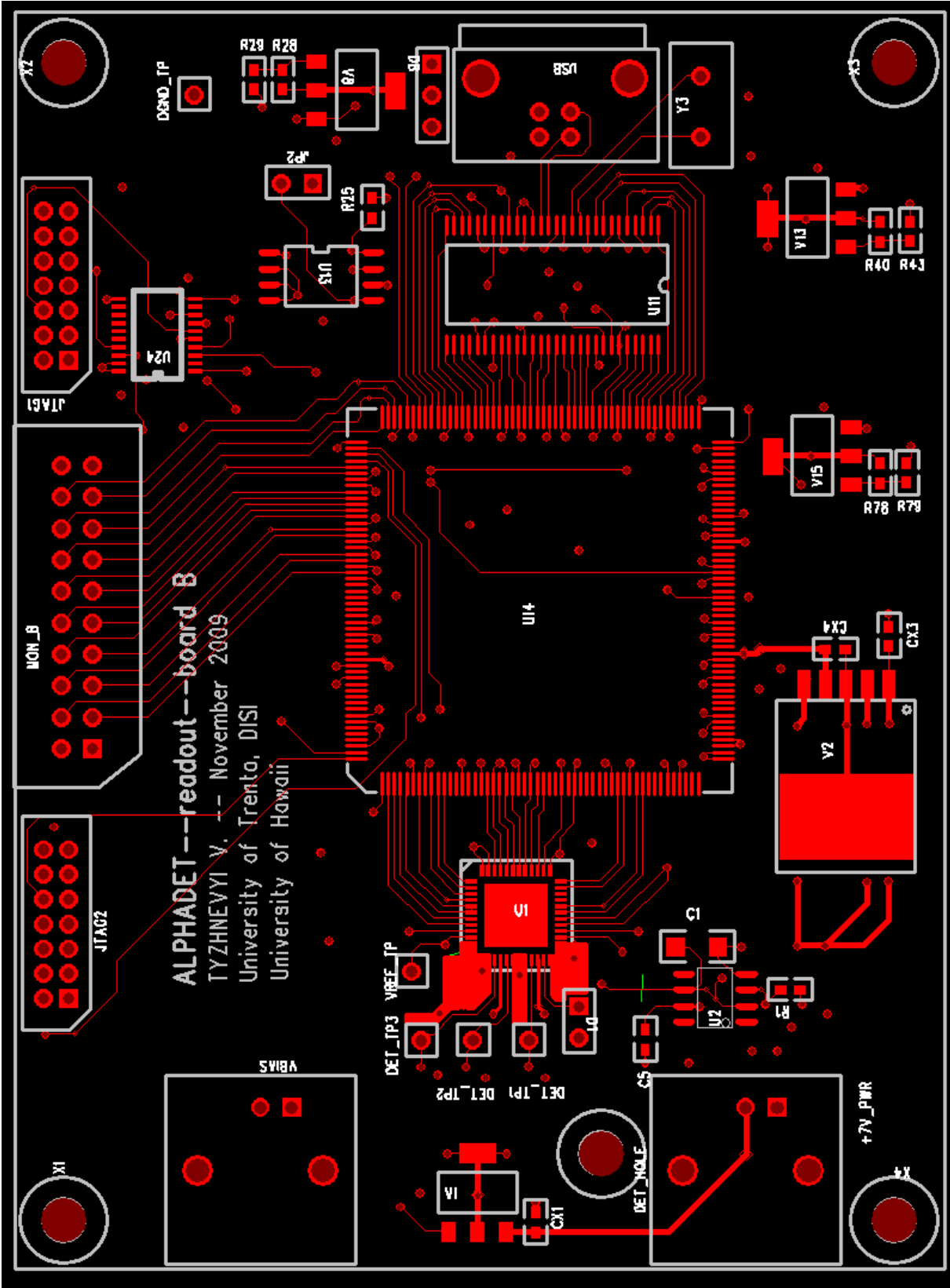
1

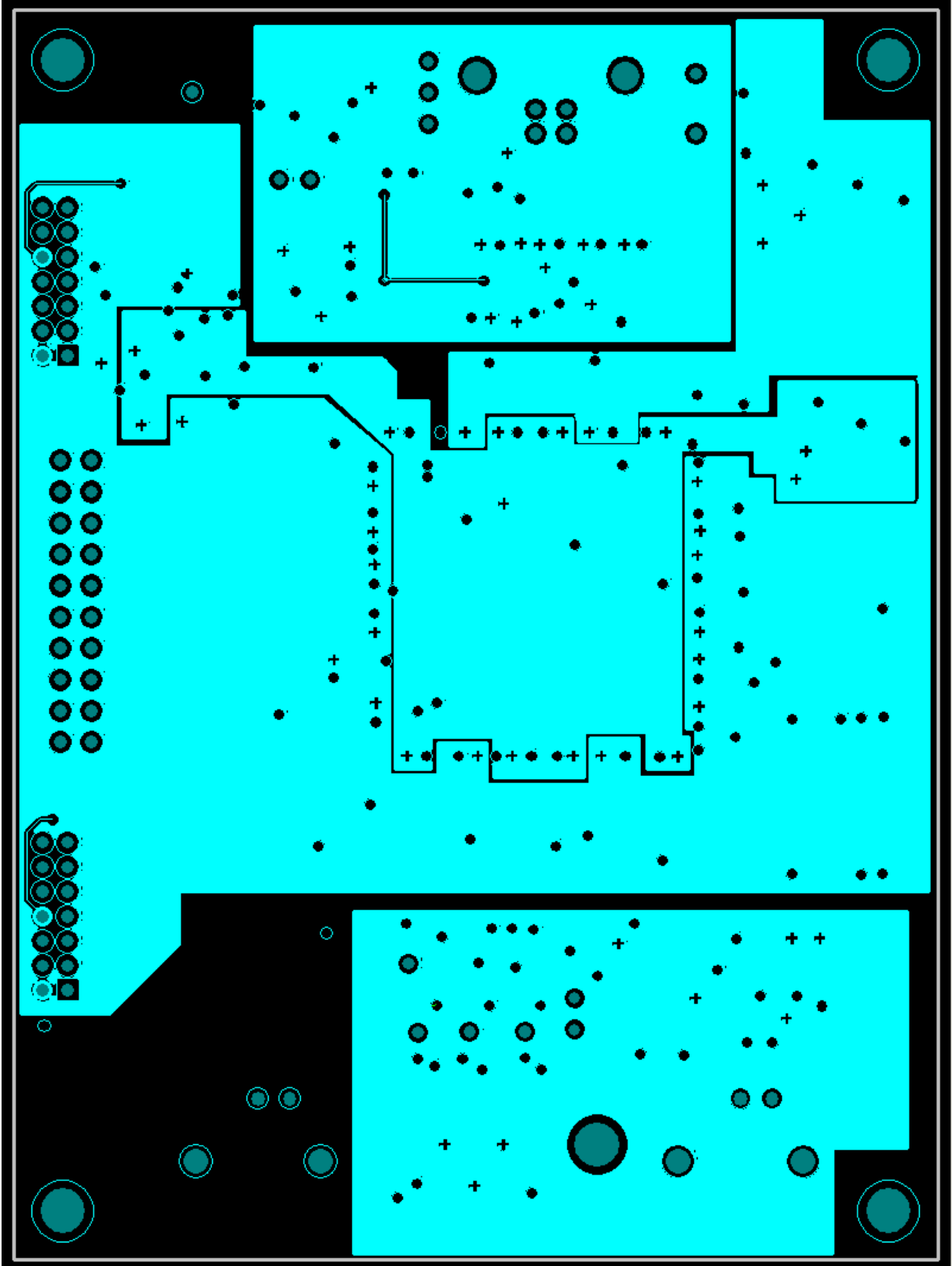


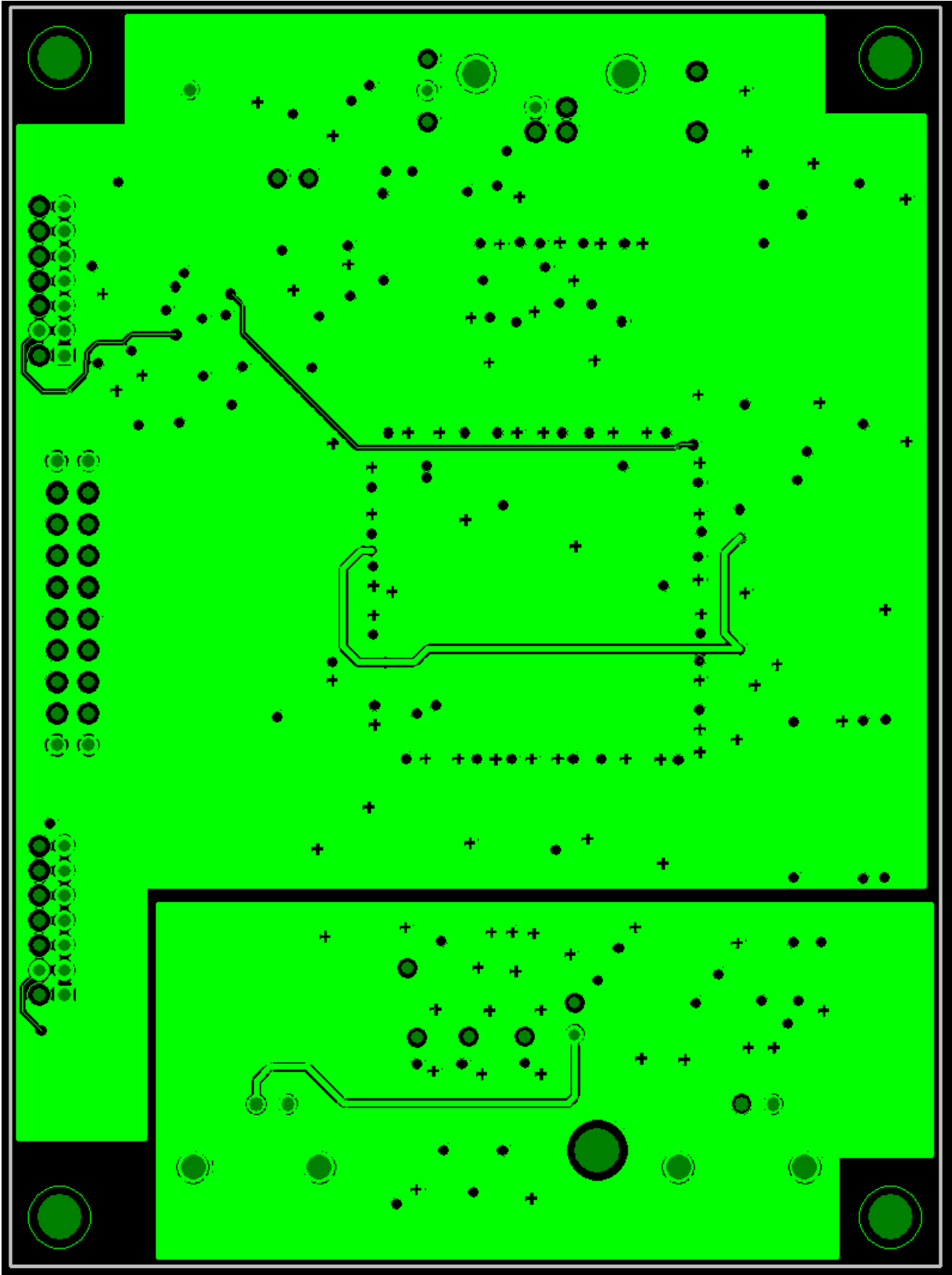
UNIVERSITÀ DEGLI STUDI
DI TRENTO
Dipartimento di Ingegneria
e Scienza dell'Informazione

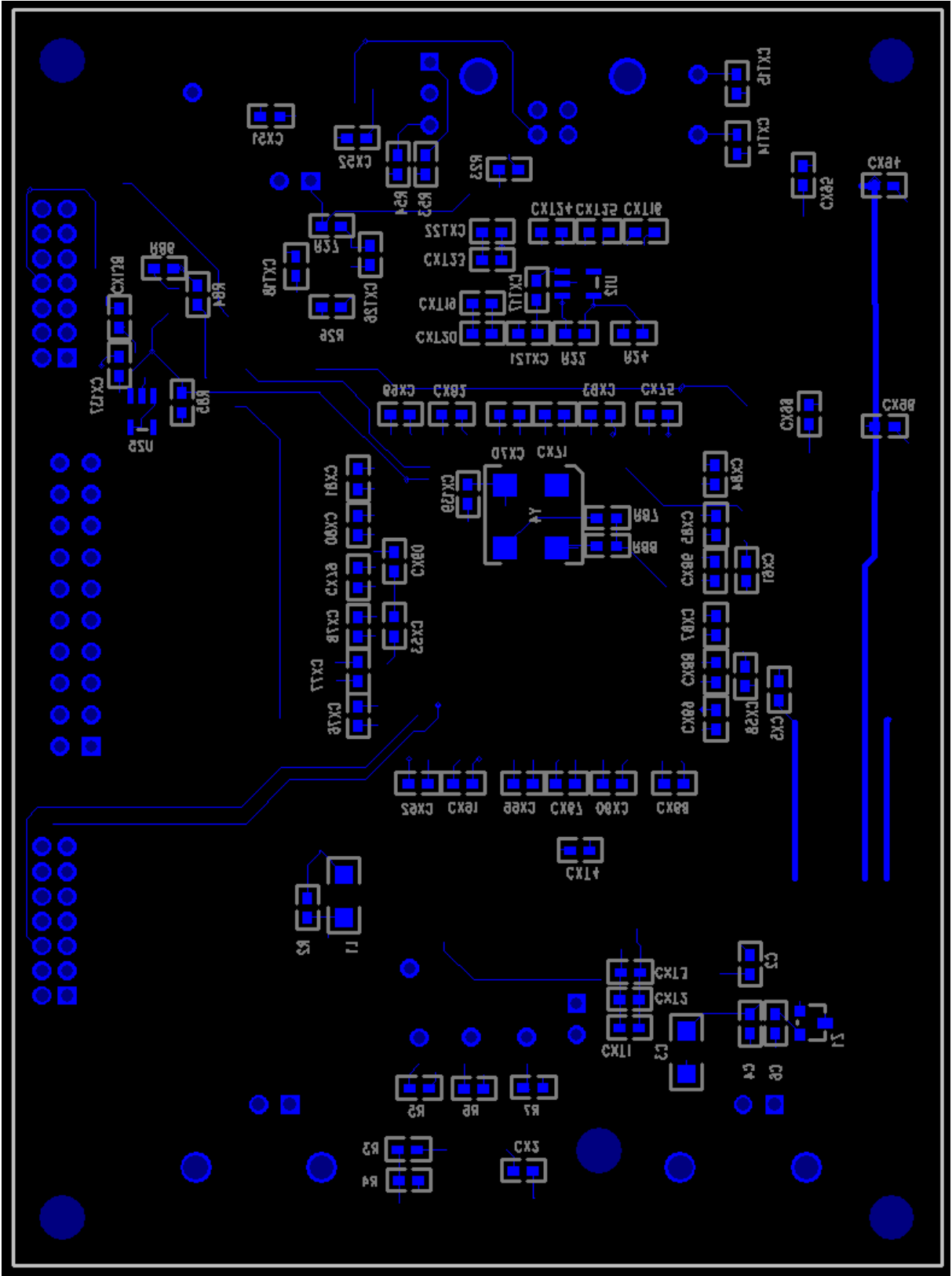
Univ. of Trento, Univ. of Hawai'i Instr. Dev. Lab.

TITLE:	ALPHADET
DESIGN:	TYZHNEVYI V. & LLR
Page Description	POWER Block
REV:	B
DAVED:	November 2009
SHEET:	6 OF 6









Appendix B

Optical system for functional characterization of radiation detectors

In order to provide reliable testing of BJT detectors (as well as of other silicon radiation detectors) with repeatable results of the experiments we have developed a laser based optical system for functional characterization of the detectors. The system consists of fiber coupling part, fiber, snap-on focuser, XYZ 1/2" travel translation stage, which is controlled by a custom designed Matlab software.

Among many available fiber coupling systems, e.g., "free-space to fiber coupler", "laser diode-to-fiber coupler" etc., we have chosen the "laser diode-to-fiber coupler" as it was fit better to the purposes of our experiment. One of the main purpose of laser test is to emulate ionizing particle using coherent laser light, which means that a weak source of coherent light can be used, i.e., 5.6 mm or 9 mm lasers with just few milliwatts of output light power. For example, in our laboratory we use 635 nm QL63D5SA, 850 nm RLT8505MG lasers with 5 mW output power and 980 nm RLT9810MG, 1060 nm RLT1060-10MG lasers with 10 mW output power. Thus, taking into account that apart from light coupling no additional light manipulations are needed in this experiment and that simple 5.6 mm laser diode can be used, KT112 fiber launch system (Thorlabs, [8]) has been used to couple light from laser diode to the fiber. Figure B.1 shows a drawing of KT112 optical component together with optical fiber and installed laser. Lens C230TME-B (600 - 1050 nm, $f = 4.51$ mm, NA = 0.55 Aspheric Lens) was used for laser light collimation and lens C220TME-B (600 - 1050 nm, $f = 11.0$ mm, NA = 0.55 Aspheric Lens) was used to focus light on the fiber input.

The fiber guides light from the laser diode to the detector. Fiber P1-980A-FC-5

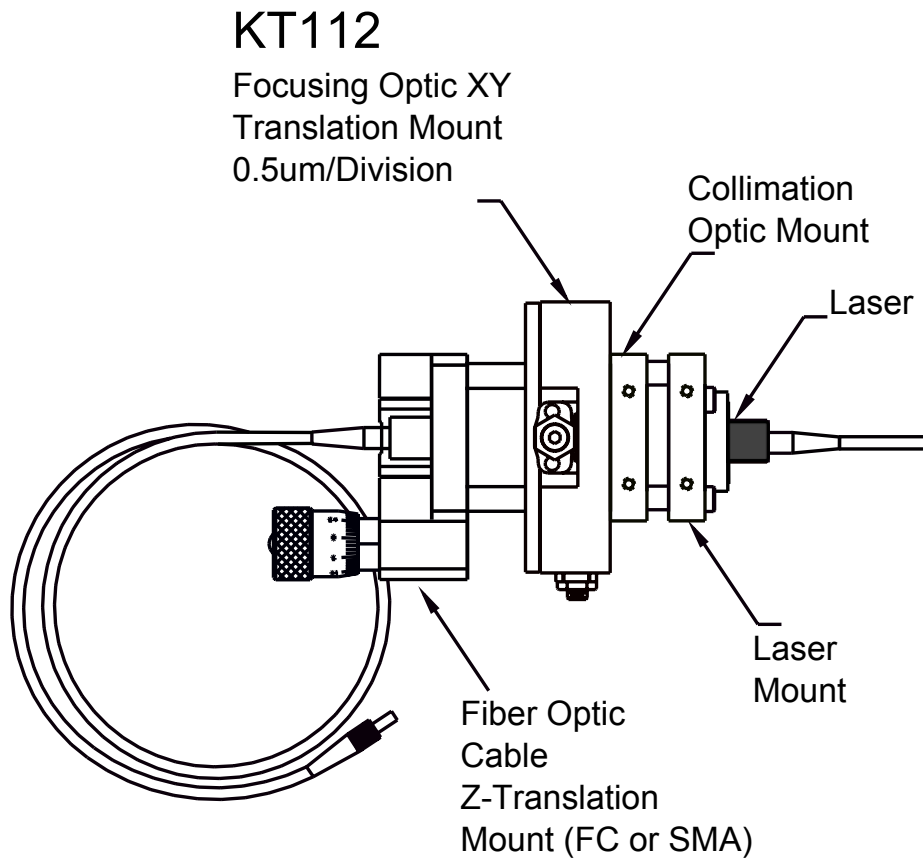


Figure B.1: KT112, single mode and multimode fiber coupler: 5.6 mm and 9 mm laser diodes [8].

was used to that purpose, this fiber is a single mode fiber patch cable with operating wavelengths 980/1064/1500 nm, numerical aperture $NA = 0.14$, mode field diameter $MFD = 5.8\mu\text{m}@980\text{ nm}$. In general, it is preferable to have a small light spot on the detector as it is possible then to scan the detector over its particular areas and test uniformity of properties of the detector, test performance of the detector, discover possible defects. All of that is impossible to do if the light spot is not small. Simple calculations show that with $NA = 0.14$ the output light spot on the distance of 1 mm would be $\sim 280\ \mu\text{m}$. However, 1 mm distance between fiber and detector could be detrimental to the bonding wires during the movements of the fiber over the detector; so, in principle, 2 mm distance would be better. The distance of 2 mm corresponds to $560\ \mu\text{m}$ light spot diameter (see fig. B.2(a)).

Obviously, this light spot diameter could not satisfy requirements of the experiment. This is why an intermediate focusing stage was introduced between fiber and a detector. This optical part is called focuser. Usually it consists of at least two lenses, one of them

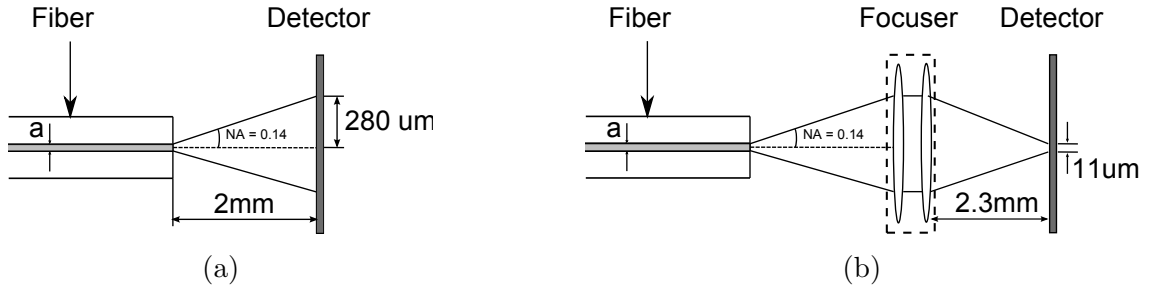


Figure B.2: (a) light beam is projected from the fiber directly on the surface of the detector. The light spot has $560 \mu\text{m}$ diameter. (b) light beam is focused.

is collimating and another is focusing, or even more lenses. A snap-on focuser FFC-8/5- λ for single mode fiber with 2.3 mm working distance and $11 \mu\text{m}$ focal spot ([81]) has been chosen as a last stage of laser light guide. This is an optical part with FC receptacle, which is a common type of a fiber-optic connector with a threaded body. Availability of a focuser with FC connector makes convenient a use of different fibers, calibration of laser light, i.e., the fiber can be easily disconnected from the focuser and connected directly to the reference detector, which can not be done if a pigtailed focuser is used, etc.

After the laser light is coupled to the fiber, guided and focused to the micrometer size spot on the detector a laser scan can be performed. To move fiber we have constructed an XYZ $1/2''$ travel translation stage with XY motorized and Z manual translator stages. Motorized XY stages had Z712B - 12 mm travel motorized actuator installed that was driven by a single channel USB DC servo controller/driver (T-Cube DC Motor Controller) TDC001. Due to the use of 256:1 gear reduction head the actuators provide very small movements, the minimum calculated step movement is 40 nm, which, however, depends on the applied load, i.e., the step can be larger if the load is high.

Schematic representation of the designed optical system is shown in fig. B.3. The right-most column of blocks consists of all components of the system related to the light generation (waveform generator, laser driver, +5 V power supply), light coupling (KT112) and light calibration. Light calibration is done via D400FC InGaAs fiber optic photo detector, which has 800-1700 nm spectral response with minimal bandwidth of 1 GHz (rise/fall time is 0.1 ns) [5], fast THS4303 amplifier (1.8 GHz bandwidth, hence, compatible with D400FC photo detector) [67] and oscilloscope to control and acquire signal. The middle column consists of components related directly to the testing of a detector, i.e., the detector under test, “laser light” block, which includes a fiber and snap-on focuser positioned above the tested detector and “readout electronics” block, which in case of BJT detector is the ALPHADET system or readout chain consisting of transimpedance amplifier and digital storage oscilloscope (see transimpedance readout in fig. 2.5 on page 27, the DSO

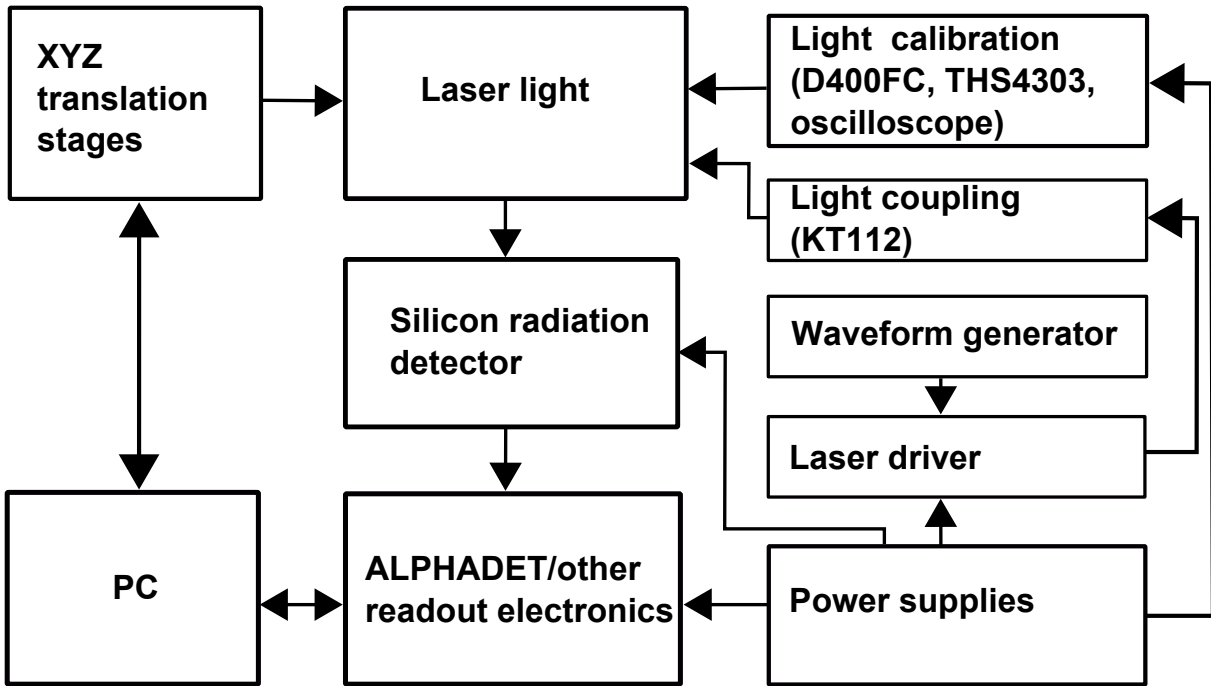


Figure B.3: Schematic representation of the designed optical system. \longleftrightarrow - double headed arrows mean that communication between components can be done in both directions, while \longrightarrow single headed arrows mean that communication can be done only in the indicated direction.

can be as a quite simple one like TDS 3052B or more advanced like ZTEC 4211). The leftmost column consists of the blocks, which had to be programmed, i.e., “PC” block represents a program written in Matlab environment to acquire data from readout electronics and to perform movements of XY translation stages¹, \longleftrightarrow such arrows mean that communication between components of the system can be done in both directions, while \longrightarrow single headed arrows mean that communication can be done only in the indicated direction.

B.1 APT system architecture

The diagram of system architecture responsible for the correct operation of XY translation stages is shown in fig. B.4; it consists of two blocks - APT² system software and APT hardware units (TDC001). APT system software (called as “PC controller” on the diagram) consists of **APT Server**, which provides an access to the hardware units and provides a set of user interface panels (each for every type of hardware unit) that allow

¹Z stage is not motorized.

²APT stands for Advanced Positioning Technology

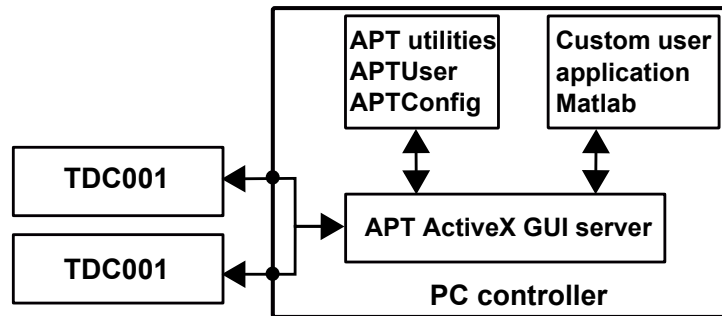


Figure B.4: APT system architecture diagram. The system comprises of APT software block (on the right) and of APT hardware unit blocks (two “TDC001” blocks on the left).

communication between client application and hardware unit via USB bus. This **APT Server** is a kind of multi-threaded ActiveX “engine” on top of which different applications can be built. The default applications supplied with T-Cubes and motors are **APT User**, **APT Config** and **APT utilities**, all of them deploy functionality of **APT Server**. **APT User** application is a graphic user interface panel allowing a complete access to all parameters and settings of hardware unit in order to provide correct hardware operation. For simple hardware operation and on the stage of software debugging in case of the development of more complicated client applications **APT User** application can provide a full functionality necessary to operate hardware units. **APT Config** allows altering certain operation conditions of the hardware such as choice of translation stage (Z712B in our case), **APT Server** settings, and Simulator configurations (for example, it is possible to enable “simulator mode” and then write, test and debug client application without motors and T-Cubes being physically connected to the PC).

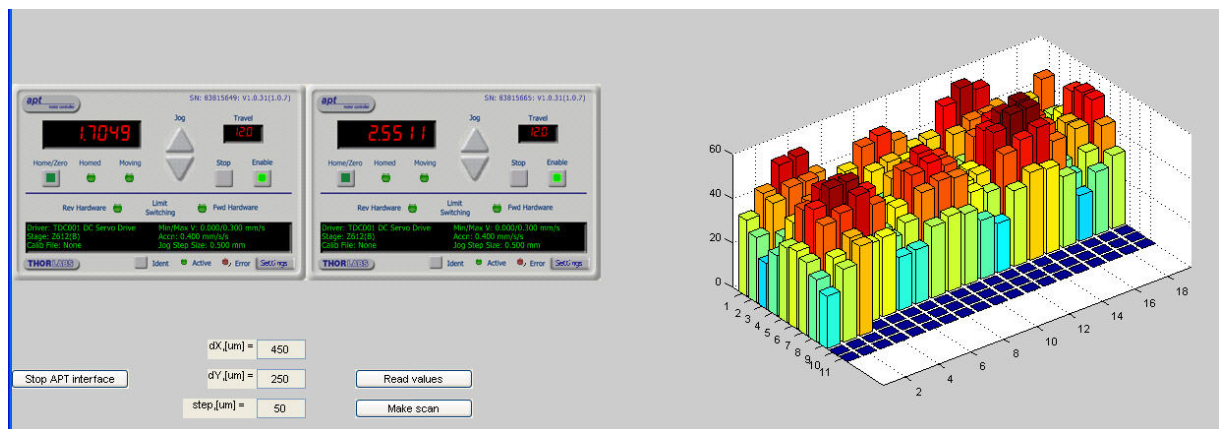


Figure B.5: KT112, single mode and multimode fiber coupler: 5.6 mm and 9 mm laser diodes [8].

A snapshot of developed software managing operation of XY translation stages is shown in fig. B.5. The snapshot shows two user interface panels driving TDC001 hardware units, editable text fields to set parameters of the scan, labels, and buttons to stop APT interface, to prepare and to start the laser scan. The developed software allows also a 3D visualization of the results of the scan.